AD NUMBER
AD920691
LIMITATION CHANGES

TO:

Approved for public release; distribution is unlimited.

FROM:

Distribution authorized to U.S. Gov't. agencies only; Test and Evaluation; APR 1974. Other requests shall be referred to Army Materials and Mechanics Research Center, Watertown, MA.

AUTHORITY

DARPA ltr 19 Dec 1974

THIS REPORT HAS BEEN DELIMITED

AND CLEARED FOR PUBLIC RELEASE

UNDER DOD DIRECTIVE 5200.20 AND

NO RESTRICTIONS ARE IMPOSED UPON

ITS USE AND DISCLOSURE.

DISTRIBUTION STATEMENT A

APPROVED FOR PUBLIC RELEASE;

DISTRIBUTION UNLIMITED.

AMMRC CTR 74-26

BRITTLE MATERIALS DESIGN, HIGH TEMPERATURE GAS TURBINE

Technical Report By:

Arthur F. McLean, Ford Motor Company, Dearborn, Michigan 48121
Eugene A. Fisher, Ford Motor Company, Dearborn, Michigan 48121
Raymond J. Bratton, Westinghouse Electric Corporation, Pittsburgh, Pennsylvania 15235

April, 1974

D D C
RECEIVED
JUL 18 1974
RECEIVED
B

Prepared for:

ARMY MATERIALS AND MECHANICS RESEARCH CENTER
Watertown, Massachusetts 02172

AMMRC CTR 74-26

BRITTLE MATERIALS DESIGN, HIGH TEMPERATURE GAS TURBINE

Technical Report By:

Arthur F. McLean, Ford Motor Company, Dearborn, Michigan 48121
Eugene A. Fisher, Ford Motor Company, Dearborn, Michigan 48121
Raymond J. Bratton, Westinghouse Electric Corporation, Pittsburgh, Pennsylvania 15235

Prepared for:

ARMY MATERIALS AND MECHANICS RESEARCH CENTER
Watertown, Massachusetts 02172

ABSTRACT

The "Brittle Materials Design, High Temperature Gas Turbine" program is to demonstrate successful use of brittle materials in demanding high temperature structural applications. A small vehicular gas turbine and a large stationary gas turbine, each utilizing uncooled ceramic components, will be used in this iterative design and materials development program. Both the contractor, Ford Motor Company, and the subcontractor, Westinghouse Electric Corporation, have had in-house research programs in this area prior to this contract.

In the vehicular turbine project, Weibull theory was utilized to predict failure probabilities of monolithic hot pressed silicon nitride turbine rotors, including the effects of varying disk contours. Good agreement with theory resulted from strength testing of silicon nitride bars and disks. Processing parameters were established for the fabrication of multi-density rotors, and a number of prototype rotors were spin tested. Thermal response of stator vanes during engine operation was determined directly using a quartz window in a stator test rig. Improvements in properties were made for both injection molded and slip cast reaction sintered silicon nitride.

In the stationary turbine project, a major objective was achieved when the first static rig test of hot pressed silicon nitride stator vanes was completed at temperatures up to $2200^{\circ}F$. Although some vanes failed due to out-of-tolerance final machining of critical interfaces, it was encouraging that two vanes which were subjected to the highest temperatures and most severe transient effects were not damaged. Additional information was also generated on the properties and corrosion resistance of hot pressed silicon nitride.

FORWARD

This report is the fifth semi-annual technical report of the "Brittle Materials Design, High Temperature Gas Turbine" program initiated by the Advanced Research Projects Agency, ARPA Order Number 1849, and monitored by the Army Materials and Mechanics Research Center, under Contract Number DAAG-46-71-C-0162. This is an incrementally-funded five year program.

Since this is an iterative design and materials development program, design concepts and materials selection and/or properties presented in this report will probably not be those finally utilized. Thus all design and property data contained in the semi-annual reports must be considered tentative, and the reports should be considered to be illustrative of the design, materials, processing, and NDT techniques being developed for brittle materials.

The principal investigator of this program is Mr. A. F. McLean, Ford Motor Company, and the technical monitor is Dr. A. E. Gorum, AMMRC. The authors would like to acknowledge the valuable contributions in the performance of this work by the following people:

Ford Motor Company

D. Alexander, R. R. Baker, P. Beardmore, D. J. Cassidy, J. C. Caverly, D. A. Davis, G. C. DeBell, A. Ezis, W. A. Fate, M. U. Goodyear, D. L. Hartsock, P. H. Havstad, D. W. Huser, R. A. Jeryan, C. F. Johnson, K. H. Kinsman, J. T. Kovach, J. G. LaFond, J. A. Mangels, S. V. McGrath, W. E. Meyer, J. J. Mittman, T. G. Mohr, P. F. Nicholls, A. Paluszny, J. J. Schuldies, J. M. Scofield, J. R. Secord, K. H. Styhr, L. Swank, W. Trela, N. F. Waugh, T. J. Whalen, W. Wu

Westinghouse Electric Corporation

G. W. Bauserman, D. Boes, C. R. Booher, Jr., E. S. Diaz, A. N. Holden, D. D. Lawthers, R. Kossowsky, T. Lam, F. F. Lange, S. Y. Lee, W. Malchman, D. G. Miller, S. Mumford, J. Owensby, T. J. Rahaim, C. Sanday, R. J. Schaller, S. C. Singhal, J. P. Smed, L. C. Szema, S. Twiss, W. Van Buren, C. Visser, R. Weidenbacker, J. H. White

Army Material and Mechanics Research Center

E. M. Lenoe, R. N. Katz, D. R. Messier, H. Priest

TABLE OF CONTENTS

x

LIST OF TABLES

1. INTRODUCTION

As stipulated by the Advanced Research Projects Agency of the Department of Defense, the major purpose of this program is to demonstrate that brittle materials can be successfully utilized in demanding high temperature structural applications. The gas turbine engine, utilizing uncooled ceramic components in the hot flow path, was chosen as the vehicle for this demonstration. Two hundred hours of operation over a representative duty cycle at ceramic temperatures up to 2500°F is required for the demonstration.

It is the further purpose of this program to develop design technology for ceramic materials on a systems basis requiring close integration of design, engineering, materials selection, materials processing and fabrication, testing and evaluation.

The progress of the gas turbine engine has been closely related to the development of materials capable of withstanding the engine's environment at high operating temperature. Since the early days of the jet engine, new metals have been developed which have allowed a gradual increase in operating temperatures. Today's nickel-chrome superalloys are in use without cooling at turbine inlet gas temperatures of 1800° to 1900°F. However, there is considerable incentive to further increase turbine inlet temperature to improve specific air and fuel consumptions. The use of ceramics in the gas turbine engine as a demonstration vehicle for this program promises to make a major step in increasing turbine inlet temperature. Success will offer significant advances in engine efficiency, power per unit weight, cost, pollution abatement, and fuel utilization.

This program will demonstrate the use of ceramics in two demanding gas turbine applications:

(1) A small-vehicular type of engine (Ford). Such an engine would have a major impact on the technology of mobile field power units, military vehicles and craft. As a consequence of its significantly increased operating temperature it would not only provide more horsepower/unit weight than current engines, but would also provide improved fuel economy. In addition, the benefits of low emissions and multi-fuel capability are attained. A simplified schematic of the flow path of this regenerative type of engine is shown in Figure 1.1. A brief explanation of this flow path will be given to familiarize the reader with the various components considered for ceramics. Air is induced through an intake silencer and filter into a radial compressor, and then is compressed and ducted through one side of each of two rotary regenerators. The hot compressed air is then supplied to a combustion chamber where fuel is added and combustion takes place.
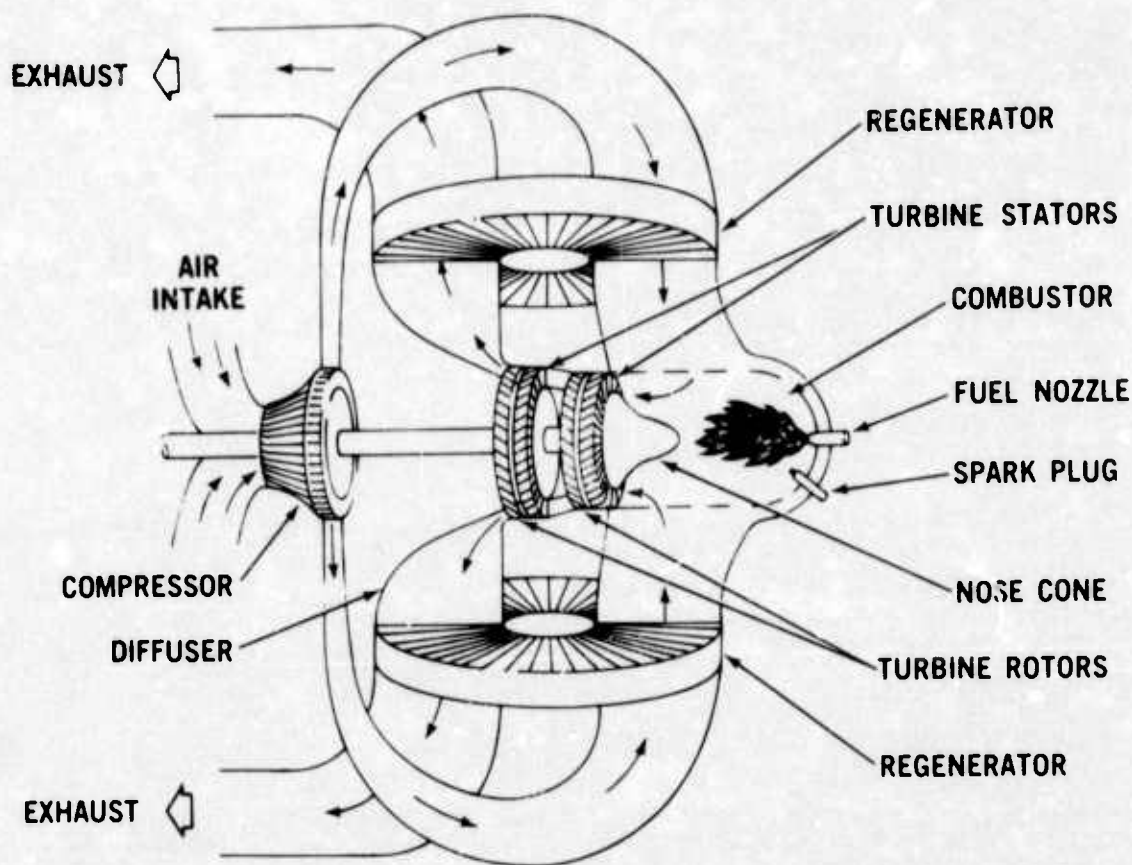
Figure 1.1 - Flow Path Schematic of Vehicular Gas Turbine

The hot gas discharging from the combustor is then directed into the turbine stages by a turbine inlet structure, in this case shown as a nose cone. The gas then passes through the turbine stages which comprise two turbine stators, each having stationary airfoil blades which direct the gas onto each corresponding turbine rotor. In passing through the turbine, the gas expands and generates work to drive the compressor and supply useful power. The expanded turbine exhaust gas is then ducted through the hot side of each of the two regenerators which, to conserve fuel consumption, transfer much of the exhaust heat back into the compressed air.

The parts which are subject to the peak cycle temperature and are made out of superalloys in today's gas turbine are the combustor, the turbine inlet nose cone, the turbine stators and the turbine rotors. These are areas where ceramics could be exploited to the fullest and have been selected for application in the vehicular turbine project.

(2) A large-stationary gas turbine for electric power production (Westinghouse). Such an engine would be most desirable for DOD installations requiring on site power generation. Not only will ceramics facilitate significantly increased operating temperatures with attendant improvement in power and fuel economy, but, because of their improved corrosion-erosion resistance they will also facilitate use of low cost residual fuel. In addition, the environmental benefits of low emissions and lack of cooling water (with its attendant thermal pollution problems) are attained. A simplified sketch of the hot flow path of the engine is shown in Figure 1.2. As with the vehicular turbine project, a brief explanation of the flow path of the stationary turbine will be given to help the reader understand the function of the components to be made from ceramic materials.
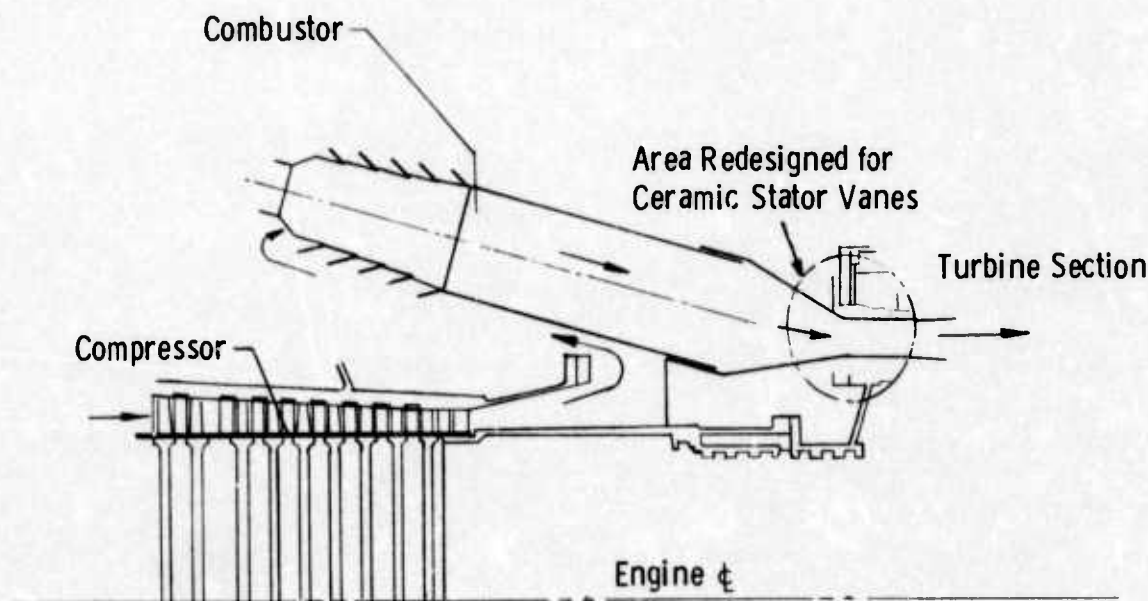
Figure 1.2 - 30 Mw Test Turbine Flow Path

Air is induced through a large intake silencer and filter into an 18 stage axial compressor where it is compressed before entering the combustor housing. The combustor housing supplies air at $650^{\circ}F$ to combustion cans assembled in a a circumferential array. Air is mixed with distillate fuel or natural gas and ignited in the primary combustion zone. The gas passes down stream through the combustors mixing with secondary air. Flow continues from the combustion section, through the transition zone, and enters the power turbine at a gas temperature of $2500^{\circ}F$. The hot gases expand through the three stage turbine section and are either exhausted through a stack or ducted into a reheat boiler as part of a combined cycle power generating unit.

The parts, where ceramics could be exploited to the fullest, selected for application in the stationary turbine project are the first stage turbine stator vanes and the first stage turbine rotor.

3

To maintain coherence, progress on the vehicular and stationary turbine projects are reported separately. Also reported separately is the common link between these two programs, materials technology. Information presented under materials technology is general, and does not specifically apply to one or the other of the gas turbine engines. On the other hand, items reported under the vehicular and stationary turbine projects are categorized by components and therefore relate directly to those projects (even these items, however, are indirectly related when it comes to such considerations as design techniques, etc.). Figure 1.3 has been prepared to help the reader understand the interrelationship between the major elements of the report.


```
┌─────────────────────────────────┐        ┌─────────────────────────────────┐
│  VEHICULAR TURBINE PROJECT      │        │  STATIONARY TURBINE PROJECT     │
│           (Ford)                │◄──────►│        (Westinghouse)           │
│     (Section 3 of Report)       │        │     (Section 4 of Report)       │
│                                 │        │                                 │
│  . Ceramic Rotors, Stators,     │        │  . Ceramic Vanes &              │
│      Shrouds & Nose Cones.      │        │      Rotors.                    │
│                                 │        │                                 │
│  . Design, Analysis, Materials, │        │  . Design, Analysis, Materials, │
│      Fabrication & Testing.     │        │      Fabrication & Testing.     │
└─────────────────────────────────┘        └─────────────────────────────────┘
                      ┌─────────────────────────────────┐
                      │     MATERIALS TECHNOLOGY        │
                      │     (Ford & Westinghouse)       │
                      │     (Section 5 of Report)       │
                      │                                 │
                      │       . Property data           │
                      │       . Microstructure          │
                      │       . NDT                     │
                      └─────────────────────────────────┘
```

Figure 1.3 - Brittle Material Design/High Temperature Gas
Turbine - Breakdown of Major Elements Reported

Successful demonstration of a high temperature gas turbine engine will involve a complex iterative development. One cannot divorce the development of ceramic materials from processes for making parts; no more so can one isolate the design of those parts from how they are made or from what they are made. Likewise, the design of mountings and attachments between metal and ceramic parts within the engine are equally important. Innovation in the control of the environment of critical engine components is another link in the chain. Each of these factors has a relationship with the others, and to obtain success in any one may involve compromises in the others. Testing plays an important role during the iterative development since it provides a positive, objective way of evaluating the various combinations of factors involved. If successful, the test forms the credibility to move on to the next link in the development chain. If unsuccessful, the test flags a warning and prompts feedback to earlier developments to seek out and solve the problem which has resulted in failure. Finally, all of the links in the chain are evaluated by a complete engine test, by which means the ultimate objective of the program will be demonstrated.

One difference in philosophy between the two turbine projects is worth noting. Because the science of ceramic materials, fabrication processes and designs is not fully developed, the vehicular turbine engine was designed as a test bed, and features ease of replacement of ceramic components. New ideas in a component's material, process, or design can therefore be engine-evaluated fairly rapidly. This work can then parallel and augment the time consuming efforts on material and component characterization, stress analysis, heat transfer analysis, etc. Some risk of damage to other components is present when following this approach, but this is considered outweighed by the more rapid acquisition of actual test information. On the other hand, the stationary gas turbine engine is so large, so expensive to test, and contains many costly components which could be damaged or lost by premature failure, that very careful material and design work must be performed to minimize the possibility of expensive, time-consuming failures.

Figure 1.4 shows a block diagram flow chart of the major factors involved including the feedback loops, which serves to illustrate this complex and comprehensive iterative development program. The starting point is the concept of a design to use brittle materials. From this, a design layout is prepared and analyzed leading to the detailed design and analysis of the gas turbine engine components made of or involving ceramics. In parallel with the design phase, ceramic materials are developed and screened for application to the gas turbine engine. Process development of candidate ceramics then takes place and material science and property evaluation are used to improve materials and processes, and to feed information back into the design phase. Next, with the first detailed designs completed and with the process for the selected ceramics reasonably developed, tooling can be designed and fabrication development started to make actual ceramic turbine engine components. Non-destructive testing of these parts will be developed to form a feedback for improving material and fabrication methods. In conjunction with non-destructive evaluation, techniques will be developed for proof testing ceramic components prior to use in engines. In parallel with ceramic part fabrication, proof testing, and non-destructive evaluation, metal parts for the ceramic turbine engine and test rigs are made per the detailed design requirements. The ceramic and metal parts are then dimensionally inspected and instrumented for engine testing. Assembly techniques for brittle materials are developed, and testing and durability development in both test rigs and engines is performed. Failure analysis from test rig and engine testing forms the feedback loops for corrective action; almost all of the factors involved in the development could be affected by experience learned in the test phase of the program. Finally, when engine durability has reached a given level of development, the 200 hour demonstration test will be conducted to meet the program objective.

It should be noted that both the contractor and subcontractor had in-house research programs in this area prior to the initiation of this program. Many ceramic materials were extensively tested and screened leading to the selection of silicon nitride and silicon carbide. In the stationary turbine program, preliminary design concepts were in existence before the award of the
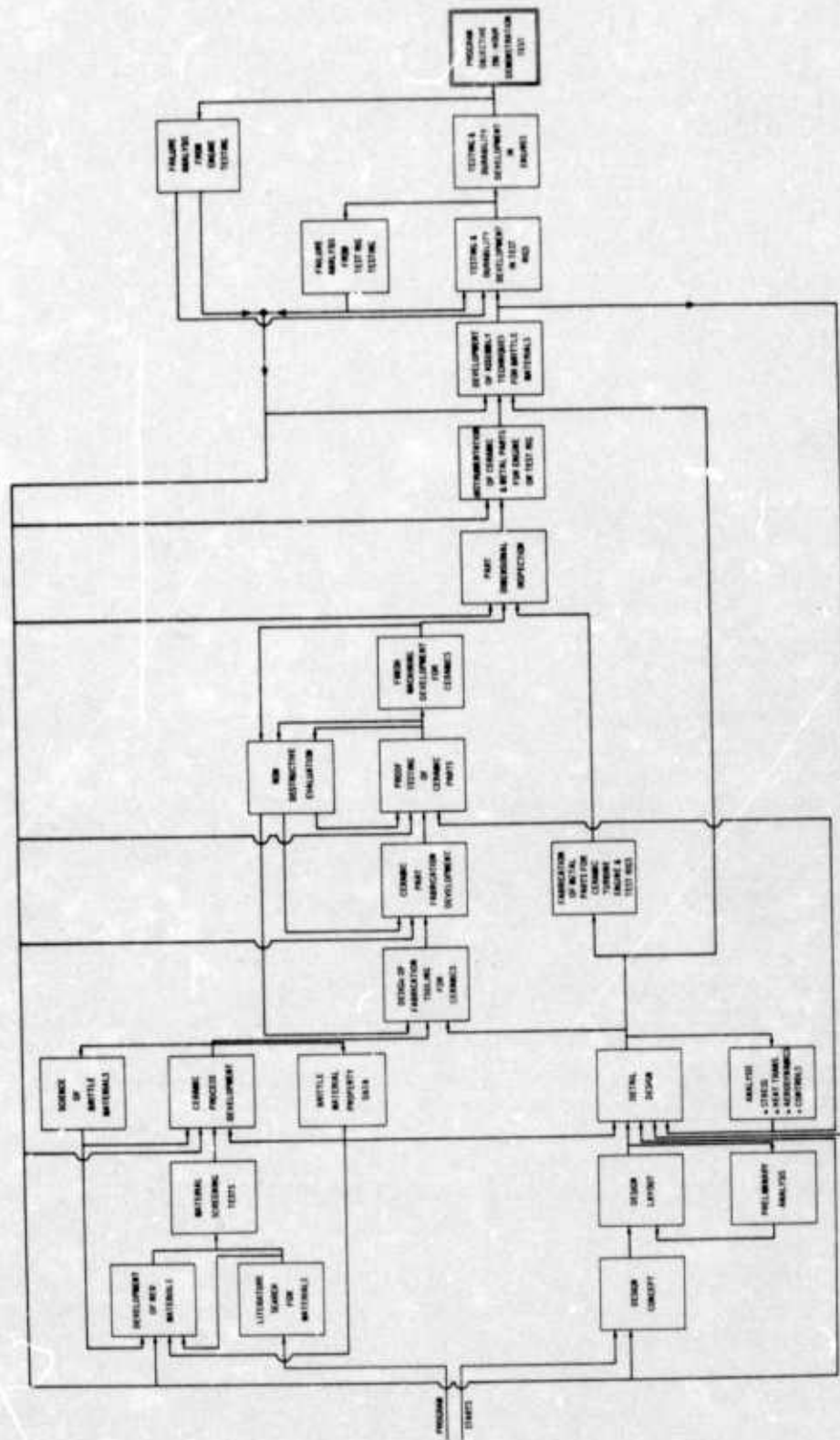
Figure 1.4 — Brittle Material Design/High Temperature Gas Turbine — Block Diagram Flow Chart of Iterative Development

6

contract. In the vehicular turbine program, development was fairly well along and at least one pass had been completed through all of the factors shown in Figure 1.4 prior to the initiation of this program. This one pass, involving many minor iterations, led to a vehicular turbine hot flow path having all ceramic stationary components and designated Design A. Based on further experience gained during engine testing, a modified flow path was generated and designated Design B.

Since initiation of this program with AMMRC and ARPA, work on both the vehicular and stationary gas turbine projects was accelerated. Work accomplished during the first reporting period [1] included, for the vehicular turbine project, initial fabrication development and preliminary testing of Design B turbine stators and nose cones made of reaction sintered silicon nitride. Design studies of ceramic turbine rotors showed that computed operating stresses can be withstood by dense silicon carbide and dense silicon nitride. Development programs were started to explore several approaches to fabricate rotors in these materials.

Accomplishments on the stationary turbine project during the first reporting period included obtaining physical property data of hot pressed silicon nitride and identifying microstructural details of this material. The initial design of ceramic stator vanes was completed and calculated vane stresses were reduced 40% by decreasing the stator vane chord.

The results of work accomplished during the second reporting period [2] included, for the vehicular turbine project, continued fabrication development as well as rig and engine testing of the second generation design (Design B) turbine stators and inlet nose cones. Ceramic turbine rotor design studies were performed on an expanded two-dimensional heat transfer computer program to include rotor attachment designs. Progress was reported on the multi-approaches being explored to fabricate a one-piece, intricately-shaped turbine rotor from candidate high strength ceramic materials.

The results of work accomplished on the stationary turbine project included the stress analysis and design of first stage vanes as well as a preliminary report on the rig for statically testing the stator vanes. Progress on the development of a new three-dimensional, finite-element, stress analysis computer program for subsequent use in ceramic rotor blade design was also reported.

Development in materials technology for both the vehicular and stationary gas turbines was reported and included continued compilation of material property data, continued characterization of material structure, and development of non-destructive evaluation techniques such as ultrasonics, radiography and acoustic emission.

The results of work accomplished during the third reporting period [3] included, for the vehicular turbine project, considerable emphasis on the development of the ceramic turbine rotor. Development was started on a new concept for a silicon nitride rotor, termed "duo-density". Progress was made on the stress analysis and the development of machining techniques for fabricating monolithic rotors from high-strength

hot-pressed materials. A cracking problem in the first stage stator blade appeared solved with the aid of a thermal shock test rig.

On the stationary turbine project, a full scale model of the first generation stator vane assembly showed that the design was functional when subjected to differential motions well in excess of design limits. Using improved physical property data, the transient thermal stresses in the first stage stator vane were recalculated. The three-dimensional stress analysis program was applied to a dense silicon nitride rotor blade.

Work on materials technology resulted in additional property data on candidate ceramic materials, and further relationships of microstructure to properties were uncovered. A number of processing parameters were examined for reaction-sintered silicon nitride.

The work accomplished during the fourth reporting period [4] included, for the vehicular turbine project, the continued development of methods for fabricating duo-density silicon nitride turbine rotors during which several rotors were made; the best of these was spin-tested to 50,500 rpm before failure. A refined stress analysis of a monolithic silicon nitride rotor was completed, and the effects of a severe flame-out transient on the duo-density rotor was analyzed. Design revisions have been made to both stator stages, which resulted in the elimination of most but not all cracking.

Work accomplished on the stationary turbine project included stator vane design modifications with improvements to aerodynamics and methods of mounting. Additional stress analyses have been performed at critical interfaces. The static test rig, for evaluation of ceramic stator vanes under realistic gas turbine conditions, has been completed and installed. Design concepts and stress analyses of rotating turbine blades continued to be investigated.

Work on materials technology was continued, and a considerable amount of mechanical and thermal property data on silicon nitride and silicon carbide was determined. The microstructure of hot pressed silicon carbide was studied, and further process improvements were made for reaction sintered silicon nitride.

During this fifth reporting period, work on the vehicular turbine project included an investigation and experimental evaluation of the use of Weibull theory for predicting probability of failure of turbine rotors. Processing development was concentrated on multi-density silicon nitride rotors, a number of which were cold spin tested. The thermal response of first stage stator vanes during engine testing was determined by direct observation through a quartz window, and correlated with thermal response data obtained on the thermal shock test rig.

Work on the stationary turbine project passed a major milestone with the completion of the first static rig testing of silicon nitride vanes at temperatures up to 2200°F. All silicon nitride vanes which met design specifications successfully survived more than 100 thermal transient cycles. Parts which did not meet design specifications cracked in a non-catastrophic manner due to an edge loading condition.

8

Work on materials technology explored the effect of impurities in hot pressed silicon nitride as well as oxidation-sulfidation testing of hot pressed silicon nitride and improvements in the properties of both injection molded and slip cast reaction sintered silicon nitride.

Summarizing the current program status, it appears that the vehicular gas turbine engine stationary flow path components will meet the final 200 hour goal with further expected improvements in design, materials, and processing. Nose cones and rotor shroud rings of current designs and materials should be capable of reaching this goal now, although further improvements are expected to improve reliability. It is also felt that design and processing modifications currently in progress will sufficiently improve stator durability to achieve the final goal. The ceramic turbine rotor development is the most critical area and requires solution to several major engineering problems. More effort is being concentrated in fabricating rotors for testing. On the stationary gas turbine engine, results to date indicate that a viable stator design has been achieved. Continued effort on quality control and material reliability should result in successful program completion, requiring only minor future modifications.

This report covers the progress in the period July 1, 1973, through December 31, 1973.

2. SUMMARY OF PROGRESS

2.1 VEHICULAR TURBINE PROJECT

The vehicular turbine project is composed of three primary section -- design, materials, and testing. Within these primary areas there exist many tasks which must be accomplished in order to achieve the program goal of 200 hours of turbine engine operation over a representative duty cycle at ceramic temperatures up to 2500°F. Each semi-annual report is really a progress report detailing the results of work over a six month time increment, and reporting on the individual accomplishments on the tasks which will culminate in the final program objective.

Work is in progress concurrently in areas of turbine engine component design and analysi ceramic material and process development, material and engine testing, materials technology, and nondestructive evaluation of ceramic engine components. Progress, made in several of these areas in this reporting period, is summarized in this section of the report.

(1) Probability of failure analyses, based on Weibull theory, were conducted on monolithic hot pressed silicon nitride rotors. Probabilities were determined for steady state and transient modes, and included an analysis of the effect of variations in rotor disk geometry. Refer to Section 3.1.1 of this report for more information.

(2) The applicability of Weibull theory for turbine rotor use was evaluated experimentally. Using hot pressed silicon nitride, the relation-ship between the strength of bars tested in four point flexural loading and disks spin-tested to failure (tensile loading) was determined for the effective volume criteria. Actual results agreed closely with predictions. Refer to Section 3.1.1 for details.

(3) A number of processing parameters have been sufficiently developed to enable duo-density and triple-density rotors to be fabricated and evaluated. Section 3.1.2 describes this work in detail.

(4) Ultrasonic machining has been successfully utilized for finishing the hot-pressed silicon nitride disks of multi-density turbine rotors. This program is described in Section 3.1.2.

(5) Thirteen rotors were cold spin tested to failure. The best of them burst at 50,300 rpm and 55,700 rpm for the duo-density and triple-density rotors respectively. Refer to Section 3.1.3 for more information.

(6) A quartz window was installed in the ceramic stator test rig, permitting direct observation and temperature measurement of first stage stator vanes during engine operation. A correlation was established with thermal shock test rig evaluation of the stator vanes. Section 3.2.2 contains the details of this investigation.

2.2 STATIONARY TURBINE PROJECT

The stationary turbine project is a design study of brittle materials in a high temperature gas turbine application, culminating with the demonstration of uncooled ceramic stator vanes in an advanced power turbine operating for 200 hours. This operation will consist of 100 sequences of peaking cycle service. A performance simulation of ceramic rotor blades will also be performed by computer. Work is currently in progress in areas of stator vane design and analysis; rotor blade design and analysis based on 3 dimensional finite element stress analysis codes; component fabrication and performance evaluation; and material technology. Progress is summarized in this section of the report.

(1) Gas path temperatures have been calculated for the advanced turbine. These data were used to define the cooling requirements for the first stage metal rotor and the second metal stage stator vane row which will remain air-cooled. Refer to section 4.1.1 of this report for more detailed information.

(2) Silicon nitride stator vane assemblies were tested successfully in the static rig under cyclic conditions to 2200°F at pressure ratios between 3 and 8:1. Cracks were observed in 4 of 8 airfoils and 2 outer end caps after 106 controlled shutdowns from peak to idle temperature. The test assembly remained totally functional at the end of the test sequence. Refer to section 4.1.2 of this report for more detailed information.

(3) Failure analysis of the Si_3N_4 stator vane assemblies tested in the static rig indicated that all of the cracks developed from areas of high stress concentration which were associated with edge loading. The condition was attributed to the vane manufacturer's inability to meet the required design tolerances at the airfoil-end cap interface. Thermal stress may have contributed to crack propagation but it was certainly not a primary cause of failure. Refer to section 4.1.1 of this report for more detailed information.

(4) Seven hot-pressed silicon carbide vane assemblies were received from the Norton Company. While dimensional accuracy is improved greatly over that observed in similar silicon nitride hardware, some rework is required to preclude the edge loading condition which presumably caused failure of the Si_3N_4 vanes in the static rig test. Refer to section 4.1.3 of this report for more detailed information.

(5) The Westinghouse Isoparametric Element Code (WISEC) for the three-dimensional stress analysis of turbine stator vanes and rotor blades has been improved by the addition of a mesh generator. The theoretical aspects of creep analysis with isotropic material properties are complete. Refer to section 4.2.1 of this report for more detailed information.

(6) The stress analysis of ceramic rotor blading has been extended to include steady state thermal and centrifugal loading conditions where the contact force is uniformly distributed at the blade root-metal disc surface. Refer to section 4.2.2 of this report for more detailed information.

12

2.3 MATERIALS TECHNOLOGY – VEHICULAR AND STATIONARY PROJECTS

Complete property characterization of the ceramic materials for turbine engine use is an enormous task, which will proceed throughout the life span of the contract. This task is complicated by the fact that many of the materials being investigated are in the developmental stage. Improvements in properties are anticipated, which will require that some, if not all of the physical properties will be re-determined eventually. Progress in materials technology is summarized in this section of the report.

(1) Weibull parameters for hot pressed silicon nitride and silicon carbide were determined from available strength data and failure probability plots were prepared. Section 5.1.1 contains more information on this work.

(2) Creep testing of injection molded reaction sintered silicon nitride has provided further proof that calcium-containing impurities are the primary cause of creep. The presence of aluminum appears to be harmful as well, but to a lesser degree than calcium. Fine grain structure also improves creep resistance. Refer to Section 5.1.2 for more information.

(3) Creep of slip cast reaction sintered silicon nitride was investigated. The use of iron oxide as a nitriding aid was also found beneficial for improved creep resistance. Section 5.1.2 contains details of this work.

(4) An experimental study of the effect of grain-boundary impurities normally found in hot pressed silicon nitride on wetting and interfacial reactions was carried out. Refer to Section 5.2.1 for details.

(5) The effect of sulfur in turbine fuel on oxidation and sulfidation of hot pressed silicon nitride and silicon carbide was investigated. Section 5.2.2 discusses this work.

(6) Improvements in the strength of injection molded reaction sintered silicon nitride have been made. The use of small amounts of hydrogen added to the nitriding atmosphere, removal of a coarse fraction from the silicon metal powder starting material, and the addition of iron oxide as a nitriding aid were all effective in increasing strength. Refer to Section 5.2.3 for more information.

(7) Slip casting processes have been developed for the fabrication of reaction sintered silicon nitride components. Section 5.2.4 presents the results of this work.

(8) Differences in the operating characteristics of ultrasonic transducers were found to have considerable influence upon defect detection in hot pressed silicon nitride. Refer to Section 5.3.1 for more information.

(9) A method was developed for monitoring acoustic emission response of silicon nitride stators during a furnace testing sequence. Section 5.3.2 contains data obtained from a second stage inverted channel stator.

(10) X-ray radiography was evaluated for locating defects in as-molded turbine rotors and inclusions in hot pressed silicon nitride. Section 5.3.3 discusses this work.

(11) Resolution limits for defects in hot-pressed Si_3N_4 and SiC have been determined for X-ray radiography and ultrasonic scanning. Refer to section 5.3 of this report for more detailed information.

3. PROGRESS ON THE VEHICULAR TURBINE PROJECT

3.1 CERAMIC ROTOR DEVELOPMENT

SUMMARY

An in-depth study has been directed to the application of Weibull Statistical Flaw Theory to predict probability of failure of monolithic hot pressed silicon nitride rotors. The effects of varying throat and bore thickness as well as disk contours were investigated. Probability of failure predictions were made for each configuration at two engine operating conditions. A correlation study using hot pressed silicon nitride was performed to evaluate the theory by spin-testing disks and breaking small transverse test samples.

Work has been initiated on the three-dimensional analysis of ceramic rotors. A structural analysis computer program and a transient thermal analysis computer program have been procured and are currently being implemented. Both computer programs are based on finite element techniques and are fully compatible with each other.

Development work is continuing on the "duo-density" silicon nitride rotor concept. Pressing parameters were established for press-bonding the injection molded blade rings and the hot pressed hubs. A modified version of this concept using a third element, a ring of slip cast silicon nitride introduced between the blade ring and the hub, called "triple-density", is being developed. The slip cast material increases the rigidity of the blade ring during press-bonding. A compression rig has been built to allow independently controlled pressures to be applied to two critical locations during the press-bonding cycle.

Several techniques are being evaluated to determine the most suitable material for supporting the blades during press-bonding. Boron nitride power was evaluated and found inadequate as a support. Work is continuing using reaction sintered silicon nitride as a blade fill material. The chemically vapor deposited silicon carbide rotor program has been terminated as a result of low strength as measured by cold spin pit testing and apparent material inhomogenity. The study of electric discharge machining of hot-pressed silicon carbide has also been stopped. Ultrasonic machining is being used successfully in machining of rotor disk contours and center bores, although work on blade machining was discontinued.

Thirteen ceramic rotors have been cold tested in the vacuum spin pit. Blade failures occurred at 50,300 rpm and 55,700 rpm for the best "duo-density" and "triple-density" rotors respectively.

The thermal shock test rig is being used to evaluate the thermal shock characteristics of ceramic rotor blades. The blades were subjected to simulated engine transient thermal loads. No failures were observed after 250 cycles at the simulated engine idle condition. Blade failures began to occur as the test rig operation increased in severity to conditions which simulated maximum engine inlet temperatures. Work is planned to investigate these failures during the next reporting period.

As an overall assessment, many approaches for a ceramic turbine rotor have been investigated and most of these have been dropped because they were judged unlikely to succeed in the time available. Currently, the primary candidate for a one-piece ceramic turbine rotor for the vehicular engine is the multi-density Si_3N_4 rotor; this choice, however, could change with material and/or fabrication breakthroughs. Several multi-density Si_3N_4 rotors have been made, although the bond quality between the hot pressed hub and injection molded blade ring is still unsatisfactory. In addition, cold spin testing of blade rings indicates that the strength of the injection molded Si_3N_4 needs further improvement to consistently withstand the stress associated with full speed operation. Planned programs to improve both the injection molded material and the bond quality are expected to result in turbine rotors suitable for hot testing. Because hot testing has not yet started, associated problems which can normally be expected in this type of development have not yet been uncovered. For this reason, the confidence for achieving a successful ceramic turbine rotor within the program timing cannot be as high as for the stationary components with are well into the iterative development phase.

3.1.1 DESIGN AND ANALYSIS

Introduction

A method of predicting the probability of failure of ceramic turbine rotors based on Weibull's statistical flaw theory is presented with predictions for various rotor geometries subjected to maximum steady state and transient stress conditions. Results from a program to correlate the strength of hot pressed silicon nitride MOR test bars with the strength of spin disks of the same material are included. A method of assembling the ceramic turbine rotors to the metallic high speed shaft with the folded bolt has been developed and is discussed.

Strength Analysis and Probability of Failure of Hot-Pressed Silicon Nitride Rotors

During this reporting period, strength and probability of failure analyses were made on the Design C monolithic hot-pressed Si_3N_4 turbine rotors.

The strength and probability of failure analyses reported are based on Weibull's statistical flaw theory. This theory was chosen since it contains a simple mathematical expression and, compared to other biaxial fracture criteria, yields more conservative strength predictions in the tension-tension quadrant in which a major portion of the turbine rotor structure will normally operate. This analysis assumes that hot-pressed Si_3N_4 has isotropic mechanical properties. While it has been shown that this material is weaker in the direction parallel to the hot pressing motion the major stresses in the rotor lie in the perpendicular or "strong direction"; therefore, any errors resulting from this assumption should be insignificant. The compressive principal stresses induced in the outer regions of the disk (above the disk throat) by thermal gradients are relatively low, and even under the extreme transient operating conditions do not exceed the ultimate strength in tension. Therefore, it is anticipated that the omission of the contribution of the compressive stresses to the fracture strength, the apparent weakness of Weibull's theory, will have negligible effect on the predicted probability of failure.

The probability of failure analysis is based on a generalized three-parameter Weibull function, providing-where applicable-a zero probability of fracture stress. For most structural ceramics, the general consensus is to assume this stress to be zero. Weibull's probability of failure for a structural component or element is:

$$P = 1 - e^{-B} \tag{1}$$

where: $B = $ risk of rupture $= \displaystyle\int_V \frac{(\sigma_n - \sigma_u)^m}{\sigma_o} dv \tag{2}$

$\sigma_n = $ the normal stress in tension

$\sigma_u = $ stress below which there is no failure; i.e. the threshold stress

$$\sigma_o = \text{normalizing stress}$$

$$m = \text{Weibull slope, a measure of the variability in material strength}$$

(m, σ_u, and σ_o are commonly referred to as the Weibull parameters)

In the general case of a structure, such as the turbine rotor where the stress distribution is arbitrary and the Weibull paprameters may vary throughout, the risk of rupture of the total structure can be expressed more conveniently as the summation of the risks of rupture of individual elements dV:

$$B = \int_V \left(\frac{dB}{dV}\right) \quad dV \tag{3}$$

where: $\frac{dB}{dV}$ is the risk of rupture per unit volume around a

point and is obtained by integrating the Weibull function

$$\left(\frac{\sigma_n - \sigma_u}{\sigma_o}\right)^m \tag{4}$$

over those directions in which tensile stresses occur

$$\frac{dB}{dV} = \iint K \left(\frac{\sigma_n - \sigma_u}{\sigma_o}\right)^m d\theta \tag{5}$$

where: $d\theta$ = the spatial angle

The constant K in the above equation depends upon the local values of the Weibull parameters and the state of stress for the element dV, whether it is uniaxial, biaxial, or triaxial. The normal stress in the direction of the spatial angle $d\theta$ is σ_n.

In an axisymmetric solid, such as the disk of a turbine rotor, the elemental volume dV in equation (3) is a ring of radius R, concentric with the rotor axis and having a cross-sectional area of dA.

$$dV = 2\pi R \, dA \tag{6}$$

Differentiating equation (3) with respect to A and substituting equation (6) we obtain the risk of rupture intensity.

$$\frac{dB}{dA} = 2\pi R \left(\frac{dB}{dV}\right) \tag{7}$$

The risk of rupture intensity contour maps for the first stage turbine rotor at maximum steady-state and two transient operating conditions are shown in Figures 3.1a, 3.2a, and 3.3a. These three conditions have been used in work reported earlier [4] to evaluate the rotor design. The maximum steady-state condition corresponds to full throttle operation and the two transients correspond to cold start and cold engine acceleration respectively. The cold start or first transient, as it is referred to throughout the remainder of this section, assumes the engine initially to be shutdown and at room temperature. The rotor blades are suddenly subjected to a hot gas stream and a rotational speed corresponding to the partial power output conditions. At maximum stress during this transient, the engine operating conditions are suddenly increased to full power. This represents full throttle acceleration of a cold engine and is termed the second transient.

18

HOT GAS FLOW

0.1

25000.

50000.

25000.

25000.

25000.

50000.

RISK OF RUPTURE INTENSITY
DISK PROBABILITY OF FAILURE = 12/10000

0.1
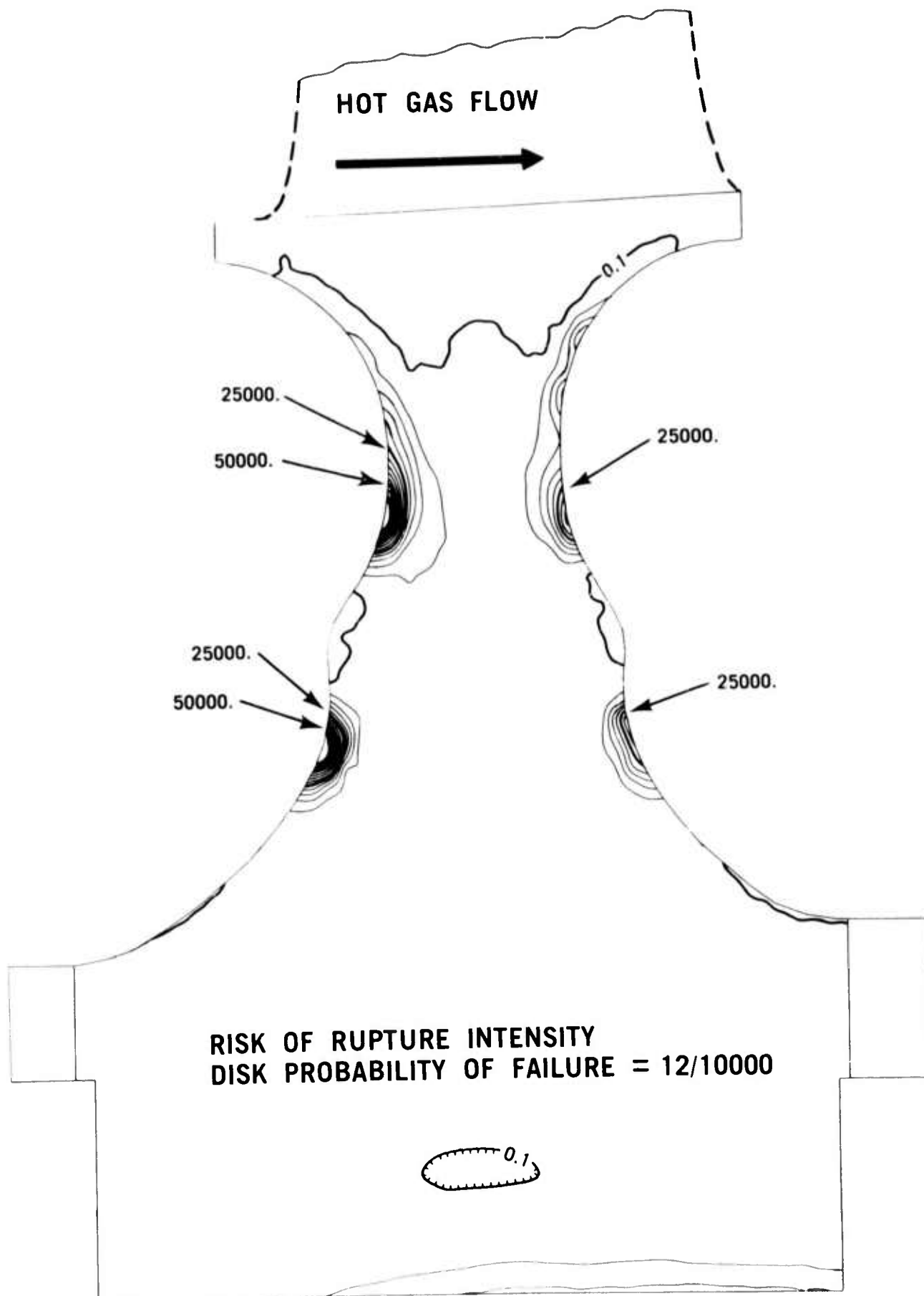
Figure 3.1a   First Stage Rotor Risk of Rupture Intensity Map
For The Maximum Steady State Condition   19
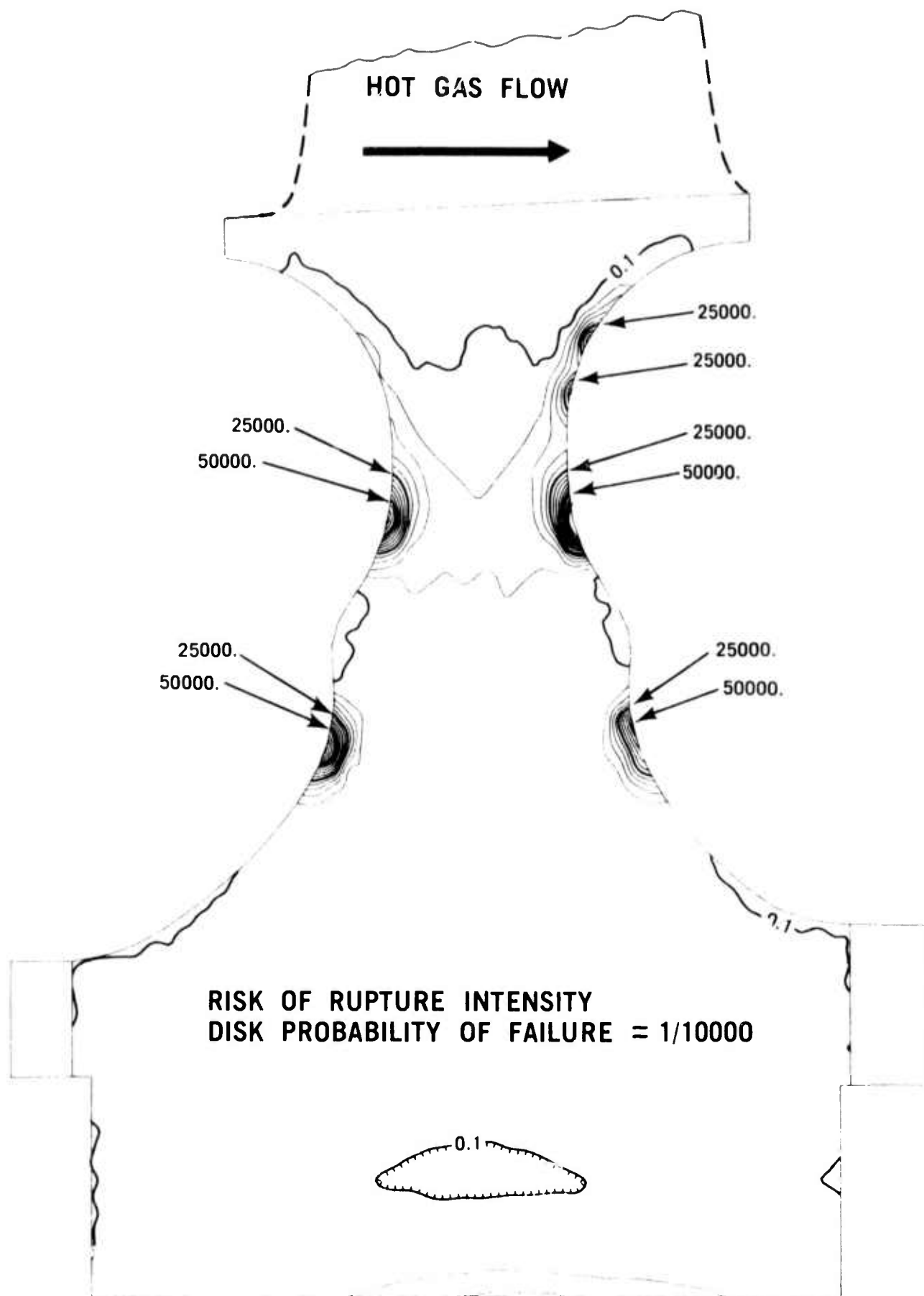
Figure 3.2a   First Stage Rotor Risk of Rupture Intensity
               Map For The First Transient Condition
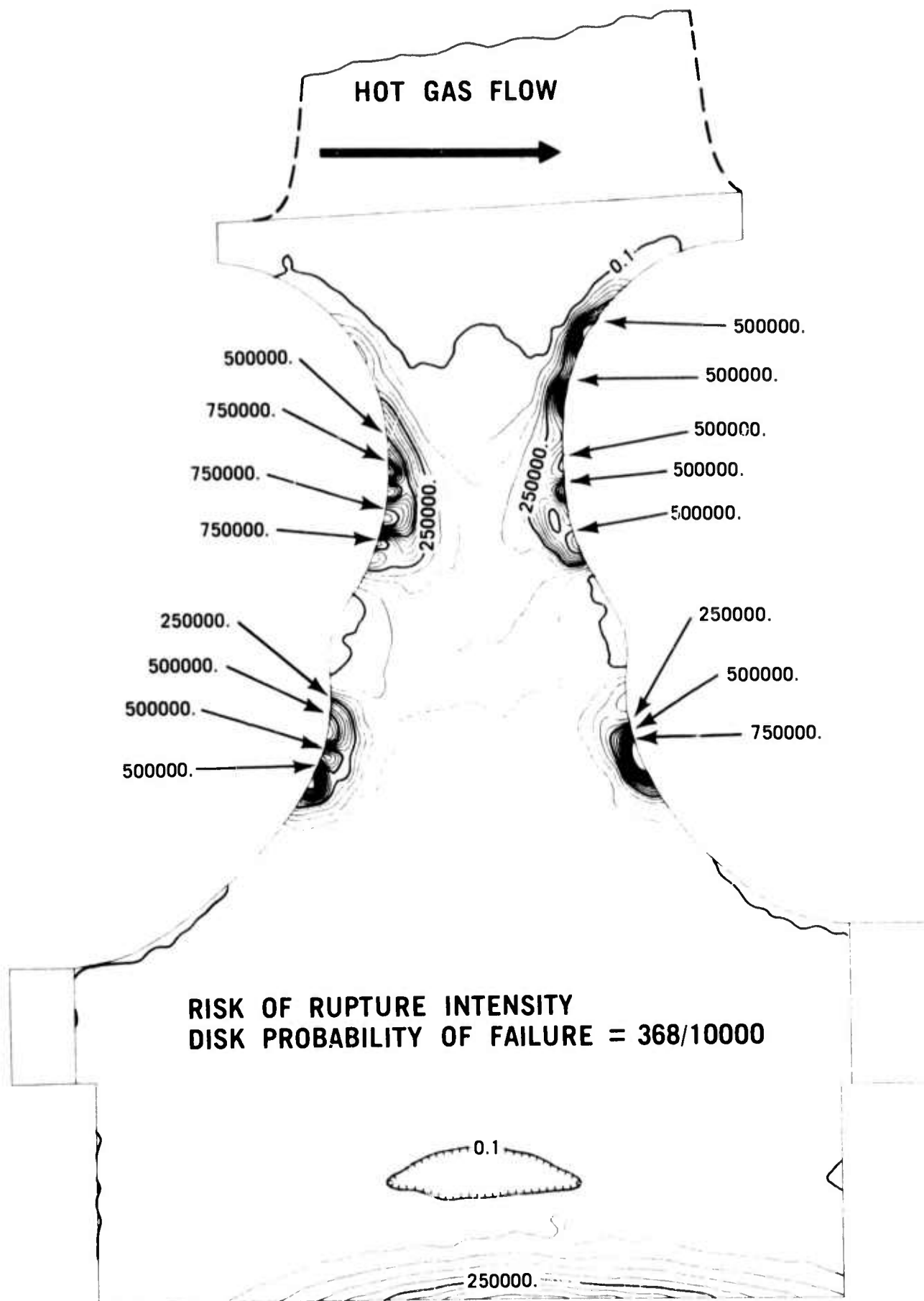
Figure 3.3a   First Stage Rotor Risk of Rupture Intensity
Map For The Second Transient Condition

Table 3.1 summarizes the total risks of rupture and probabilities of failure for both rotor disks at the conditions described above. In these computations the blade loads were included but the contribution of the blades to the failure probability of the rotor was omitted. It should be noted that the values shown describe the failure probabilities or strengths for the loading conditions upon which they are calculated and should not be interpreted as the probabilities of failure in service.

The values of the Weibull parameters used in this analysis were obtained from modulus of rupture (MOR) tests of hot-pressed Si_3N_4 bars. It is to be noted that, at this point in the study, the purpose is to determine the effect probability analysis will have on the design of a rotor rather than exact values of failure probability.

The risk of rupture intensity contour maps are similar in appearance to the stress contour maps, which are shown in Figures 3.1b, 3.2b, and 3.3b. They also accentuate the areas of stress concentration in the neck, and particularly around the balancing rings. These areas are the locations where failure is most likely to occur. In contrast, the immediate area of the bore, which is as equally severely stressed as is the neck, is less likely to be an area of failure initiation, strictly due to the fact that a much smaller volume is exposed to high stresses. This is indicated in Equation (7), which shows that when two areas have the same stress level and therefore the same risk of rupture per unit volume (dB/dV), the one which has the larger radius and thus the larger volume will have a higher failure probability.

Table 3.1 Summary of Total Risks of Rupture and Probabilities of Failure For Design C Monolithic Hot Pressed Silicon Nitride Turbine Rotor Disks.

CONDITION	MAXIMUM STEADY STATE	FIRST TRANSIENT	SECOND TRANSIENT
First Stage Turbine Disk			
Risk of Rupture	12/10000	1/10000	375/10000
Probability of Failure	12/10000	1/10000	368/10000
Second Stage Turbine Disk			
Risk of Rupture	24/10000	0.9/10000	235/10000
Probability of Failure	24/10000	0.9/10000	232/10000

Weibull Parameters $\sigma m = 9.6$
$\sigma u = 0$
$\sigma_o = 57,800$ psi

Typical of HS-130 Hot Pressed Silicon Nitride, Based on Work at Norton, Lucas, and Westinghouse.
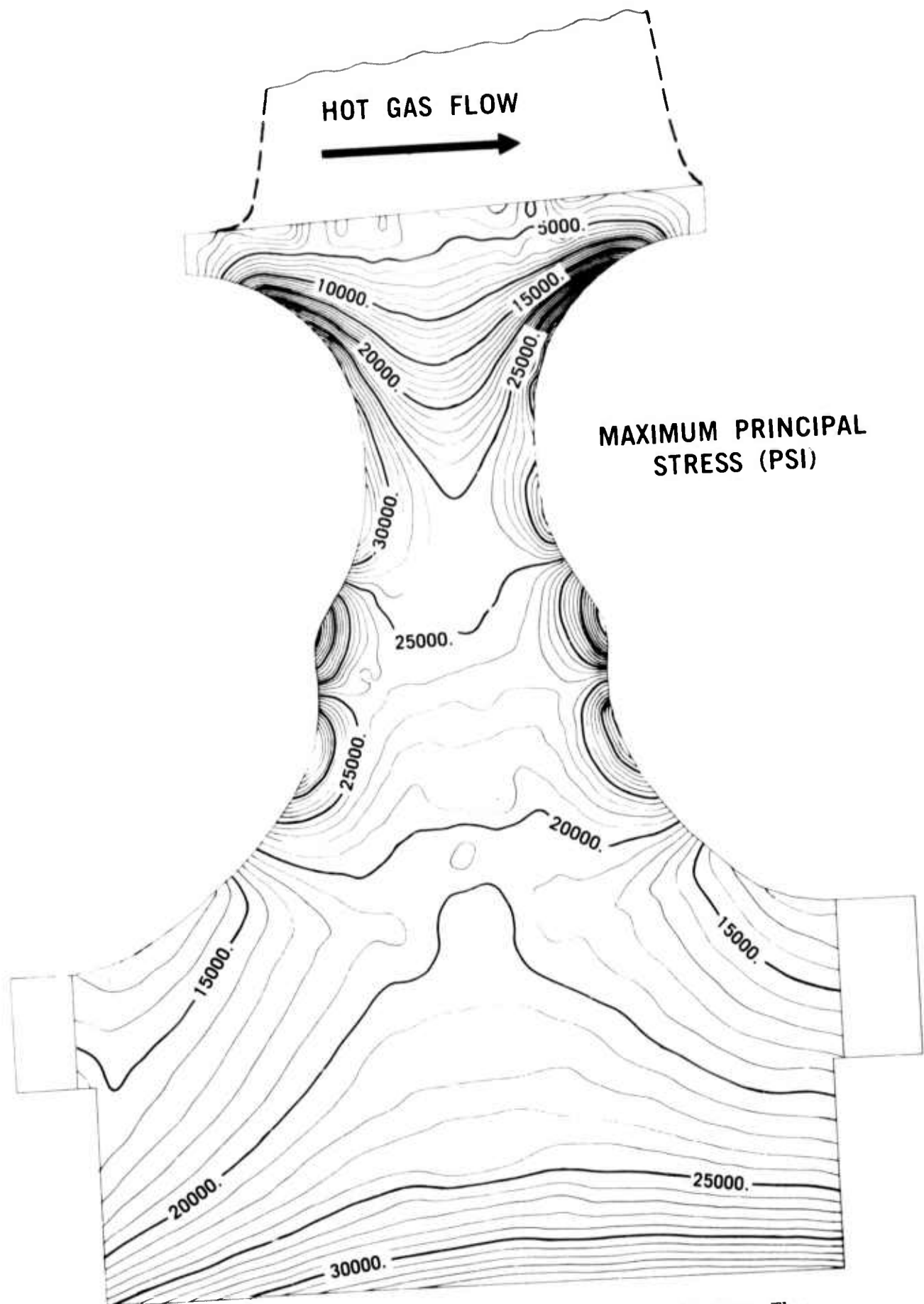
Figure 3.1b   First Stage Rotor Stress Contour Map For The
Maximum Steady State Condition

HOT GAS FLOW

MAXIMUM PRINCIPAL
STRESS (PSI)
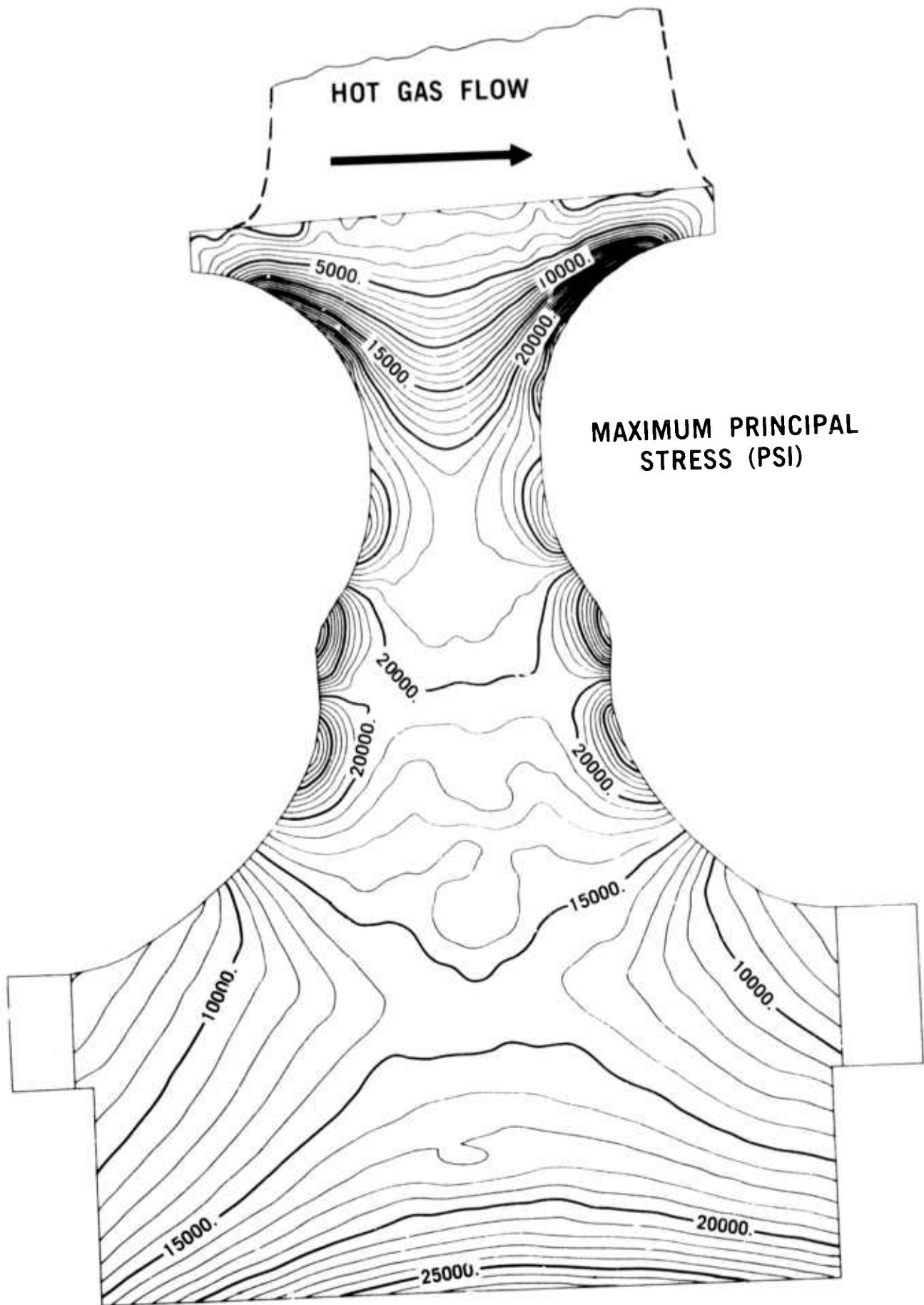
Figure 3.2b   First Stage Rotor Stress Contour Map For
The First Transient Condition
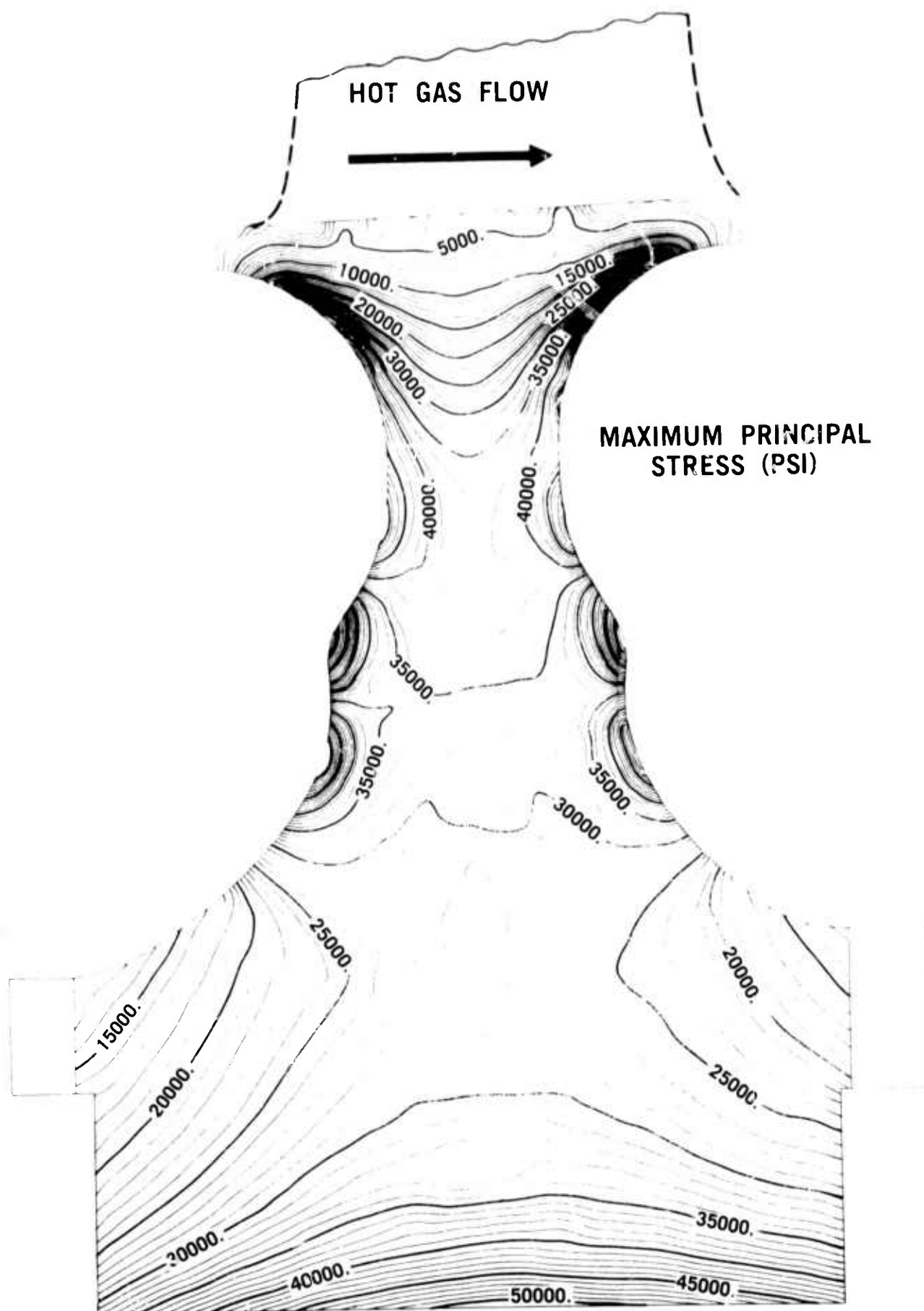
Figure 3.3b   First Stage Rotor Stress Contour Map For The
Second Transient Condition

With this in mind, a series of modifications were conducted on the basic disk contour of the first stage rotor, primarily in the areas where it appeared that the material was least effectively utilized, and the effect of these modifications on the risk of rupture intensity distribution and on the total probability of failure was evaluated. Some selected risk of rupture intensity distribution maps from this study are shown in Figures 3.4 and 3.5.
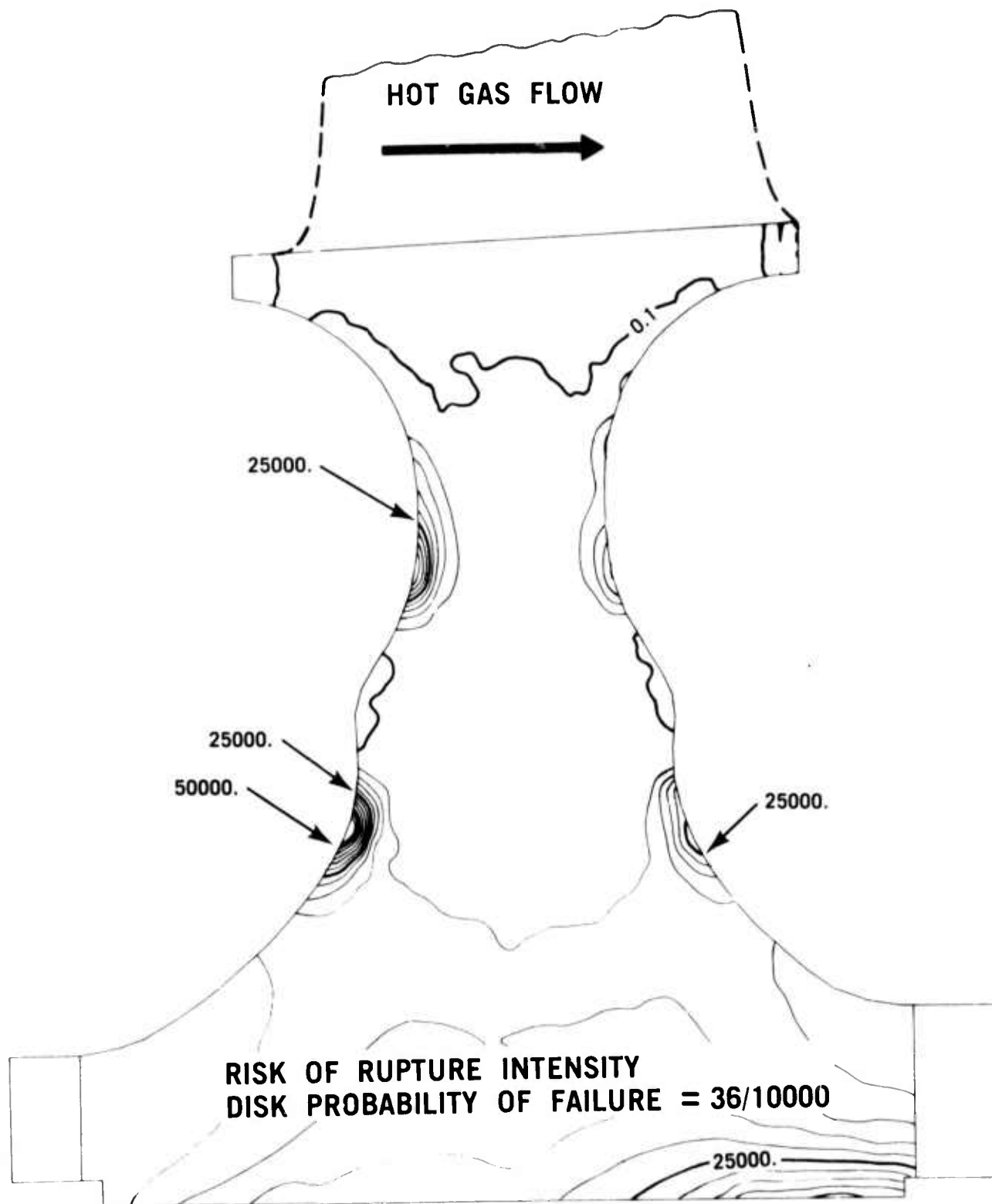
Figure 3.4   Modified Disk Contour First Stage Rotor Risk of Rupture Intensity Map For The Maximum Steady State Condition

It is seen that a more uniform distribution of the risk of rupture intensity contour lines is obtained in the modified disk (Figures 3.4 and 3.5), as compared to the original one (Figures 3.1 and 3.3). This is evidenced by the increased density of contour lines in the bore region. Furthermore, it is seen that the risk of rupture in the stress concentration area immediately above the balancing ring has been greatly reduced.
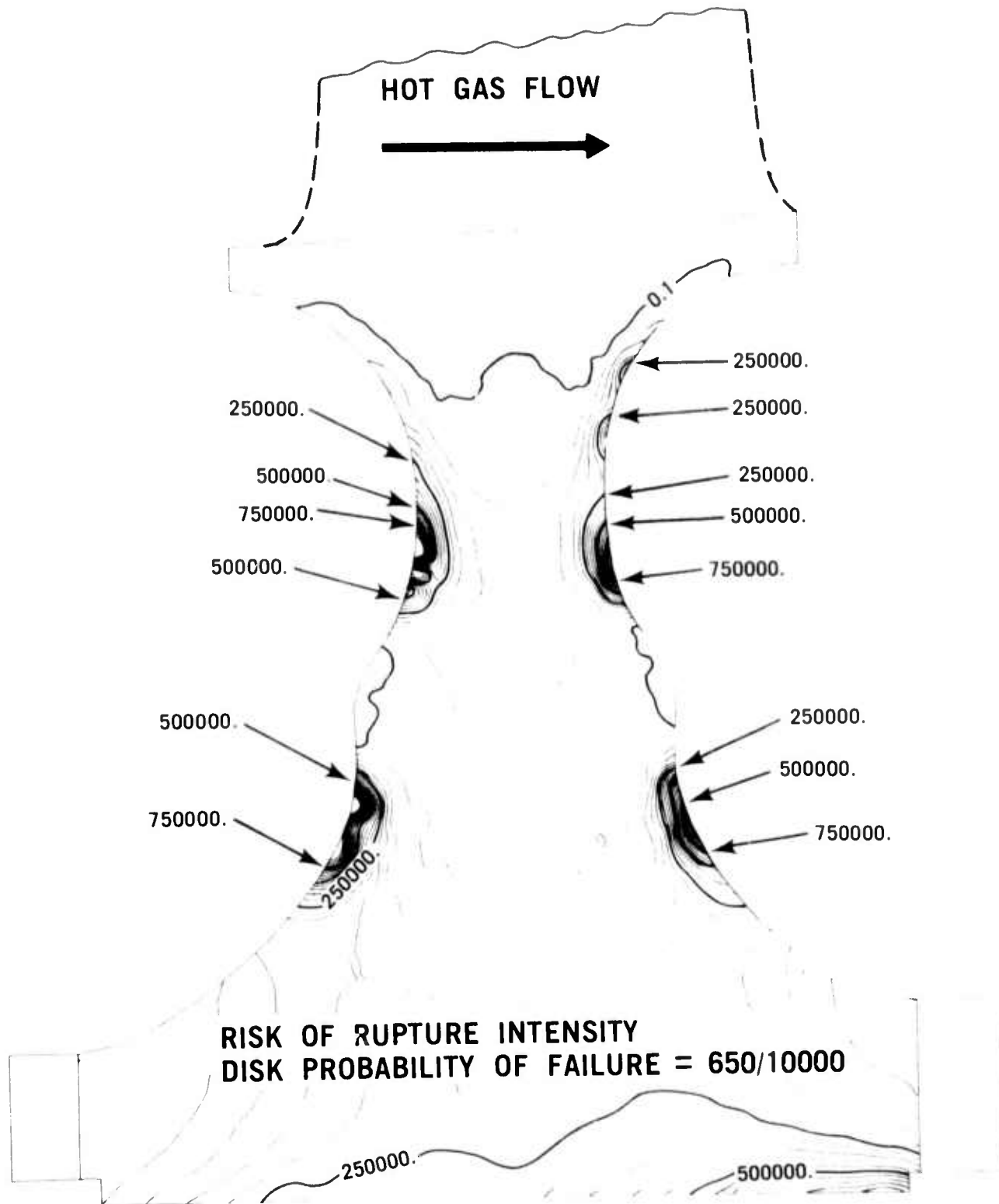
Figure 3.5   Modified Disk Contour First Stage Rotor Risk of Rupture Intensity Map For The Second Transient Condition

27

Figure 3.6 summarizes the disk contour modifications that were studied and shows the total disk probability of failure for the maximum steady-state and for the maximum (second) transient engine operating conditions.

Contrary to expectation, the original disk profile (1A or 2A with the balancing rings removed) which was designed with the conventional deterministic approach, proved to have the lowest probability of failure, thus indicating that the stress distribution rather than the volumetric effects still play the decisive role. Th s is further evidenced in disk configuration 2C in Figure 3.6. This configuration features increased throat width, and therefore, a greater volume than configuration 2A. The stresses in the throat region have been reduced, however, by the addition of material and as seen in Figure 3.6, so was the probability of failure.

MAX. STEADY STATE   12/10000
MAX. TRANSIENT   370/10000

MAX. STEADY STATE   13/10000
MAX. TRANSIENT   400/10000

MAX. STEADY STATE   32/10000
MAX. TRANSIENT   690/10000

MAX. STEADY STATE   36/10000
MAX. TRANSIENT   650/10000

MAX. STEADY STATE   33/10000
MAX. TRANSIENT   620/10000

MAX. STEADY STATE   66/10000
MAX. TRANSIENT   1700/10000

MAX. STEADY STATE   12/10000
MAX. TRANSIENT   340/10000

MAX. STEADY STATE   170/10000
MAX TRANSIENT   3100/10000

Figure 3.6   Effects of Geometry on Probability of Failure of Hot Pressed Silicon Nitride Rotor Disk

Material Testing Program

To ascertain the applicability of the Weibull model to turbine rotor-like structures a test program was conducted to determine the relationship between the failure strength of MOR test bar and that of a flat sided spin disk. The ceramic material that was used in the testing was Norton HS-130 hot-pressed silicon nitride. Four separate material billet lots were used. Twenty-five MOR bars (0.125 in. x 0.125 in. x 2.0 in. long) and four spin disks (3.0 in. O.D., 0.5 in. I.D., 0.5 in. thick) were machined in the strong direction of each billet. All samples were ground with 320 grit diamond wheels to insure a uniform surface finish. The edges of MOR bars were chamfered to 0.015 in. x 45° and the disk bore had a fillet radius of 0.060 in. so as to minimize effects of sharp edges.

28

The MOR bars were tested on an Instron Machine using four-point loading (outer span of 1.50 in., inner span of 0.75 in.) at room temperature with a cross-head rate of 0.02 in/min. The burst strength of the spin disk is obtained from the following equation:

$$\sigma_{Disk} = \sigma_{MOR} \left(\frac{Veff.MOR}{Veff.Disk} \right)^{\frac{1}{m}} + \sigma_u \left\{ 1 - \left(\frac{Veff.MOR}{Veff.Disk} \right)^{\frac{1}{m}} \right\} \quad (8)$$

In this equation σ_{disk} and σ_{MOR} represent the strength or the fracture stress in the spin disk and in the MOR bar respectively. The Weibull slope is m, while σ_u is the threshold stress. As stated earlier, it is customary for structural ceramics to set σ_u equal to zero. Veff disk and Veff MOR are respectively the effective volumes of the spin disk and the MOR bar. The effective volume of a component is defined as the volume of a tensile specimen of the same statistical material which will have the same survival probability under an equal magnitude of applied stress.

The effective volume is a function of the structure geometry and of the loading. The geometry and the loading for the MOR test bar and for the spin disk are shown in Figures 3.7 and 3.8 respectively. Integrating the risk of rupture expression (Equation 2) and normalizing with respect to the maximum stress ($\sigma_{n_{max}}$) which for the MOR bar is at the outer fiber and for the spin disk is at the bore, gives the respective effective volumes for the bar and the disk.
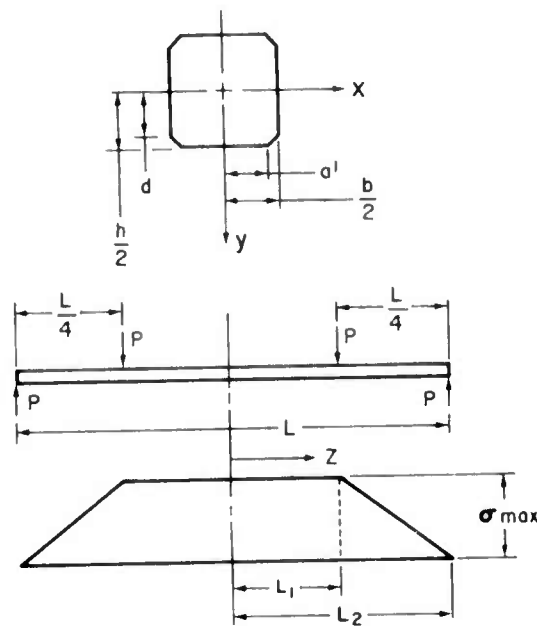
From $Z = 0$ to $Z = L_1$ $\sigma_n = \frac{2}{h} \max Y$

From $Z = L_1$ to $Z = L_2$ $\sigma_n = \frac{2Y}{h} \left\{ \sigma_{max} - \frac{\sigma_{max} (Z = L_1)}{(L_2 - L_1)} \right\}$

From $Y = o$ to $Y = d$ $X = \frac{b}{2}$

From $Y = d$ to $Y = \frac{h}{2}$ $X = \frac{b}{2} - \left\{ \frac{b - 2a}{h - 2d} \right\} \cdot (Y - d)$

Figure 3.7   Geometry and Loading of Modulus of Rupture Test Bar

29

Knowing σ_{MOR} and σ_μ one can now predict the strength of the spin disk or its burst speed using for σ_{disk} the expression for the maximum normal stress as shown in Figure 3.8. Solving this equation for the angular velocity ω gives the predicted burst speed

$$\omega = \sqrt{\frac{4\ \sigma_{MOR}}{(3+\nu)\ R_0^2 + \frac{1-\nu}{3+\nu}\ R_i^2}} \left(\frac{V_{effMOR}}{V_{effDisk}}\right)^{\frac{1}{m}} \qquad (9)$$
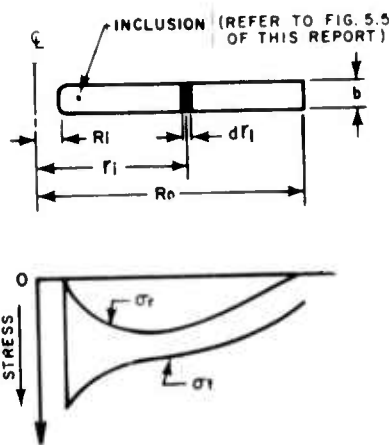
$$\text{RADIAL STRESS} = \sigma_{r_i} = \frac{3+\nu}{8}\rho\omega^2\left(R_0^2 + R_i^2 - \left(\frac{R_0 R_i}{r_i}\right)^2 - r_i^2\right)$$

$$\text{TANGENTIAL STRESS} = \sigma_{t_i} = \frac{3+\nu}{8}\rho\omega^2\left(R_0^2 + R_i^2 + \left(\frac{R_0 R_i}{r_i}\right)^2 - \frac{1+3\nu}{3+\nu}r_i^2\right)$$

$$\text{NORMAL STRESS} = \sigma_{n_i} = \sigma_{t_i}\ \text{Cos}^2\theta + \sigma_{r_i}\ \text{Sin}^2\theta$$

θ = ANGLE BETWEEN σ_{ni} AND σ_{ti}

$\rho = \frac{r}{g}$

ν = POISSON RATIO

ω = ANGULAR VELOCITY

MAXIMUM NORMAL STRESS OCCURS AT THE BORE $\quad r_i = R_i$
$\qquad\qquad\qquad\qquad\qquad\qquad\qquad\qquad\qquad\qquad \theta = 0°$

$$\sigma_{n\ max} = (\sigma_{ti})_{r_i = R_i} = \frac{3+\nu}{4}\rho\omega^2\left(R_0^2 + \frac{1-\nu}{3+\nu}R_i^2\right)$$

Figure 3.8   Geometry and Loading of Spin Disk

The three inch diameter spin disks were tested in an evacuated spin pit (2) so as to minimize frictional resistance and heating. The disks were driven by a Barbour-Stockwell Model 1131 1.5 inch air turbine which can operate to a maximum speed of 150,000 rpm. The disks were accelerated at an average rate of 19,260 rpm/min. Tests results along with analytical predictions are shown in Figure 3.9.

As shown, there is a good agreement between the predicted and actual values for the first lot of disks. However, the test values for the second lot are somewhat lower than the predicted ones. This has been traced to the presence of macro-inclusions located at the highly stressed bore region of the disk (Figure 3.8). Examination of the fracture area has shown these inclusions to be the origins of failure.

CORNER CHAMFERS
.015 X 45°

BORE FILLET
RADIUS .060

MOR BAR
0.125 X 0.125 X 2.00
VOLUME = 0.0312 IN.³

SPIN DISK
3.0 O.D., 0.5 I.D., 0.5 THICK
VOLUME = 3.4344 IN.³

TEST RESULTS, 4-POINT LOADING SAMPLE SIZE: 25 / BATCH		PREDICTIONS		TEST RESULTS SAMPLE SIZE: 4 / BATCH		
m	STRENGTH PSI	DISK STRENGTH PSI	BURST SPEED, RPM	m	DISK STRENGTH PSI	BURST SPEED, RPM
5.77	114,550					
		49,030	90,380	5.20	51,040	91,700
6.56	126,380					
		61,700	101,380	6.10	55,980	96,110
4.57	110,360					
		35,050	76,410			
10.95	123,540					
		84,670	118,770			

Figure 3.9   Correlation of Modulus of Rupture and Spin Test Results For Norton HS-130 Hot Pressed Silicon Nitride With $\sigma_u = 0$

As discussed previously, the Weibull analysis was conducted assuming the threshold stress (σ_u) equals zero. To check out this assumption a parametric analysis was made using the first lot of bars and disks. The results are:

MOR PREDICTIONS

σ_u PSI	DISK BURST SPEED, RPM	DISK STRENGTH, PSI
0	90,380	49,030
37,560	87,890	45,050

ACTUAL DISK TEST RESULTS

DISK BURST SPEED, RPM	DISK STRENGTH, PSI
91,700	51,040

These results show that the assumption of $\sigma_u = 0$ is more applicable in this case judging by the correlation with test results.

This is a first step in developing this theory. Future studies in the field of probability analysis will involve investigations of the relative importance between the material mean strength (σ mean) and the material variability (m), as they effect the failure probability of the rotor. Since surface flaws have a significant effect upon the probability of failure, this condition

31

is presently being studied. Also, once 3-dimensional analytical capability has been developed, the contribution of the blade and platform will be incorporated into the failure analysis of the rotor. Finally, to complete the evaluation of the ceramic rotor for the vehicular applications, the probability aspects of structural strength must be combined with those of load occurrence at all engine operating conditions.

Three Dimensional Stress Analysis of Ceramic Rotors

The rotor analyses in the previous reports modeled the turbine rotors as axisymmetric structures with the individual blades replaced by an equivalent axisymmetric loading. This axisymmetric analysis is valid except for the blades themselves and the immediate neighborhood of the blade-platform intersection. In this region, a three dimensional analysis is necessary to determine the stress concentrations caused by the blades. A three dimensional analysis is particularly important for the duo-density rotor since the bond interface is expected to lie in the region where axisymmetric analysis is not valid.

Ford has procured a three dimensional finite element stress analysis program (SAP) and a three dimensional finite element transient thermal analysis program (TAP). The basic element of these programs is an eight noded isoparametric solid capable of thermal and mechanical loading.

TAP is currently being adapted to Ford's computer system and should be operational in early 1974. SAP is operational and has been modified to include centrifugal loading. The three-dimensional analytical model is a slice which includes one blade and the attached disk. Figure 3.10 shows a sketch of the model as viewed parallel to the rotor centerline.
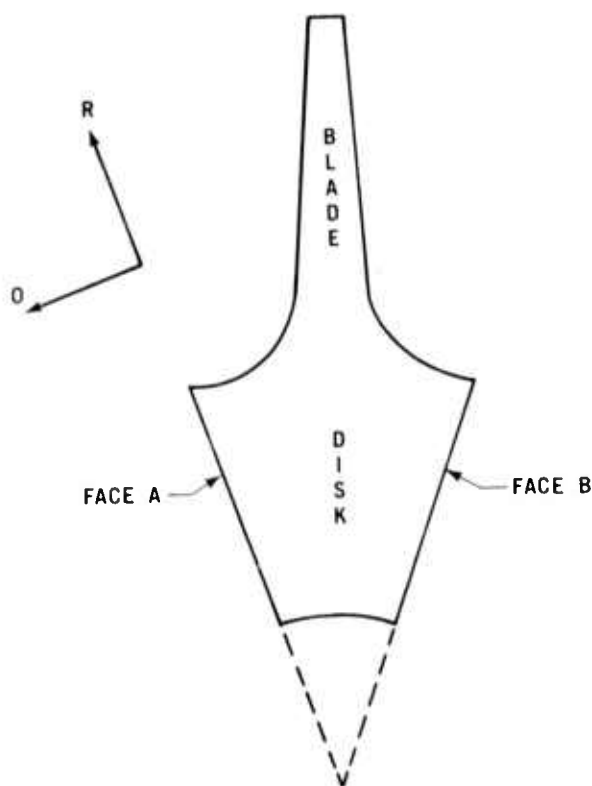
Figure 3.10   Sketch of Three Dimensional Rotor Model Parallel to Rotor Centerline

32

Continuity requires that the radial and circumferential deflections on face A equal, respectively, the radial and circumferential deflections on face B. This boundary condition requirement is currently being incorporated into the SAP code. A program has been written to assist in the generation of the 3-D rotor models. Preliminary rotor models have been constructed and are being prepared for analysis.

Ceramic Rotor Attachment

The folded bolt and the curvic coupling designs for the attachment of the ceramic rotors have been discussed in previous reports [1,2,4]. The folded bolt is made up of a tensile member of Inconel alloy 718 and a compressive member of A-286. The difference in the thermal expansion coefficients of these two materials will reduce the relaxation of the clamping load due to the thermal expansion of the rotor bolt. To further control the bolt re-laxation, cooling air is passed over the compressive member and through the center of the tensile member. The final assembly design, along with the installation tool (cross-hatched) is shown in Figure 3.11. A metallic locating adapter has been placed in front of the first stage rotor to position the bolt for minimum imbalance. The installation tool is designed to preload the bolt to the desired level without placing the bolt in torsion.

Assembly is accomplished by placing the adaptor and the anti-rotation star washer on the shaft and tightening the rotor nut by hand. The installation tool is then threaded onto the bolt and, with the puller body held stationary, the installation nut is tightened to the correct preload. The load is measured with an aluminum load ring which has been strain-gaged and calibrated. The rotor nut is then tightened with the tightening ring until a small change in the load ring output is read. The installation nut can be removed along with the rest of the tool and the bolt will retain the desired preload. The rotor nut is locked in place by a star washer which engages both the nut and the
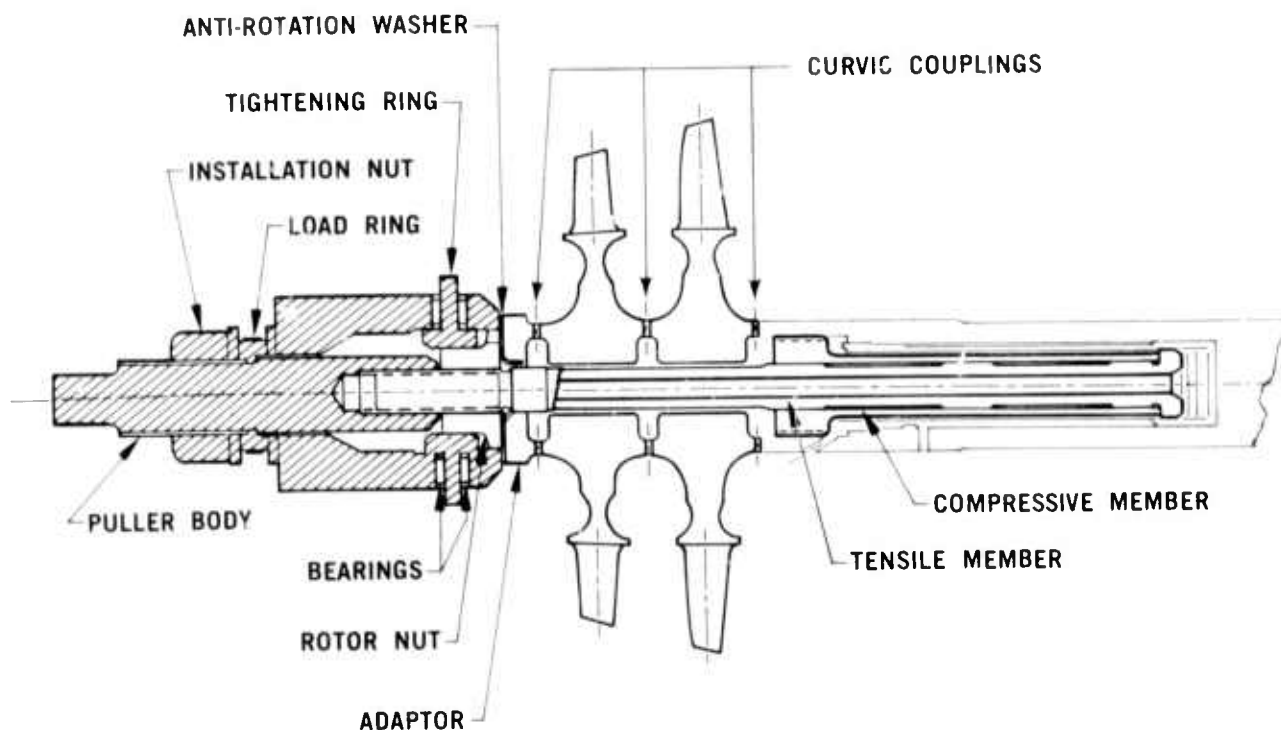
Figure 3.11   Turbine Rotor and Shaft Assembly Showing Installation Tool

33

adaptor. The installation tool and procedure has been designed so that the rotors may be readily installed and replaced in the engine without the necessity of removing the engine from its test installation.

The curvic coupling used to attach the individual rotors has been changed from a 15 tooth 30° pressure angle coupling to a 10 tooth 40° pressure angle coupling. The ten tooth curvic coupling design has been bench tested under thermal and mechanical cyclic loads. The test cycle consisted of an axial clamping load and a thermal transient load designed to simulate the engine start-up and cool-down cycles. Heat is applied to the ceramic test specimen [2] and a thermocouple is used to monitor temperature of the metal test specimen during the test.

Two sets of the ten tooth ceramic-to-metal curvic coupling test specimens have been tested. The first set failed under the first thermal cycle at approximately 220°F and 6200 lbs. load. Failure was attributed to friction. The curvic couplings are machined at near-production rates (approximately thirty-six seconds machining per tooth) resulting in surface finishes in the order of 20-40 μ in. AA. This finish apparently was too coarse to allow sliding under the high axial loads being imposed. Therefore, a high temperature nickel-base lubricant was added at the interface between the metal and ceramic teeth of the second test specimen set. Testing is continuing with this lubricant in the assembly. No indications of damage have been observed after several thermal cycles to 500°F and 9000 lbs. This is encouraging in regard to prospects for this design.

3.1.2 MATERIALS AND FABRICATION

Introduction

The primary "in-house" technique being developed for the fabrication
of ceramic turbine rotors involves the assembly of two or more grades of silicon
nitride. The major emphasis was placed on the duo-density concept, consisting
of an injection molded blade ring and a hot pressed hub. Several techniques
have been evaluated for the application of uniform pressure to the joint
between the two elements. A compression rig was fabricated to allow independent
pressures to be applied both to the blade ring, through graphite wedges, and
to the hot pressed hub.

Inability to properly support the blade ring during press bonding led to
the introduction of a slip cast rim chemically bonded to the inside surface
of the injection molded blade rim. Several rotors have been fabricated using
this technique and are being processed through final machining. This concept
is called triple density, since the slip cast material has a density
intermediate between injection molded and hot pressed grades of Si_3N_4. A pseudo-
isostatic pressing technique and a blade fill restraint system to eliminate
blade fracture during press bonding have also been developed during this report
period.

Evaluation of two monolithic rotor concepts developed by outside sources
has been completed. The CVD silicon carbide rotor program and EDM programs
have been terminated upon completion of these evaluations.

The installation of a Cavitron ultrasonic impact grinder is complete and
several rotor machining operations were developed. Disk contouring, center
boring and counterbore machining operations were performed ultrasonically on
the multi-element rotors.

A precision casting program has been initiated with Georgia Institute of
Technology directed toward development of investment slip-casting casting
techniques for forming precision cast ceramic shapes, aimed primarily at rotor
development.

Duo-Density Si_3N_4 Rotors

The duo-density concept [3] is one of several techniques being investigated
for fabricating a ceramic turbine rotor. In this concept, the high strength
of the hot-pressed Si_3N_4 is utilized in the disk region where stresses are
highest but temperatures are moderate and, therefore, creep problems are
minimized. Reaction bonded Si_3N_4, which can be readily formed into complex
air-foil blade shapes by injection-molding, is utilized for the blades which
are exposed to the highest temperature but lowest stress levels.

Work during this reporting period was directed toward developing fabrication
techniques for bonding the reaction-sintered Si_3N_4 blade ring and hot-pressed
Si_3N_4 disk or hub together. Although other fabrication techniques were investi-
gated, the major emphasis involved the graphite wedge technique described in
the last report [4]. The blade ring assembly was injection molded in one piece
from silicon metal powder and subsequently nitrided to form Si_3N_4 having
a density of 2.2 gm/cm^3. The Si_3N_4 hub component was prepared by hot-pressing
alpha Si_3N_4 (AME) powder containing 2 w/o MgO into theoretically dense disks.
The MgO is a densification additive which enables the alpha Si_3N_4 powder to
be hot-pressed to theoretical density. The bond surfaces of all component
parts were machined to remove any oxide or reaction surface layers.

35

Several potential assembly techniques were evaluated during the last reporting period [4]. However, fracture of the reaction-bonded blade ring was the predominant problem preventing the fabrication of acceptable turbine rotors using these techniques. This led to the design of a graphite wedge system which permitted the application of pressure to the blade ring periphery. This design is shown in Figure 3.12. Force is applied to the graphite wedges and graphite spacer by the large graphite piston which in turn simultaneously transmits pressure to the blade ring periphery and the hub component. However, rotors fabricated by this technique had a considerable amount of variation in the degree of bonding between the blade ring and hub. The main factor which contributed to the inconsistant bonding was the lack of a way to individually control the pressure to the blade ring and hub. An uneven application of pressure on either component resulted in weak bonds and/or fractured blade rings.

A stainless steel compression rig was designed and built to enable individual control and monitoring of the applied pressure on both the outside graphite wedge and inside hub component. The compression rig is shown in Figure 3.13. The large top plate transmits pressure from the top ram to the outside cooling ram while the small hand operated hydraulic piston exerts pressure to the center cooling ram. Figure 3.14 illustrates the graphite wedge system used in conjunction with the pressure application from the compression rig.

FORCE

TAPERED GRAPHITE RING

TAPERED GRAPHITE INSERTS

GRAPHITE SPACER

REACTION SINTERED Si_3N_4 BLADE RING

HOT-PRESSED Si_3N_4 HUB
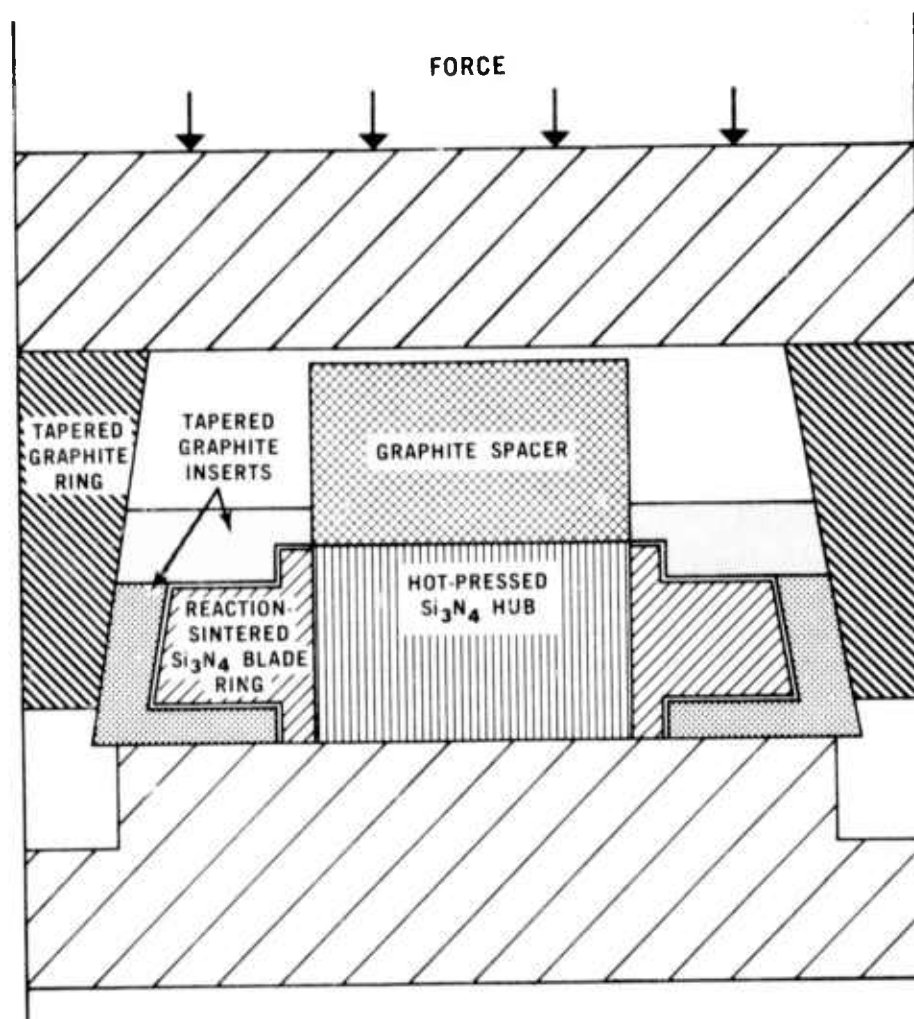
Figure 3.12   Graphite Wedge Technique for Fabrication of Duo-Density Rotors

However, after many unsuccessful attempts at fabricating a duo-density turbine rotor, it was concluded that the strength of the blade rim was insufficient to withstand a pressure of 2000 psi necessary to produce a bond. Since the rim is restrained only at the top and bottom, the rim must have enough strength and stiffness to prevent deformation and/or fracture during hot-press bonding. To accomplish this, the blade rim thickness was increased from 0.280 inches to 0.400 inches, and the rim was built up with higher density slip-cast Si_3N_4 rather than injection molded Si_3N_4. This concept, a molded blade ring with a high strength slip-cast rim, has been termed the triple density rotor. This design uses an injection molded silicon blade ring (with a corresponding Si_3N_4 density of 2.2 g/cm^3) with a rim wall thickness of approximately 0.400 inches with slip-cast silicon (having a corresponding Si_3N_4 density of 2.6 g/cm^3). The silicon rotor is then nitrided to Si_3N_4, forming a chemical bond at the injection molded slip-cast interface. Slight shrinkage variations during drying have caused inconsistant bonding at the interface but silicon slips having lower shrinkage characteristics are being prepared to eliminate this problem.
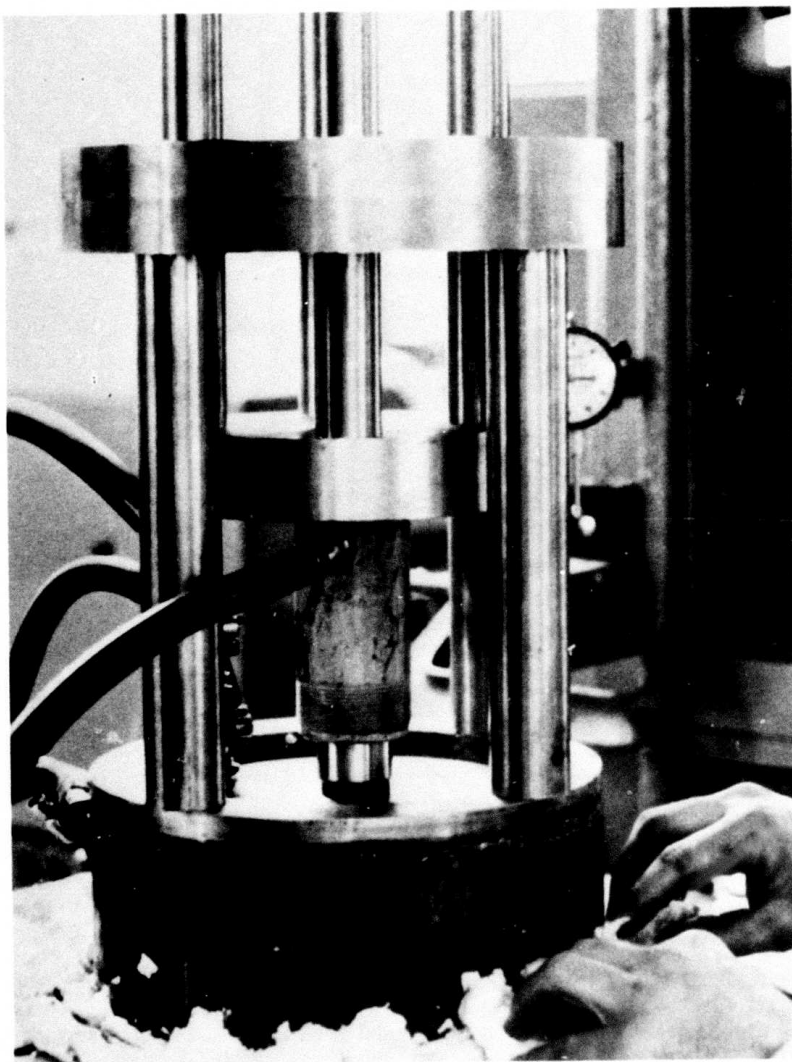
Figure 3.13   Stainless Steel Compression Rig
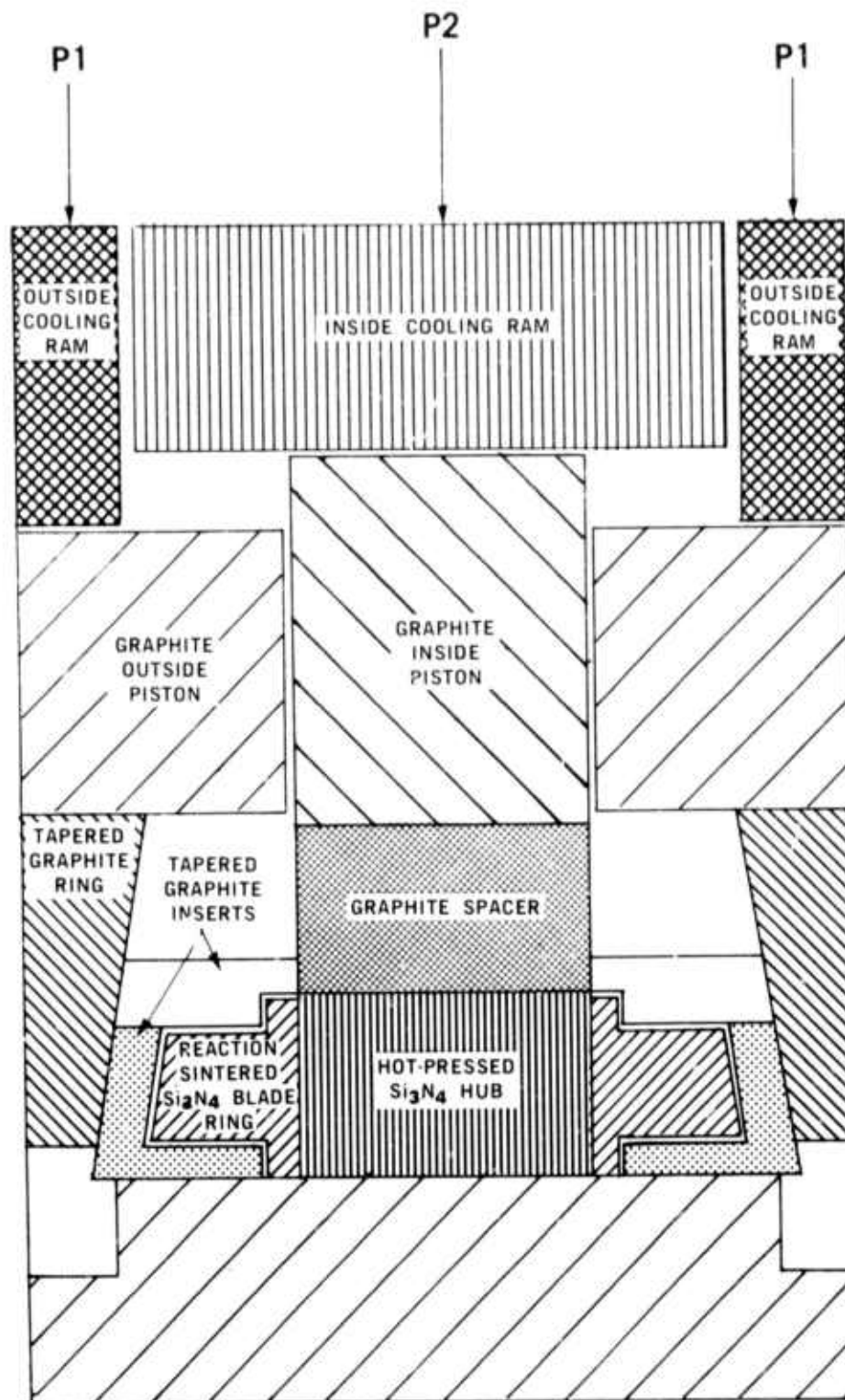
Figure 3.14   Graphite Wedge System for Fabrication of Multi-
                Density Rotors Showing the Individual Pressure
                Application

Several turbine rotors were hot-press bonded at $1650^{\circ}C$ for 2 hours at
various pressures on the hub ranging from 2000 to 3500 psi. All the rotors
press-bonded at pressures up to 3000 psi exhibited excellent bonds at the
hot pressed-slip cast Si_3N_4 interface, as shown in Figure 3.15, without any
deformation, fracture, or increase in the dimensions of the blade ring rim.

38

However, hub pressures above 3000 psi resulted in some tearing and deformation of the rotor rim. These results are encouraging and indicate that fabricating a triple density Si_3N_4 turbine rotor by hot-press bonding remains a promising approach.

HOT-PRESSED Si_3N_4 HUB

SLIP-CAST Si_3N_4 RIM
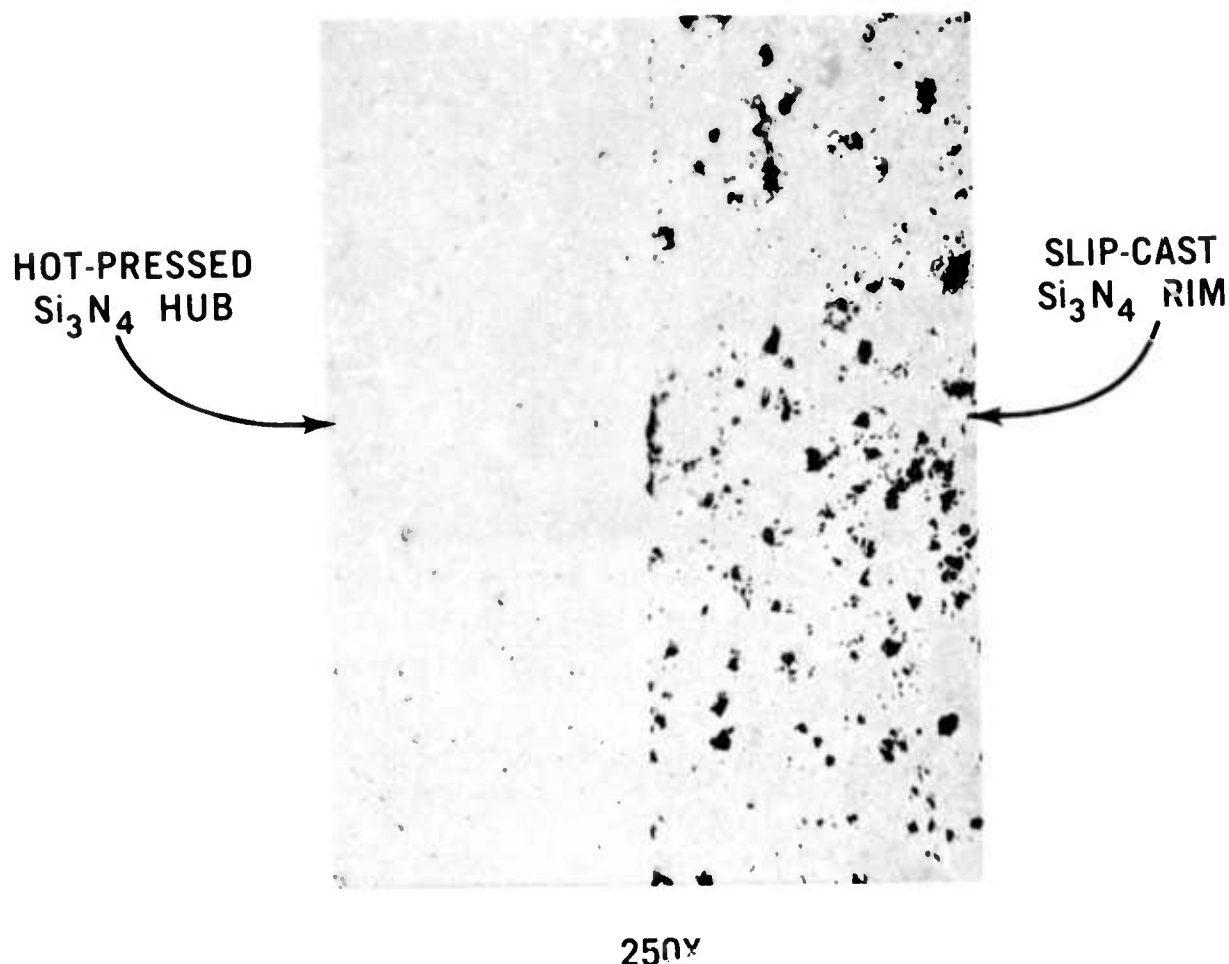
250X

Figure 3.15   Microstructure at   Between Hot-Pressed and Slip Cast Silicon Nitride (250X)

In an effort to minimize final machining of the multi-density turbine rotors, hub components were hot-pressed to the approximate hub contour using pre-shaped graphite dies. Figure 3.16 shows a hot-press bonded triple density turbine rotor that was bonded using a preformed contoured hub and the graphite wedge system. It was necessary to ultrasonically machine approximately 0.030 inches from the hub surfaces to meet final dimensions.

Other fabrication techniques for hot-press bonding duo-density Si_3N_4 turbine rotors were considered. One method involved pseudo-isostatic bonding the blade ring onto the hub at high temperatures. A sketch illustrating a cut-away view of this technique is shown in Figure 3.17. This method utilizes the radial flow of boron nitride through the blades rather than the previously reported [3] axial flow method. The blade ring and hub are pre-assembled and placed in the graphite fixture as shown. The cavity is filled with boron nitride powder and pressure applied to the top cylindrical graphite piston to force the boron nitride powder radially through the blades and pseudo-isostatically apply pressure evenly over the outside diameter of the blade rim. Although bonding between the blade ring and hub was accom-

39
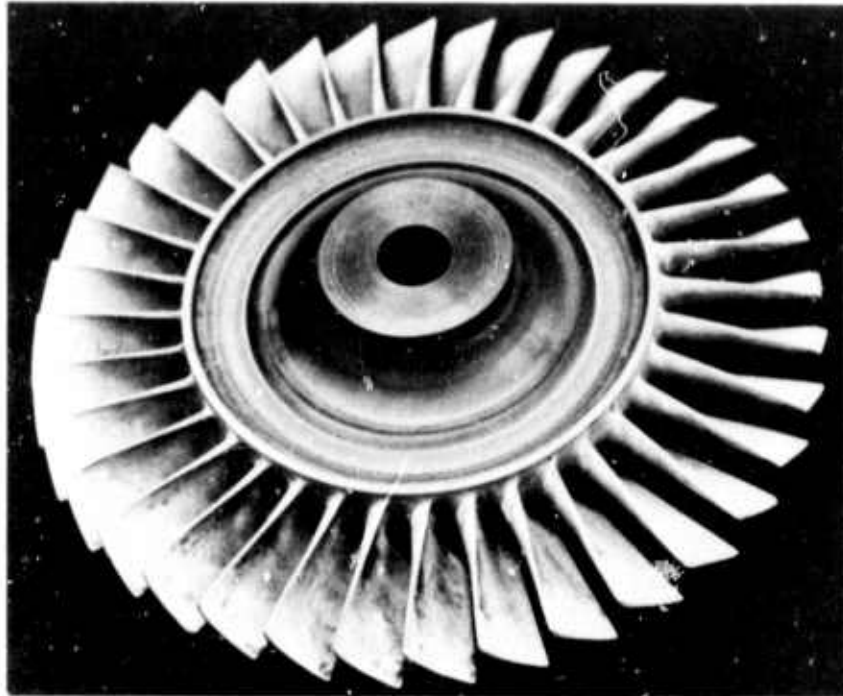
Figure 3.16   Press Bonded Triple Density Silicon Nitride Rotor
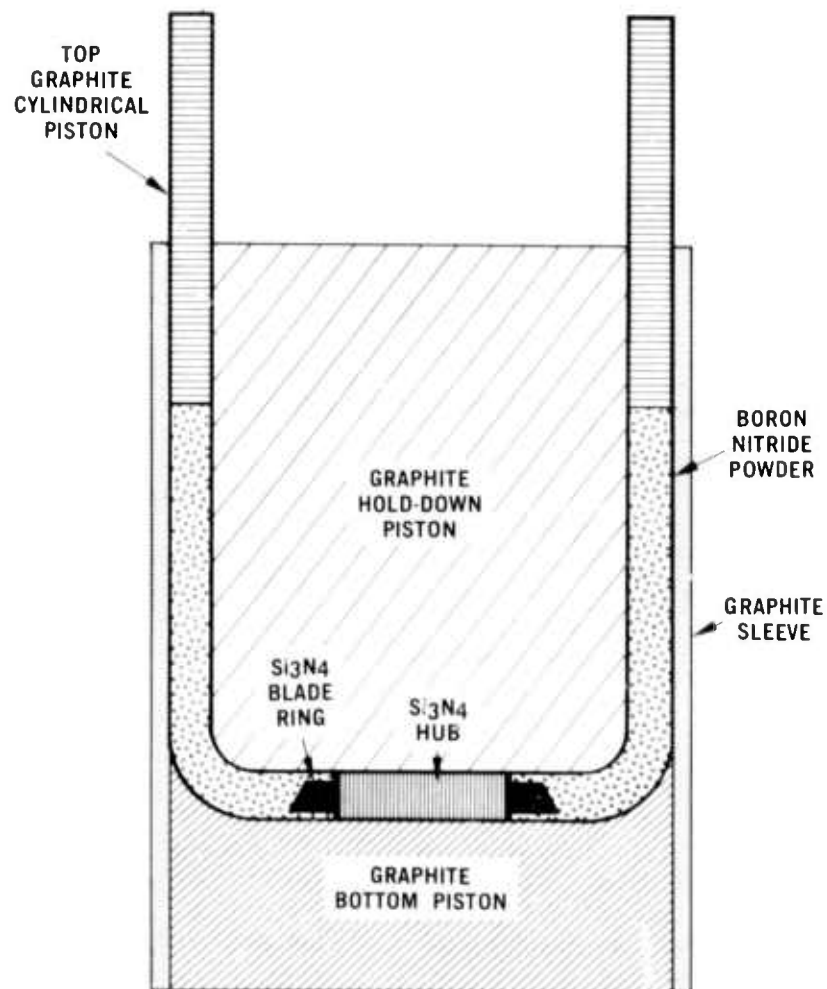
Figure 3.17   Die Design for Pseudo-Isostatic Fabrication Technique

plished at 1750°C and 2000 psi for 2 hours by this technique, the blades completely fractured in every case indicating non-uniform pressure distribution at the rotor blades.

Another fabrication technique being worked on involves filling the spaces between the blades of the Si_3N_4 blade ring with material which will restrain the rim during hot-press bonding, after which the material is removed. This approach may enable the bonding of duo-density Si_3N_4 rotors with relatively thin (0.040 to 0.080 inch) blade rim thicknesses. A heavy boron nitride coating is applied to the blades of the blade ring to enable removal of the blade fill material after hot-press bonding. Silicon metal is injected into the inter-blade spaces, the binders are burned out, and the silicon blade fill material is nitrided to form Si_3N_4. The rotor components (hub and blade ring) are assembled and hot-press bonded using the previously described wedge technique. Preliminary experiments are in progress and results are incomplete thus far.

Monolithic Rotors

Ford/Energy Research CVD Silicon Carbide

It was previously reported [4] that four of seven free standing full scale turbine rotors produced by chemical vapor deposition (CVD) of silicon carbide had been cold spin tested to failure in a spin test facility. Examination and analysis of the photographs taken at failure and of the parts remaining after failure revealed substantial regions of incomplete deposition, particularly at the base of the blades in the transition to the rotor platform. Further, there was evidence of inhomogeneity in the hoop and significant residual stress appeared to exist within the deposited silicon carbide.

It was concluded that the magnitude of the problems yet to be solved in the CVD silicon carbide process are such that it is not likely to provide successful ceramic turbine rotors in time to meet the ARPA goals. For these reasons, in spite of the long range potential of the process, it was decided to suspend work on this approach.

Electric Discharge Machining of Hot-Pressed Silicon Carbide

A study to determine feasibility of machining aerodynamic blade shapes by electric discharge machining (EDM) of electrically conductive, hot pressed silicon carbide has been previously described [2,3,4]. Four types of SIC had been obtained and evaluated, all of which exhibited rough surfaces relative to diamond ground SiC and a preponderance of surface cracks.

Simulated blade shapes were also machined in a new ultra fine grain high strength hot pressed silicon carbide, developed under Navy contract [5] by the General Electric Co. Examination by SEM indicated many cracks were present after the EDM operation even after large reductions in process parameters (voltage and current) which reduced cutting rates to 10% of the original one inch per hour rate. In order to establish material property degradation due to micro cracks, test bar 1/8" x 1/8" x 1-1/4" long were machined from the GE material both by EDM and by conventional diamond slicing and surface grinding techniques. Results of room temperature 3 point bending tests on the two groups of samples cut from the same billet are shown in Table 3.2. Because of the large reduction in strength and the damage visible in the SEM photograph, shown in Figure 3.18, further work on machining airfoil shapes from conductive SiC by EDM techniques has been discontinued.

41

TABLE 3.2

Strength in Three-Point Bending of Machined Hot Pressed Silicon Carbide

Conventional Diamond Grinding

Sample No.			
	1	101,000 psi	
	2	104,000	99,700 avg.
	3	103,500	
	4	86,000	
	5	104,000	

EDM Machined

Sample No.			
	1	76,400 psi	
	2	33,600	
	3	38,200	46,000 avg.
	4	45,100	
	5	36,700	
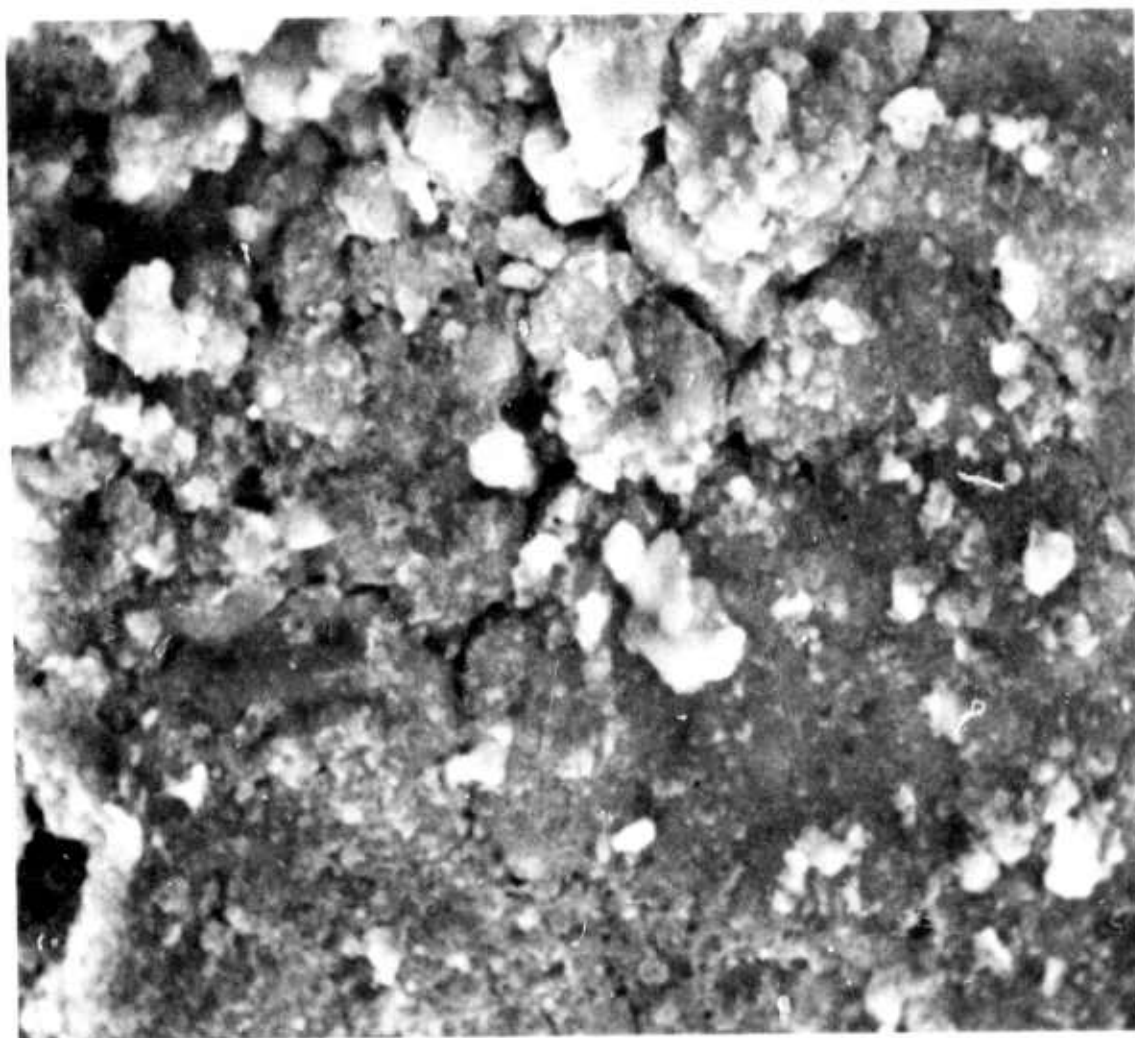
Figure 3.18   Scanning Electron Micrograph Showing Damage from
EDM Evaluation of Silicon Carbide (750X)

42

Ultrasonic Machining

It has been reported [1,2,3,4] that work was in progress directed toward ultrasonic machining of airfoil shaped blades. Successful rough cutting of constant cross section airfoils by inward radial impact machining was described in a prior report [3].

Repeated attempts at side cutting the desired tapered, twisted air foil from the rough form have been unsuccessful; therefore, further effort toward that goal has been suspended, and ultrasonic machining work was redirected toward disk final machining. Installation of a rebuilt Cavitron ultrasonic impact grinding machine has been completed. This machine, converted from a glass processing production facility, consists of two horizontally-mounted 1000 watt transducers. The tool is motor driven into the workpiece and constant pressure is controlled by a magnetic clutch. The workpiece is mounted on a variable speed rotary table. A vacuum system is available on this machine and is connected to the tool holder, providing a continuous slurry feed between the workpiece and tool.

Ultrasonic machining of the contoured hot-pressed Si_3N_4 disk area has been successfully performed. The forming of the approximate hub contour during the hot pressing of the hub and the press bonding to form the multi-density Si_3N_4 rotor has been described earlier in this section. Ultrasonic contour finish machining is being employed to achieve the required dimensional tolerances. A ceramic rotor, with a rubber protective material cast around the blades, and mounted on the Cavitron is shown in Figure 3.19. The disk contour tool is shown in the retracted position. The tools used in disk contouring are cold rolled steel. A 320 grit Norbide slurry is used in machining the disk contours. In addition to disk contouring, the Cavitron is used for core drilling and machining the counterbores prior to curvic coupling grinding. The centerbore is subsequently diamond ground to achieve the close tolerances
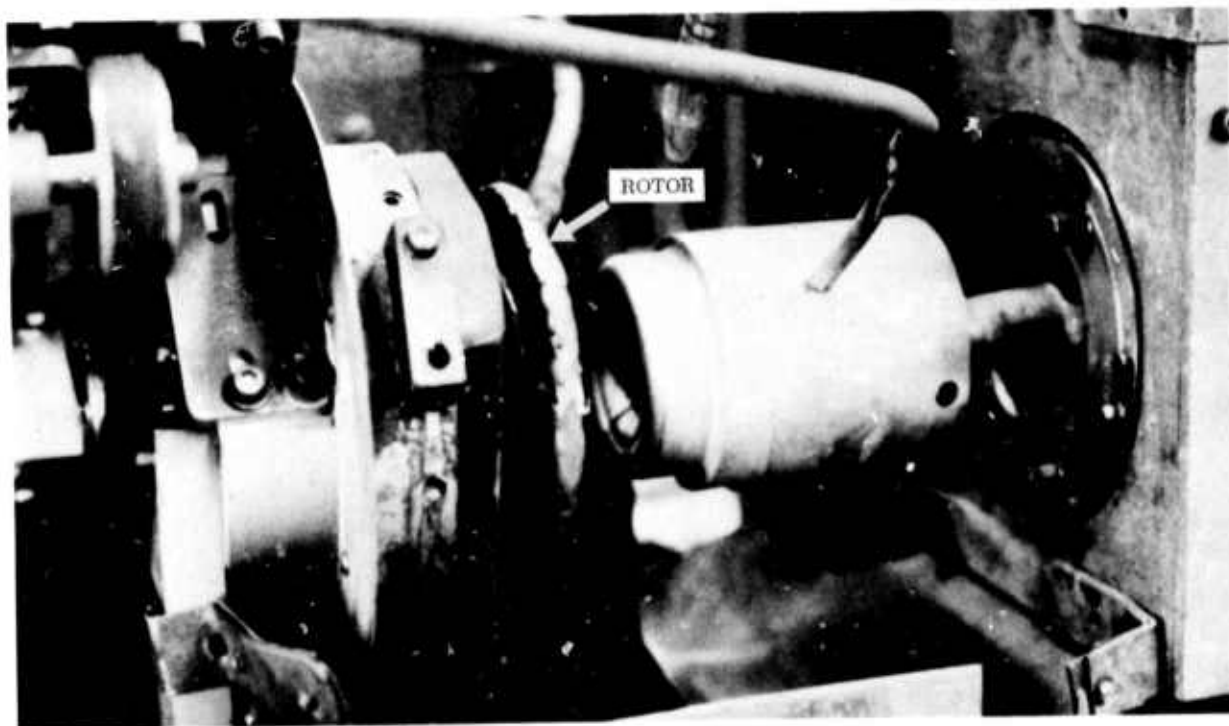
Figure 3.19   Silicon Nitride Rotor Mounted in Ultrasonic Grinding Machine

required. Thus far, six triple density Si_3N_4 rotors have been ultrasonically machined (see Figure 3.16).

Georgia Institute of Technology Precision Cast Si_3N_4 Program

An effort has been initiated at the Georgia Tech Experiment Station directed at the development of investment casting techniques for forming precision cast ceramic shapes. Initial experiments indicate that a porous ceramic mold may be formed into which a silicon metal powder shape may be slip cast. By proper control of the mold composition, porosity, and strength, nitridation of the shape within the mold is possible. Removal of the mold from the shape can be accomplished at several stages of nitridation depending upon the relative properties of the mold/shape system.

Experiments to date have been limited to test bars and simple shapes; however, the process will be evaluated using simulated airfoil shapes and. complete rotor assemblies early in 1974.

44

3.1.3 TESTING

Introduction

The new turbine rotor test rig is undergoing shakedown evaluations in preparation for initial testing of ceramic rotors. Cold testing to design speed and some hot testing utilizing metal rotors have been completed during this reporting period. Spin testing of ceramic rotors is continuing and eight duo-density and five triple density rotors were evaluated by spinning to destruction.

A test program has been initiated to evaluate the thermal shock characteristics of ceramic rotors using the thermal shock test rig. A cyclic temperature profile was used to simulate engine transient thermal conditions. Analytical studies have been initiated to investigate the thermal stresses in the blade.

Turbine Rotor Test Rig

Shakedown evaluation of the turbine rotor test rig (TRTR) was continued with metal turbine rotors. Final cold testing at 100% engine speed has been completed and hot testing has progressed to 56% speed and a turbine inlet temperature of $1800^{\circ}F$. A labyrinth seal rub occurred at this point necessitating teardown and inspection of the rig. Build-up of the rig with new hardware will begin upon completion of the failure analysis of the labyrinth seal. When this testing is completed, the TRTR will be used to accomplish the following objectives:

1) Testing of ceramic turbine rotors at various speeds up to 64,240 rpm at various turbine inlet temperatures up to $2500^{\circ}F$.

2) Establishment of endurance levels of ceramic turbine rotor materials at various speeds and temperatures, and

3) Testing of other ceramic components without the need for a complete turbine engine. The previous report [4] shows the TRTR in its current configuration as installed in the test facility.

The test rig should be ready to accept ceramic turbine rotors when they become available. Testing of these rotors will be done in the TRTR prior to their approval for use in a turbine engine.

Ceramic Rotor Cold Spin Testing

The equipment and test procedures used for spin testing of ceramic turbine rotors have been shown in previous reports [2,4]. Ceramic rotors are spin tested at room temperature, in a partial vacuum, and at gradually increasing speed until destruction occurs.

Eight duo density rotors which consisted of silicon nitride injection molded blade rings bonded to hot-pressed Si_3N_4 slab-sided hubs were spin tested to destruction with failures occurring in the range of 20,000 to 50,300 rpm (up to 78% of design speed). Each specimen exhibited some degree of defect such as voids in the blades, regions of low material density, or unbonded areas located in the press bonded joint between the blade ring and hub.

45

Five triple density rotors which consisted of an injection molded Si_3N_4 blade ring with a slip cast Si_3N_4 insert to provide a thicker rim (see Section 3.1.2 for more details), were press bonded to a hot pressed Si_3N_4 slab sided hub. Failure of these rotors occurred in the range 36,000 to 55,070 rpm or up to 86% speed. Most specimens exhibited similar flaws as mentioned earlier or a poor bond between the molded and slip cast rings. Figure 3.20 is a photograph of a triple-density rotor at the moment of failure at 55,070 rpm. No apparent defect was detected in the single blade that failed first.

During the manufacture of rotors for cold spin testing, various techniques are being employed to improve the materials and the bonding, including molding of blade rings of higher density. Both duo and triple density rotors of improved and more consistent quality are now being processed incorporating the contoured hot pressed hub. These rotors will be spun at room temperature to a predetermined qualifying speed prior to use in the hot spin rig and ultimately in the turbine engine.

Thermal Shock Testing of Rotor Blades

The first and second stage rotor blades are subjected to severe thermal shock in engine and turbine rotor test rig operation, caused by rapid heating and cooling of the blade during start up and shutdown. In order to obtain a
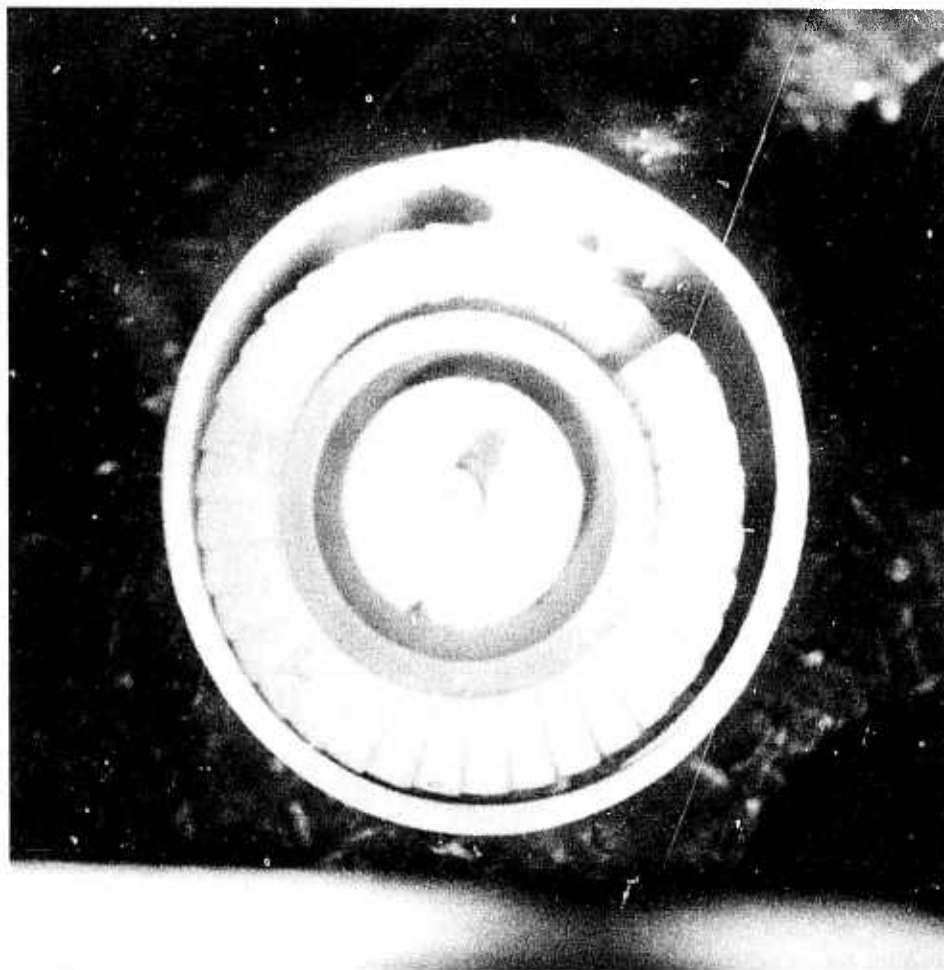
Figure 3.20   Triple-Density Rotor at Point of Failure (55,070 rpm)
During Spin Testing

46

preliminary indication of thermal shock problems that may be encountered in the initial hot testing of ceramic rotors, a test program was initiated using the thermal shock test rig. The thermal shock test rig has been previously described [3,4].

The test rig is used to subject a blade to a controlled cycle of heating and cooling, simulating the upshock caused by engine starting and downshock caused by engine shutdown. The thermal cycle chosen for this test is shown in Figure 3.21 and is the same as the time-temperature profile used for thermal shock rig testing of the first stage stator vanes.

The first stage rotor blades should actually experience a less severe thermal cycle, but this cycle was chosen as a conservative evaluation. Analytical work is in progress to calculate the actual thermal stresses in the rotor blade (see Section 3.1.1).

The components chosen for testing were all sectioned from triple-density rotors, and were evaluated after the press-bonding assembly operation. The first 250 cycles of testing were conducted at a blade temperature 2100°F. This cycle was used initially because it simulates the operating conditions the rotors will be subjected to in the preliminary testing in the turbine rotor test rig. After 250 cycles, when no visible evidence of failure was observed, the thermal cycle was increased to that shown in Figure 3.21. The results of this thermal shock testing are shown in Table 3.3. Six blades were tested and the numbers correspond to the positions they occupied on the table of the thermal shock rig. At a total of 308 cycles, or 58 cycles into the more severe thermal cycle of Figure 3.21, the first crack appeared in the blade at position 2. From 308 cycles on, cracks continued to appear and propagate until at 2488 cycles, when the test was terminated, all the blades had cracked or failed. This test is a preliminary test and was done to determine if there were any

TEMPERATURE OF FLAME = 3000°F

QUENCH AIR = 130 CFH

POINT AT MIDSPAN LEADING EDGE

THIS CURVE IS AN AVERAGE OF 3 RUNS
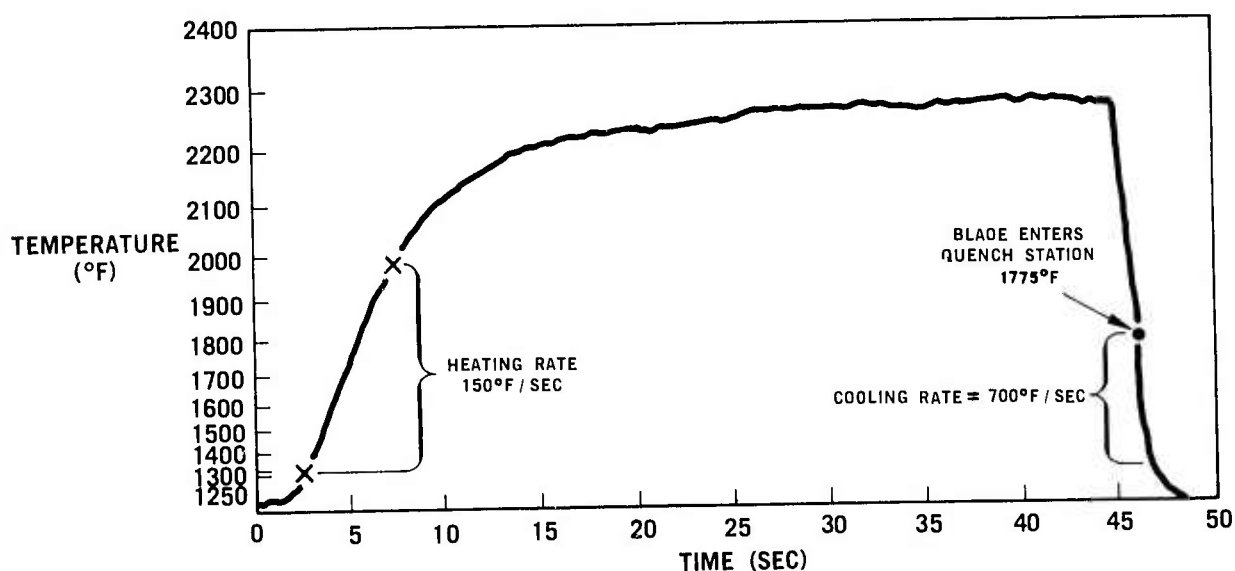
Figure 3.21   Thermal Shock Cycle

immediate thermal shock problems that would cause problems in the initial turbine rotor test rig testing. Further testing is planned. When analytical results are available the rotor blades will be tested to the calculated thermal cycle. It should also be noted that these blades are of developmental quality and may not be representative of the blades that will be used in the turbine test rig and the engine. There is also a strong possibility that the blades were damaged or degraded during the press-bonding operation. The effect of press bonding upon properties of the injection molded material will be evaluated in the future.

TABLE 3.3

THERMAL SHOCK TEST RESULTS FOR INJECTION
MOLDED SILICON NITRIDE ROTOR BLADES WHICH WERE
SECTIONED FROM TRIPLE DENSITY ROTORS

Position on Rig	Cycles	Description If Damage Occurred
2	308	Midspan Crack
1	730	Root Crack
7	730	Root Crack
1	1090	Root Failure
6	1090	Midspan Crack
7	1090	Root Failure
8	1090	Midspan Crack
2	2488	Midspan Failure
4	2488	Tip Crack
6	2488	Midspan Crack Growth
8	2488	Root Failure

Test Rig Conditions:

Flame Temperature of 3000°F, Blade Temperature of 2250°F At
Midspan Leading Edge, Cycle Time of 45 Sec. In Flame, Cooling
Air Flow Of 130 C.F.H.

3.2   CERAMIC STATORS, ROTOR SHROUDS AND NOSE CONES

SUMMARY

Some improvement in the quality of first stage stators was achieved by closely controlling the temperature of the vane molding tool during fabrication. These modifications resulted in the elimination of visual defects in the vane root. Several Design C first stage stators were evaluated in the stator and engine test rigs. Failures during this testing were attributed to a molding flaw, accidental damage, and thermal shock. One stator did, however, survive 111 hours and 403 engine lights.

Engine testing of second stage inverted channel stators showed that axial cracking of the outer shroud remains a problem. A furnace test of stator assemblies was developed in an effort to screen defective parts. This test duplicated the type of axial shroud crack experienced during engine testing.

Work was initiated on molding of Design C first stage stators as a single unit, rather than as an assembly of individual segments. The tool has been designed and is currently being manufactured. The one piece stator is expected to eliminate outer shroud failures which are believed caused by the notch effect of the joints between individual segments.

Stability testing of slip cast Si_3N_4 rotor shrouds was carried out to 450 hours at 1900°F, showing no stability problems exist with this material. One shroud ring of slip cast Si_3N_4 was further tested in the stator test rig for 78 hours without failure or excessive creep.

The incidence of internal molding voids associated with nose cone failures has been minimized by preferentially heating the tool during injection molding. Provisions were made to incorporate these modifications using automatic control in future molding.

The ceramic stator test rig was fitted with a quartz window which permitted temperature measurements of various points on the stator vanes under operating conditions. Correlations were established between these temperatures and those obtained on stator vanes tested in the thermal shock rig which showed the vane heating rate was faster and the vane cooling rate was slower in the stator test rig. These results will be used to correlate actual vane temperatures with theoretical values obtained from a three-dimensional heat transfer and stress analysis program currently under development.

As an overall assessment, the durability of ceramic stators, rotor shrouds, and nose cones continues to improve by means of iterative development to uncover and resolve unanticipated problems. It is judged that the nose cone and turbine shrouds of the latest design configuration, with anticipated material improvements, can meet the 200 hour durability objective. It is also expected that the planned one-piece first stage stator configuration will resolve the problem of stator outer shroud failure and thereby pave the way for the 200 hour durability objective. When this is confirmed, serious consideration will be given to a one-piece 2nd stage stator even though this would mean new tooling for a completely new design somewhat compromising aerodynamic efficiency.

3.2.1 MATERIALS AND FABRICATION

Introduction

The achievement of acceptable reliability is the main goal in the development of stators for the vehicular gas turbine. Although improvements in first stage vane design were made which have considerably improved the durability of this component [4], engine tests have revealed that some parts last for a considerable period of time and others fail relatively quickly. Many of these failures are caused by accidental breakage and fabrication defects. Work during this reporting period was directed toward the elimination of first stage stator vane root failures, and stator outer shroud axial cracking of both stages. In this effort temperature-controlled molding dies were utilized to reduce the incidence of vane root cracks resulting from molding stresses. Work on the stator shroud axial cracking problem continued with the development of a furnace test which duplicated the failures from the test engine and established a time-temperature relationship for this failure.

Rotor shroud furnace testing was continued for 450 hours duration, and the effect of nitriding aids on the stability of Si_3N_4 slip cast shroud rings was determined.

Modifications were made in the molding procedure for nose cones to eliminate internal molding flaws believed instrumental in previous nose cone failures.

Stator Fabrication and Assembly

During this reporting period, work continued in an effort to eliminate vane and shroud failures experienced in stator assemblies during engine operation.

Detailed inspection and testing procedures have been applied in an effort to detect stator defects prior to engine testing. Hairline cracks were detected visually in unfired vane roots in approximately 5% of all molded vanes. These cracks were attributed to stresses exerted on the vane during molding. Reduction of shrinkage during cooling of the molded part in the tool was achieved by controlled heating of the vane tool during molding. The reduced shrinkage eliminated the visual vane cracks. Presence of visual vane root cracks suggested the possibility of smaller undetected cracks which would later grow to a critical size and cause vane failure during engine operation. A preliminary correlation between crack shape and location in stator vanes which failed during engine testing and visual molding cracks was established. Further engine testing will be conducted with vanes molded in temperature-controlled tools. A furnace pre-test and more rigid post-firing inspection is expected to further reduce the incidence of undetected vane root cracks.

Attempts to improve the thermal shock resistance of Design C second stage stator vanes through design modification has to date been unsuccessful. These vanes were evaluated on the thermal shock test rig, and proved to be slightly easier to crack than Design B vanes. Reduction of the inner shroud thickness and cutting back the vane cord width failed to improve performance of the vane on the thermal shock test rig. Until improvements can be made, engine testing will be continued with Design B second stage stators.

Work is in progress to make possible the molding of first stage Design C stators as a single unit. A one shot molded stator will eliminate the notch effect of individual segment joints currently believed responsible for outer shroud failures. A molding tool for one shot axial draw molding of the entire stator was designed and is scheduled for delivery during the first quarter of 1974. As noted in the previous report [4] the inverted channel design improved the engine life of the second stage stator assembly shown in Figure 3.22; however, axial cracking of the outer shroud was still present.

Figure 3.22   Second Stage Inverted Channel Stator Assembly

A furnace test was initiated to facilitate screening all fully assembled inverted channel stators before release for engine testing. The pre-test consisted of soaking the assemblies in an air-atmosphere furnace at 1900^0F, for 50 hour increments, for a total of 200 hours. After each 50 hour increment the assemblies were fully inspected.

Testing results duplicated the axial cracking of the outer shroud experienced during engine testing. All failures were time-temperature dependent. Between 75-100 hours at 1900^0F an axial crack propogates and grows to 1/8 - 1/4 inch in length. Increasing the time at temperature produces a fine network of cracks in the slip cast outer shroud and in the platform region of the stator.

These test results indicate a material instability problem and/or an incompatibility between the injection molded blades and the slip cast outer ring. Tests are underway to identify the causes of this problem.

Nose Cone Development

Molding modifications have been made in order to eliminate the internal molding flaws believed responsible for some nose cone failures. The previous report [4] describes typical axial and circumferential cracking which was encountered during nose cone testing. Various design modifications were also

51

described, consisting of section thickness reductions and pre-slotting of the nose cone outer shroud. During the processing of the redesigned nose cone, machining exposed internal flaws in the nose cone as shown in Figure 3.23. The flaws were mainly caused by uneven cooling shrinkage of the ceramic material in the tool. Selective heating of the tool was performed, using a hand-held heat gun in an attempt to minimize shrinkage. This technique was successful in controlling the solidification of the ceramic molding composition, thereby eliminating these internal voids. Provisions have been made to electrically heat various critical portions of the die, using automatic control, for future molding runs.
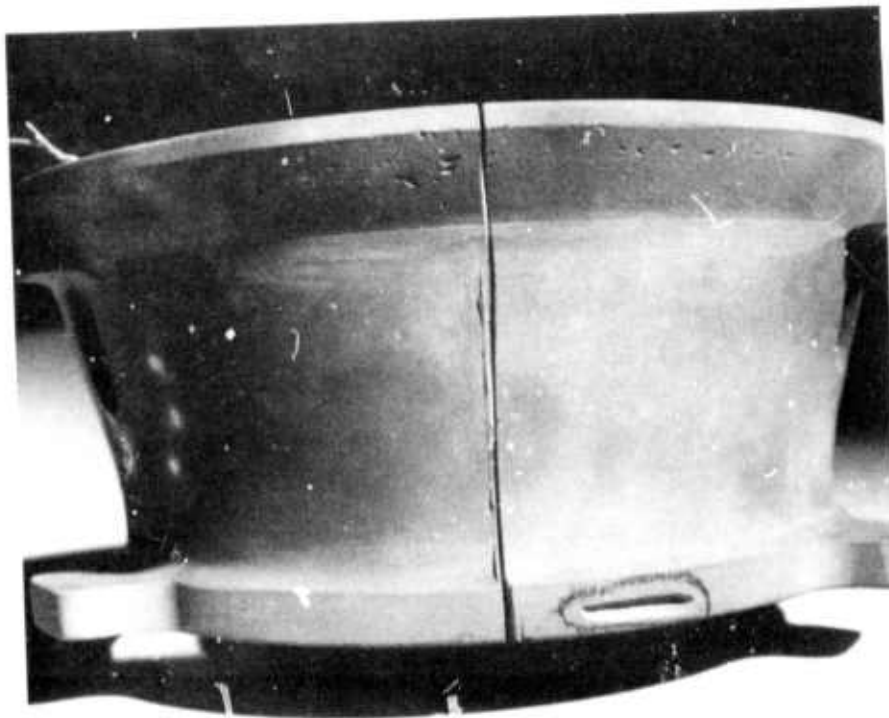
Figure 3.23   Nose Cone Illustrating Molding Flaws

Rotor Shroud Development

Rotor shroud rings, shown in Figure 3.24, are located directly downstream from each stator stage in the engine assembly and form the rotor tip shroud. As noted in the last report [4], these shroud rings are made of slip cast reaction sintered Si_3N_4. Cracking of these parts is not a problem, but difficulty has been experienced due to changing dimensions during operation [4].

Shroud rings containing additives of 1% and 3% Fe_2O_3 as nitriding aids were bench tested for periods up to 450 hours. The test procedure as described in some detail in the last report [4] and consisted of furnace heating at 1900°F with an applied load simulating engine conditions.

Results of testing during this reporting period showed a characteristic decrease in shroud gap width of 0.007 inches within the first 10 hours for materials containing both 1% and 3% Fe_2O_3. After this initial change, the gap width remained constant for 450 hours. Preliminary engine testing (refer to Section 3.2.2 of this report) indicates improved performance of these shroud rings.

52
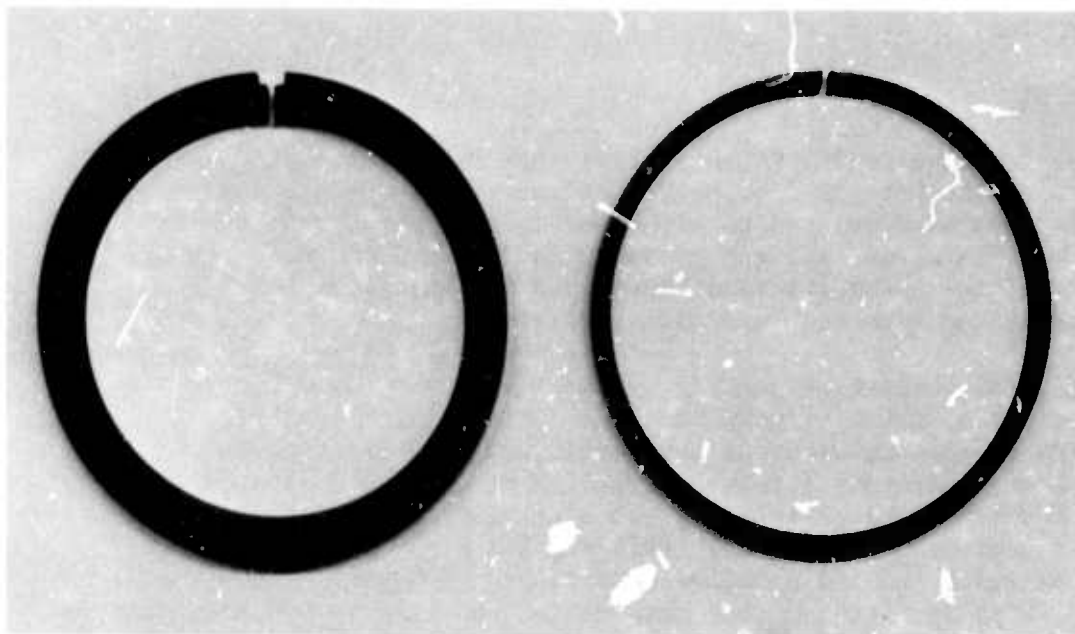
Figure 3.24   First and Second Stage Rotor Shroud Rings

3.2.2 TESTING

Introduction

The inlet nose cone turbine stators, and rotor tip shrouds are classified as the hot gas flow path stationary components. These components must be developed to withstand thermal shock upon engine startups and shutdowns, hot gas pressure loading and thermal stresses imposed by engine operating conditions, and mechanical and vibratory loads transmitted from the surrounding structures.

During this reporting period, two test rigs were used for most of the evaluation of these components. The thermal shock test rig [4] is very useful because it provides repeatable and readily observable thermal shock conditions for the evaluation of changes in stator vane design. A ceramic stator test rig was also developed and utilized for stationary component evaluation. This rig was a converted engine test rig, and provided realistic engine conditions. A quartz window was installed which permitted direct observation and temperature measurement of stator vanes. The inlet nose cone and rotor tip shrouds were also tested in this rig, since they made up the balance of the ceramic hot flow path.

In addition to component testing performed in these two rigs, further evaluation was conducted in test engines.

Thermal Shock Rig Testing

During this reporting period, the thermal shock test rig and Ircon pyrometer installation previously described [4] were utilized to determine both heating and cooling thermal response behavior of Design C first stage stator vanes. Figure 3.25 is a schematic diagram of the
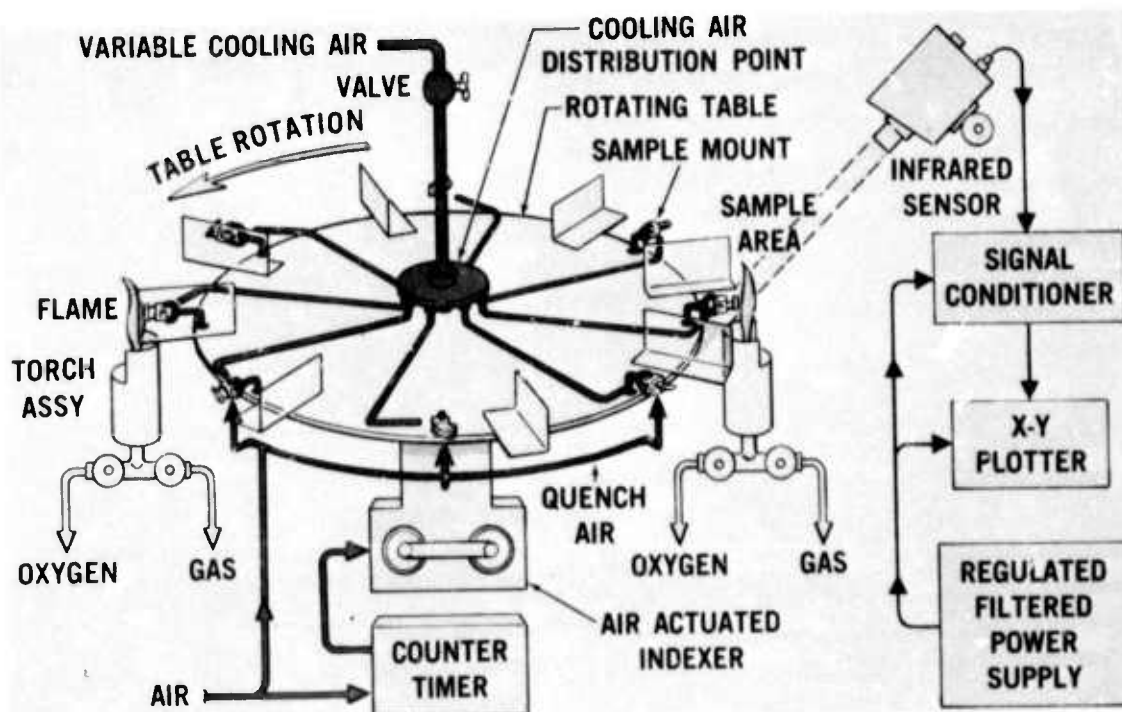
Figure 3.25   Thermal Shock Test Rig Schematic

test rig and the temperature measurement and data acquisition system. The stator vanes evaluated were injection-molded reaction-sintered silicon nitride.

Heating and cooling rates were measured at various locations on the stator vane. Representative curves for six points are shown in Figures 3.26 and 3.27. The sketch of a vane shows the point locations for each curve; temperatures were measured on a 1/16 inch diameter spot by the pyrometer. The triangles represent the maximum temperature change over a one second interval for each point.

The curves show that the thermal shock rig heated vanes at a slower rate than did the ceramic stator test rig. Cooling rates were faster on the thermal shock rig in comparison to the ceramic stator test rig. Curves of heating and cooling rates measured in the stator test rig are presented later in this section.

The predicted failure mode for stator vanes was tensile failure at the trailing edge on downshock. It was found by increasing the severity of the test that a cooling rate of more than 800°F/sec. at the midspan trailing edge was required to fail a Design C first stage stator vane. As shown in the next section, this cooling rate is significantly greater than that encountered in engine operation. Thus, the faster cooling rate of the thermal shock test rig permitted downshock testing under more extreme conditions than would be expected during engine operation.
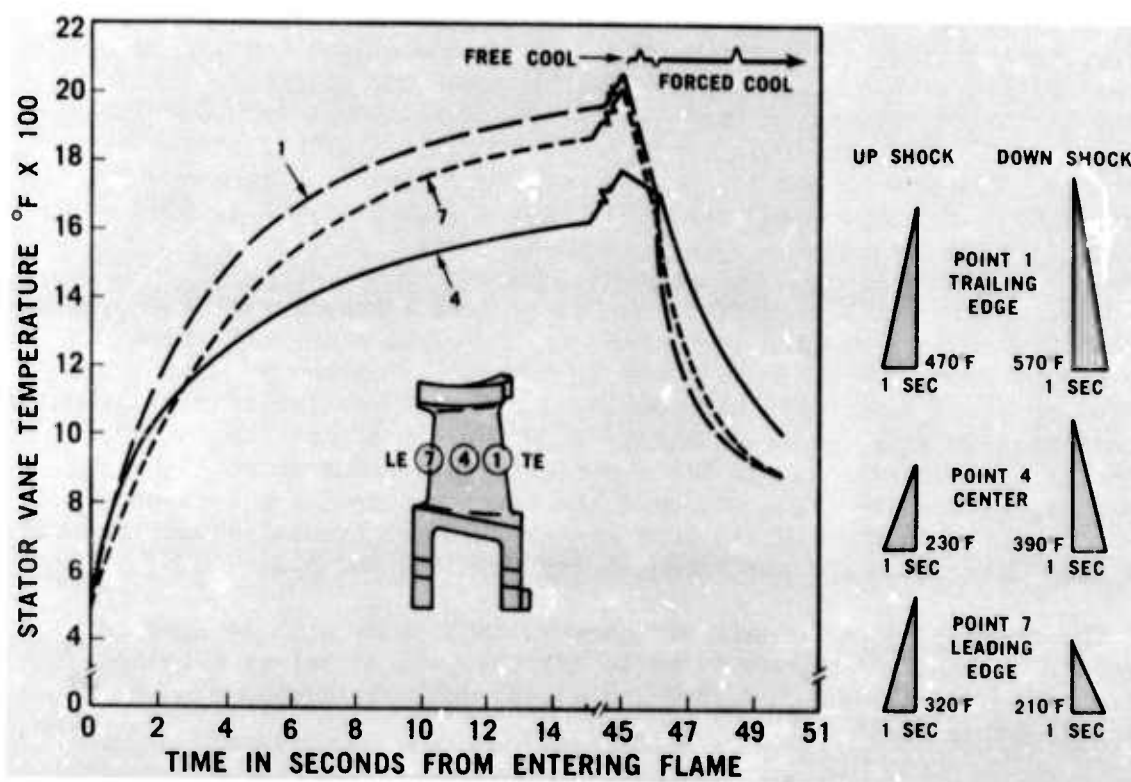
Figure 3.26   Heating and Cooling Behavior of First Stage Design C Stator Vanes on the Thermal Shock Rig
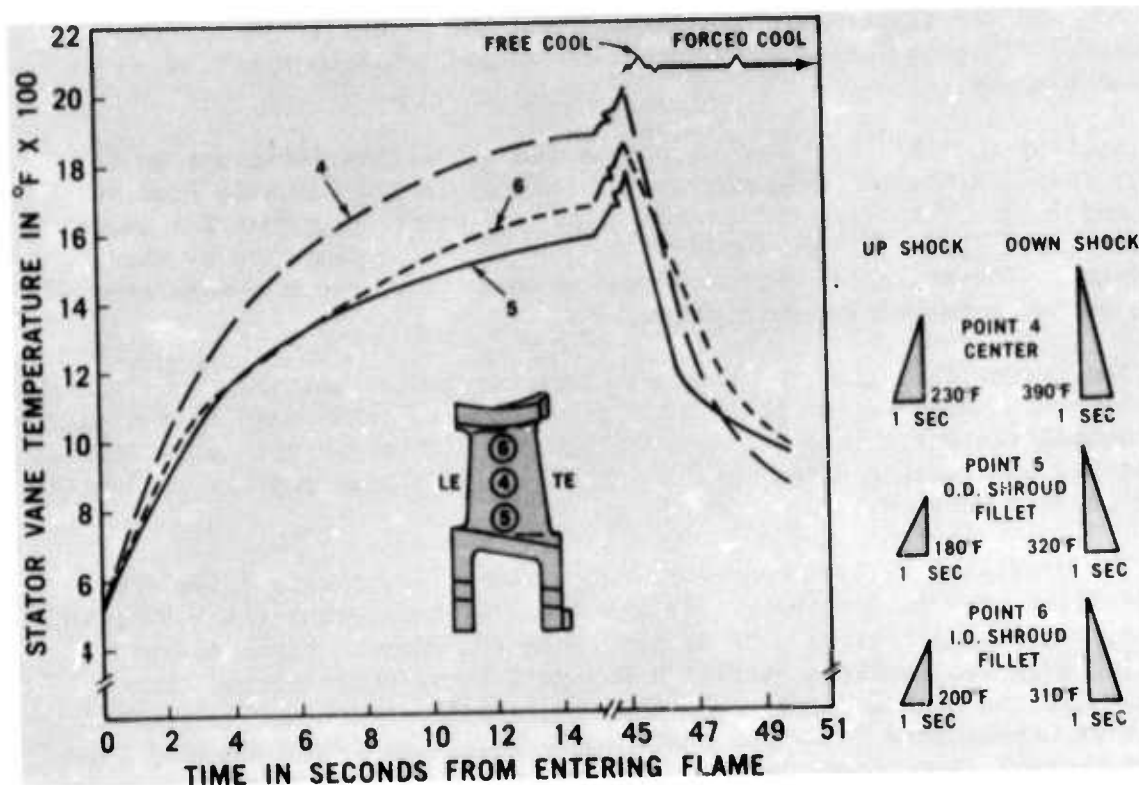
Figure 3.27   Heating and Cooling Behavior For First Stage
Design C Stator Vanes on the Thermal Shock Rig

Ceramic Stator Rig Testing

In order to evaluate the thermal response of the ceramic stators
when operating under realistic turbine engine conditions, an engine test
rig was fitted with a quartz window in the combustor assembly.   This
window permitted viewing of the first stage stator vanes from outside the
engine, and this rig was designated as the ceramic stator test rig.   A
schematic of the combustor and stator portion of this rig is shown in
Figure 3.28.   The same Ircon pyrometer that was used on the thermal shock
test rig just described was also used on this rig.

Before using this pyrometer to measure vane temperatures, the system
was calibrated by comparing its output to that from a chromel-alumel
thermocouple whose location is shown in Figure 3.28.   The pyrometer was
sighted on the thermocouple head during a number of cycles of rig operation.
The calibration data, shown in Figure 3.29 indicated that the infrared
pyrometer was accurate except for the first few seconds after light off
when a high-intensity flame obscured the target.   The thermal response of
the same points on the vane as were measured on the thermal shock test rig
were then determined and are shown in Figures 3.30 and 3.31.

The thermal response data obtained in this study will be used to
correlate actual vane temperatures to the theoretical values obtained from
a three-dimensional heat transfer and stress analysis computer program
presently being developed.

56
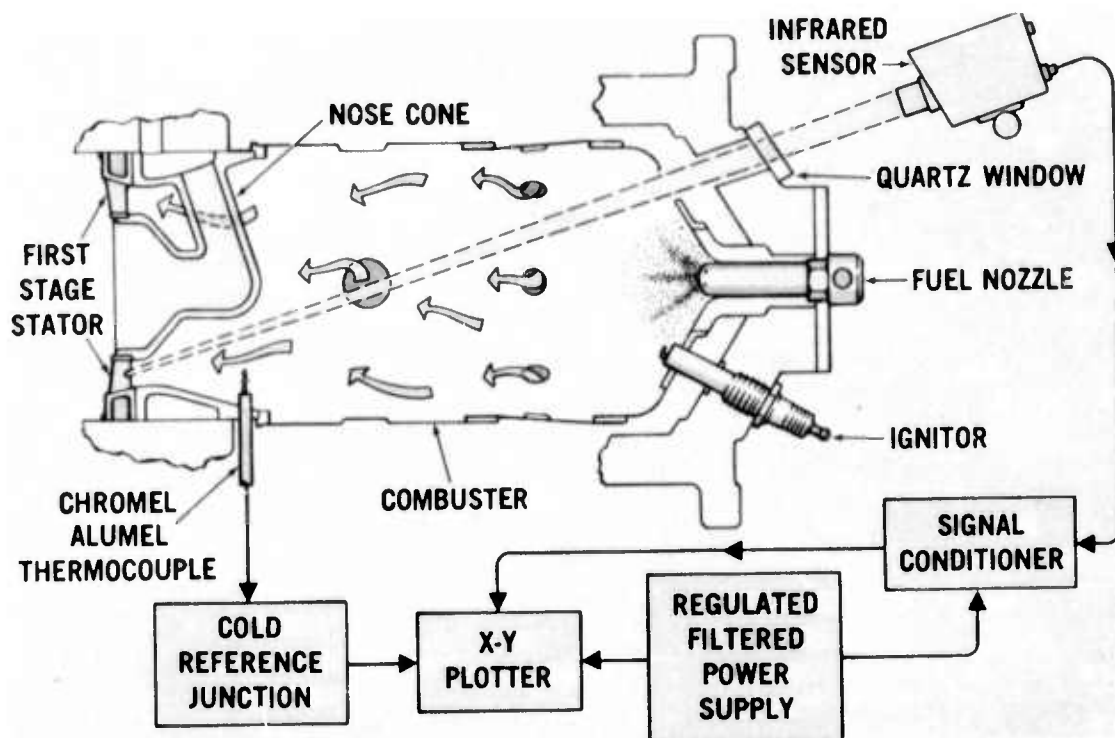
Figure 3.28   Ceramic Stator Test Rig Schematic
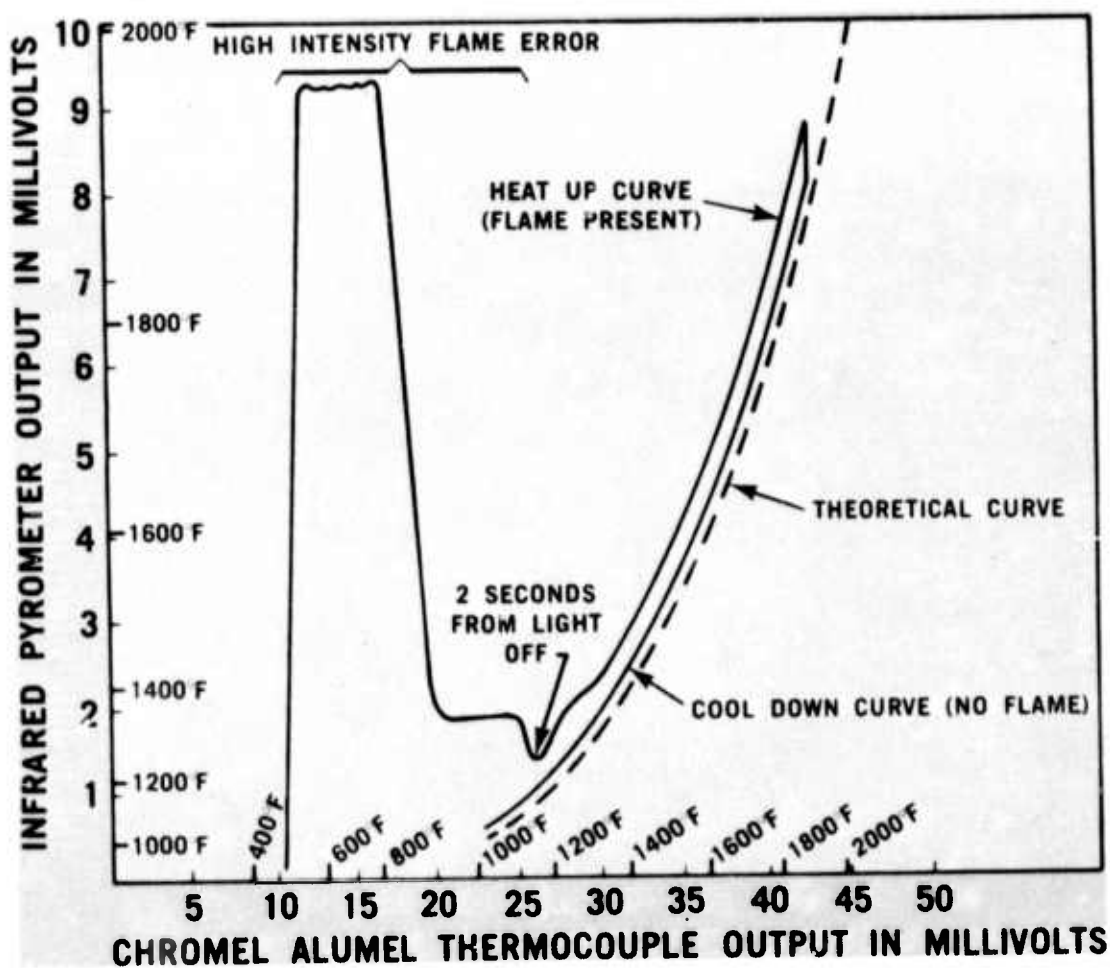
Figure 3.29   Infrared Pyrometer Calibration Curve For The
Ceramic Stator Test Rig
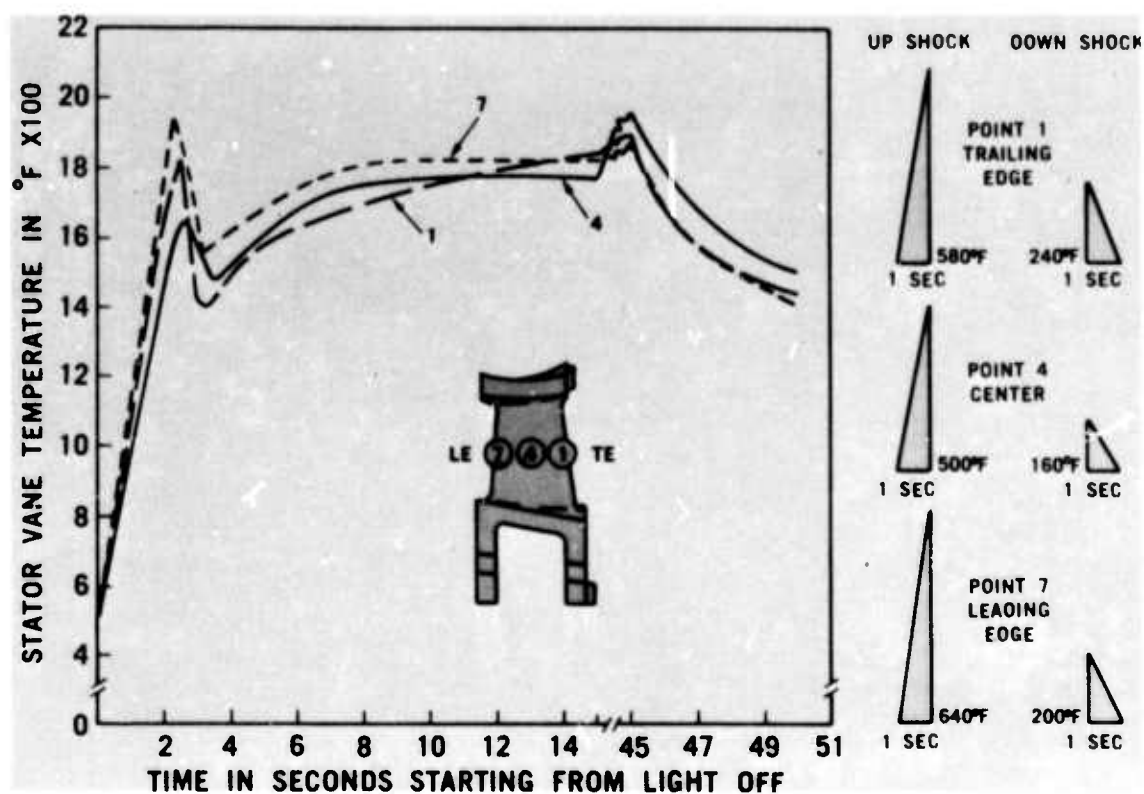
Figure 3.30   Heating and Cooling Behavior of First Stage
Design C Stator Vanes in the Stator Test Rig
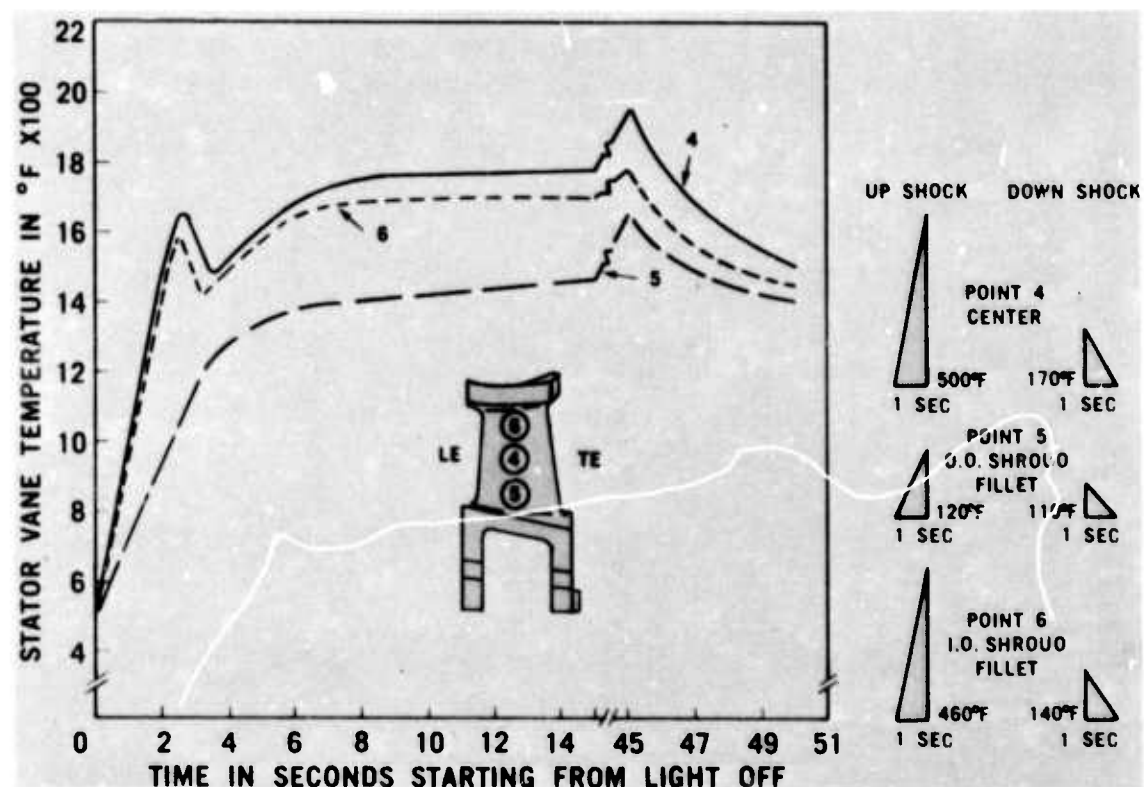
Figure 3.31   Heating and Cooling Behavior of First Stage
Design C Stator Vanes in the Stator Test Rig

Hot Static and Dynamic Testing of Stators, Shrouds, and Nose Cones

The ceramic stators, shrouds and nose cones were qualified in an engine test rig prior to incorporation in a complete engine for continued testing and development.

Component qualification consisted of the following:

(1) 25 static light cycles
(2) 3 hours of static testing, and
(3) 25 hours of dynamic testing

Testing without rotors was referred to as static testing whereas testing with rotors was referred to as dynamic testing. The various test conditions under which the ceramic stators, nose cones, and shrouds were qualified were as follows:

.Static Light Cycle - sequence of (1) lightoff and acceleration to 55% speed, and (2) shutdown (zero fuel) and speed reduction back to lightoff condition. This condition is held until the turbine inlet temperature falls to $500^{\circ}F$ whereupon the sequence is repeated for the desired number of cycles. One of these cycles is termed the one light test.

.Static Testing - 55% engine speed with turbine inlet temperature limited to $1900^{\circ}F$.

.Dynamic Testing - 60% speed with turbine inlet temperature limited to $2000^{\circ}F$.

The evaluation of Design B and C nose cones, stators and shrouds was accomplished in engine test rigs, and the results are summarized in Table 3.4 which gives the total time on all components which underwent any testing during this reporting period. Most of the components listed were manufactured from reaction-sintered silicon nitride except those with the superscript .4 which were made from lithium-aluminum-silicate.

The evaluation of eight Design C first stage stators resulted in a total of seven vane failures occurring with five of these stators. One of these vane failures was caused by impact from foreign matter in the flow path and another one was caused by a large flaw in the vane. The remaining five vane failures were due to thermal shock. The three remaining first stage stators failed due to improper assembly or by rough handling. However, one stator did survive 111 hours of testing and another lasted for 403 lights before both were damaged by other causes.

As shown in Table 3.4, one inverted channel first stage stator was tested. This stator was the first of its type and had many vane failures. These failures may have been caused by poor assembly of the stator. More tests will be required to properly identify the problem.

The evaluation of eight inverted channel design second stage stators resulted in six failures. Two of these stators had vane failures due to molding defects. The remaining four failures were due to cracks in the outer shroud.

As was mentioned in the last report [4] the first and second stage silicon nitride rotor shrouds were creeping under hot running conditions. This problem was investigated, and the nitriding agent used in these slip cast parts was changed (see Section 3.2.1 of this report). One shroud of this modified material has undergone 78 hours of hot rig testing and is still serviceable. Further testing is presently underway.

As discussed in the last report [4] the modified "scalloped" nose cones still dev-'oped axial cracks in the outer shroud. These cracks were believed to be caused by thermal stress due to different heating and cooling rates of the struts and shroud during transient engine operation. In order to alleviate this condition and to prevent the occurrence of dangerous circumferential cracks, the outer shroud was cut axially in three places. This nose cone is termed Design C. Five nose cones of this configuration were evaluated and two failed. One of these failures was caused by improper assembly of adjoining parts and the other may have been caused by foreign material lodging in a slot. One nose cone of this design has undergone 88 hours of testing and another one 411 lights and both are still uncracked. Although these results have not yet proven that this design modification has completely solved the cracking problem, they do show that this nose cone design is significantly better than the Design B nose cone.

TABLE 3.4

SUMMARY OF TESTING OF CERAMIC NOSE CONES, STATORS, AND SHROUDS

First Stage Stator

Component	268	361[2]	363[2]	366[2]	367[2]	368[2]	369[2]	370[2]	371[2]	1[3]	Totals
Hot Static Hrs.	5.5	10.5	111	3.5	45.5	1	0.5	62	1.5	0	241
Hot Dynamic Hrs.	0	19	0	27.5	0	0	0	3	0	0	49.5
Total Hot Hrs.	5.5	29.5	111	31	45.5	1	0.5	65	1.5	0	290.5
Total Lights	192	172	78	403	289	52	26	69	55	2	1338
Status	F,V	F,V	F,C	F,X	F,V	F,V	F,V	F,C	F,H	F,V	

Second Stage Stator

Component	5[3]	7[3]	8[3]	9[3]	15[3]	16[3]	18[3]	25[3]	Totals
Hot Static Hrs.	35.5	0.5	.5	0	1	1	0	.5	39
Hot Dynamic Hrs.	3	5	18	13	0	0	0	0	39
Total Hot Hrs.	38.5	5.5	18.5	13	1	1	0	.5	78
Total Lights	16	163	38	119	25	25	15	51	452
Status	S	S	F,C	F,C	F,C	F,V	F,V	F,C	

First Stage Shroud

Component	1[4]	2[4]	8[4]	10[4]	13[4]	14[4]	15[4]	16[4]	4	8B	9	11	19	21	23	24	25	26	Totals
Hot Static Hrs.	111	14.5	.5	5.5	5	3	25	3	134.5	109	94.5	16.5	21.5	50	50	78	10	10	741.5
Hot Dynamic Hrs.	23.5	.5	27.5	0	0	7.5	4	0.5	31	6	28.5	42	0	0	0	0	0	0	171
Total Hot Hrs.	134.5	15	28	5.5	5	10.5	29	3.5	165.5	115	123	58.5	21.5	50	50	78	10	10	912.5
Total Lights	371	457	65	360	55	38	71	37	308	157	747	246	11	764	498	33	2	2	4222
Status	F,C	F,C	S	S	S	S	S	S	F,K	F,K	F,K	F,K	F,C	F,K	F,K	S	F,K	F,K	

Second Stage Shroud

Component	1[4]	3[4]	4[4]	8[4]	10[4]	11[4]	12A[4]	12B[4]	19[4]	22[4]	14	15	33	34	35	36	37	Totals
Hot Static Hrs.	4.5	109.5	8	0.5	0	8.5	0	2.5	0	8.5	7	0	10	78	11	1.5	18.5	268
Hot Dynamic Hrs.	3	0	4	16	11.5	0	3	0	27.5	0	0	3.5	0	0	0	0	0	68.5
Total Hot Hrs.	7.5	109.5	12	16.5	11.5	8.5	3	2.5	27.5	8.5	7	3.5	10	78	11	1.5	18.5	336.5
Total Lights	106	322	319	126	185	105	6	105	34	36	201	53	2	33	7	133	16	1789
Status	S	S	S	S	F,C	S	S	S	F,K	S	F,K	F,C	F,K	F,K	F,K	F,K	S	

Nose Cone

Component	20[6]	35	36	40	58[5]	70[6]	71[6]	73	81[5]	86[6]	103[6]	Totals
Hot Static Hrs.	88	143.5	86	210.5	1	11.5	9	7.5	0	4	18.5	579.5
Hot Dynamic Hrs.	0	3	0	10.5	8	3	0	1	19.5	0	0	45
Total Hot Hrs.	88	146.5	86	221	9	14.5	9	8.5	19.5	4	18.5	624.5
Total Lights	35	219	159	113	104	16	411	140	7	162	16	1382
Status	S	S,C	F,C	F,C	F,C	F,X	S	S	S	F,C	S	

Status Legend
C-Cracked shroud
F-Failed
H-Broken during handling
K-Part failed due to creep
S-Serviceable; at present nose cones are considered serviceable if the outer shroud
   has only axial cracks. First stage stators are considered serviceable
   if outer shroud is cracked
V-Cracked or broken vane (5)
X-Result of other component failure

[2] Design "C"
[3] Inverted Channel Design
[4] Lithium-Aluminum-Silicate material
[5] Scalloped nose cone-Design B
[6] Scalloped and slotted nose cone-Design C

4.0 PROGRESS ON THE STATONARY TURBINE PROJECT

4.1 STATOR VANE DEVELOPMENT

SUMMARY

Design studies for the modification of the advanced turbine test and demonstration have been initiated. Gas path temperatures have been calculated and used to define the cooling requirements for the first stage metal rotor, the second stage metal stators, and the second stage metal rotor. Only the first stage turbine rotor blade must be redesigned. All other components can be modified to meet the higher temperature requirement.

Silicon nitride stator vane assemblies manufactured by the Norton Company were tested successfully in the static rig at $2200^{\circ}F$ under cyclic conditions at pressure ratios up to 8:1. Cracks were observed in four of eight airfoils and two outer end caps. Failure resulted from areas of local stress concentration caused by edge loading. All of the LAS insulators were cracked badly at the conclusion of testing.

The static rig is being modified for operation at a peak temperature of $2500^{\circ}F$. Silicon carbide stator vane assemblies have been delivered and will be tested with additional silicon nitride vane assemblies at $2500^{\circ}F$. The test configuration will contain eight vane assemblies. At least two will be silicon nitride components (2 airfoils and 4 end caps) previously tested to $2200^{\circ}F$.

An assessment of the current status of stator vane development indicates that the three-piece vane assembly proved to be a valid design concept for the use of brittle materials in large stationary gas turbines, although the results of the $2200^{\circ}F$ static rig tests demonstrated the criticality of design tolerances in component manufacture. The tests failed to disclose any performance limiting characteristics in Norton HS-130 silicon nitride vane material. Design changes are anticipated to reflect the results of subsequent static rig tests at $2500^{\circ}F$ and to improve the aerodynamic qualities of Si_3N_4 and SiC vanes for the advanced turbine test. The cracking of the LAS insulators indicates the need for design review and additional material study in this area. Strong emphasis is now being placed on design of the modification of the 30 MW frame size turbine to be used for the ceramic vane demonstration of a peak temperature of $2500^{\circ}F$. The redesigned first stage rotor blade represents the major long lead item in the procurement of metal hot section components.

4.1.1 DESIGN AND ANALYSIS

Introduction

A three-piece ceramic stator vane assembly is currently being evaluated for application in an advanced stationary gas turbine. The use of silicon nitride or silicon carbide stator vanes is intended to increase the service temperature from 1955°F to a peak of 2500°F without having to cool the first stage stator row.

The large size of the Westinghouse turbine permits a design which is better suited to brittle materials than the more conventional geometry in which the airfoil is integral with the shrouds. The 3-piece vane assembly eliminates stresses that normally result from abrupt changes in section and it provides for relative adjustment of the parts under thermal and mechanical forces. Separate pieces of simpler geometry are also easier to fabricate from presently available Si_3N_4 and SiC billet materials.

Now that ceramic stator vane assemblies have been tested successfully in a static rig under cyclic conditions to a peak temperature of 2200°F (ref. section 4.12 of this report), the design effort has been expanded to establish the rotor and stator systems for the advanced turbine test facility. Some modification of the static rig component geometry is required in order to incorporate ceramic stator vanes into the full first stage stator row of an existing W-251 test turbine (Fig. 4.1). The remainder of the test turbine's power section and exhaust system must also be upgraded for 2500°F operation.

The Rotating Test Turbine

Before actual hardware can be designed or modified for use in the rotating test turbine, it is necessary to predict temperatures along the proposed gas path in an effort to determine appropriate turbine conditions. Typical results of such computer calculations appear in Fig. 4.2 for an average turbine inlet temperature (TIT) of 2300°F using the current W-251 test turbine as the model. Here a peak temperature of 2400°F in the gas temperature profile occurs at 60% of the vane height for a first row stator location. An average turbine inlet temperature between 2300 and 2350°F is expected to produce the required peak temperature of 2500°F in the first row ceramic vanes of the advanced test turbine. Any increase in turbine inlet temperature represents a proportional increase in temperature at any blade or vane position downstream in the power section. Peaks in the gas temperature profiles will be correspondingly sharper. The cooling requirements for the first stage rotor blades (Fig. 4.3) and the second stage stator vanes (Fig. 4.4) were estimated from the gas temperature data. Cooling flow comparisons are presented in Fig. 4.5.

A critical review indicates that most of the hot section components of the existing machine can be modified for use in the high temperature turbine. Only the first stage superalloy rotor blades must be redesigned to incorporate advanced cooling concepts. An investment cast structure is currently being designed to use impingement-convection cooling within the present blade envelope. The cooling air will be supplied through the blade root in the same manner as the existing blade. The air supply system and disc will be similar to the present arrangement with some modification. Cooling is required in the cavity between the first

two discs and a system must be designed to supply cooling air to the second stage rotor blades. The second row vanes will also be cooled more extensively for the purpose of the test.

2nd Stage
Stator Vane

1st Stage
Rotor Blade

1st Stage
Stator Vanes

Combustor
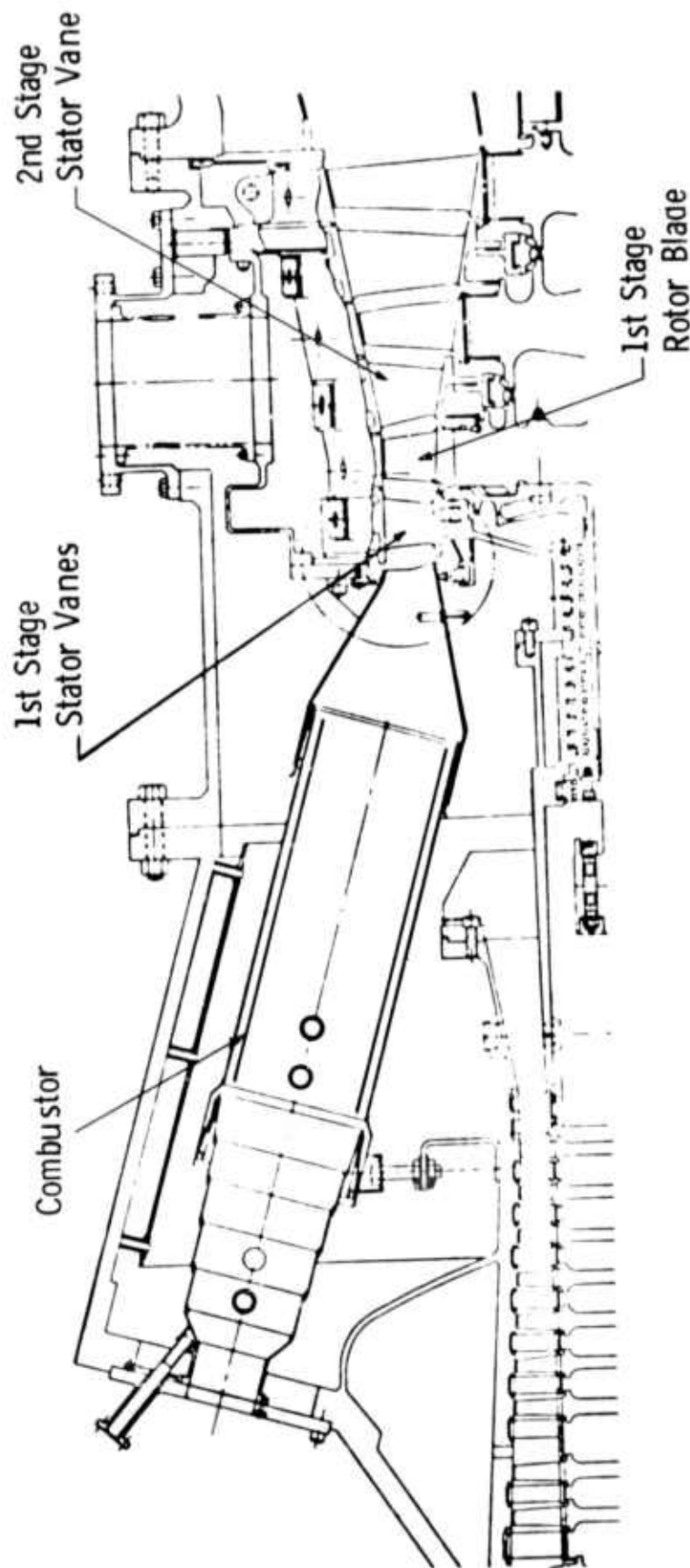
Figure 4.1   Advanced Test Turbine Flow Path
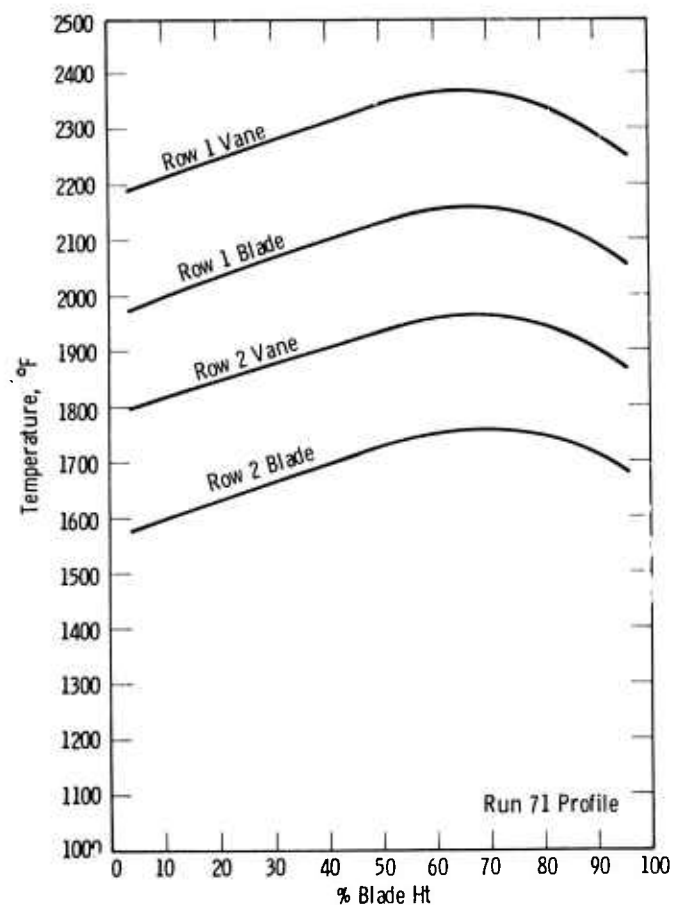
Figure 4.2   Calculated Gas Temperatures at Various Stage Locations in
the Power Turbine for 2300°F Turbine Inlet Conditions
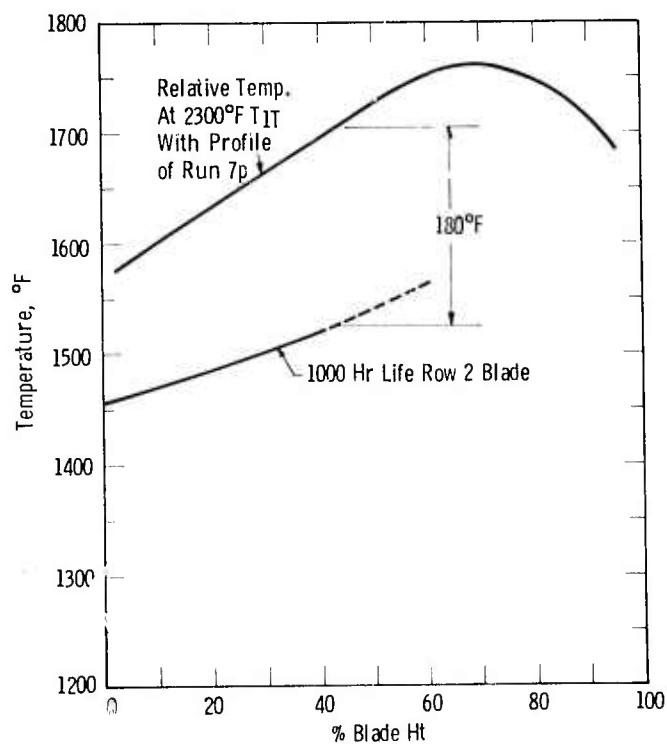
Figure 4.3   Row Two Blade Cooling Requirements
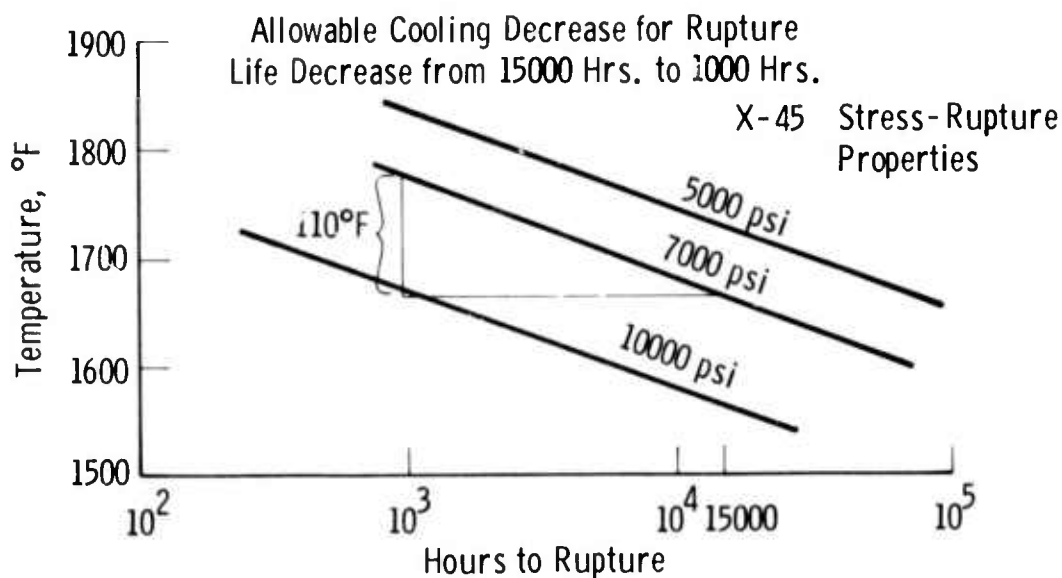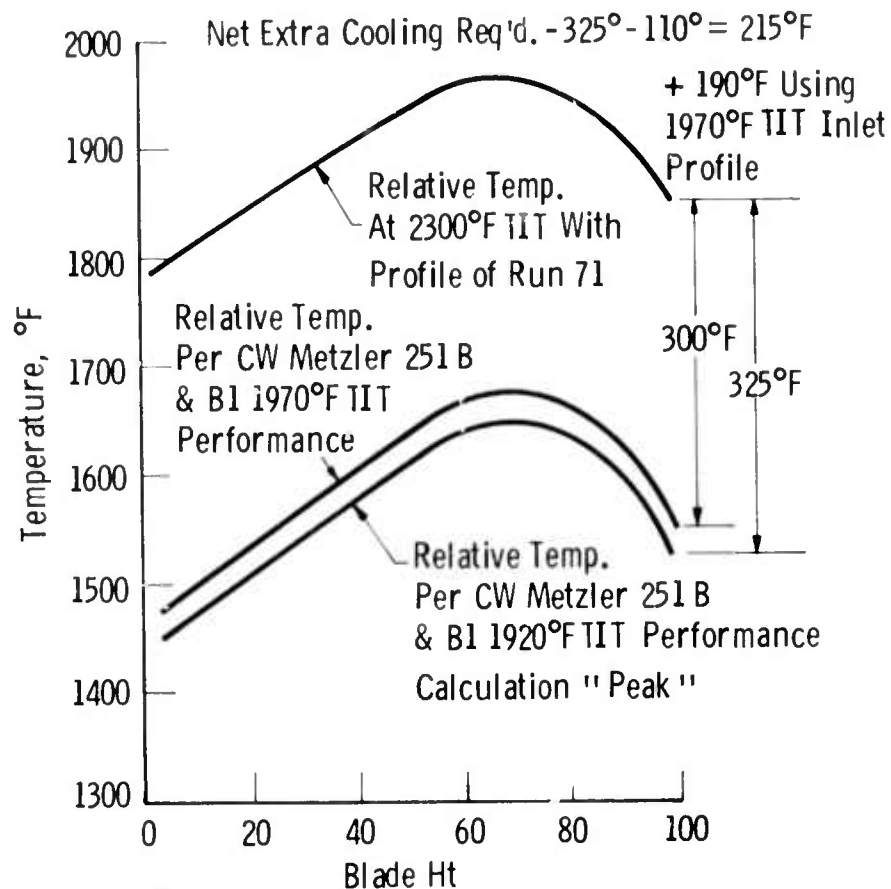
Figure 4.4   Row Two Vane Cooling Requirements

Emphasis is being placed upon the first stage blade design because it represents the only long lead time item in the procurement of metal hot section component parts.

1950°F TIT
Data Modified From
251 B-1 Cooling Flow Tabulation

Exh Station

2300°F TIT
Estimated Cooling Flows

Exh Station
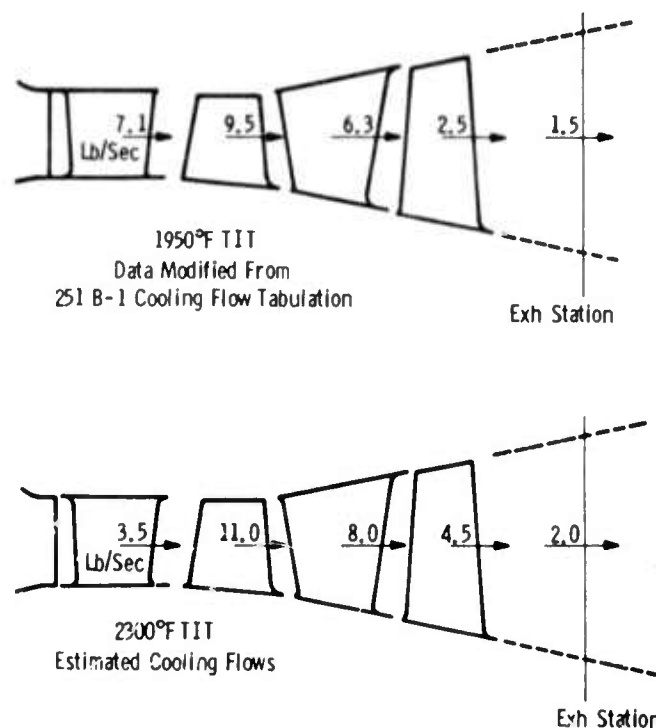
Figure 4.5   A Comparison of Cooling Flow Requirements at 1950°F and
2300°F Turbine Inlet Temperatures

Preliminary layouts have been completed for the ceramic vane
assembly for the rotating rig test. Except for mounting and installation,
the insulators, seals and metal support system will be similar to
those employed in the static rig. The total configuration will contain
a full compliment of 80 vanes.

The majority of the vane assemblies to be tested in the full
turbine test will be similar to the first generation design which was
tested in the static rig. A tapered, twisted airfoil will be used to
properly orient the air flow entering the first rotating stage, however.
The end cap cavity will be reduced approximately 25% and the airfoil tenon
geometry will be redesigned to minimize the aerodynamic inadequacies inherent
in the use of a large symmetric cavity and the exaggerated trailing edge
relief, respectively. The curvature at the end cap-insulator interface
will be increased to insure proper location regardless of the friction
characteristics at the interface.

A limited number of second generation design stator vane assemblies
(8-10)[4] will be tested in the turbine if their performance in subsequent
static rig tests proves satisfactory. The second generation design
differs from the first in that the airfoil tenon is formed to fill the
end cap cavity completely. The need for specific trailing edge relief
is eliminated by making the major radius of the airfoil tenon equal to
half the chord at the airfoil extremities. Unfortunately, this particular
configuration has proven difficult and expensive to machine from billet
material. Since the tenons extend beyond the airfoil envelope in the
transverse plane, the airfoil must be blended to form the tenon by means
of a fillet radius. Fixturing becomes a problem and three dimensional
diamond grinding must be employed to remove excessive amounts of material
to form the airfoil itself.

68

4.1.2 STATIC RIG TESTING

Introduction

The program reached its first critical milestone with the completion of the first phase of static rig testing at 2200°F. A cascade of eight prototype silicon nitride vanes successfully survived the 100 start-up and shut-down cycles selected to simulate peaking service in power generation. Typical turbine operation includes cold start, acceleration to idle, load increase to peak power, power generation and scheduled shut-down. Occasionally, emergency shut-downs or fuel trip-outs occur. Under these conditions, the fuel supply is interrupted causing the turbine to coast to a stop. Severe transient thermal stresses are imposed as the compressor continues to discharge unheated air to the hot section.

The test conditions matched the service sequence in all practical aspects. After ignition, temperatures were increased repetitiously from idle (1200°F) to peak (2200°F) following each controlled reduction to idle. Two full-flow flameouts were imposed; one at 50% simulation, the other at 80%. Percent simulation is used to compare the test condition with that of an actual turbine based on pressure ratio. Static rig tests were conducted at pressure ratios of 3:1 (30%), 5:1 (50%) and 8:1 (80%).

The Static Rig

A plane view of the static test rig is given in Fig. 4.6. This facility was designed and constructed specifically to create an environment identical to that of a gas turbine. Ceramic vane assemblies are tested in their true radial configuration and actually perform a gas turning
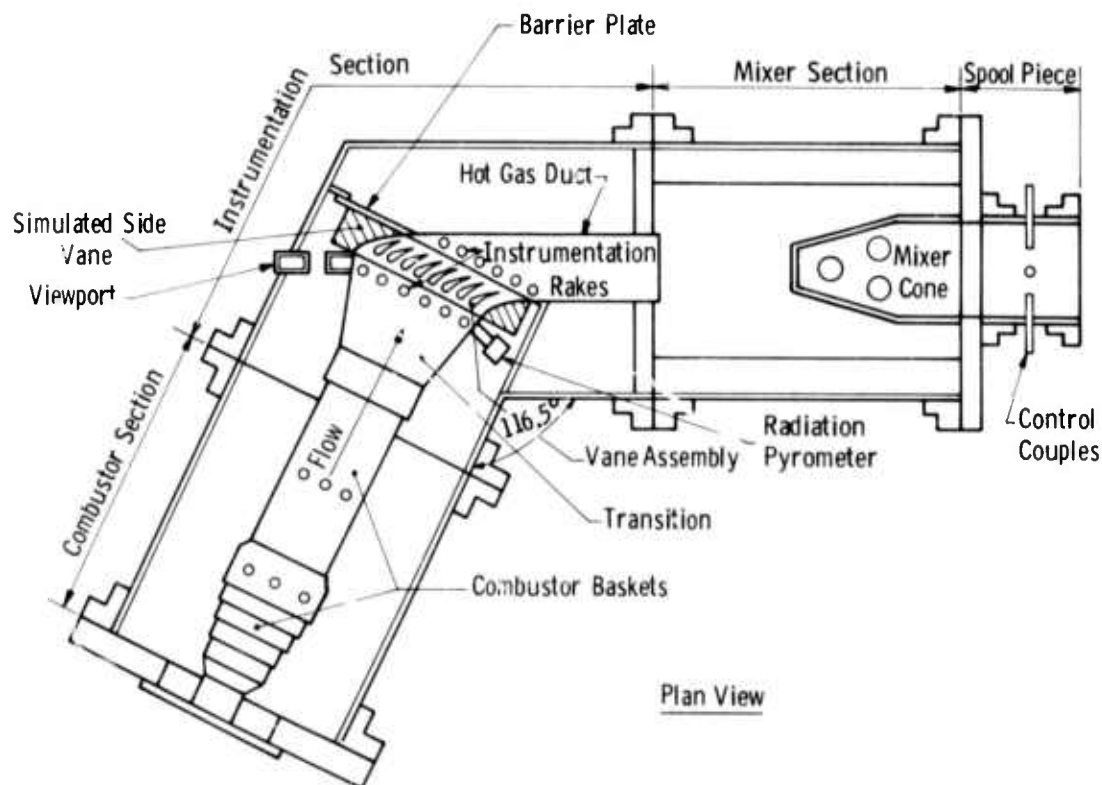
Figure 4.6   Schematic of Static Rig for 2200°F Test of Ceramic Vanes

69

function. Scale-up problems are eliminated by employing full size combustor hardware and fuel nozzle assemblies. Internal flow baffles are used to direct inlet air flow and simulate the shell geometry that surrounds the combustion system in a gas turbine. A number of sight glasses permit test hardware to be observed under test.

The use of a cooled-wall combustor produces a temperature-profiled gas stream which passes from the transition piece, through the vane segments in the mitered section, and into a complex exhaust duct which channels the gas to the mixer. The mixer section tends to smooth the temperature profile of the gas stream by turbulence so that hot gas of a more uniform temperature is monitored by control instrumentation. A high temperature composite refractory material is employed to insulate the mixer for applications up to 3000°F. The operating pressure level of the rig is controlled by the back pressure valve located downstream of the measurement section. Actual photographs of these key components are shown in Figs. 4.7 through 4.9.

Aspirating thermocouple rakes are inserted in the gas stream both upstream (42 thermocouples) and downstream (49 thermocouples) of the test assembly. These are used to measure the temperature profile of the gas stream and to approximate vane temperatures. The data are corroborated by readings from a radiation pyrometer focused mid-height on the pressure side of the number 4 vane.

The metal components of the vane assembly, namely; shoes, air baffles, metal side vanes, and housing rings were instrumented with swaged metal thermocouples to monitor the thermal response of the test assembly. These data are used to verify heat transfer analyses.
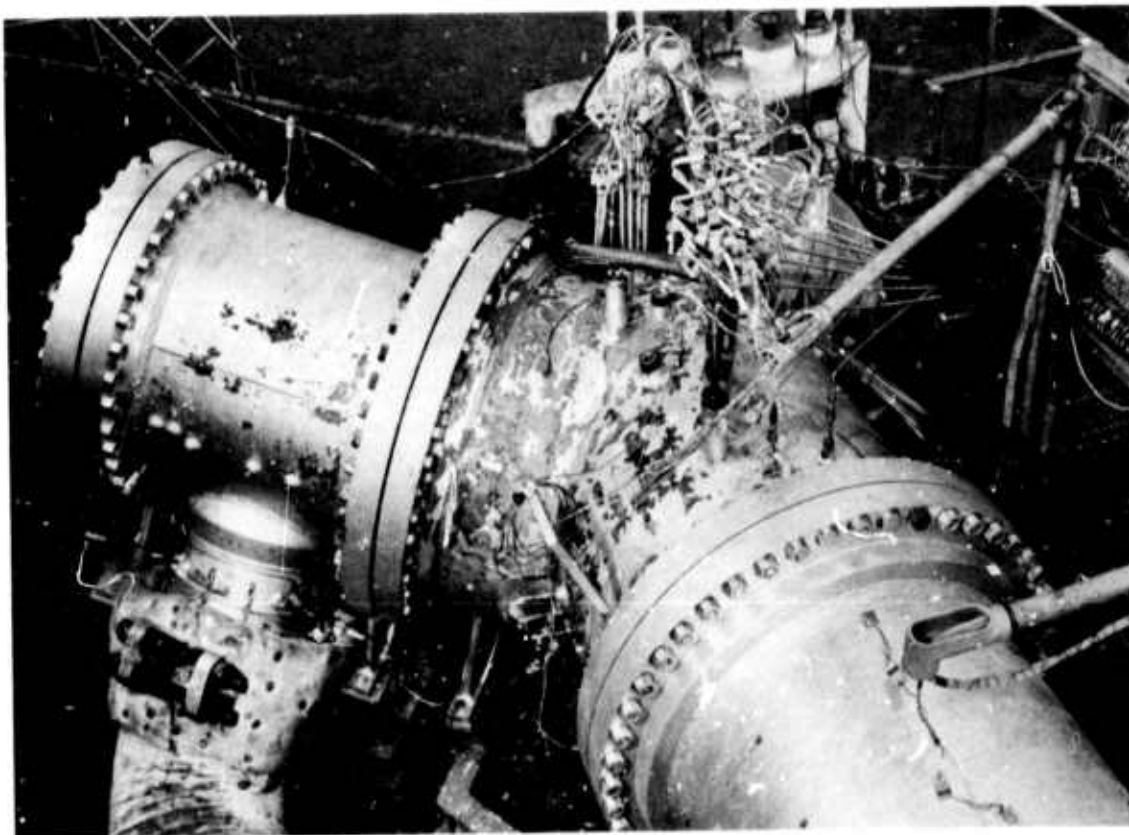
Figure 4.7   Exterior View of Static Test Rig

70
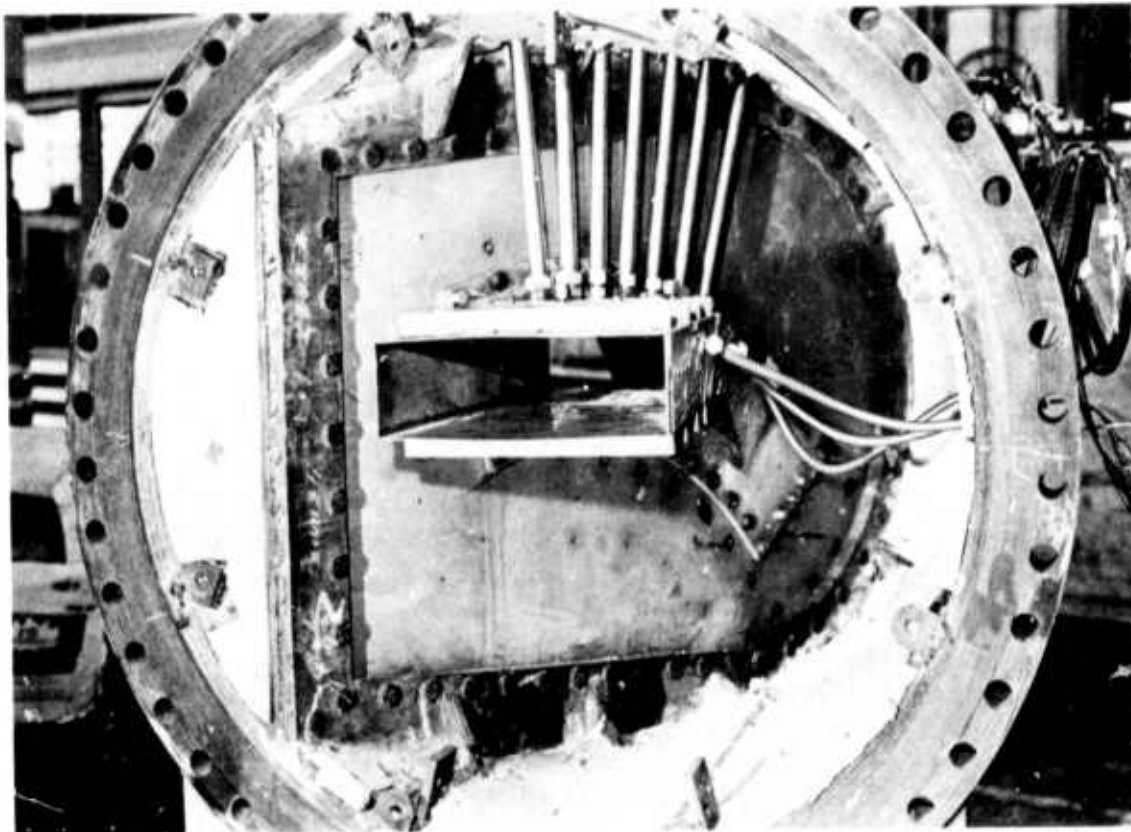
Figure 4.8   Hot Gas Duct for 2200°F Static Rig Test
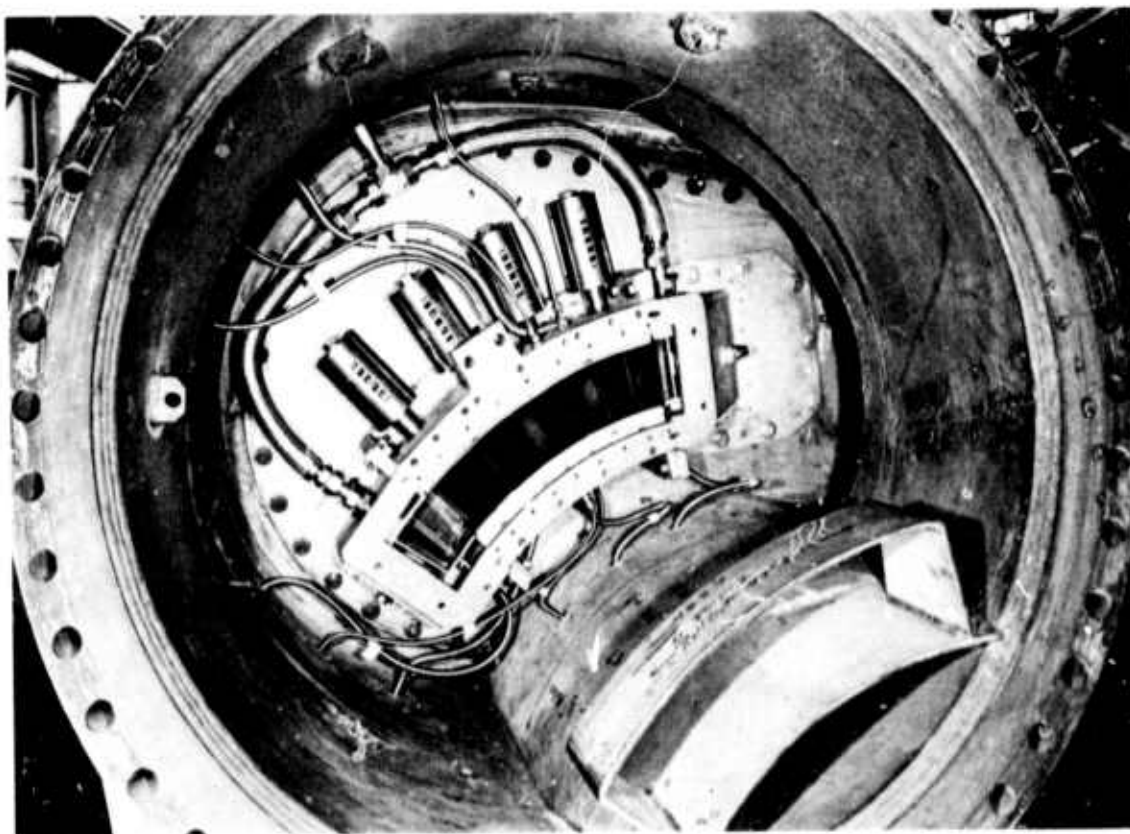
Figure 4.9   Mitered Section of the Static Rig with Test Assembly
              Installed

Existing laboratory facilities accurately record air and fuel flows, pressures, and temperatures. A Westinghouse Veritrak temperature controller accurately and reproducibly follows a prescribed mode of operation, by sensing and responding to the uniform operating temperature of the gas, downstream of the mixer section, through a system of feedback loops and variable function generators.

The raw data, whether in the transient or steady state mode, are collected by a rapid data acquisition system. Various data sequencing tapes control data retrieval during transient operation at acquisition rates of seven pieces of information per second. Computer programs convert the values directly into engineering units.

A rugged platinum-platinum/rhodium aspirating thermocouple, which monitors the peak gas temperature in the transition piece, functions to exclude extreme temperature excursions. If the gas temperature exceeds 2450°F, fuel flow to the rig is interrupted automatically.

The Test Assembly

The test section itself contained eight ceramic stator vane assemblies (Norton HS-130 silicon nitride) positioned between two air-cooled metal side vanes (X-45 alloy) which enclose the gas passage on each side. The ceramic vane assemblies (an airfoil seated in torroidal cavities between an inner and an outer end cap) were supported in pairs between lithium aluminum silicate insulators (Owen Illinois CERVET C-140), woven metal cushion material, and Haynes 188 metal shoes (Fig. 4.10). Two metal pivots support each inner shoe while a single spring loaded plunger and pivot are used at each outer shoe location. The entire assembly was fastened between inner and outer metal (Type 405 stainless) housing ring segments. Suitable cooling, seals, and air baffles were provided to keep the metal support system within specified temperature limits. The fully instrumented assembly, as it appeared before test, is illustrated in Fig. 4.11.

Flow →
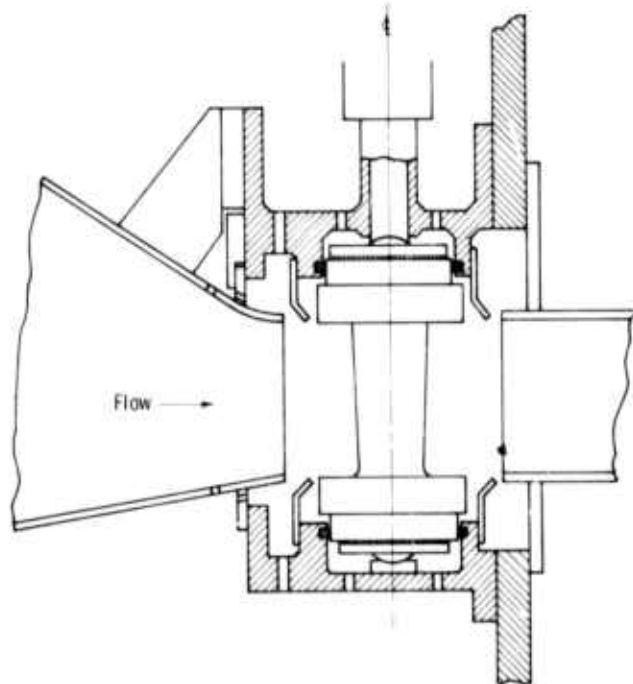
Figure 4.10   Ceramic Stator Vane Assembly for Static Rig Testing
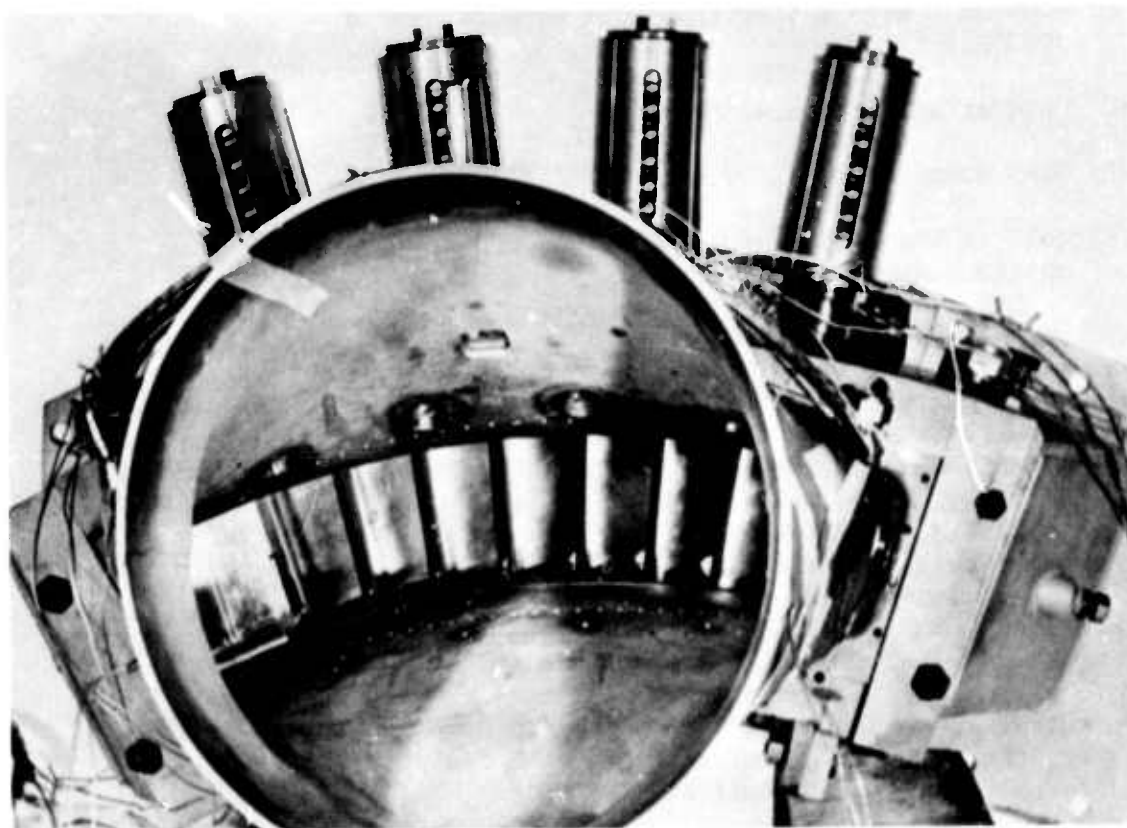
Figure 4.11   Instrumented Test Assembly for the 2200°F Static Rig
Testing of Silicon Nitride Stator Vanes

The individual elements of each ceramic vane assembly, i.e., the
airfoils and end caps as shown in Fig. 4.11, were fabricated by diamond
grinding from hot-pressed Si_3N_4 billets. Unfortunately, the vane
manufacturer was not able to meet all of the tolerances specified. The
end cap torroidal cavities, in particular, were ground too deep, up to
0.020 in.,[4] causing an edge loading condition, in certain instances,
when the airfoils were combined with the end caps under a compressive
spring load.

The 2200°F Test Cycle

The 2200°F static rig tests were performed under cyclic conditions
to emphasize the effect of transient operation as the turbine was
increased to full power and then shut-down. No attempt was made to
represent long periods at steady state because stresses were calculated
to be too low to influence vane performance significantly. Since it
was considered impractical to begin each cycle from a cold start,
the following test sequence was adopted:

(A) Increase from idle 1200°F (gas temperature at the
     vane location) to a peak at 2230°F in 120 seconds.

(B) Hold at peak 2230°F for 600 seconds to permit steady
     state data retrieval. Hold period was reduced to
     180 seconds during non-data taking runs.

(C) Shut-down with a step change in temperature to 2000°F.

(D) Hold at 2000°F for 45 seconds.

(E) Ramp down to idle 1200°F at 25°F/second.

(F) Hold at idle 1200°F for 120-600 seconds depending on the mode of data retrieval.

Although the silicon nitride vane assemblies were subjected to 106 cycles in all, the actual conditions varied from test to test as indicated in Fig. 4.12. The initial 8 cycles were run at a pressure ratio of 3:1 with shut-down controlled at 12.5°F/second (30% simulation). Subsequent tests were performed at pressure ratios of 3:1, 5:1, and 8:1, respectively. Two cycles were run to represent full-flow emergency shut-down at pressure ratios of 5:1 and 8:1, respectively. The emergency shut-down at the 5:1 pressure ratio occurred accidently; the other was planned.

A pressure ratio of 8:1 is the maximum which can be achieved in the static rig using the compressor facilities presently available. Since actual turbines are expected to operate at pressure ratios of 10:1 and higher, the static rig conditions must be scaled by simulation factors to be truly representative. Therefore:

$$\text{Simulation} = \frac{\text{Pressure}_{\text{static rig}}}{\text{Pressure}_{\text{turbine}}} = \frac{\text{Air flow}_{\text{static rig}}}{\text{Air flow}_{\text{turbine}}}$$
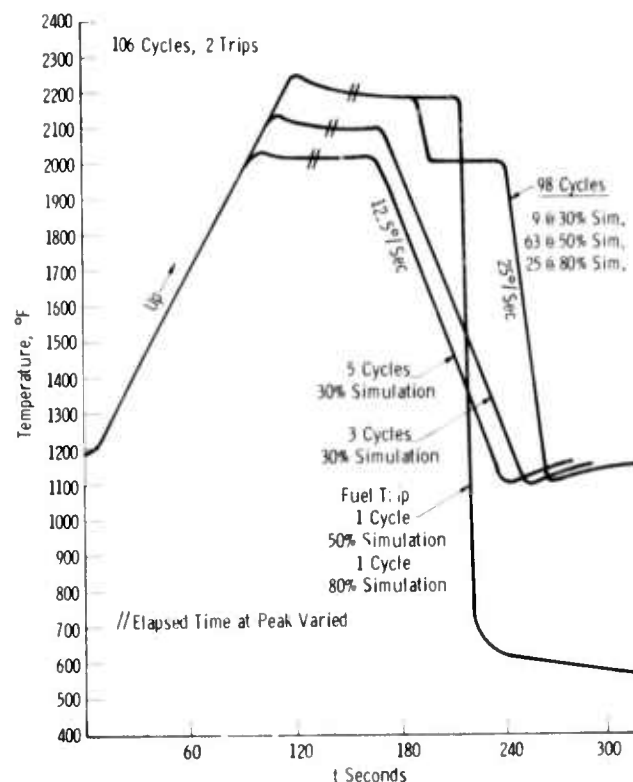
Figure 4.12   The Cyclic History of 2200°F Static Rig Tests of Silicon Nitride Vanes

74

The effect obviously influences the relative severity of the test because different heat transfer coefficients are involved. In order to place the tests in proper perspective, the heat transfer coefficients are reduced effectively in proportion to the ratio of the respective Reynold's numbers raised to the 0.8 power; specifically, 0.84 x h at 80% simulation, 0.57 x h at 50% simulation, and 0.38 x h at 30% simulation, where h represents heat transfer coefficients for a machine operation at a 10:1 pressure ratio.

Transient heat transfer and stress analyses were performed to determine the state of stress in the ceramic airfoils for any particular set of static rig test conditions. The preliminary two dimensional model is presented in Fig. 4.13. By symmetry, only half of the airfoil is considered. The boundary conditions are such that there is no displacement in the z-direction for all points in the plane of symmetry. Rotation is prevented by putting constraint on two points in the plane.

A three dimensional finite element plot for the model with 20 cubic elements is shown in Fig. 4.14. A more refined element mesh was placed in the leading edge area of the airfoil in order to calculate the high stress gradients that occur in that region. A modified model with two layers of cubic elements in the radial direction, a total of 40 elements, is being used to check the convergence of the stress solution.

The calculated variations in heat transfer coefficient around the airfoil at mid-height is shown in Fig. 4.15. The heat transfer coefficients at the end of the airfoil were assumed to vary from 525 BTU/ft^2-hr-°F at the leading edge to 10 BTU/ft^2-hr-°F on the end buried in the end cap cavity.
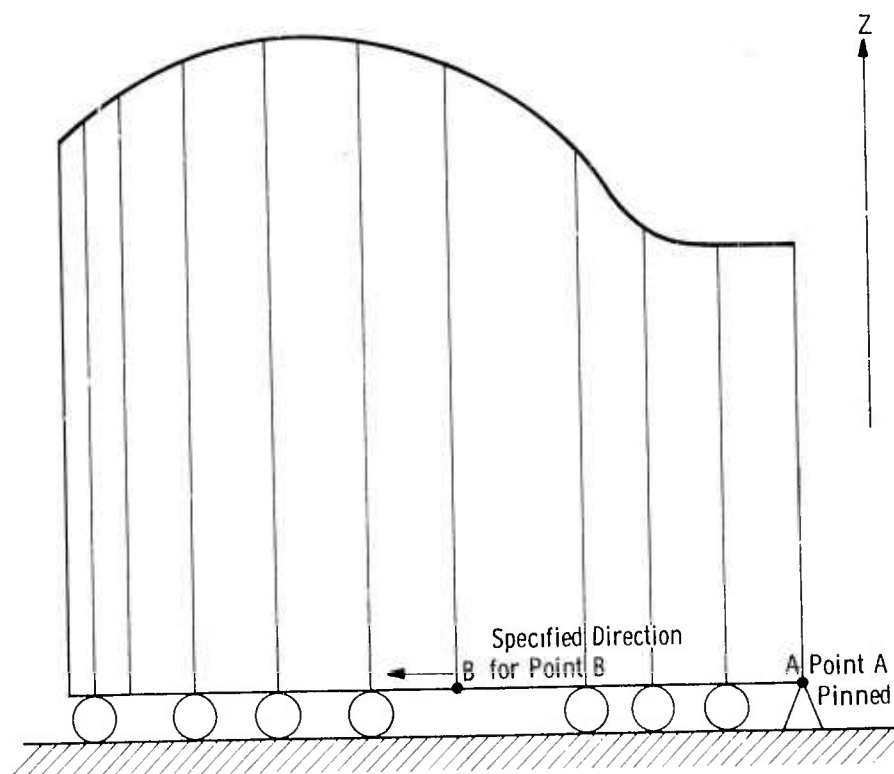
Figure 4.13   Preliminary Model for Two-Dimensional Transient Heat Transfer and Stress Analyses of Silicon Nitride Vanes under Static Rig Test Conditions at 2200°F Peak Temperature
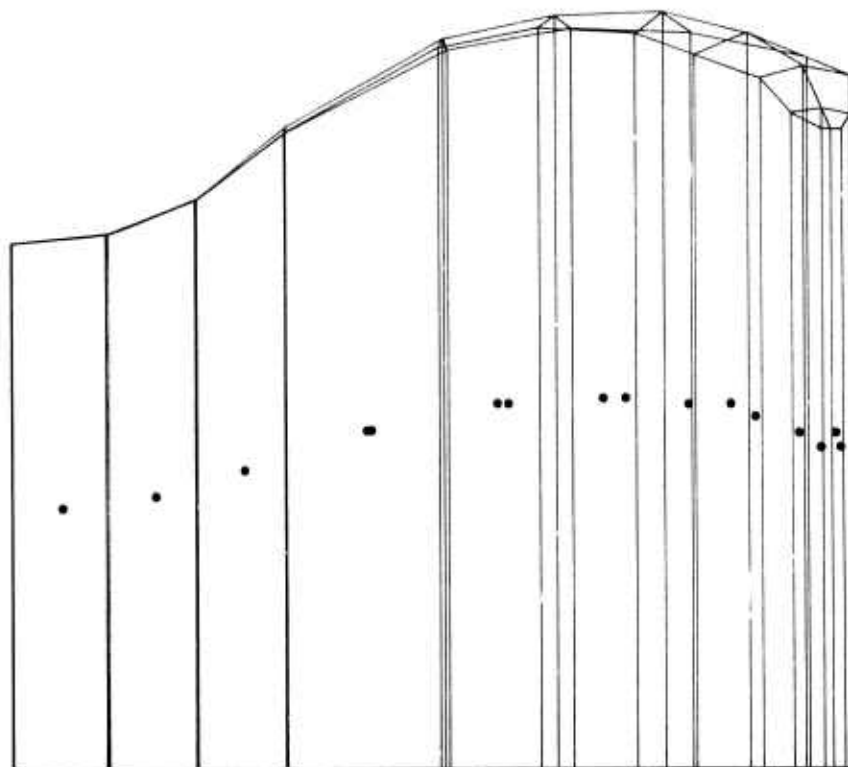
Figure 4.14   A Three-Dimensional Finite Element Plot for Heat Transfer
and Stress Calculations -- Silicon Nitride Vanes
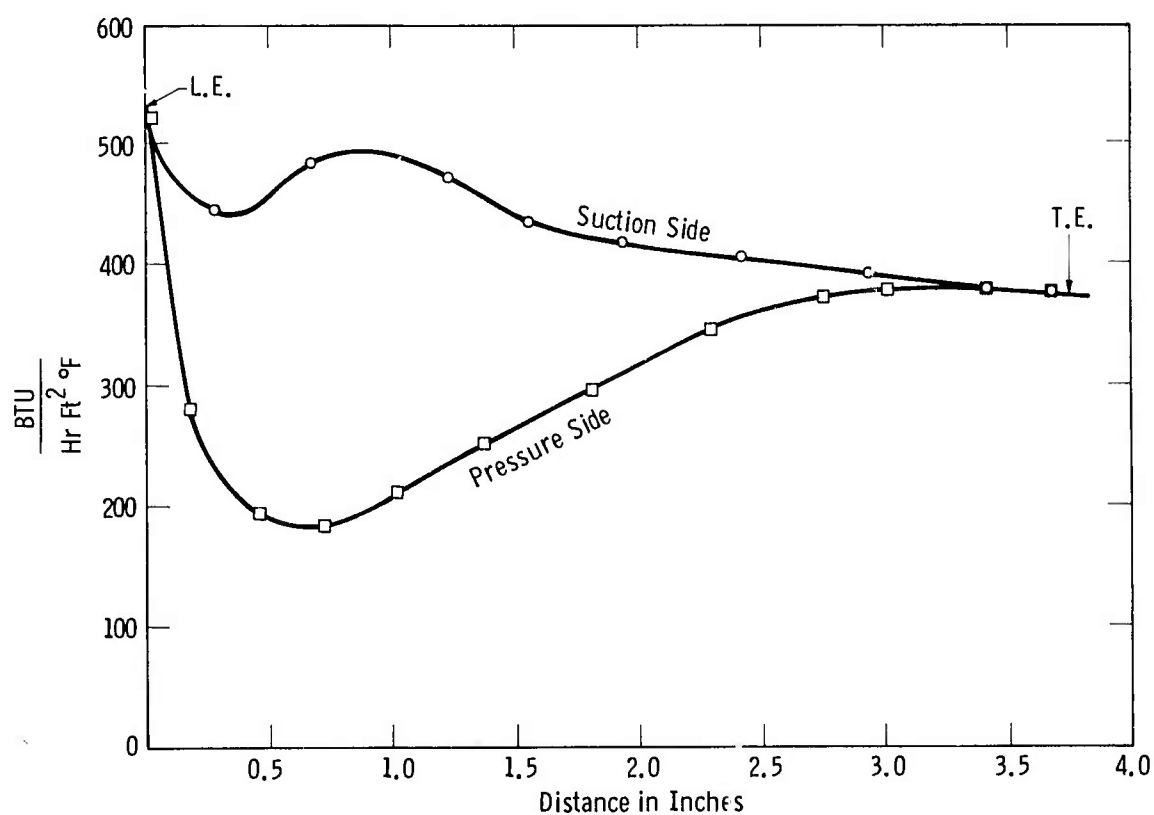
Figure 4.15   Calculated Variations in Heat Transfer Coefficients at
Mid-Height Surface Locations Around a Silicon Nitride Vane

76

Under the controlled shut-down condition at 25°F/second (0.8 simulation), the out-of-plane transient thermal stress reaches a maximum of 25,000 psi on the leading edge of the airfoil at mid-height. A maximum calculated in-plane transient thermal stress of 20,000 psi occurs at the top of the airfoil. Maximum stress is developed after 24 seconds at a material temperature of 1500°F. The average tensile strength of silicon nitride exceeds 50,000 psi at this temperature.[4]

The emergency shut-down condition at 80% simulation (Fig. 4.16) was analyzed also. Here, the maximum transient thermal stresses approach 60,000 psi at mid-height, near the leading edge, about 8 seconds after shut-down at a material temperature of 1700°F. Stress distributions on the suction and pressure surfaces of the airfoil are plotted in Figs. 4.17 and 4.18, respectively. These results do not predict vane failure necessarily since stress maxima are represented as points on the airfoil surface. Stress distributions must be integrated over discrete areas or volumes for direct comparison with tensile strength data before any meaningful assessment of vane performance can be made.
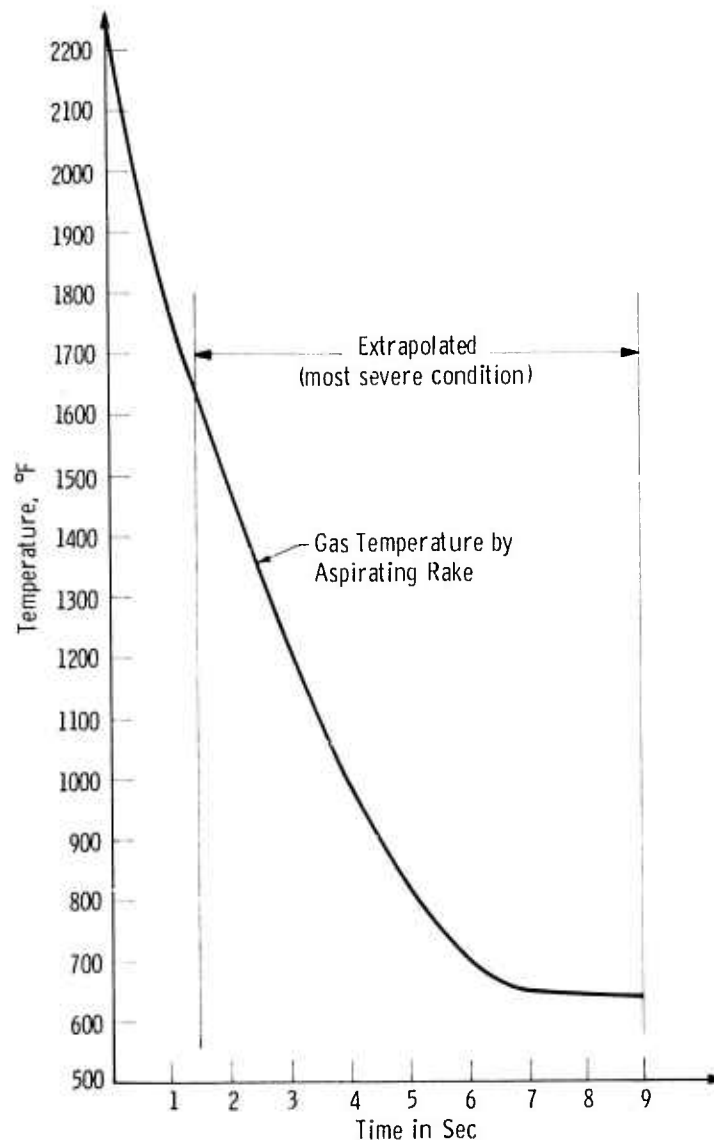
Figure 4.16   Emergency Shutdown Ramp for Ceramic Static Rig Test at 0.8 Simulation
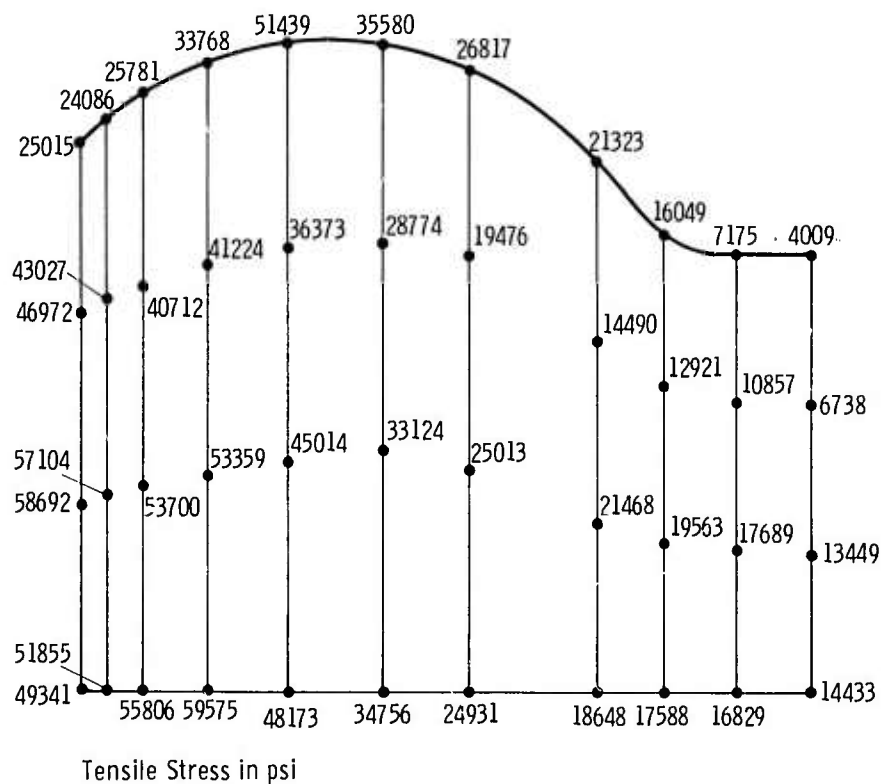
Figure 4.17   Transient Stress Distribution on the Suction Side of
               Silicon Nitride Vanes as a Result of Emergency Shutdown
               from 2225°F Peak Temperature
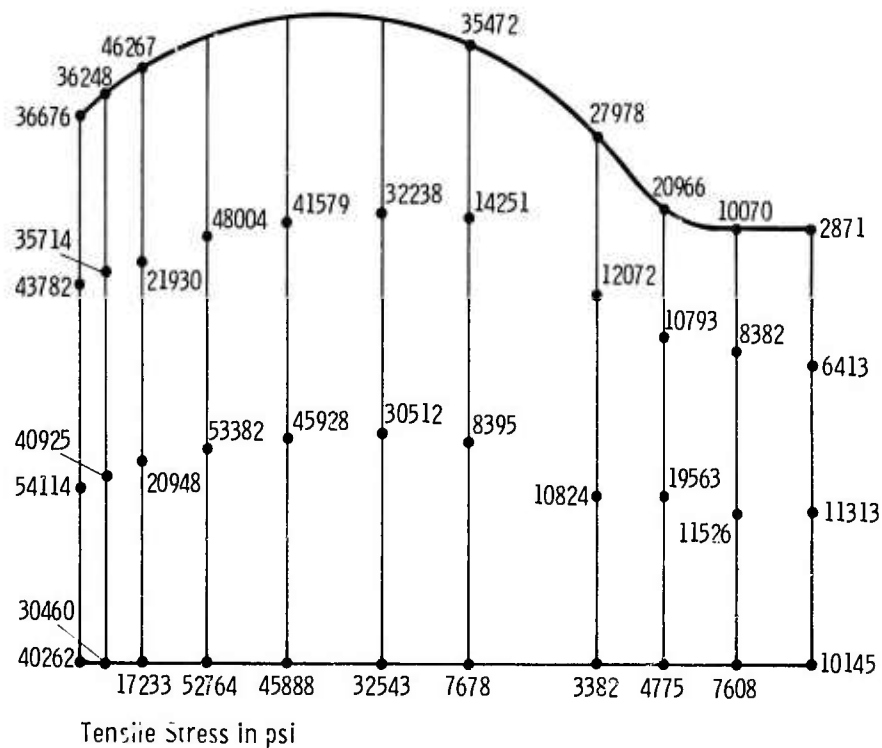
Figure 4.18   Transient Stress Distribution on the Pressure Side of
               Silicon Nitride Vanes as a Result of Emergency Shutdown
               from 2225°F Peak Temperature

The temperature profile of the gas at the combustor exit was determined by the upstream thermocouple rake. Data for 80% simulation are compared with ceramic vane surface temperatures, as measured by radiation pyrometry, in Fig. 4.19. The agreement between the gas stream thermocouples and the pyrometer is close enough to establish steady state radial and circumferential gradients across the ceramic vanes from local gas temperature measurements.

Optical Pyrometer = 2240°F
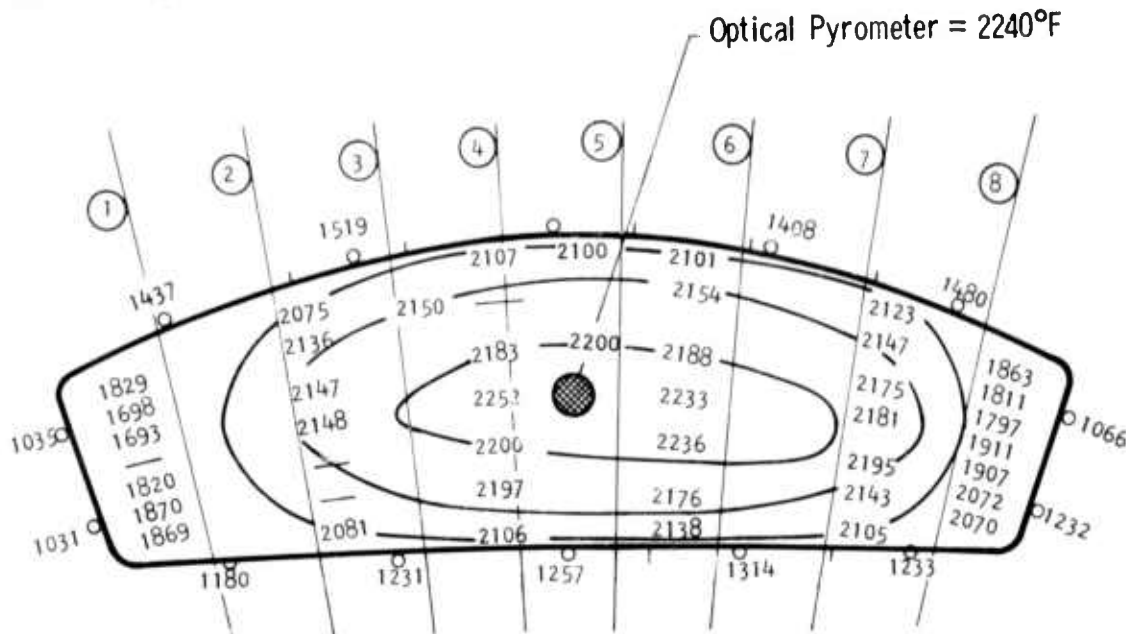
Figure 4.19 Gas and Vane Temperature Profile for 2200°F Static Rig Tests

Figure 4.20 is used to compare the transient thermal response of the vane surface to that of the local gas stream and the gas stream at the control position. The average temperature at the control position is measured downstream where temperatures are lowered by mixing and by an influx of cooling air from the side guide vanes. The difference in shutdown rates of the upstream gas measurement (38.8°F/second) and the average control temperature (26.3°F/second) is explained by the thermal lag of the insulating refractories. The Veritrak controller compensated for the extraction of this stored energy by a steeper cutback in fuel flow; i.e., faster ramp down. Since ceramic vanes have thermal inertia, they cool down at about the programmed rate.

Vanes at locations 3 and 4 (Fig. 4.21) were observed through the view port during the test program. At 2230°F steady state operation, a flickering flame impinged upon the vane (possibly combustion of carbon monoxide). The amount of flame in the area of the vanes increased with pressure ratio. At 80% simulation, burning was almost continuous with the leading edge of the vanes acting as a flame holder. At 30% simulation, the flame was sporadic and much less concentrated.

After several cycles at 80% simulation, streaks and spots on the vane surfaces increased in intensity. They changed in size and location during a run, but always appeared to initiate near the leading edge. Vane leading edges appeared hotter than the bulk of the vane.

79
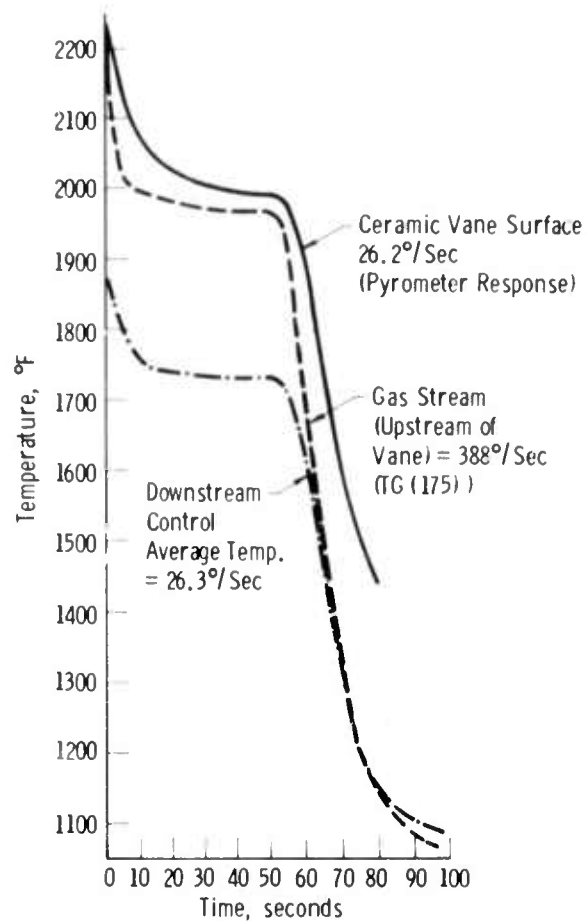
Figure 4.20   Comparison of Temperature Transients as Measured by
Downstream Control Thermocouples, Upstream Gas Thermocouple
Rakes, and the Radiation Pyrometer

Figure 4.21   Silicon Nitride Stator Vanes as Seen from View Port
during 2200°F Tests in the Static Rig

Following each series of tests, the rig was disassembled to inspect the vanes and associated components. After the initial 8 cycles at 30% simulation and 2100°F maximum gas temperature, a thin deposit of red dust was observed on the end caps. This was identified as NiO, Fe_2O_3, and a nickel ferrite spinel; all corrosion products of alloys used in the rig. An additional 9 cycles at the same simulation and 2200°F peak temperature simply increased the amount of this red deposit. After the 63 cycles at 50% simulation, the vane surfaces appeared slightly etched and dark gray in color. The red deposit on the end caps persisted. Adherent glassy spots and stringers or streaks were present on the vane surfaces after 21 cycles at 80% simulation. These deposits and streaks apparently caused the luminescent areas noted previously. No damage to the ceramic parts was observed at this point in testing.

After the final test, which included 5 controlled shut-downs and an intentional flameout transient at 80% simulation, cracks were observed in the ceramic airfoils at positions 1, 2 and 8. The end caps survived intact. The vane assemblies remained totally functional after the tests were completed as shown by Fig. 4.22. A cracked insulator can be observed in this photograph above the vane assembly at position 8 where the upper baffle failed.

Si₃N4 Vanes

A detailed failure analysis, using optical microscopy, Xyglo dye penetrant, X-ray radiography, and ultrasonic scanning, revealed extensive crack patterns in airfoils 1, 2, 6 and 8. This is illustrated in Fig. 4.23, an ultraviolet photograph of airfoil 6 using Xyglo dye
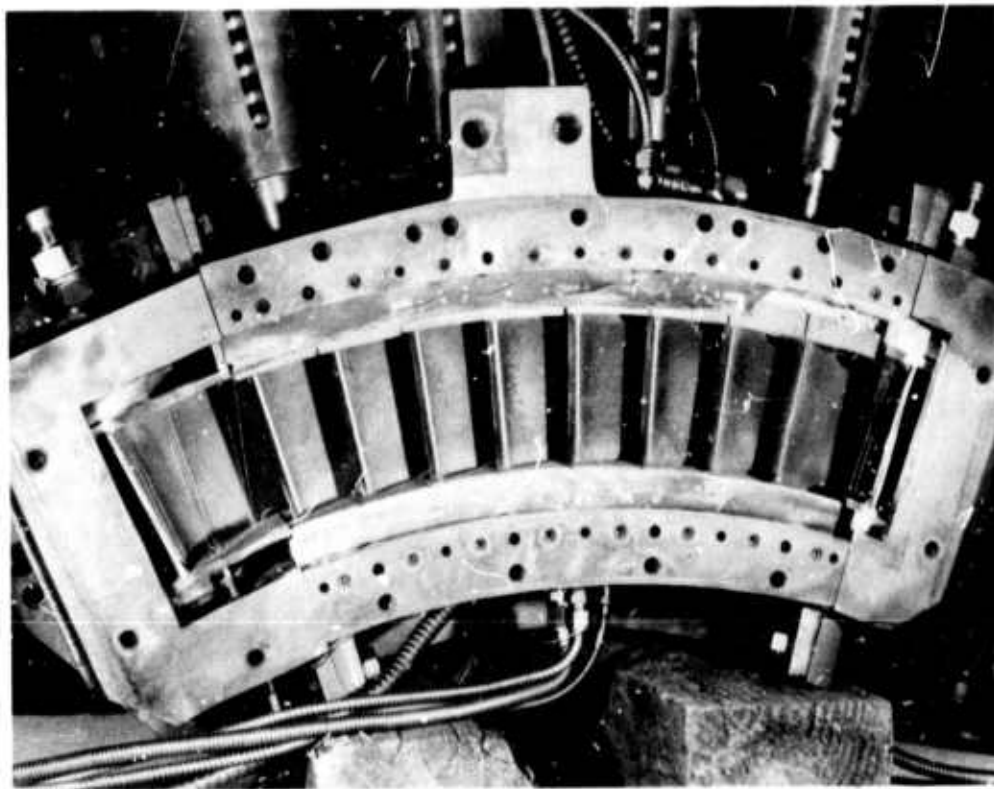
Figure 4.22   Silicon Nitride Vanes in Static Rig Test Assembly at the Completion of 2200°F Tests

81
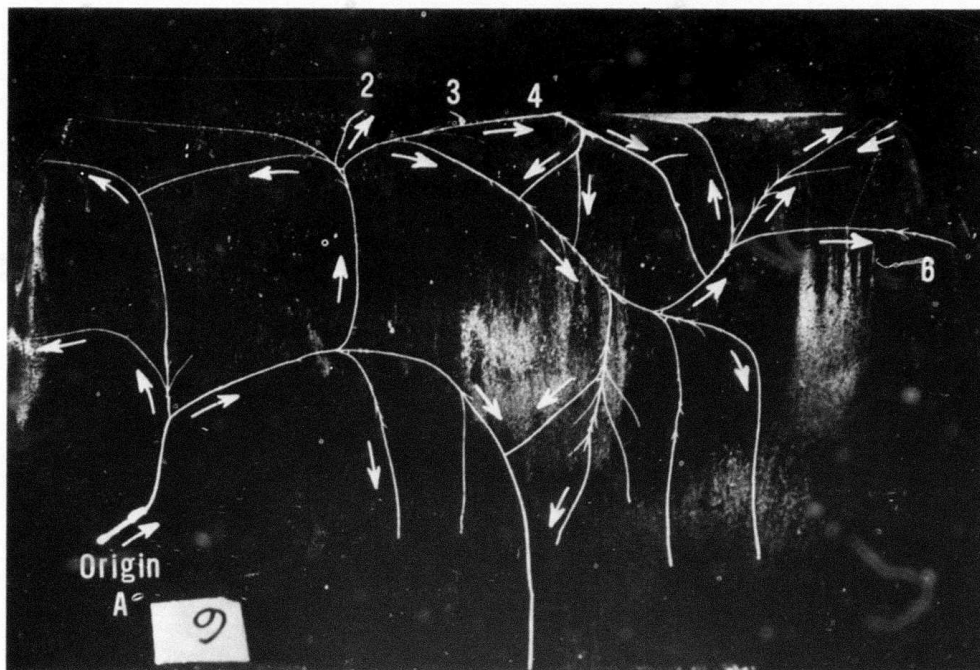
Figure 4.23   Ultraviolet Xyglo Photograph of Si$_3$N$_4$ Airfoil Showing
Typical Crack Patterns after 2200°F Static Rig Tests
(Suction Side of Airfoil)

penetrant. Arrows indicate the direction of crack propagation. All of
the cracks can be traced unequivically to a single origin which is
identified clearly. This crack origin, which was common to all
failures, was at a point contact location (an edge loading condition)
resulting from the non-conformed fit at the airfoil-end cap interface.
As indicated earlier, this condition is expected when design tolerances
are not met. It is apparent from Fig. 4.24, that cracking is not as
extensive on the pressure side of the airfoil as on the suction side
(Fig. 4.23).

Further evidence for edge loading failures was obtained through
detailed analysis of both airfoils and end caps. A single fracture
origin was identified at the leading edge of airfoil 1 where the tenon
contacts the torroidal groove in the outer end cap. In airfoil 2,
failure originated in the trailing edge area where the tenon contacts
the outer end cap (identical to airfoil 6). Cracking initiated at
both the inner and outer trailing edge contact locations on airfoil 8.
The failure origin at the outer end cap position was marked clearly
by a concoidal chip. Similar crack patterns persisted on the surface
of all fractured airfoils.

The Xyglo dye penetrant technique revealed cracking in the outer
end caps at vane assembly positions 1 and 6. These observations were
verified by X-ray radiography and ultrasonic scanning. Outer end cap 6
is used to illustrate the failure (Fig. 4.25). The crack system develops
from a single contact point at a trailing edge location which incidentally
coincides exactly with the failure origin in airfoil 6. A Hertzian cone
crack marks the point of origin which is coincident with very small
wear scars.

82
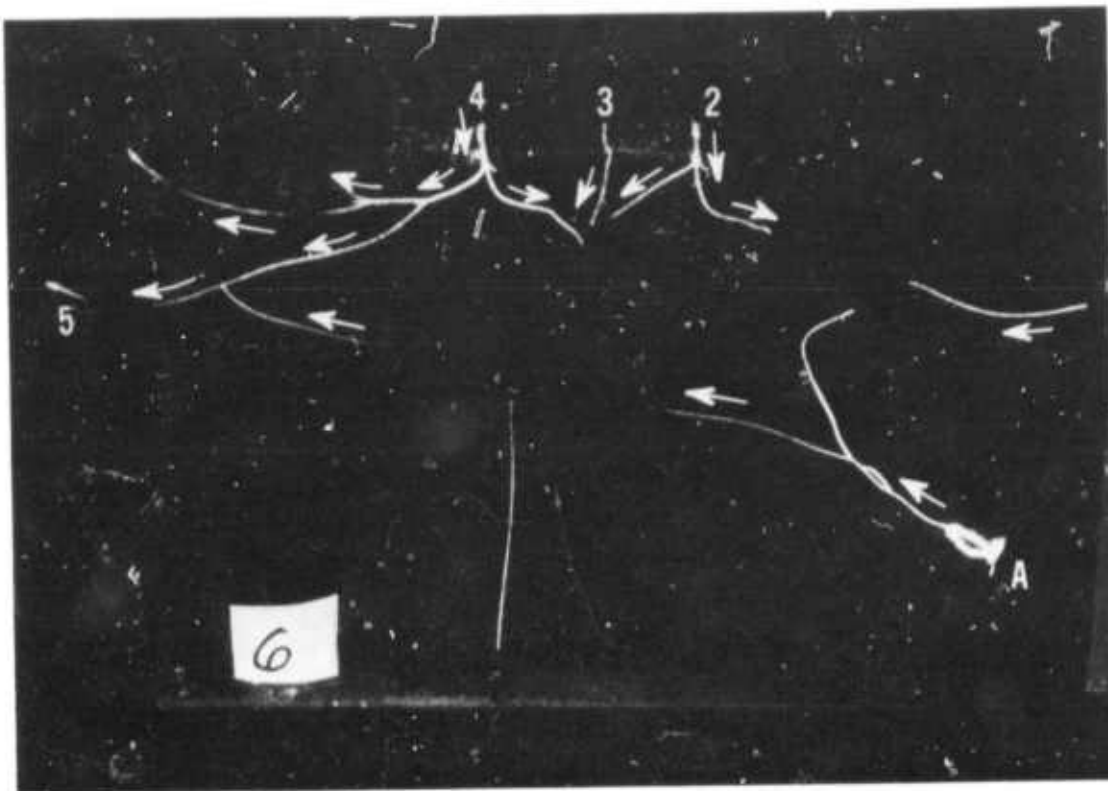
Figure 4.24   Ultraviolet Xyglo Photograph of Typical Crack Pattern
Development on the Pressure Side of Si_3N_4 Airfoil after
2200°F Static Rig Tests
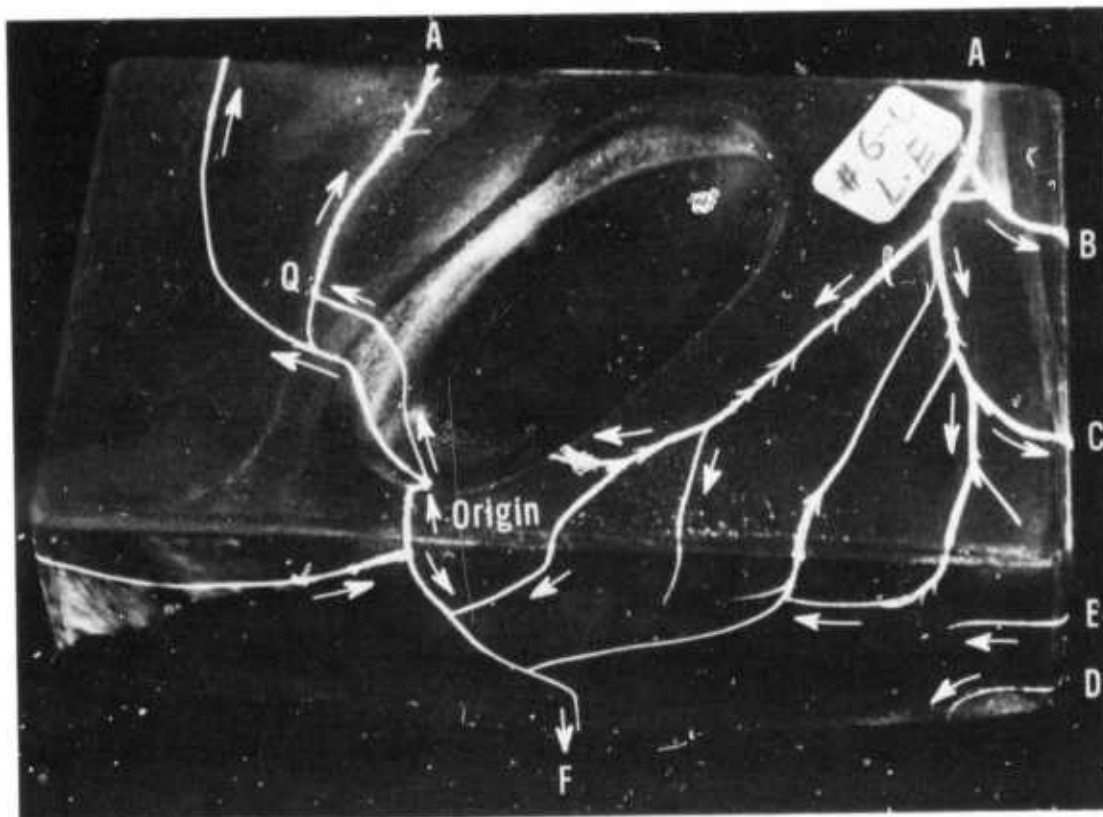
Figure 4.25   Ultraviolet Xyglo Photograph of Failure Indications in Outer
End Cap 6 after 2200°F Static Rig Tests

83

The situation with outer end cap 1 is similar. As indicated in Fig. 4.26, failure is associated with edge loading in the leading edge position. Again, the points of failure in both the end cap and airfoil correspond to the small area of contact between the two elements.

As stated previously, the primary cause of failure in airfoils and end caps is stress concentration at points of contact or an edge loading condition. Transient thermal stresses probably are superimposed on these locally, highly-stressed areas to initiate failure and crack propagation. Certainly, the effect of transient thermal stresses cannot be ignored completely because cracking is more extensive on the suction surfaces of the airfoils where heat transfer coefficients are high (Fig. 4.15).

It is interesting to note, however, that failure was not observed in the vane assemblies at positions 4 and 5 where peak temperatures were recorded and thermal transients were most severe. Furthermore, there was no evidence of edge loading or point contact along the airfoil-end cap interface. The deposit pattern and wear scarring indicated that area contact deep within the end cap cavity had been achieved.

While it was impossible to determine the time of failure, there is ample evidence to indicate that the cracking did not result from the emergency shutdown at 80% simulation which characterized the final cycle. Some oxidation was detected on the fracture surface of airfoil 2 for example. Since the maximum transient thermal stress develops at 1500°F in a 2 second shutdown to 600°F, oxide formation on the fracture surface during this last cycle is highly improbable. In one area, the
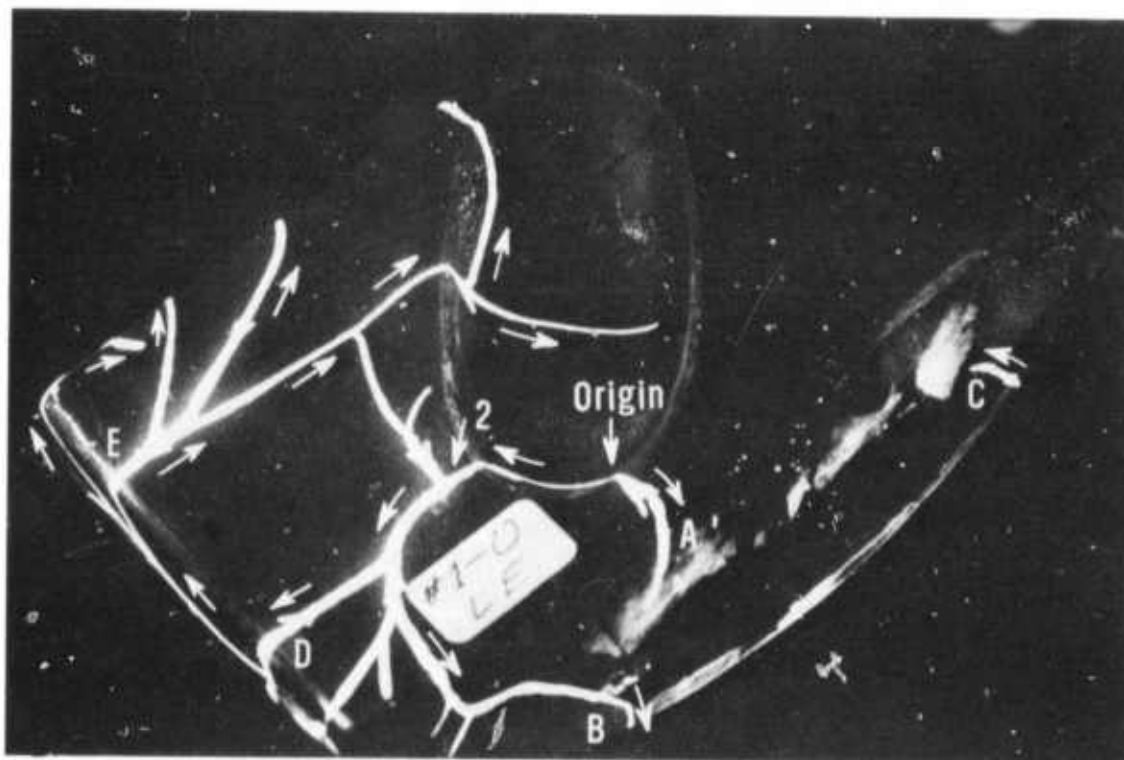
Figure 4.26   Ultraviolet Xyglo Photograph of Crack Pattern Development in Outer End Cap 1 after 2200°F Static Rig Tests

oxide coating on an airfoil had spalled from the surface. The exposed surface had reoxidized presenting additional evidence to support the premise that cracks formed early in the testing sequence. Xyglo examination before and after the removal of surface deposits indicated that the crack patterns were masked by a continuous oxide film in many areas.

Failure, then, is attributed to non-conforming fit at the airfoil-end cap interface which created an edge loading condition or small area of high stress concentration. The situation resulted from the manufacturer's inability to meet the design tolerances. Inspection records confirm the fact that end cap cavities were ground as much as 0.020 in. too deep in certain instances. Attempts had been made to correct these discrepancies by remachining and matching airfoils to end caps on a best fit basis. There is radiographic evidence which indicates, however, that this was not achieved. In summary, defects in the material itself or the inate inability of the material to survive the maximum transient condition has been discounted as a cause of failure.

Substantial amounts of surface deposits developed on the pressure side of the airfoils during the entire test program. These ranged in color from white to rust brown and purple to black. The area designated white in Fig. 4.27 were identified as $CaSO_4$ with small amounts of $CaSiO_3$ (Wollastonite), $CaSiO_3$ (psuedo-wollastonite) and α-cristobalite. The brown and purple deposits were identified as α-Fe_2O_3 with traces of $FeO(OH)$ and spinel. The suction side of all airfoils remained relatively free of surface deposits (Fig. 4.28). Where present, these appeared glassy and dark in color. Silica was identified along with α-Fe_2O_3, $CaSiO_3$, $CaSO_4$, and α-spinel in trace amounts.

Similar deposits were observed on the gas passage surface of the end caps and in the torroidal grooves as illustrated in Fig. 4.29. The deposits ranged in color from white, rust brown, and purple to black. Glassy silica was very minimal compared to that exhibited on the airfoils and α-Fe_2O_3, $CaSO_4$, and some $CaSiO_3$ were present.

5

Dark Glassy Edge (SiO_2)

Rust-brown (α-Fe_2O_3, FeO (OH), Spinel)

Brown, Purple (α-Fe_2O_3, SiO_2, $CaSO_4$)

White, Purple ($CaSO_4$, $CaSiO_3$, SiO_2)

White and Purple ($CaSiO_3$, $CaSO_4$)

Dark Black ($CaSiO_3$, SiO_2, $CaSO_4$)

Dark Glassy Edge (α-Fe_2O_3, SiO_2)
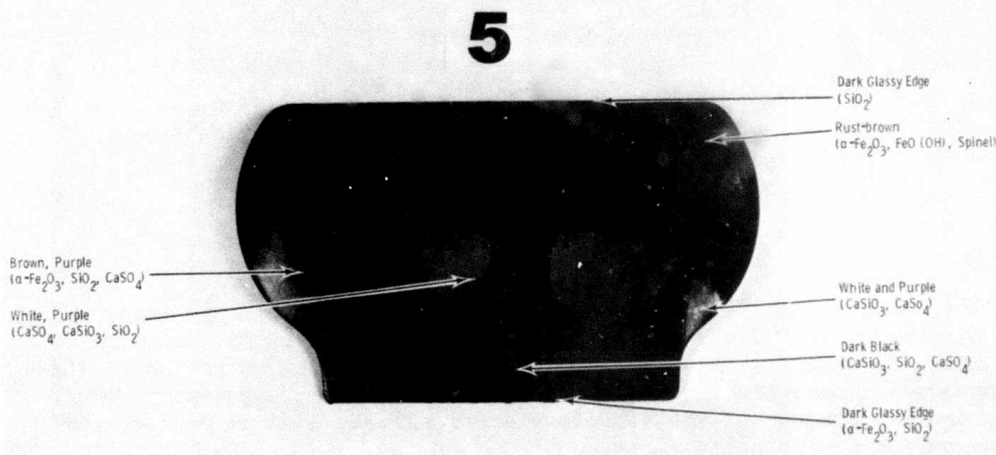
Figure 4.27   The Concave Surface View (Pressure Side) of a Typical Airfoil Section after Exposure to Hot Combustion Gases in the Static Test Rig at 2200°F Peak Test Temperature
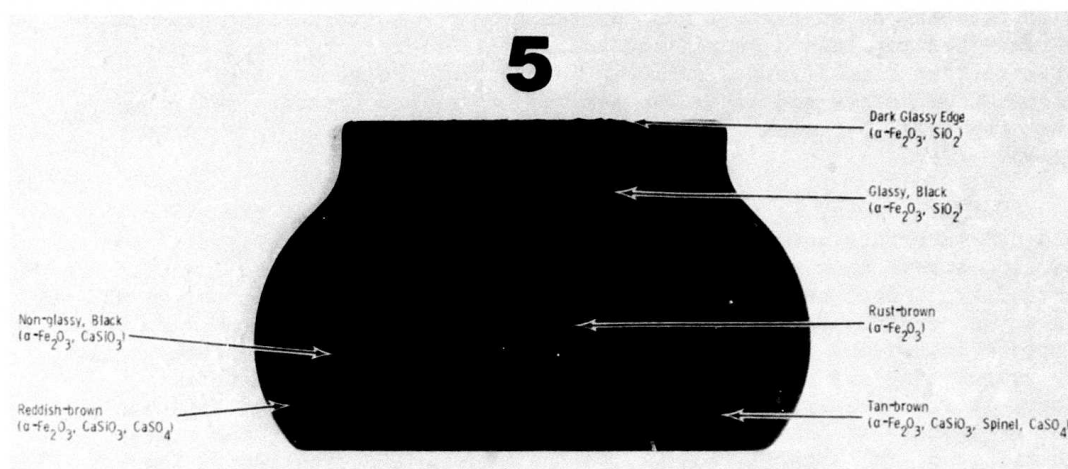
Figure 4.28   The Convex Surface View (Suction Side) of a Typical Airfoil
Section after Exposure to Hot Combustion Gases in the Static
Rig at 2200°F Peak Test Temperature
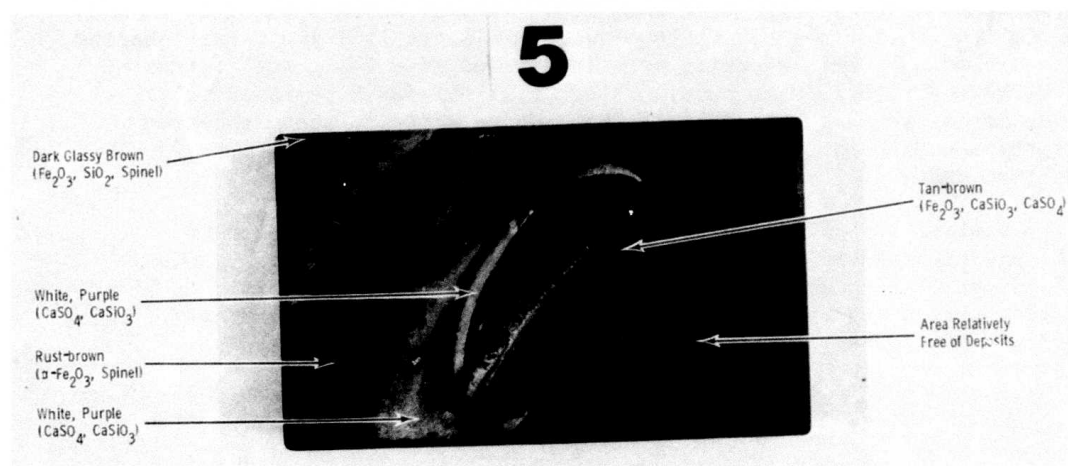
Figure 4.29   Inside Surface of an Outer End Cap after Exposure to Hot
Combustion Gases -- Static Rig Test at 2200°F Peak
Temperature

The $CaSO_4$ (a major ingredient of cement and concrete) apparently
was ingested as very finely dispersed particles from the air. Some of
the $CaSO_4$ apparently reacted with surface silica to form wollastonite ($CaSiO_3$)
and pseudo-wollastonite ($CaSiO_3$). The rustlike α-Fe_2O_3 apparently formed
as an erosion product of the stainless steel shields used to protect the
thermocouples during photography.

Weight gains resulting from deposition were very small; 258 mg average
for airfoils and 40 and 21 mg for inner and outer end caps, respectively.
The deposits were not associated with surface damage in any way.

86

LAS Insulators

Six of the LAS insulators (two outer and four inner), were reconstructed and examined to determine the probable cause of failure. All fracture surfaces were observed first to locate fracture origins. Dye penetrant was used after that to observe stable cracks.

The following observations were made:

1) General Appearance

a) Marks caused by the wire mesh between the insulators and their restraining metal shoes indicated that the insulators moved in the direction of gas flow by as much as 1/16 inch with respect to the metal shoe. Similar observations showed that the insulators were displaced in the relative direction of the spring load by as much as 1/8 inch with respect to the side seals.

b) A small molten area at one edge of an insulator indicated that the melting point of the material had been exceeded locally. No other surface degradation was observed.

2) Fracture Phenomena

a) All detectable fracture origins were located on the surface forming the end cap interface.

b) Except for chips, all large fracture paths were parallel to gas stream (see crack A in Fig. 4.30).
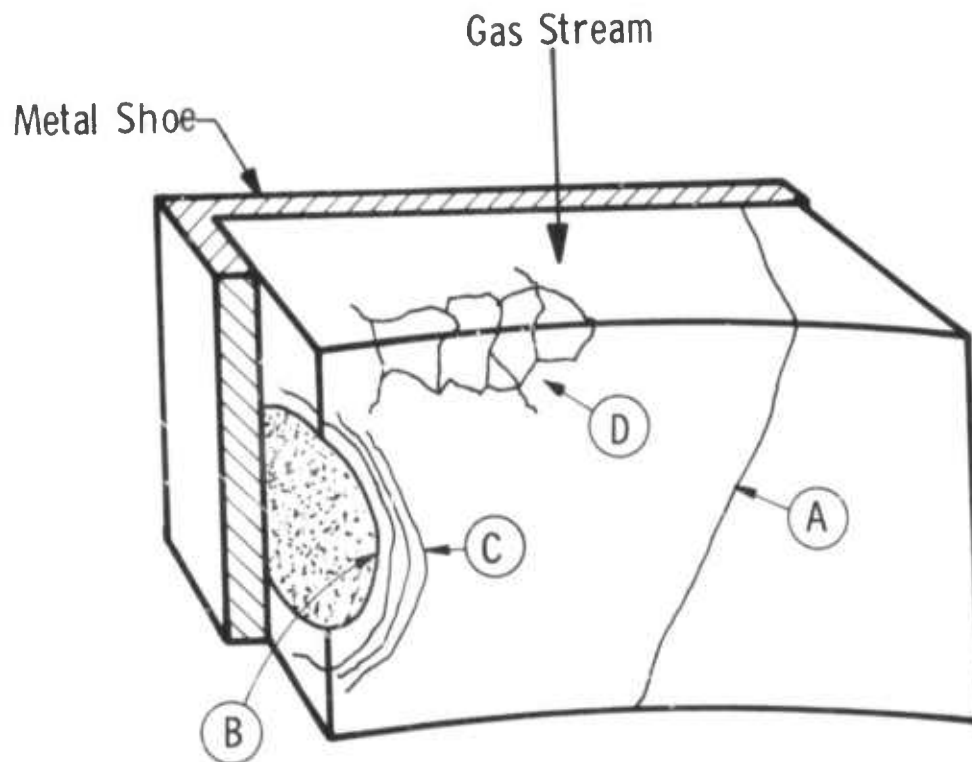
Figure 4.30   Typical Failure Indication in LAS Insulators as Seen From the End Cap-Insulator Interface

87

c) Most insulators contained large, conical-shaped fractures as shown by B in Fig. 4.30. Many fractures of this type were associated with a series of curved, closely-spaced stable cracks as represented by C in Fig. 4.30.

d) Cracks induced by transient thermal stresses were observed on the forwa ' edge of both outer insulators. These displayed a characteristic 'mud-crack' pattern as shown by D in Fig. 4.30. Similar crack patterns were not observed on the inner insulators.

These observations lead to the conclusion that the transient thermal stresses are large enough to induce small cracks in LAS material, when the surface temperatures exceed 1800°F. The external applied loads are large enough to cause these cracks to propagate to failure. This conclusion is supported by the observation that a large crack (A in Fig. 4.30) is associated with a 'mud-crack' pattern in one of the outer insulators.

Causes for this cracking other than thermal stresses are also possible. The crack pattern C (Fig. 4.30) cannot be due to thermal stresses because these cracks are too closely spaced and too long, i.e., the stress field relieved by one would not allow others to increase in length. The conical type of fracture (B in Fig. 4.30) apparently was caused by wedging action.

Two changes will be made to improve insulator performance. First, the honeycomb seal material, used at the housing ring-insulator location, will be replaced by a permeable feltmetal to insure the flow of cooling air through the seal itself rather than along the insulator-insulator interface to the gas passage. This is expected to reduce the steady state thermal gradients in the insulator appreciably. Second, the circumferential edges of the insulator will be crowned or radiused to eliminate edge loading and wedging at this location.

Static Rig Modification for 2500°F Testing

The instrumentation capability for the 2500°F (1371°C) test program has been improved. Initial static rig tests had only a single radiation pyrometer permanently focused on the pressure side of No. 4 vane, 1/2" downstream of the leading edge at the mid-height span. For the 2500°F tests, two additional pyrometers will be utilized to measure the temperature gradient across one vane of the ceramic assembly. These data will be used to verify the heat transfer analysis upon which the design is predicated. The pyrometers will be permanently mounted on the transition piece so as to give the temperature readings at the following locations:

1. Mid-height span suction side, 0.66" back from vane leading edge

2. Mid-height span, pressure side, trailing edge region

3. 90% blade height, suction side, 0.66" back from vane leading edge.

The pyrometers are encapsulated in water cooled jackets to protect them from the shell environment. The fast output response of the instruments

88

permit the recording of the transient shutdown cycles as demonstrated
in 2200°F testing.

Attempts were made to fabricate ceramic thermocouple rakes from
reaction sintered Si_3N_4. The rake design was difficult to execute in
ceramic hardware. Only one rake was completed and tested after many
abortive attempts. It does not appear practical to obtain these
thermocouple rakes for 2500°F testing during the next quarter. Therefore,
radiation pyrometers will be used exclusively.

The static rig was equipped with a sight port containing two
quartz sight windows in series, which permitted the viewing of the outer
end cap-airfoil region of vanes 3 and 4 during the 2200°F testing.
An air-cooled borescope will be added to the instrumentation to broaden
the visual aspects of testing. The borescope is mounted on the pressure
shell and is sighted through the rig transition piece. By means of a
lens system with a cone view angle of 45°, it will be possible to view
six of the eight airfoil-end cap assemblies during actual rig operation.
The borescope is equipped with a mirror box which provides two eyepieces.
One eyepiece provides manual viewing while the second has a Nikkon
camera adapter for photographic records.

All of the thermocouples will be changed from Chromel-Alumel to
Platinum-Platinum/10% Rhodium for 2500°F capability. The platinum
thermocouples will only be utilized where a direct measurement of the
gas stream is required. An aspirating thermocouple design that minimizes
radiation error and increases response time is specified for the
transition piece and exhaust temperature measurement installations. The
Westinghouse Veritrak controller will be modified to respond correctly
to the platinum-platinum/rhodium thermocouples.

The metal rig components which are exposed to combustion gases
must be replaced by ceramic parts for the higher temperature testing.
A silicon nitride bonded silicon carbide duct has been installed in
the static rig downstream of the stator vane assembly to sustain a
hot face temperature as high as 3200°F. Tiles of this material are
supported by an insulating castable, Fiberfrax paper, and a stainless
steel shell. The duct is attached to the rear surface of the rig barrier
plate to direct the gases axially into the mixer section. The duct is
shown in Fig. 4.31.

A new mixer section will be built from 9 silicon nitride bonded
silicon carbide cylinders arranged in a criss-cross pattern to redistribute
the hot and cold regions of the profiled combustion gases. The upstream
flange plates will be replaced by a segmented ceramic wall.
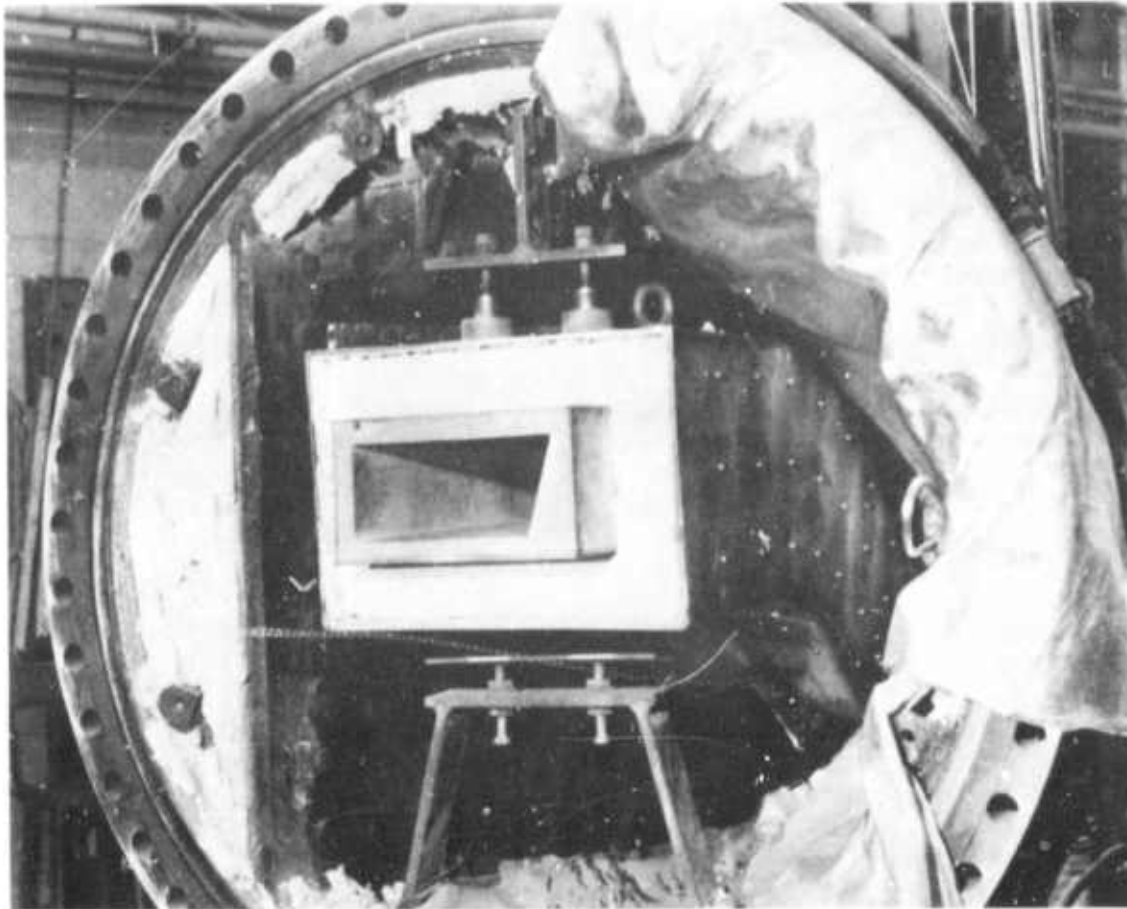
Figure 4.31   Installation of Ceramic Duct in the Static Rig for Tests
at 2500°F Peak Temperature

4.1.3 VANE FABRICATION

Introduction

The Norton Company continues as the sole source of hot-pressed silicon nitride and silicon carbide for the fabrication of stator vane assemblies. Seven sets of silicon carbide hardware were delivered. Second generation stator vane assemblies for static rig testing at 2500°F are currently being machined from Noralide NC 132 silicon nitride and Noralide NC 203 silicon carbide.

First Generation Silicon Carbide Vane Assemblies

Seven complete silicon carbide stator vane assemblies (8 airfoils and 14 end caps) were delivered by Norton in July. Xyglo, X-ray radiography, and ultrasonic inspection did not disclose any problems other than machining marks and randomly oriented scratches from lapping operations.

Dimensional checks indicate that an overall improvement in quality control has been achieved. The airfoils, for the most part, meet the drawing tolerances and designated surface finish. The tenon geometry (critical compound curvature at each end of the airfoil) was 0.001 in. out of tolerance, however.

The end caps must be reworked to eliminate the edge loading condition that caused failure of the Si_3N_4 vanes in the 2200°F static rig tests as noted in section 4.1.2 of this report. For example, the edge contour radii of both the inner and outer end cap cavities were 0.001 to 0.002 inches too small and somewhat irregular. All cavities were also asymmetric with respect to the minor radius. The inner end cap cavities were ground 0.001 to 0.003 inches too shallow. (This condition is not considered critical.) The outer end cap cavities were ground 0.001 to 0.005 inches too deep. Edge loading is unavoidable in this instance.

All 14 end caps were returned for rework to regrind the end cap cavities thereby increasing the major and minor radii to 1.505 and and 0.505 inches, respectively. This should correct the problem.

Second Generation Si_3N_4 and SiC Vane Assemblies

All of the billet material for the second generation silicon nitride and silicon carbide stator vane assemblies have been prepared. Norton has certified the Noralide NC 132 material with respect to the properties listed in Table 4.1. Billet certification for the Noralide NC 203 silicon carbide was reported previously.[4]

Four sets each of silicon nitride and silicon carbide hardware were scheduled formerly for delivery in December 1973. Due to delays in obtaining formed grinding wheels, Norton now expects to complete machining and inspection of all parts by March 1, 1974.

TABLE 4.1

PROPERTY CERTIFICATION OF NORTON NORALIDE NC 132 SILICON NITRIDE

Billet	Average Strength* (psi)	Std. Dev. psi	Density gm/cc
1	148,000	14,000	3.24
2	146,213	17,562	3.26
3	153,300	12,600	3.24
4	145,800	17,200	3.24
5	147,200	25,000	3.25
6	162,347	11,748	3.25
7	144,591	9,061	3.22
8	150,700	12,700	3.22
9	134,200	16,500	3.25
10	140,800	13,200	3.24
11	132,900	16,100	3.28
12	154,299	17,674	3.25
13	151,219	25,355	3.26
14	142,800	19,700	3.25

* Flexural strength in 3 pt. loading; specimen
  1/8 x 1/8 x 6 in., span 3/4 in.; multiple
  breaks; load rate (cross head) .02 in/min,
  average of 20 values at room temperature.

4.2 ROTOR BLADE DEVELOPMENT

SUMMARY

The Westinghouse Isoparametric Finite Element Stress Analysis Code (WISEC) has been expanded to include a mesh generator and plotting capabilities. Creep and contact stress problems are now being programmed. The stress analysis of ceramic rotor blades has been modified to reflect the effect of uniformly distributed loads across the attachment interface. Stresses approach 19,000 psi in the root area at 3600 rpm.

The development of the three dimensional finite element capability, which is required for accurate stress and heat transfer analyses of blades, should be concluded by the end of the current fiscal year. At this point, the creep and contact stress programs should be completed. The remaining task will be the computer simulation of ceramic rotor blade performance.

4.2.1 THREE-DIMENSIONAL FINITE ELEMENT STRESS ANALYSIS

The Westinghouse Isoparametric Element Code (WISEC) for three-dimensional elastic stress analysis has been expanded to include the capability for solving problems with materials that exhibit both anisotropic and temperature dependent properties. In addition, the program has been improved by including mesh generators, which reduce the amount of work necessary to prepare the input for the program, and temperature and stress plotting capabilities which aid in the interpretation of the stress analysis. The theoretical development for the inclusion of creep in the analysis of isotropic materials has been completed. The development of elastic-plastic creep procedures have been initiated. Progress has been made programming the elastic-plastic subroutines for isotropic materials.

It is difficult to discuss the continuing development of the three-dimensional stress analysis code and its specific programming in specific detail because much of the current activity represents refinement or the theoretical aspects of supplementary functions. The results, however, become increasingly evident with successive analyses of a tentative rotor blade design. The most recent, reported in section 4.2.2, shows the effect of distributing the contact forces at the blade root-disc interface over a finite area rather than using knife edge or roller support. All analyses now reflect the effects of property changes with temperature and the anisotropic properties of Norton HS-130 silicon nitride.

The steady state heat conduction analyses has been combined with centrifugal loading and gas bending forces to describe a steady state state stress distribution, elements of which have been verified by two-dimensional techniques. The three-dimensional plotting capability was illustrated previously.(3,4)

94

4.2.2 STRESS ANALYSIS OF BLADES

Introduction

Additional work in the area of preliminary design concepts and the stress analysis of ceramic rotor blading has been carried out. The contact area and friction between the root of a ceramic blade and a metal disc were considered in a two-dimensional study.

A steady-state heat conduction analysis of a three-dimensional blade model was performed to obtain an appropriate temperature distribution in the blade due to gas flow from the combustor. The temperature distribution, centrifugal loading, and the gas bending forces determine the steady state condition of stress currently being analyzed. The stress analysis itself has been modified by the assumption of a uniform distribution of contact force over a finite area; a knife edge or roller support had been assumed previously.[3,4]

Contact Stress Analysis

A two-dimensional model of the ceramic blade root and the steel rotor is shown in Fig. 4.32. The loading consists of the centrifugal force, F_c, the contact force, F_n, acting normal to the area contact, A_c, between the ceramic root and the steel disc, and the friction force, F_s, acting tangent to A_c. The finite element model of the root and a
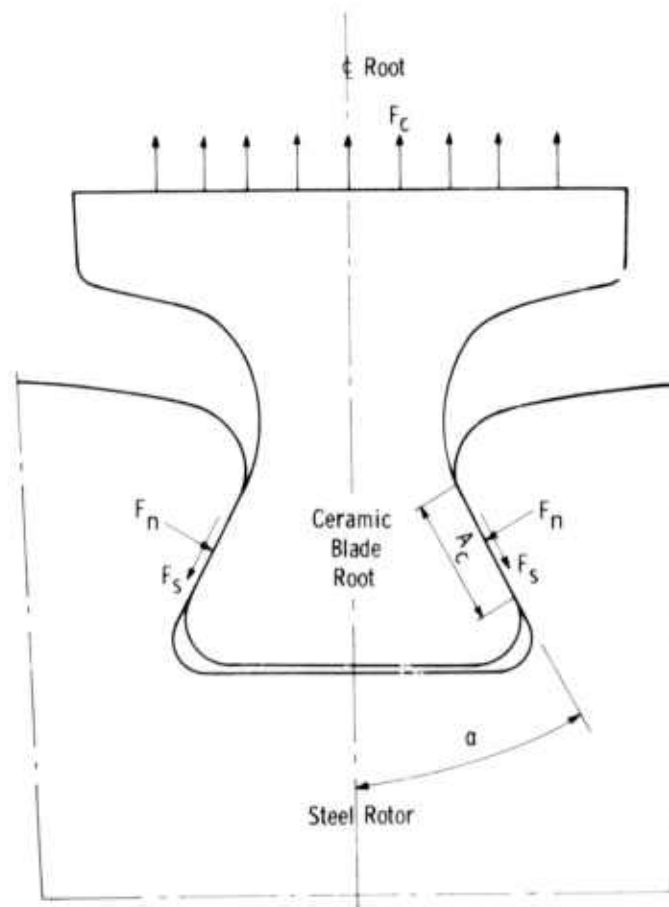
Figure 4.32   Schematic Drawing of Proposed Ceramic Blade Attachment with Metal Rotor Disc

portion of the disc are shown in Fig. 4.33. Only half of the root is modeled because of symmetry. Constant strain triangles are used. In this analysis, the contact area per unit of thickness along the root, the root angle, the coefficient of friction, and the rotational speed are as follows: A_c = 0.165 in^2, α = 30°, μ = 1.732 and w = 3600 rpm, respectively. The finite element program considers the contact between the rotor and the root by determining the contact force, F_n, and the friction force, Fs. The solution is iterative because of the non-linear nature of the contact analysis.

Some of the results are shown in Fig. 4.34 where the maximum principal stresses are displayed as contours. The maximum in-plane tensile stress (18274 psi) was observed at approximately the same location in the blade root at which the maximum radial stress had occurred in previous analyses of three dimensional models. The deformations obtained appear in Fig. 4.35. The dotted lines depict the deformed shape of the root and disc boundaries.

The analysis of a 30° root was repeated using a uniform distribution of the contact force, F_n, and the friction force, F_s, acting on the root only. This time, the rotor portion of the finite element model (Fig. 4.33) and the contact analysis were omitted to reduce computer costs. The results agreed with those reported within a few percent.
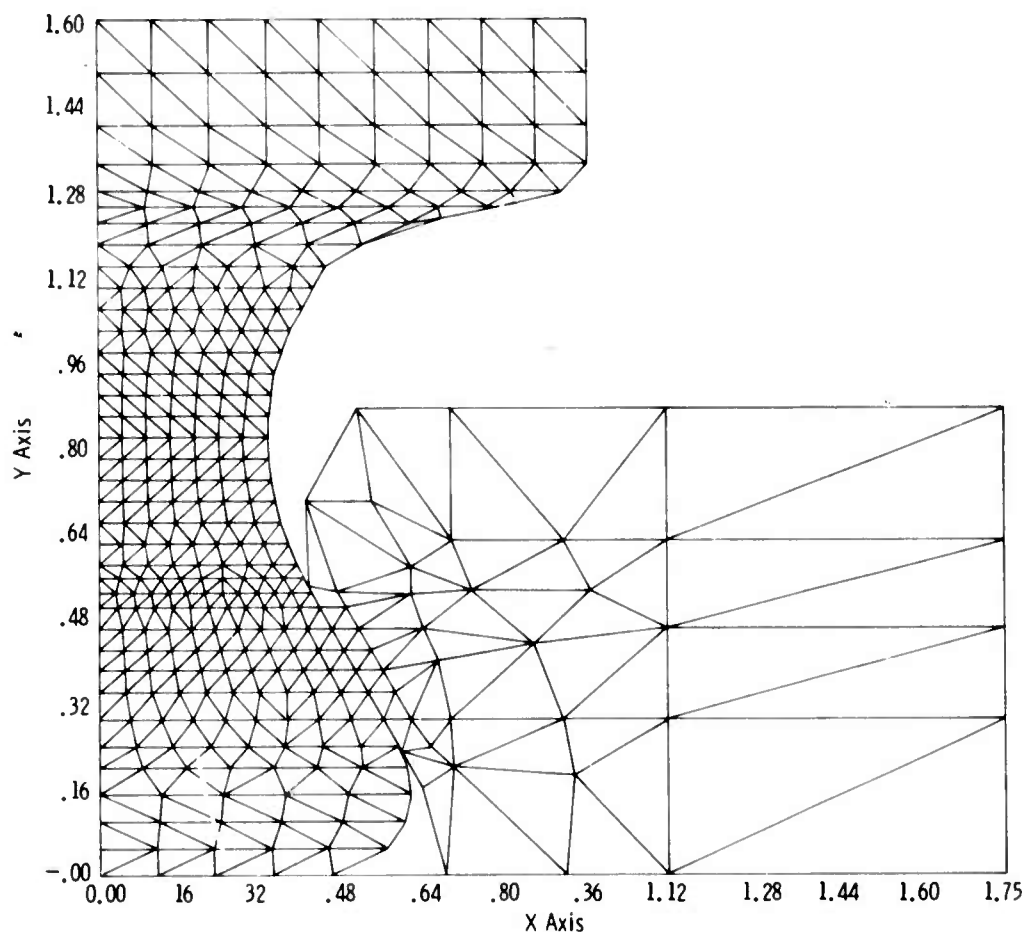
Figure 4.33   Two-Dimensional Finite Element Model of Ceramic Blade Root and Metal Rotor Disc
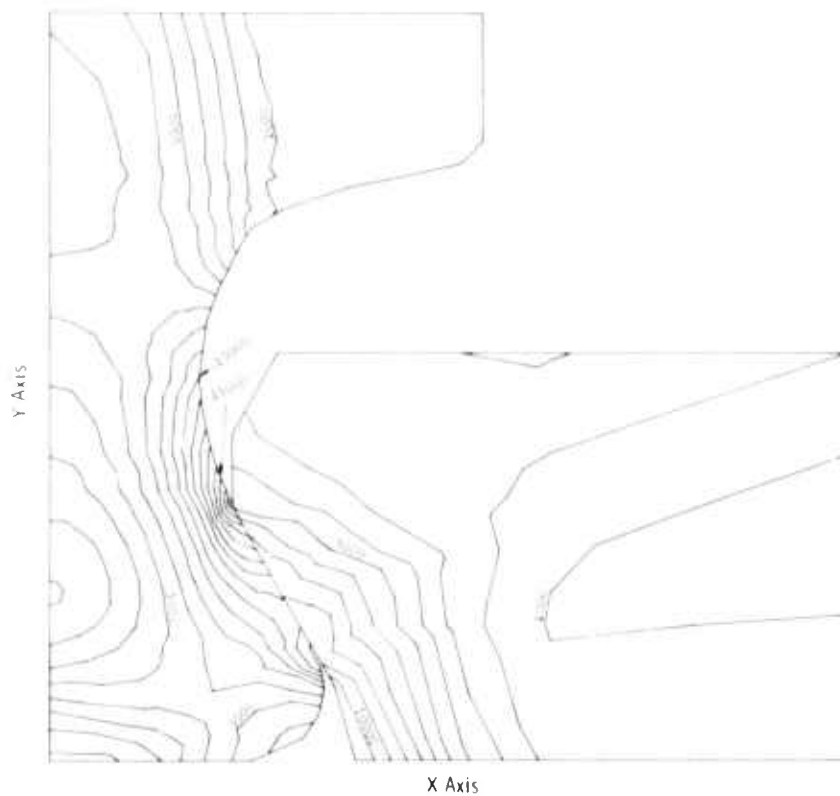
Figure 4.34   Maximum Principal Stress Distribution in Ceramic Blade
               Root (Left) and Metal Rotor Disc (Right)
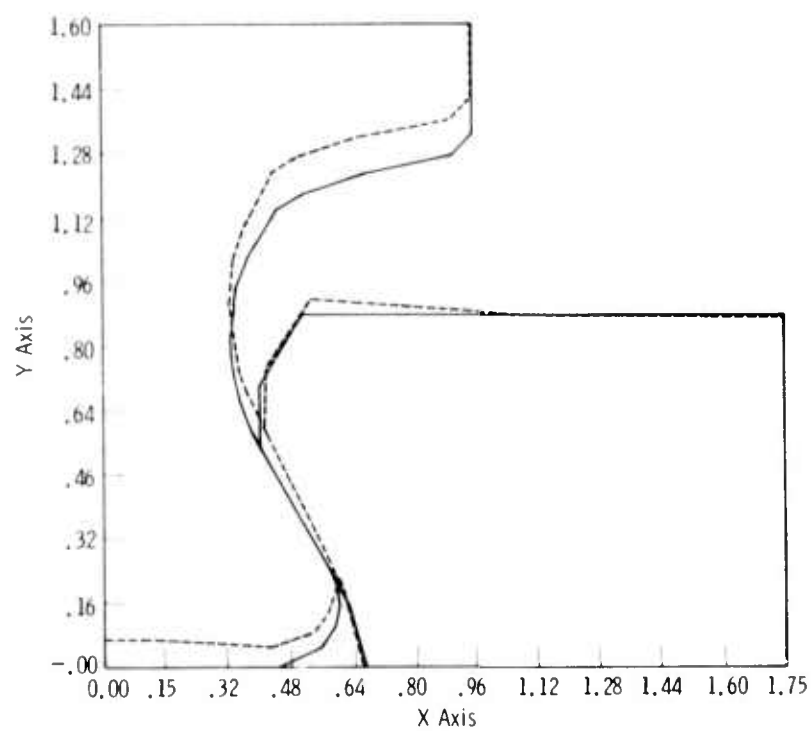
Figure 4.35   Component Deformation under Load (Deformed Ceramic Blade
               Root, Left, and Metal Rotor Disc, Right, Denoted by
               Dashed Lines)

5. PROGRESS ON MATERIALS TECHNOLOGY - VEHICULAR
   AND STATIONARY TURBINE PROJECTS

5.1 MATERIALS ENGINEERING DATA

SUMMARY

Design technology is highly dependent upon mechanical, chemical, and physical properties of the materials being used. This section deals with work performed during this reporting period on the acquisition of physical property information. Many of the materials being investigated are in the development stage and improvements in properties are anticipated; this will require that some, if not all, of the physical properties must from time to time be re-determined. Therefore, property characterization of the ceramic materials for turbine engine use is a task which will continue throughout the life span of the contract.

Weibull parameters have been determined for both hot pressed silicon nitride and silicon carbide based upon volume and area being stressed. Agreement between measured and predicted values was not as close as expected. Hot pressed silicon carbide exhibited low creep but failed in stress-rupture at 15000 psi when tested at 2300°F.

Corrosion-erosion testing of both hot pressed silicon nitride and silicon carbide was carried out at 2500°F in the turbine test passage, but invalid results were obtained due to contamination from insulation which was added to the test passage.

Creep testing of reaction sintered silicon nitride was carried out using samples made from silicon metal powders of various purity levels. Creep strain was found to decrease significantly as the amount of calcium decreased. Material made from silicon containing 0.05% calcium exhibited 0.04% plastic strain after 200 hours at 10,000 psi and 2300°F, as measured in four point bending. The use of even purer silicon metal and hydrogen-nitrogen nitriding atmospheres resulted in even less creep. Slip cast reaction sintered silicon nitride was found to have very low creep, especially when iron oxide was added as a nitriding aid.

It is anticipated that the statistical characterization of mechanical and thermal properties will be completed shortly for Norton hot pressed silicon nitride and silicon carbide. Thereafter, critical properties of hot pressed billets will be monitored in order to qualify materials for stator vane fabrication. Iterative development of molded and slip cast reaction sintered silicon nitride materials will continue and will include continued characterization and data analysis. Creep of reaction sintered silicon nitride no longer appears to be a serious problem, providing continued attention to control of the chemical purity of this material is exercised.

5.1.1 PROPERTIES OF HOT-PRESSED MATERIALS

Introduction

The comprehensive program to evaluate the mechanical and thermal
properties of many varieties of silicon nitride, silicon carbide, and
lithium aluminum silicate in gas turbine applications is continuing.
These data not only contribute valuable fundamental information about
the materials but also are considered essential to an optimum design
with brittle materials in order to provide the maximum safety factor.
All of the candidate materials have been improved significantly. Since
the potential for greater improvement exists, the Material Engineering
task is expected to continue for the full term of the turbine project.

Statistical Aspects of Mechanical Responses

The Weibull parameters for Norton HS-130 silicon nitride and
hot-pressed silicon carbide were determined from the available flexural
strength data. These data were used to predict strength as a function
of effective volume or area under stress at room temperature, 1000,
1800, and 2300°F. The 2 parameter Weibull results based on the volume
prediction are presented in Figs. 5.1-5.3. Average tensile test values
also appear for purposes of correlation. The best agreement between
measured tensile and predicted values was obtained at 2300°F.

A series of 4 point bend tests were made at a strain rate of
0.001 in/in/min to determine the effect of specimen size on the strength
of Si₃N₄ and SiC at room temperature by actual measurement. Specimens

Figure 5.1   The Strength of Norton HS-130 Silicon Nitride (Strong
              Direction) as Predicted by Weibull Statistics Based on
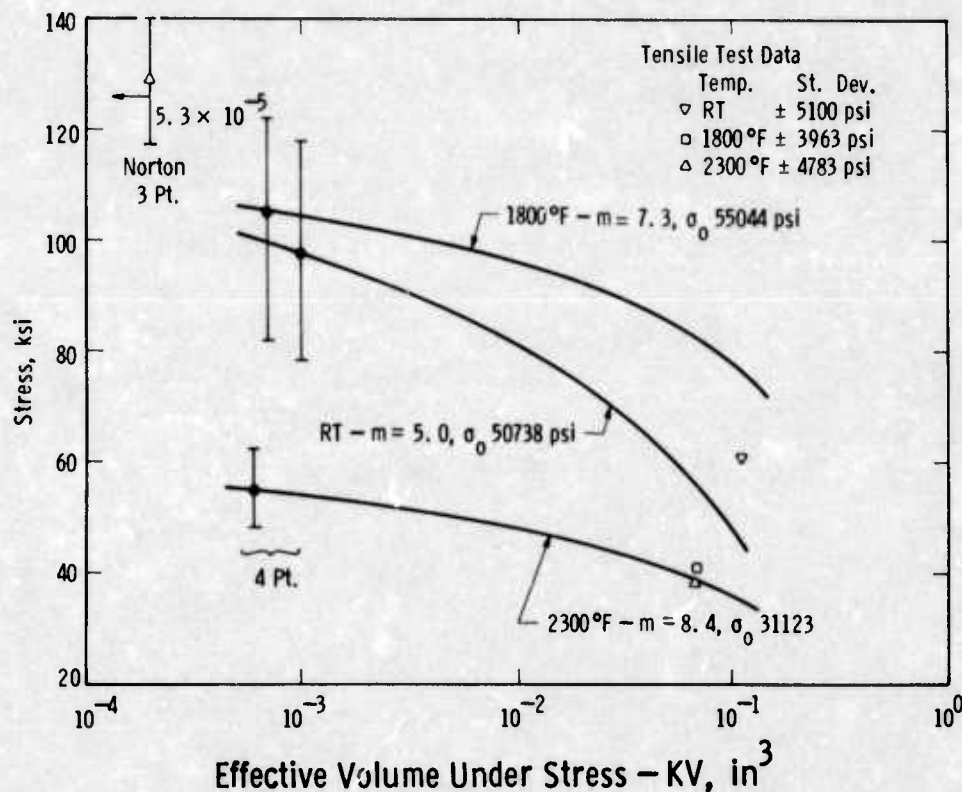   Volume
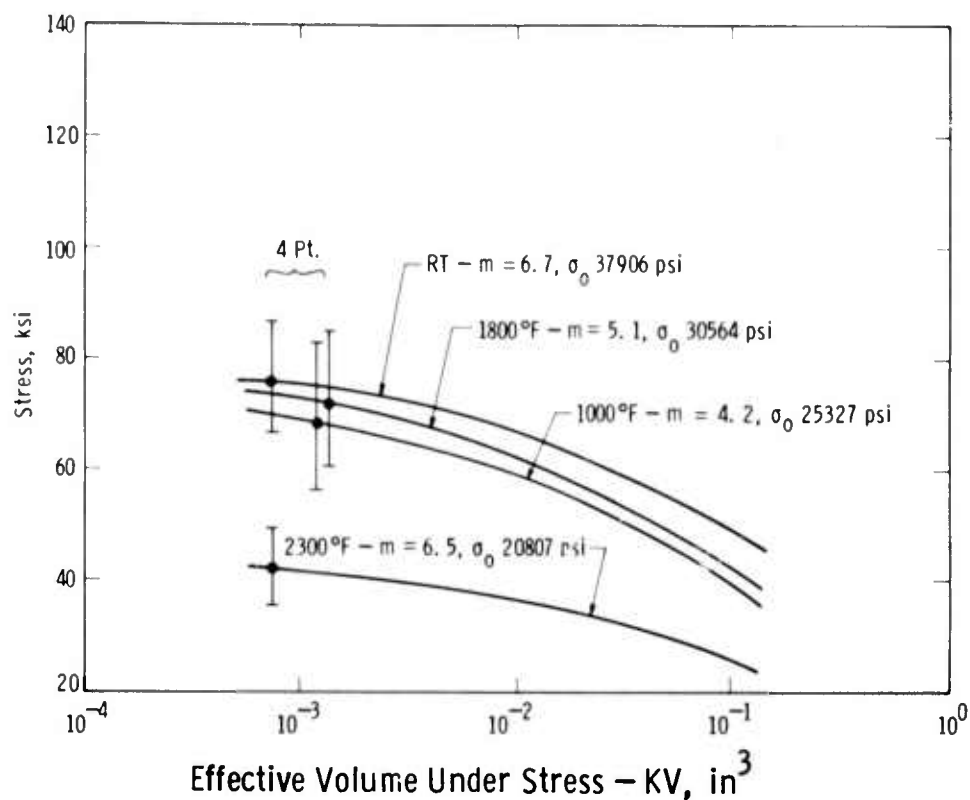
Figure 5.2   The Strength of Norton HS-130 Silicon Nitride (Weak
              Direction) as Predicted by Weibull Statistics Based on
              Volume
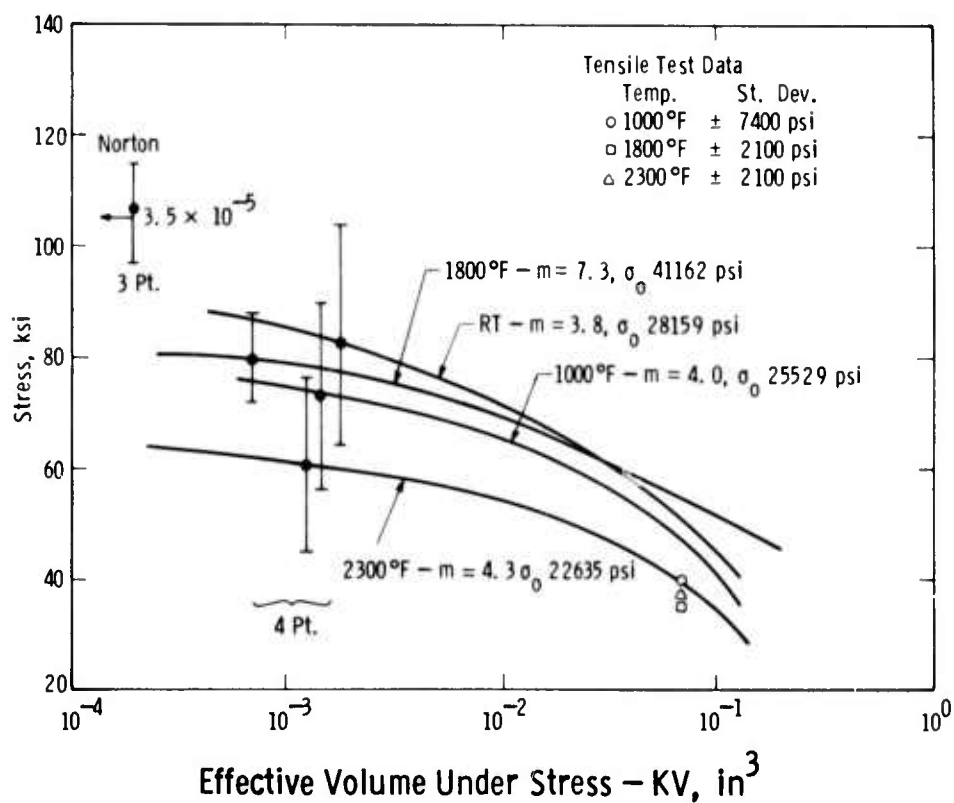
Figure 5.3   The Strength of Norton Hot-Pressed Silicon Carbide as
              Predicted by Weibull Statistics Based on Volume

0.125 x 0.250 x 1.125 in., 0.125 x 0.250 x 2.0 in., 0.125 x 0.250 x 3.0 in., and 0.125 x 0.250 x 6.0 in. were tested in both the beam and plate orientation so that both the volume and area under stress could be varied. The results appear in Table 5.1. While the flexural strength data can be extrapolated to meet the Weibull prediction in the vicinity of the tensile size specimen, the correlation between the measured and the Weibull estimates are not good for the range of sizes tested.

The best estimates of tensile strength for hot-pressed silicon nitride in the weak direction are 42,000 psi at room temperature, 39,500 psi at 1000°F, 35,000 psi at 1800°F and 22,000 psi at 2300°F based on Weibull theory of random flaw distribution. Since the billet thickness does not exceed 1.25 inches it is impossible to measure the tensile strength or modulus by actual test.

Table 5.1

ROOM TEMPERATURE STRENGTH PROPERTIES OF HOT-PRESSED SILICON NITRIDE AND SILICON CARBIDE

Silicon Nitride (Strong Direction)			Silicon Carbide		
Mode	Stress psi	Specimen Size (Stressed Vol, KV, in^3)	Mode	Stress psi	Specimen Size (Stressed Vol, KV, in^3)
Flexural, base^P	98,500	1×10^{-3}	Flexural, base^P	80,000	3×10^{-3}
			Measured Flex^B	82,000	3×10^{-3}
Measured Flex^B	132,000	9.0×10^{-2}			
Measured Flex^P	93,000	9.0×10^{-2}	Measured Flex^{P,B}	77,000	9.3×10^{-1}
Weibull Estimate	92,000	9.0×10^{-2}	Weibull Estimate	70,000	9.3×10^{-1}
Measured Flex^B	100,000	9.4×10^{-1}	Measured Flex^{P,B}	72,000	5×10^{-1}
Measured Flex^P	85,000	9.4×10^{-1}	Weibull Estimate	58,000	5×10^{-1}
Weibull Estimate	78,000	9.4×10^{-1}			
Measured Flex^B	94,000	8.5×10^{-1}	Extrapolated Tensile	45,000	3×10^{-1}
Measured Flex^P	80,000	8.5×10^{-1}	Extrapolated Flex	71,000	3×10^{-1}
Weibull Estimate	69,000	8.5×10^{-1}	Weibull Estimate	52,000	3×10^{-1}
Measured Flex^B	80,000	4.9×10^{-1}			
Measured Flex^P	80,000	4.9×10^{-1}			
Weibull Estimate	60,000	4.9×10^{-1}			
Measured Tensile	61,000	9.9×10^{0}			
Weibull Estimate	42,000	9.9×10^{0}			
Extrapolated Flex	62,000	9.9×10^{0}			

P = Plate orientation   h x 2h x X in
B = Beam orientation   h x 1/2 h x X in
                                height x width x length

Failure probability plots have been prepared for hot-pressed silicon nitride (Fig. 5.4) and silicon carbide (Fig. 5.5). Assuming the same probability of failure applies regardless of test mode, average tensile strength must be reduced by 25% when designing to 5% probability of failure.

Tensile Strength of Hot-Pressed Si3N4 and SiC

No new tensile strength data are available at this time. Forty additional SiC specimens and 25 additional Si3N4 specimens have been ordered, however. Elastic modulus has been determined from all of the stress-strain curves generated to date. These data are reported in Table 5.2.

102
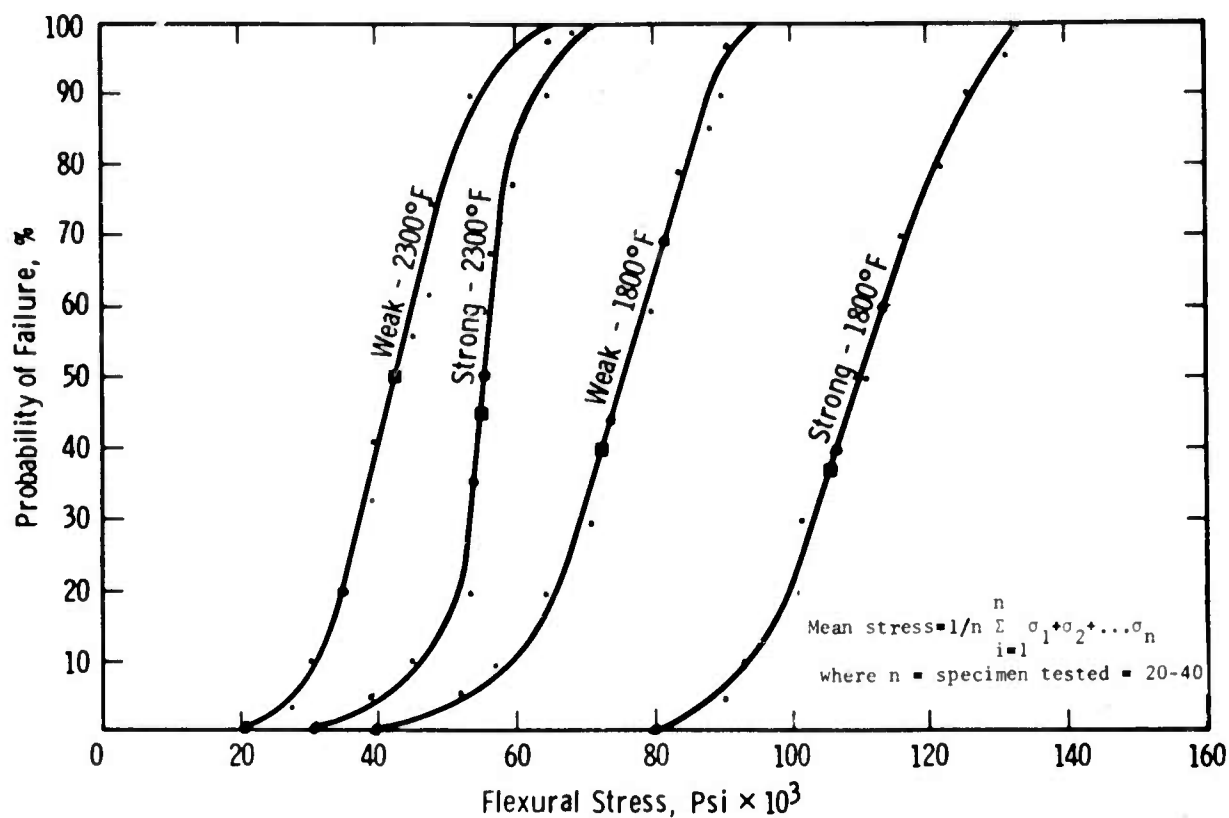
Figure 5.4   Failure Probability for Norton HS-130 Si_3N_4
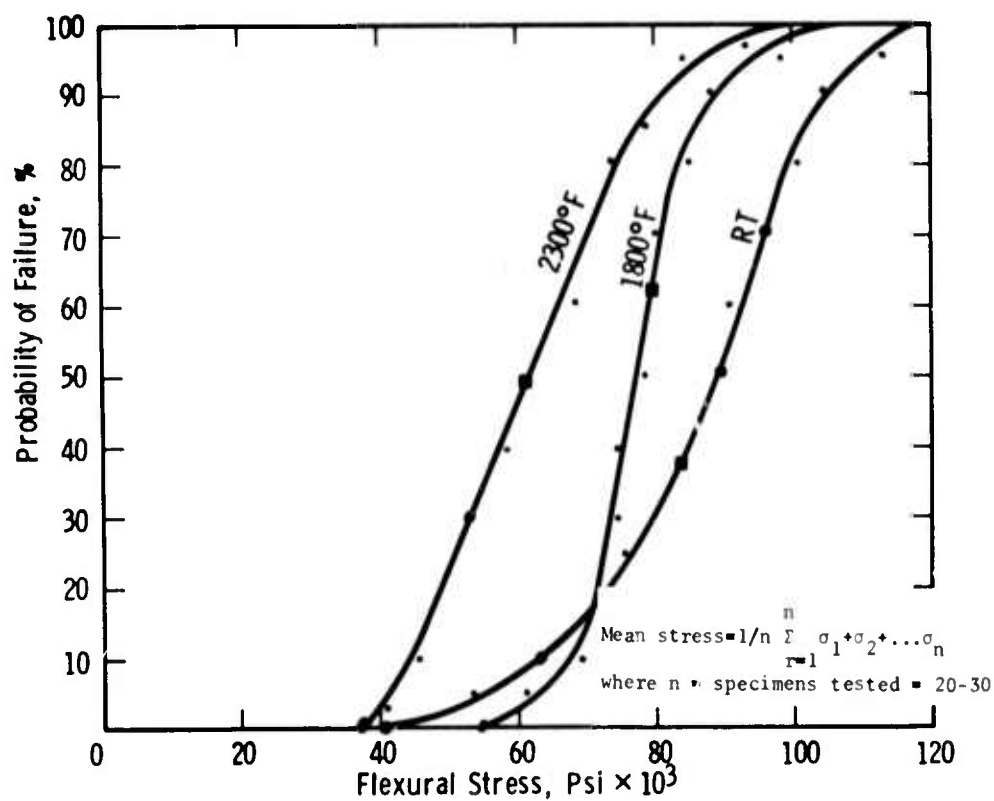
Figure 5.5   Failure Probability for Norton Hot-Pressed SiC

105

Table 5.2

ELASTIC MODULUS OF HOT-PRESSED SILICON NITRIDE AND SILICON CARBIDE

HS-130 Si$_3$N$_4$		HP SiC	
Temp °F	Elastic Mod. psi x 10^6	Temp °F	Elastic Mod. psi x 10^6
RT	45.2	1000	65.7
	43.9		64.2
	45.3		64.8
	Ave. 44.8		Ave. 64.7
1800	44.7	1800	65.6
	44.5		64.0
	45.4		65.4
	46.5		64.2
	45.9		64.6
	45.3		Ave. 64.8
	46.1		
	45.9		
	Ave. 45.5		
2300	46.8	2300	65.6
	45.6		68.5
	46.6		65.5
	46.3		65.4
	45.3		69.2
	46.8		66.0
	47.2		65.7
	45.8		Ave. 66.5
	Ave. 46.3		
2500	46.4	2500	66.2
	44.4		67.0
	45.2		64.1
	44.5		65.3
	Ave. 45.2		64.8
			64.2
			64.3
			Ave. 65.1

Tensile Creep Properties of Hot-Pressed Silicon Nitride and Silicon Carbide

Tests to determine the tensile creep properties of HS-130 Si$_3$N$_4$ are continuing. Additional data support the contention that the strength and performance of hot-pressed silicon nitride at high temperatures are strongly dependent upon the oxide impurities of Ca, Na, and K.

The billet chemistry is summarized in Table 5.3. Norton HS-130 material was arbitrarily classified as A or B on the basis of calcium

Table 5.3

CHEMISTRY OF Si_3N_4 BILLETS

in wt %

Group Designation	Ca	Na	K	Al	Fe	Mg
HS-110-A	0.5	0.002-0.004	0.002-0.004	0.5-1.0	1.0	0.5
HS-110-B	0.1-0.2	0.004-0.005	0.004-0.008	0.1	1.0	0.5
HS-130-A	0.06-0.08	0.006-0.01	0.004-0.008	0.1-0.2	0.5	0.3-0.4
HS-130-B	0.03-0.05	0.004-0.006	0.004-0.006	0.2	0.5	0.3-0.4

The first four elements in Table 5.3 were analyzed by a precision spectrographic method[5] with accuracies of ± 50% of the reported values.

content because the majority of tensile creep results fell into two distinct categories. When rupture life is plotted as a function of stress at 2300°F (Fig. 5.6), the Si_3N_4 data are represented better by two straight lines for HS-130A and HS-130B, respectively, than by a single line representing the data collectively.

Steady state creep rate is plotted as a function of stress for different temperatures in Fig. 5.7. The effect of Ca concentration on creep rate is clearly evident. Single datum points at 2500°F and 1800°F (10,000 psi stress), where creep rates approach 1.8×10^{-3} and 1.6×10^{-7} %/hr, respectively, are not shown.

The effect of atmosphere on creep in HS-130 Si_3N_4 is apparent in both Figs. 5.6 and 5.7. However, neither figure demonstrates the most significant effect of atmosphere. Total elongation in helium rarely exceeds 1% whereas 2.5 to 3.0% strain at rupture is characteristic of the hot-pressed silicon nitride in air. Since turbine rotor blading must meet a total strain requirement, creep life has been expressed in terms of maximum allowable tensile strain or 1% elongation. The data are reduced to reflect this strain criterion in Fig. 5.8. Under conditions of 20,000 stress, the life estimates at 2100°F range from 500 to 2000 hours depending upon the calcium concentration of the parent HS-130 billet material. There is no need to impose a tensile strain requirement in stator vane applications because the steady state stresses are not expected to exceed 4000 psi. If the vanes were to deform up to 3% by bowing, for example, the effect on performance would be inconsequencial.

The creep properties of hot-pressed silicon nitride are compared with selected nickel and cobalt base superalloys in Figs. 5.9 and 5.10. The Larson-Miller plot and 1000 Hour Stress Rupture Life are used here because both represent common engineering practice.
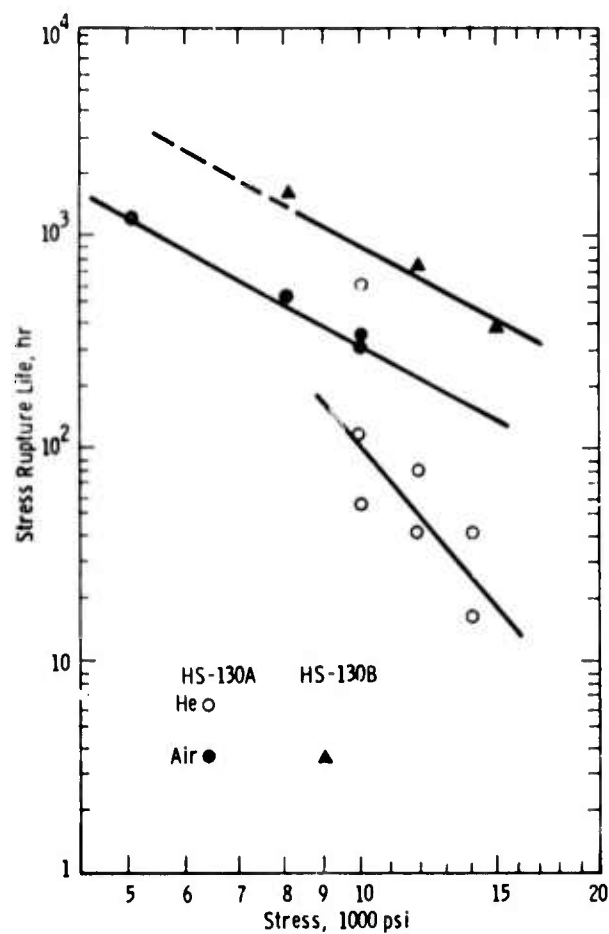
Figure 5.6   The Stress Rupture Properties of Norton HS-130 Silicon
              Nitride at 2300°F
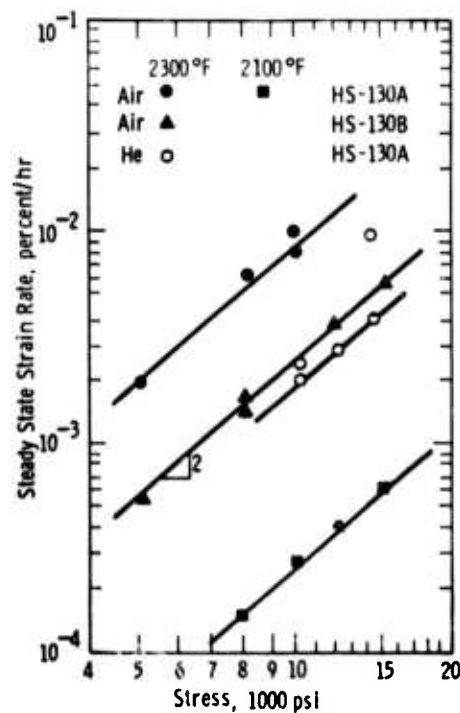
Figure 5.7   Steady State Tensile Creep Properties of Norton HS-130
              Silicon Nitride
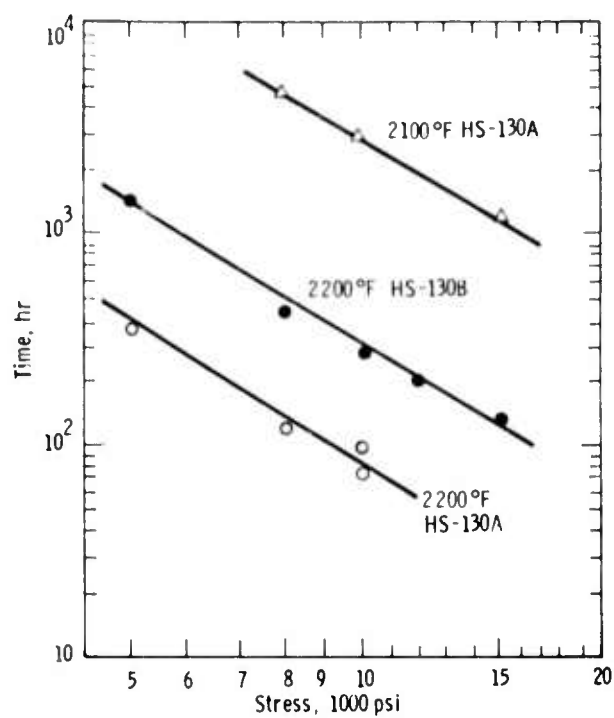
Figure 5.8   The Tensile Creep Life of Norton HS-130 Silicon Nitride
               Based on 1% Strain Criterion
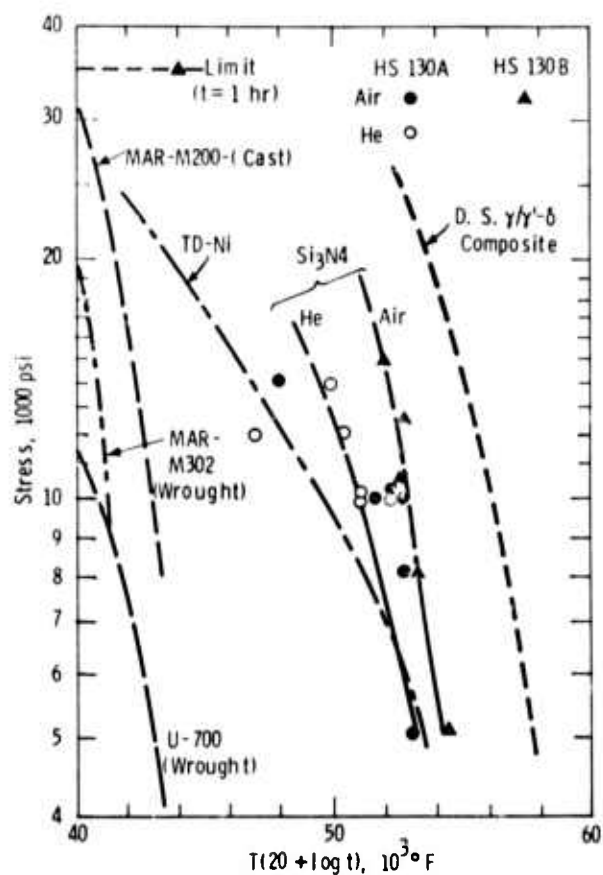
Figure 5.9   Larson-Miller Plots Comparing the Stress Rupture Properties
               of Si_3N_4 with Superalloys and Metal Matrix Composites
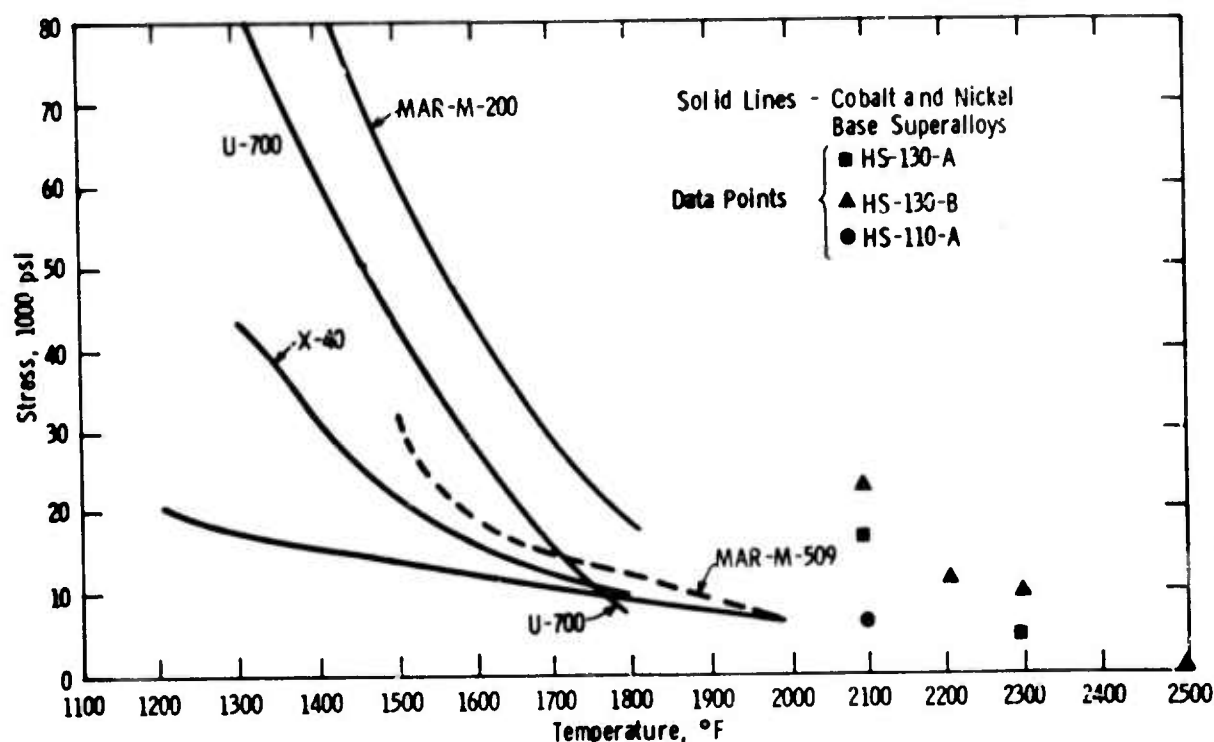
Figure 5.10   The 1000 Hour Stress Rupture Characteristics of Si_3N_4
and Selected Superalloys

It is generally agreed that creep deformation results from
dislocation motion and/or diffusional creep. In the case of hot-pressed
silicon nitride,grain boundary sliding, which is a diffusional process,
presumably predominates. Creep, therefore, can be expressed by:

$$\dot{\varepsilon} = A\, \sigma^n\, \exp^{\Delta H/RT}$$

where ΔH is the activation enthalpy for creep and n is an exponent equal
to 2 denoting grain boundary sliding.

Dislocations have been identified in silicon nitride.[2]   However,
the dislocation density was very low and there was no detectable change
in dislocation density as a result of creep deformation. The contribution
of dislocation motion to creep strain is, at best, a few orders of
magnitude less than the observed creep strain.

Since the grains cannot accommodate the deformation, grain boundary
sliding leads to the initiation and steady state growth of triple-point
grain boundary wedges which dominate creep deformation in Si_3N_4
(classical second stage of creep). The wedges coalesce to form stable
cracks which characterize the third stage of accelerated creep to
almost immediate failure. The viscosity of the glass phase at the
grain boundary presumably influences the rate of grain boundary sliding.

Three hot-pressed silicon carbide specimens have been creep tested in
air at 2300°F. Two of these were loaded to 15,000 psi; both failed in
less than one minute. The third specimen was loaded at 10,000 psi.
Approximately 0.2% elongation was recorded after 250 hours. This test
is continuing.

108

While it has been difficult to accumulate meaningful tensile creep data on Norton hot-pressed silicon carbide, certain conclusions may be drawn from the creep testing at this time:

(1) Hot-pressed silicon carbide appears to be stress rupture limited.

(2) Hot-pressed silicon nitride appears to be creep limited in its present form. Experiments indicate that significant improvement is possible by controlling the level of alkaline impurities.

Flexural Testing - A Critical Evaluation of Si₃N₄

The flexure test is commonly used to determine the strength and failure strain of brittle materials because the specimen configuration is simple and the test is relatively easy to perform. It is valid as long as the stress-strain function remains linear and the material reacts equivalently in a state of tension or compression. Under these conditions, well established elastic beam theory can be used to determine the maximum stresses and strains. Unfortunately, plastic deformation has been observed in hot-pressed silicon nitride at elevated temperatures. Since plastic deformation indicates a deviation from true elastic response, the continued use of elastic beam theory in the calculation of maximum flexural stresses and strains in Si₃N₄ leads to erroneously high values, especially, at temperatures above 2000°F where the effect is considered significant. An attempt has been made to define the effect of plastic behavior in the determination of flexural properties of hot-pressed silicon nitride and to modify the flexural results accordingly.

There are three conditions which must be met during bending. First, the cross-sections must remain planar, i.e., a linear relationship must exist between strain, ε, and a distance, y, from some neutral axis at which both stress and strain are zero:

$$\varepsilon = \frac{y}{R} \qquad (1)$$

where R is the radius of curvature of the neutral axis. Second, a compressive and tensile force balance is required:

$$F = \int \sigma \, dA = 0 \qquad (2)$$

where F is the force, σ is the stress as a function of position, and A is the area as a function of position. The resisting moment of a rectangular specimen under conditions of 4 point bending must equal the applied bending moment, M:

$$M = \int \sigma \, y \, dA \qquad (3)$$

If the elastic behavior is the same for tension and compression, a specimen under applied load will bend such that the strain differential between the extreme tensile and compressive surfaces is determined by deflection (D), fixture geometry (a = inner span, L = outer span distances),

and specimen thickness (h). From beam-deflection theory, the strain differential (ε) is:

$$\varepsilon = \frac{6 h D}{3aL - 4a^2} \tag{4}$$

Tensile (ε_t) and compressive (ε_c) components of strain;

$$\varepsilon = \varepsilon_t + \varepsilon_c \tag{5}$$

depend upon the character of the stress-strain relationships which must be determined. The radius of specimen curvature (R) is a function of deflection and inner span dimension:

$$R = \frac{3aL - 4a^2}{6D}$$

Since strain is linearly proportional to the distance from the neutral axis, the force balance equation (2) can be rewritten as:

$$F = \int_{-\varepsilon_c}^{\varepsilon_t} \sigma \, d\varepsilon = 0 \tag{7}$$

and the moment Eq. (3) becomes:

$$M = \frac{P}{4} (L-a) = bR^2 \int_{\varepsilon_c}^{\varepsilon_t} \sigma \, \varepsilon \, d\varepsilon \tag{8}$$

where P = applied load and b = specimen width.

Two extremes of plastic response were considered:

(1) The tensile and compressive stress-strain relationships are non-linear, but identical.

(2) The compressive stress-strain behavior is linear while the tensile stress-strain behavior is non-linear.

For the case where the tensile and compressive stress-strain curves are the same, the neutral axis remains centrally located and the compressive stresses and strains are of the same magnitude but of opposite sign as the tensile stresses and strains. The load-deflection curve in Fig. 5.11 is first adjusted for machine deflection and then divided into n even increments, ΔD, beyond some arbitrary deflection, D_0, on the straight line portion. The curve is analyzed incrementally over the total deflection range:

$$D_i = D_{i-1} + \Delta D, \quad i = 1 \text{ to } n \tag{9}$$

P_i as functions of D_i are known. Using data from Fig. 5.12 the modified moment Eq. (8) may be written as:

$$\frac{M_i}{2bR_i^2} = \sum_{i=1}^{j-1} \sigma_i \Delta\varepsilon_i \left(\varepsilon_{i-1} + \frac{\Delta\varepsilon_i}{2}\right) + \sigma_j \Delta\varepsilon_j \left(\varepsilon_{j-1} + \frac{\Delta\varepsilon_j}{2}\right)$$
$$+ \frac{1}{3} \sigma_c \varepsilon_0^2, \quad j = 1 \text{ to } n \tag{10}$$

110

Figure 5.11   Treatment of a Measured Load-Deflection Curve

where $\Delta\epsilon_i = \epsilon_i - \epsilon_{i-1}$ (11)

The ϵ_i are half the values determined from Eq. (4). The stress-strain curve is incrementally constructed by solving for σ_j and ϵ_j.

When the stress-strain curves are not the same, the neutral axis shifts from its central location and the location of the neutral axis must be determined continuously. The tensile stresses and strains no longer are of the same magnitude as the corresponding compressive stresses and strains. The method is similar to the case cited above. From Fig. 5.13, the force balance Eq. (7) takes the form:

$$\frac{c}{2}(\epsilon_o^2 - \epsilon_{c_j}^2) + \sum_{i=1}^{j-1} \sigma_{t_i} \Delta\epsilon_i + \sigma_{t_j} \Delta\epsilon_j = 0 \tag{12}$$

where c is the elastic modulus and ϵ_{c_j} is the outer surface compressive strain. The expanded moment equation is:

$$\frac{M_i}{bR_i^2} = \frac{c}{3}(\epsilon_o^3 - \epsilon_{c_j}^3) + \sum_{i=1}^{j-1} \sigma_{t_i} \Delta\epsilon_i (\epsilon_{t_{i-1}} + \frac{\Delta\epsilon_i}{2})$$

$$+ \sigma_{t_j} \Delta\epsilon_j (\epsilon_{t_{j-1}} + \frac{\Delta\epsilon_j}{2}), \quad j = 1 \text{ to } n \tag{13}$$

and the strain equation becomes:

$$\frac{3h\, D_j}{3al - 4a^2} = -\epsilon_{c_j} + \epsilon_{t_j} = -\epsilon_{c_j} + \epsilon_{t_{j-1}} + \Delta\epsilon_j. \tag{14}$$
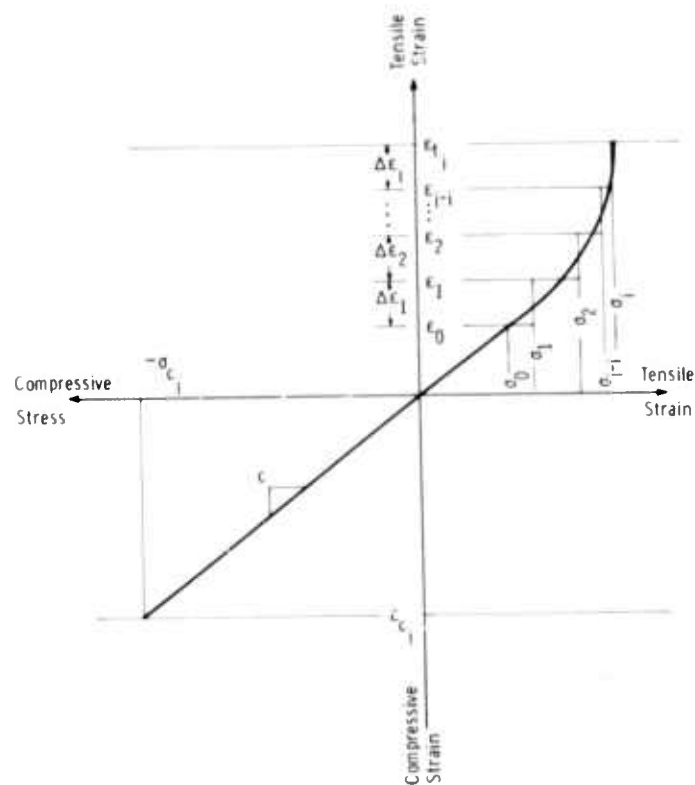
111

Figure 5.12   The Stress-Strain Relationship Across a Rectangular Flexural
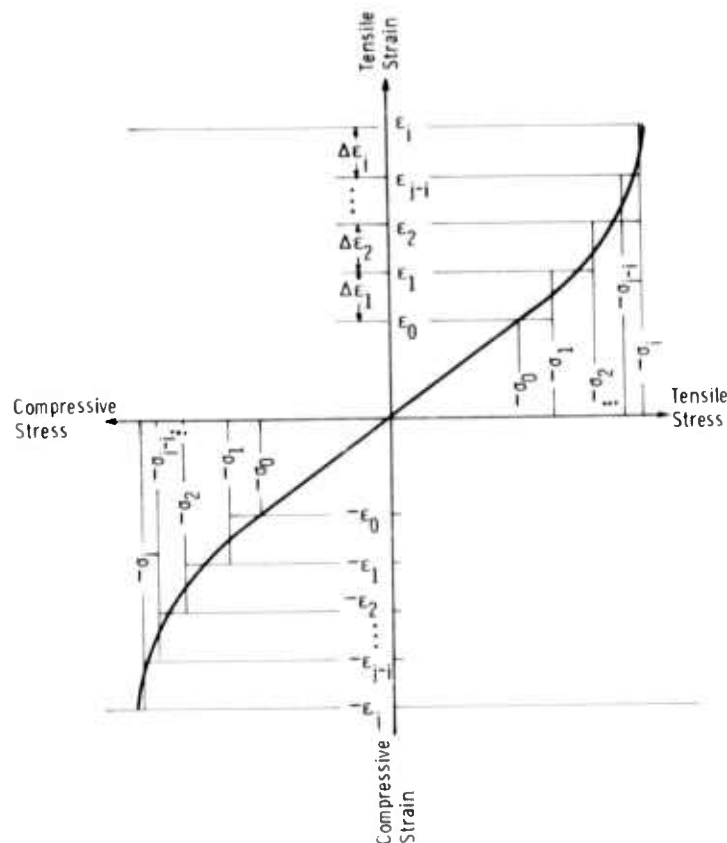Bar for Equivalent Non-Linear Tensile and Compressive
Functions

Figure 5.13   The Stress-Strain Relationship Across a Rectangular Flexural
Bar for Linear Compressive and Non-Linear Tensile Functions

Equations (12), (13) and (14) are solved simultaneously to obtain (a) the outer compressive strain, ε_{cj}, (b) the outer fiber tensile strain, ε_{tj}, and (c) the outer fiber tensile stress, σ_{tj}. The compressive stress is calculated from:

$$\sigma_{cj} = c\varepsilon_{cj} \tag{15}$$

The load-deflection curve is expressed analytically as a polynomial. The deflection increments can be adjusted arbitrarily to be as small as necessary to reduce errors in the rectangular increment.

A load-deflection curve from an actual 2350°F 4-point bend test of HS-130 silicon nitride at a crosshead speed of 0.002 in/min is shown in Fig. 5.14. Figure 5.15 represents the results of the analyses for three conditions: (A) elastic tension and compression, (B) equivalent plastic tension and compression, and (C) plastic tension and elastic compression.
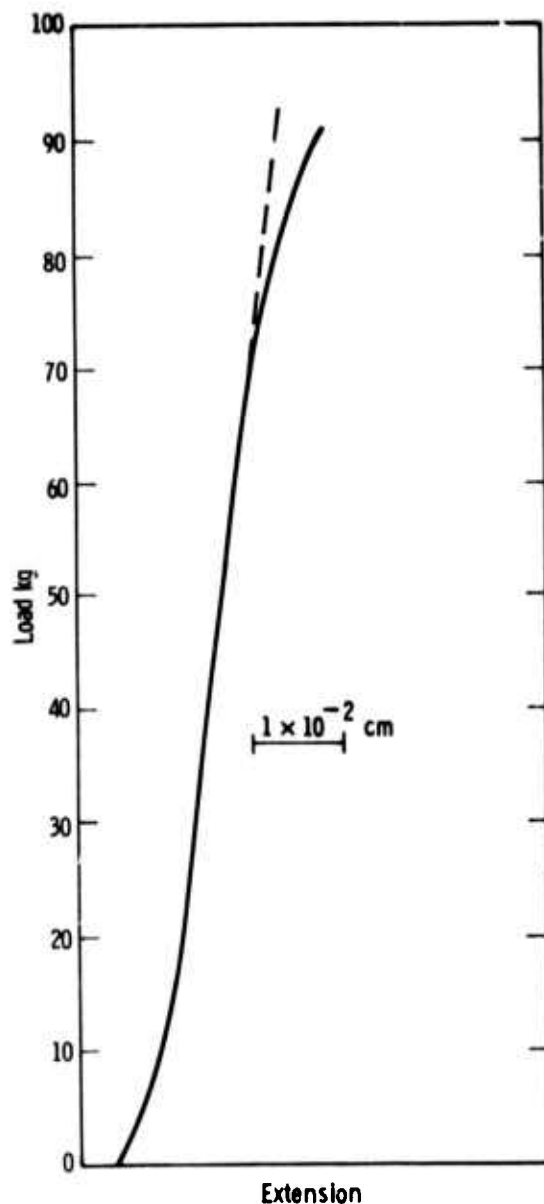

Figure 5.14   Typical Load Extension Curve for Silicon Nitride in the Weak Direction at 2350°F
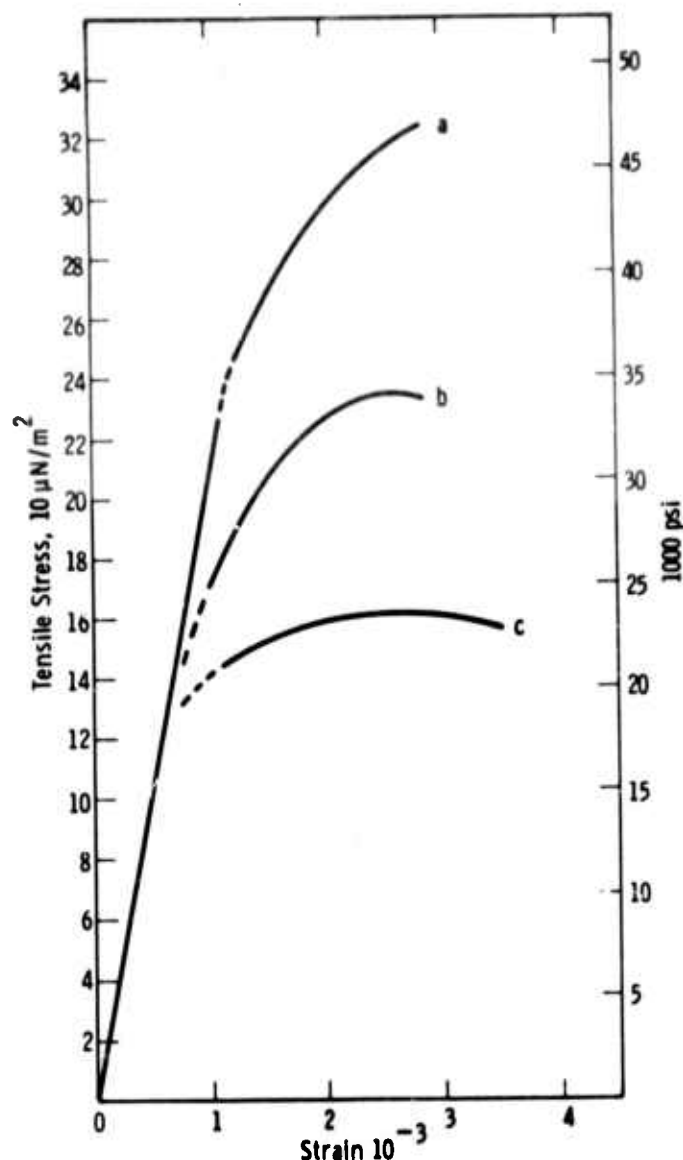
Figure 5.15   Computed Stress-Strain Curves for (a) an Elastic Solution,
(b) a Plastic Solution; and (c) a Tensile Plastic-Compression
Plastic Solution (Si_3N_4 Weak Direction)

It is apparent that the use of the elastic beam equation exclusively,
yields the highest values of stress. The maximum tensile stress for
condition B is greater than that for condition C, whereas the case for
maximum compressive stresses is reversed. It should also be noted that
the maximum tensile stress for any of the conditions does not necessarily
occur at the outside fiber. Finally, the greatest tensile strains occur
for condition C, since it exhibits the greatest neutral axis shift.
Representative data are summarized in Table 5.4 for three conditions of
elastic strain rate. The actual flexural properties of Si_3N_4 probably
lie somewhere between curves B and C (Fig. 5.15) and columns 2 and 3 of
Table 5.4 depending upon the compressional stress-strain characteristics.

Shear Properties of Hot-Pressed Silicon Nitride and Silicon Carbide

The torsion test apparatus and shear specimen used to measure the
shear strength and shear modulus of Si_3N_4 and SiC from RT to 2500°F

114

have been described.[3] An angle of twist indicator, with a gage
length of 1.50 inches, was cemented to the specimen. The specimens
were torqued three times at each temperature condition in both the
clockwise and counter-clockwise directions to a maximum shear stress of
26,000 psi for Si_3N_4 and 20,000 psi for SiC.

Table 5.4

MAXIMUM OUTER FIBER STRESSES AND STRAINS, 4 pt. BENDING IN AIR AT 2350°F

(Average 4 billets, specimen cut in strong direction)

Elastic Strain Rate min^{-1}	Elastic		Plastic		Plastic-Elastic	
	σ_{max} 10^{-3} psi	ε_{max} 10^{-6}	σ_{max} 10^{-3} psi	ε_{max} 10^{-6}	σ_{max} 10^{-3} psi	ε_{max} 10^{-6}
0.01	65.7	41	50.1	36	38.1	47
0.001	50.3	51	39.1	47	26.5	71
0.0001	42.8	71	30.4	66	19.8	117

Shear modulus was calculated from the X-Y records of torque versus
the angle of twist. The effects of temperature on the shear modulus of
Si_3N_4 and SiC appear in Figs. 5.16 and 5.17, respectively. A torque
versus angle of twist curve was obtained to failure at the highest test
temperature. Figure 5.18 is typical of Si_3N_4 at 2300°F. No plasticity
was evident in SiC specimens tested to 2500°F. The shear properties of
Norton HS-130 silicon carbide and hot-pressed silicon nitride are
summarized in Tables 5.5 and 5.6, respectively.
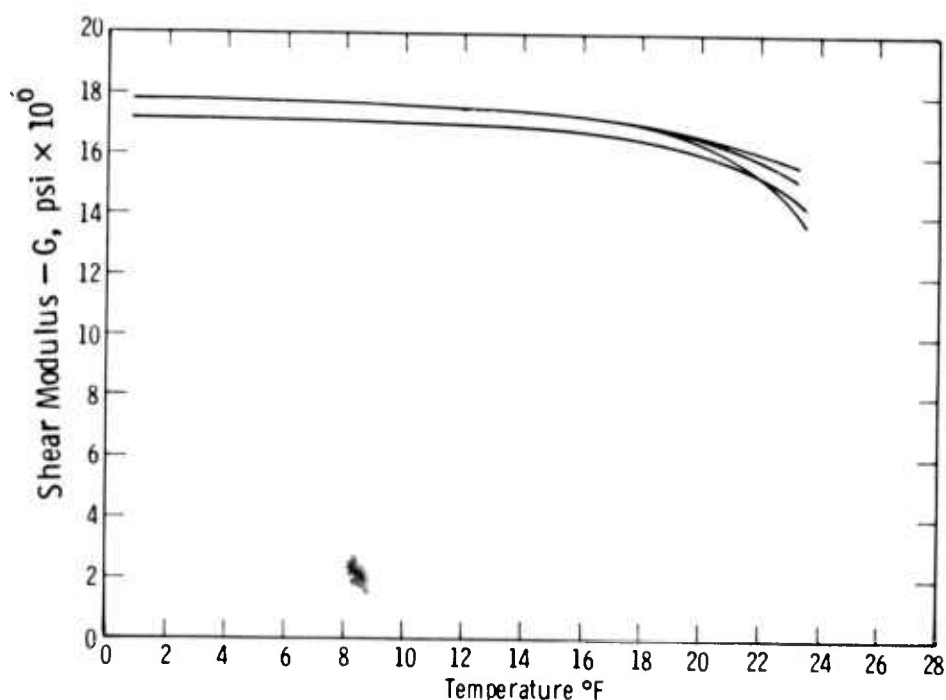

Figure 5.16   The Effect of Temperature on the Shear Modulus of Si_3N_4
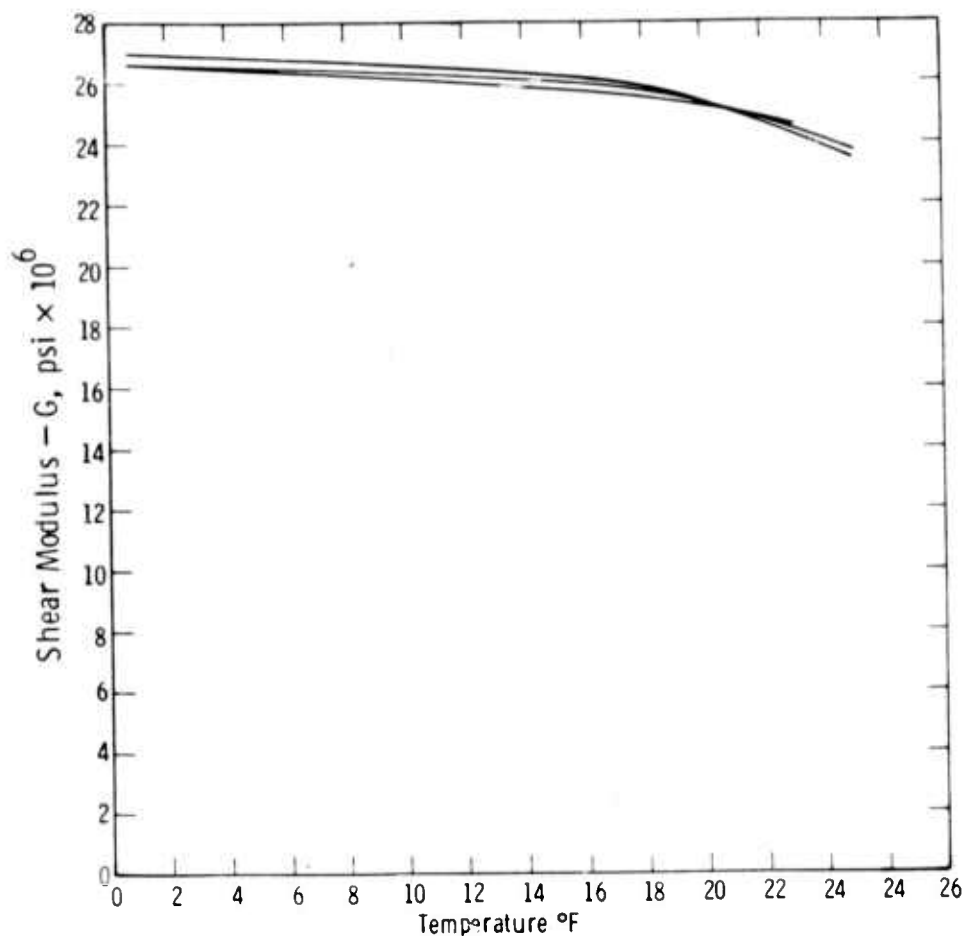
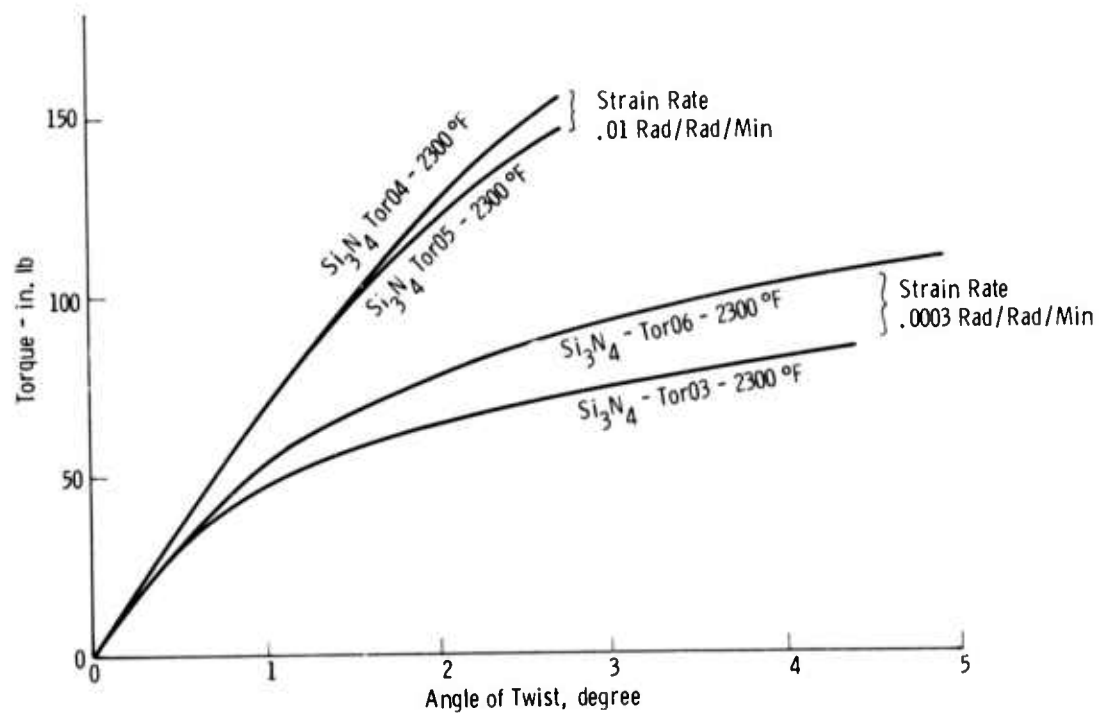Figure 5.17   The Effect of Temperature on the Shear Modulus of SiC

Figure 5.18   Torque vs Angle of Twist Curves for Silicon Nitride Tested at 2300°F

116

Table 5.5

SHEAR PROPERTIES OF SILICON NITRIDE

Specimen Si$_3$N$_4$-TOR03-2300 Billet No. 10-A		Specimen Si$_3$N$_4$-TOR04-2300 Billet No. 9-B		Specimen Si$_3$N$_4$-TOR05-2300 Billet No. 10-B		Specimen Si$_3$N$_4$-TOR06-2300 Billet No. 9-A	
Test Temp.°F	Shear Modulus G, psi x 10^6	Test Temp.°F	Shear Modulus G, psi x 10^6	Test Temp.°F	Shear Modulus G, psi x 10^6	Test Temp.°F	Shear Modulus G, psi x 10^6
75	17.8	75	17.8	75	17.8	75	17.2
1800	17.0	1818	17.1	1830	17.0	1822	16.5
2135	16.0	2108	16.4	2119	16.4	2120	15.7
2340	13.7	2329	15.7	2319	15.2	2321	14.4
2340	Ult. Shear Stress 27,900 psi	2329	Ult. Shear Stress 50,950 psi	2319	Ult. Shear Stress 47,800 psi	2321	Ult. Shear Stress 36,000 psi
Strain Rate	.003 RAD/RAD/MIN		.01 RAD/RAD/MIN		.003 RAD/RAD/MIN		.01 RAD/RAD/MIN

Table 5.6

SHEAR PROPERTIES OF SILICON CARBIDE

Specimen SiC-TOR01-2300 Billet No. 872-2-1		Specimen SiC-TOR02-2500 Billet No. 872-7-2		Specimen SiC-TOR03-2500 Billet No. 872-8-3	
Test Temp.°F	Shear Modulus G, psi x 10^6	Test Temp.°F	Shear Modulus G, psi x 10^6	Test Temp.°F	Shear Modulus G, psi x 10^6
75	26.6	75	27.0	75	26.6
1808	25.6	1808	25.9	1811	25.8
2100	25.0	2104	24.9	2108	24.9
2296	24.6	2306	24.3	2307	24.5
		2493	23.5	2507	23.8
2296	Ult. Shear Stress 37,200 psi	2493	Ult. Shear Stress 23,200 psi	2507	Ult. Shear Stress 41,750 psi
Strain Rate	.001 RAD/RAD/MIN		.001 RAD/RAD/MIN		.001 RAD/RAD/MIN

Corrosion-Erosion Testing

While corrosion-erosion testing of Norton HS-130 silicon nitride and hot-pressed silicon carbide continued in the turbine test passage at 2500°F, 3 atmospheres pressure, and 500 ft/sec gas velocity insufficient data were collected during the period to warrant reporting at this time. A white glassy deposit collected on all specimens early in the test indicating the possible reaction of alumina from the test passage liner with Si$_3$N$_4$ and SiC. Since aluminum oxide is not a representative constituent of the gas turbine environment, these results are considered suspect.

Ultrasonic Attenuation Measurements of Hot Pressed Silicon Nitride and Lithium-Aluminum-Silicate

Previously reported ultrasonic attenuation measurements [4] for 10 MHz shear sound waves have been extended to 1550°C in Norton HS-130 hot pressed silicon nitride. The attenuation rises rapidly near 1000°C, levels off be-

tween 1300 and 1400°C, then increases slowly above 1450°C as shown in Figure 5.19. No evidence for an attenuation decrease at high temperatures has been found. Thus the present attenuation effect appears unlike the usual internal friction effects in metals which are associated with grain boundary motion. It is believed to result from softening of a second viscous phase known to reside at grain boundaries in this material.

A broad, high temperature internal friction peak has been found for 10 MHz shear sound waves in Corning 9458 lithium aluminum silicate, as shown in Figure 5.20. The peak maximum occurs at 370°C. Further work will be done to see if the temperature of the maximum is frequency dependent. If not, the sound obsorption may be associated with the minimum thermal expansion of this material which occurs near 400°C.
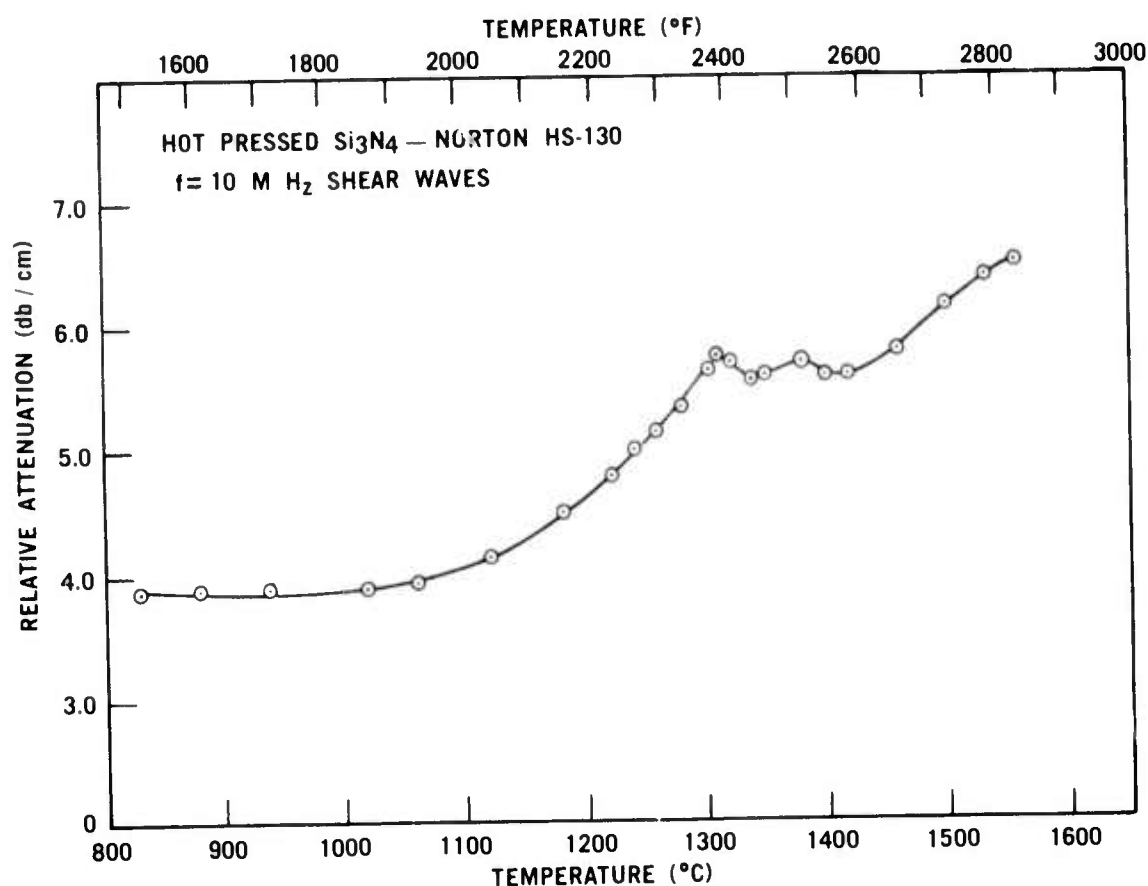

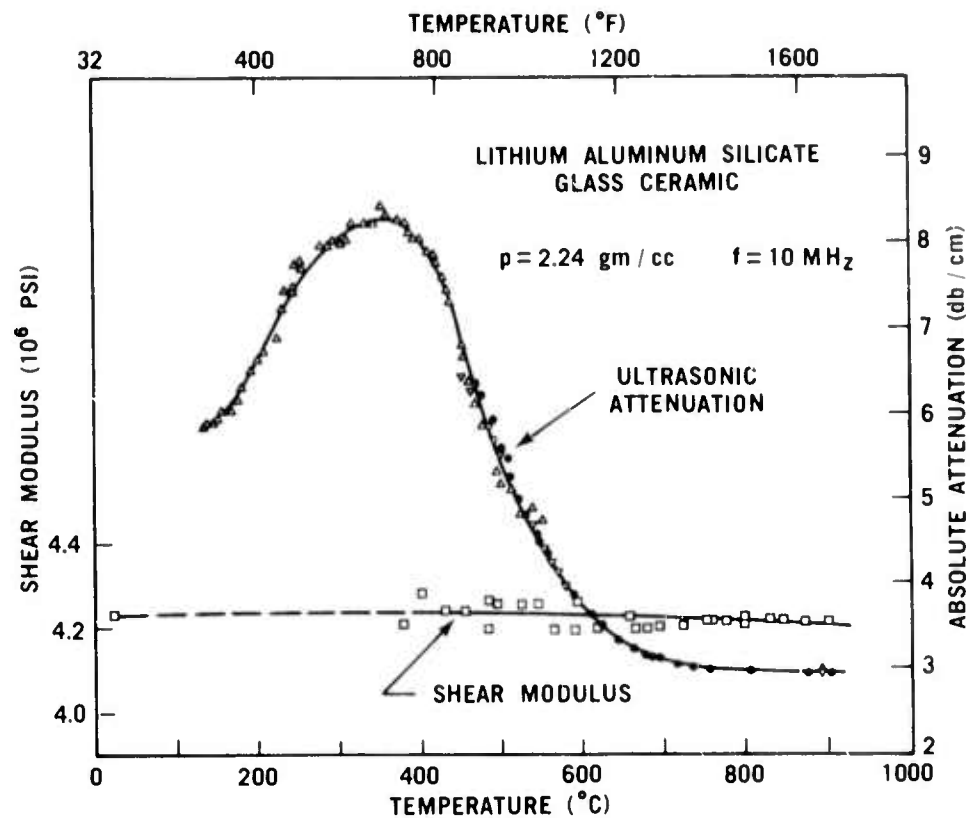Figure 5.19   Ultrasonic Attenuation of Hot-Pressed Silicon Nitride

118

Figure 5.20   Attenuation and Shear Modulus Behavior For Lithium
              Aluminum Silicate

5.1.2 CREEP OF REACTION SINTERED SILICON NITRIDE

Introduction

In the last report [4], the creep properties of the then-current injection molded reaction sintered silicon nitride were discussed.* Creep testing has now been expanded to include two additional grades of injection molded Si_3N_4 and four varieties of slip cast Si_3N_4.

Satisfactory creep properties of injection molded Si_3N_4 are critical to the successful operation of the Ford duo-density turbine rotor. Creep data may also provide useful information on material behavior which is helpful in the further development of improved materials.

A study was initiated to investigate the creep behavior of various grades of slip cast Si_3N_4. One method of rotor fabrication (the triple-density technique) requires the use of a high strength slip cast Si_3N_4 in the rotor rim. This area is subjected to high stresses and high temperatures. Also, engine testing of slip cast rotor shrouds identified a deformation problem, presumed to be caused by creep of the material[4].

The data derived from this investigation will be used primarily as a material development tool to determine the best material for use in the triple density rotors and to help analyze and solve the shroud deformation problem.

Creep of Injection Molded Si_3N_4

Creep measurements were made using four point bending in an air atmosphere [4]. Test samples were injection molded into rectangular preforms and nitrided according to the conditions shown in Table 5.7. Test samples measuring 5/32 in. x 1/2 in. x 3 in. long were diamond ground from the rectangular preforms.

TABLE 5.7

Creep Sample Processing History, Injection Molded Si_3N_4

Mat'l	Nitriding Cycle*	Nitriding Atm.	Density	Average MOR +
Type A	24/24	N_2	2.30 gm/cm^3	17000 psi
Type B	36/24	N_2	2.36 gm/cm^3	19100 psi
Type C	36/24	1.8% H_2+ N_2	2.35 gm/cm^3	24650 psi
Type D	36/24	1.8% H_2+ N_2	2.34 gm/cm^3	24300 psi

* 24/24 Cycle is defined as 24 hours at $2300^\circ F$ and 24 hours at $2660^\circ F$.

  36/24 Cycle is defined as 36 hours at $2300^\circ F$ and 24 hours at $2660^\circ F$.

+ 1/8" x 1/8" x 1-1/2" sample, 4 point bending (3/8" x 1-1/8" fixture), cross head speed = 0.10 in/min.

---

*In the previous report [4], the creep strains and strain rates as shown in Table 5.12, Figure 5.44 and Figure 5.45 were incorrectly presented. This data has been corrected and updated and presented in Figure 5.21 and Figure 5.22 of this report.

120

The materials were characterized according to density and strength (Table 5.7). Little variation was found in density; however, the materials nitrided with hydrogen additions (Types C & D) exhibited significantly higher strengths. Impurity analyses of the materials are shown in Table 5.8. The Type A material had a high calcium content, due to the addition of CaF_2 as a nitriding aid, and the Type D material had a significantly lower Al content and the lowest Ca content, due to improved purity of the starting silicon metal. X-ray diffraction analysis showed that all samples had been completely nitrided with a similar phase composition of 65 Wt% $\propto$ Si_3N_4 and 35 Wt% β Si_3N_4.

Figure 5.21 shows representative creep curves for Si_3N_4 materials A, B, C, and D. These materials exhibit both primary and secondary creep. However, all tests were concluded before any evidence of tertiary creep could be observed.

Figure 5.22 shows steady state creep rate ($\dot{\epsilon}_s$) as a function of stress for the various test temperatures and materials studied. Figures 5.21 and 5.22

TABLE 5.8

Typical Impurity Analysis of Injection Molded Si_3N_4 Creep Samples (Wt %)

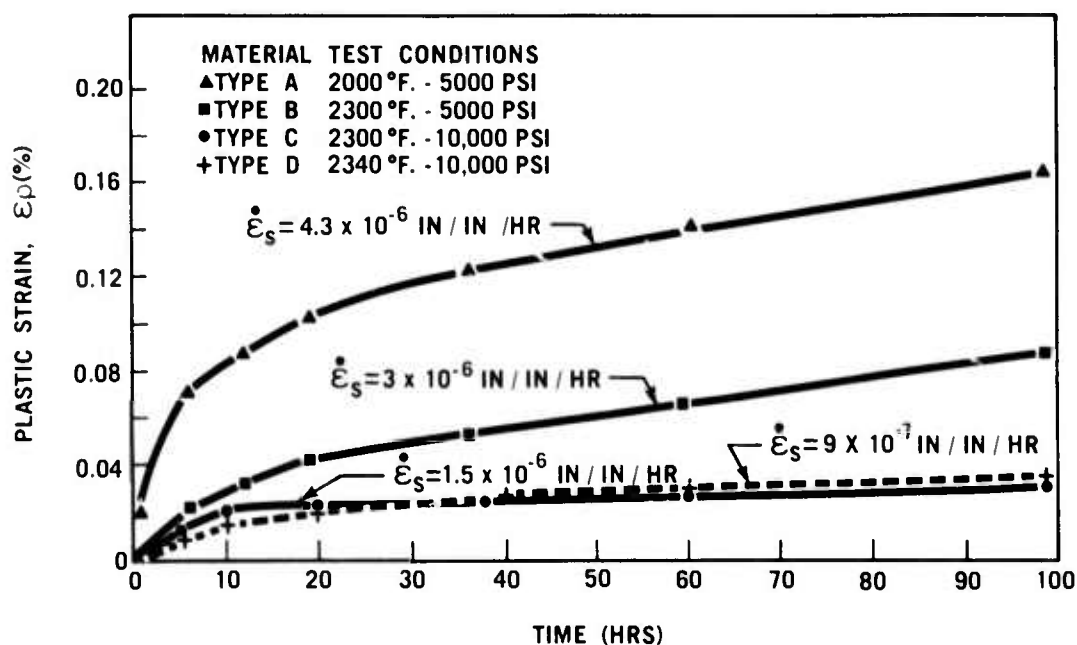| Mat'l	Fe	Al	Ca	Mg	Ni	W	Co	V
Type A	0.50-0.70	0.35-0.48	0.40	0.03	0.02	<0.01	0.01	0.01
Type B	.66- .76	.38- .60	.02-.08	.02	.02	< .01	.01	.01
Type C	.66- .76	.38- .60	.02-.08	.02	.02	< .01	.01	.01
Type D	.60- .94	.10- .23	.01-.05	.02	.04	-	-	.03

Figure 5.21   Plastic Strain vs Time For Several Types of Reaction Sintered Silicon Nitride

illustrate the large differences in creep behavior of the materials studied. The Type A material, which contains 0.40% calcium, exhibits the most plastic deformation and the highest creep rates. Reducing the calcium content to an average of 0.05% (Type B) resulted in less plastic deformation and lower creep rates, even though the testing temperature and stress were increased. The Type C material with the same calcium content (0.05%) but nitrided with 1.8% H_2 shows an significant improvement in creep resistance over the Type B material under the same stress and temperature conditions.

Type D material (0.15% Al, 0.03% Ca, nitrided in 1.8% H_2) was tested at one condition only; $2340^\circ F$ and 10,000 psi (Figures 5.21 and 5.22). This material exhibits a lower creep rate than the Type C material at a higher test temperature. From this one test, it appears that by increasing the purity of the material (with respect to Ca and Al), greater creep resistance can be obtained. However, more tests are necessary to determine if the stress or temperature dependence of the steady state creep has also changed.

The stress exponent values from Figure 5.22 (to be used in the equation $\dot{\varepsilon}_s = K\sigma^n$) of 1.3 to 2.0 are typical of those obtained in viscous flow. Examination of the microstructure after creep testing showed a glassy phase on the fracture surface. This glass layer was analyzed using Auger electron spectroscopy. Converting the elemental concentration to oxide form, the approximate glass compositions for the Type A and Type B materials are as follows:

Type A: $CaO \cdot 2\ Al_2O_3 \cdot 2\ SiO_2$

Type B: $CaO \cdot 11\ Al_2O_3 \cdot 7.5\ SiO_2$

Examination of the phase diagram for this system shows that the Type B composition is the more refractory. This agrees with the creep results obtained for these two materials, and is consistent with the observation that
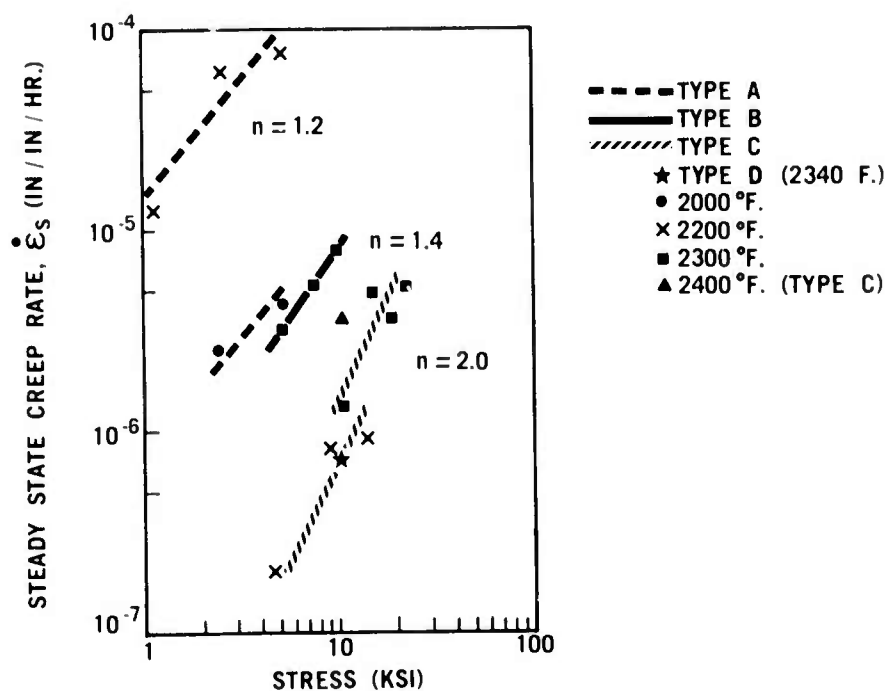

Figure 5.22   Steady State Creep Rate vs Stress For Several Types of Reaction Sintered Silicon Nitride

122

the Type B material exhibits less creep at higher temperatures than the
Type A material. Since the Auger analysis yielded results proportional to
the initial spectrographic analysis, it can be assumed that the Type C glass
composition is approximately equal to the Type B composition and that the
Type D glass will be lower in both Ca and Al, and is therefore more refractory
than the Type B glass phase.

Examination of the microstructure also delineates a large difference in
grain size between the Type C and the Types A & B Si_3N_4. The Type C has much
smaller grains with more particle-to-particle contact area between the grains
This increased contact area between grains would require more force to be
applied to the sample to generate an equivalent stress condition at the grain
boundaries. This may account for the improved creep properties of the Type C
material over the Type B. The open structure of the Typ A and B materials
also allows for larger movement of grains into the open areas of the structure,
thereby allowing more overall deformation to occur. This could account for
the observed differences in primary creep of the various grades of material.

The combination of increased purity, especially with respect to Ca, and
a modified microstructure due to the H_2 addition in the nitriding atmosphere,
are the two factors contributing to the improved creep resistance of the
Type C reaction sintered Si_3N_4. Combining these improvements with a lower
level of Al impurity resulted in the superior creep resistance of the Type D
material.

Limited stress rupture data was obtained and is summarized in Table 5.9.
The Type A material shows a very short rupture life (<2 hours) at $2000^{\circ}F$ and
7500 psi stress. In contrast, the Type C material exhibits a rupture life
in excess of 200 hours at $2300^{\circ}F$ and 10,000 psi, and a rupture life greater
than 145 hours at $2400^{\circ}F$ and 10,000 psi. Further stress rupture testing
will be performed during the next reporting period, including the Type D
material.

TABLE 5.9

Effect of Calcium Level and Nitriding Atmosphere
on Stress Rupture Life of Injection Molded Si_3N_4

Mat'l	Wt% Ca	Nitriding Atmosphere	Temp, $^{\circ}F$	Stress, psi	Rupture Life, hrs.
Type A	0.40	N_2	2300	10,000	0
Type A	.40	N_2	2000	7,500	1.8
Type A	.40	N_2	2000	7,500	0.67
Type B	.05	N_2	2200	12,500	0
Type C	.05	1.8% H_2+N_2	2300	10,000	> 200
Type C	.05	1.8% H_2+N_2	2300	20,000	19
Type C	.05	1.8% H_2+N_2	2400	10,000	> 145
Type D	.02	1.8% H_2+N_2	2340	10,000	> 170

123

Creep of Slip Cast Si_3N_4

The slip cast materials were prepared according to procedures described in Section 5.2.4 of this report. Data on nitriding additions and sintered density is given in Table 5.10. All creep tests were conducted in an air atmosphere using 4-point bending, similar to the testing described earlier in this section. The stress reported is the outer fiber tensile stress calculated using elastic theory and the strains are calculated using the measured deflection of the test sample. The test rig used in this work was not the same unit used to study injection molded Si_3N_4. The sample size was smaller (1/8 in. x 1/8 in. x 1-1/2 in. long samples and 3/8 in. x 3/4 in. span lengths), and the technique used to measure deflection of the sample was different. Rather than measuring the deflection directly by using a probe to contact the sample, the deflection was determined by measuring the movement of the load train with an LVDT transformer mounted outside the furnace. These two differences made this test rig less sensitive and creep rates less than 1×10^{-5} in/in/hr could not be determined.

The creep test results are presented in Table 5.11. In general the creep of slip cast Si_3N_4 is very small and superior to that of the injection molded Si_3N_4. It is significant to note that the material with the Fe_2O_3 nitriding addition appears to have the best creep resistance. For example, at a temperature of $2400^\circ F$ and stress of 15,000 psi, no detectable creep of this material was observed after 70 hours. This information, however, does not correlate with engine test results where deformation of rotor tip shrouds was observed [4]. Shrouds with a 1% Fe_2O_3 additive were found to have a gap change of 0.008 inches after 70 hours of engine operation. The stresses in this component are calculated at between 500 and 2000 psi and the part temperature was only $1900^\circ F$. This indicates that possibly another mechanism is causing the deformation of these shroud rings.

TABLE 5.10

Creep Sample Processing History of Slip Cast Silicon Nitride

Code No.	Nitriding Additive	Density
NE8	None	2.69 gm/cm^3
NE9	3% CaF_2	2.65 gm/cm^3
NE10	1% Fe_2O_3	2.72 gm/cm^3
NE12	3% Fe_2O_3	2.72 gm/cm^3

TABLE 5.11

Creep Test Results of Slip Cast Silicon Nitride

Material	Test Temp. ($^\circ F$)	Stress (psi)	Duration of Test (hrs.)	$\dot{\varepsilon}_s$ (in/in/hr)
NE8	2300	10,000	70	1×10^{-5}
NE9	2300	10,000	65	3.5×10^{-5}
NE10	2300	10,000	65	No Detectable Creep
NE10	2400	12,500	70	No Detectable Creep
NE10	2400	15,000	70	No Detectable Creep
NE12	2300	10,000	65	No Detectable Creep

5.2 MATERIAL SCIENCES

SUMMARY

The purpose of detailed investigations into material sciences
is to develop an understanding of material behavior which will
lead to improved material through better control of composition,
processing, and fabrication. This is of particular importance
since the ceramic materials being utilized in turbine engines
are relatively new and appear capable of considerable improvement.
Various phases of the material sciences investigation will be
continued throughout the life of the program.

The wetting of hot-pressed silicon nitride by enstatite com-
position glasses containing Ca, Na, and K was studied to determine the
effect of oxide impurities on the solution-reprecipitation stage of
liquid phase sintering. These impurities improve wetting, lower the
liquid-solid interfacial energy, and increase adhesion. Full densi-
fication apparently results from the diffusion of magnesium from the
grain boundary glass phase into silicon nitride grains.

The effects of sulfur in turbine fuels on the corrosion behavior
of hot pressed silicon nitride have been analyzed. Oxidation-sulfidation
experiments resulted in weight change vs time curves identical to those
obtained in pure dry oxygen at all temperatures.

The use of both small amounts of hydrogen added to the nitriding atmosphere
and iron oxide as a nitriding aid, plus the elimination of particles of silicon
metal greater than 40μ in size from the starting material, has resulted in
reaction sintered silicon nitride of finer grain structure with a 50% strength
improvement.

A considerable amount of process development has been done on slip
cast reaction sintered silicon nitride. Methods were developed for producing
stable slips using fine-grained silicon metal, and the use of alginate skins
on plaster molds was found to be very beneficial in producing good quality
castings. Very high green density specimens were produced by careful control
of casting parameters.

Regarding the status of material science investigations, the micro-
structural characterization of Norton hot-pressed silicon nitride and
silicon carbide is essentially complete. Examination of billet materials
used in stator vane fabrication will continue to insure that initial standards
are maintained. The study of oxidation kinetics in hot-pressed silicon nitride
and silicon carbide will be completed soon in pure oxygen, air, and oxygen,
nitrogen, and sulfur dioxide mixtures. For the vehicular turbine project,
further improvements in the strength of molded reaction sintered silicon nitride
are needed and expected for the multi-density rotor blade. Future work will
concentrate on improving strength through attainment of higher density and
continued optimization of nitriding cycles and atmospheres. These expected
improvements will also provide a greater margin of safety for the nose cone
and the stators.

5.2.1 MICROSTRUCTURE OF HOT-PRESSED SILICON NITRIDE

Introduction

High strength and high density Si3N4 are produced by hot-pressing with 1-5 w/o·MgO additive. The magnesia is thought to react with silica to form enstatite (MgSiO3), which promotes densification by liquid phase sintering. The alkali metal oxides of sodium and potassium together with calcium oxide (an oxide of an alkaline earth metal), collectively referred to here as combined alkaline oxide impurities, have been identified in the grain boundaries where they apparently affect the strength of the material at elevated temperatures. A significant improvement in the high temperature strength and creep resistance is achieved when the final product is shown to contain 200-400 ppm calcium (lower range of HS-130 Si3N4 and experimental materials) as compared to 500-800 ppm calcium which characterizes the upper range of HS-130 silicon nitride or 0.5% calcium in HS-110 silicon nitride. Since hot-pressing experiments with high purity Plessy silicon nitride powder containing < 10 ppm total alkaline oxide impurity (defined in terms of K, Na and Ca) failed to reach high strength or full density, a study was performed to determine the effect of these alkaline oxide impurities on the wetting and viscous behavior of magnesia containing silicate glasses.

The Wetting Behavior of Glass on Polycrystalline Silicon Nitride

Fourteen glass compositions (Table 5.12) were prepared from high purity powders of SiO2 and MgO.* CaO was added as the oxide while the three alkali metal oxides were added in the form of carbonates.** The powders were dry milled with high purity Al2O3 balls for 48 hours and pressed into 0.45 in. diameter buttons which were melted in graphite crucibles in a purified N2 atmosphere at 2820°F. After melting, the buttons were kept at temperature for 2 hours and then furnace cooled. Each family of glass compositions, the glasses containing CaO, for example, were fired separately to avoid cross contamination. Phases were identified by Debye-Scherer powder X-ray diffraction. The exact composition was determined by wet chemical analysis.

Wetting is defined by the contact angle, θ, that a drop of liquid forms at the point of contact with a solid (Fig. 5.23). A non-wetting configuration is one where the contact angle, θ, is equal to, or greater than 90 degrees. When full wetting is achieved, θ = 0. The degree of wetting is determined by the surface forces acting on the system where

$$\cos \theta = \frac{\sigma_{SV} - \sigma_{SL}}{\sigma_{LV}} \tag{1}$$

Here σ_{SV}, σ_{Sl}, and σ_{LV} are the surface energies of the solid-vapor, solid-liquid, and liquid-vapor interfaces, respectively. If $\sigma_{SL} > \sigma_{SV}$, the contact angle can never equal zero. However, when $\sigma_{SV} > \sigma_{SL}$ as it is in liquid phase sintering, the degree of wetting is controlled by the σ_{SL} term. Diffusion, chemical reaction, or mutual solubility at the liquid-solid interface affects the interfacial energy whereby influencing the degree of wetting.

---

* Fisher Scientific S-153 silica, M-51 magnesium oxide and C-117 calcium oxide.
** Cerac P-1049 K2CO3, Johnson Mathery Chemicals Li2CO3 Grade #1 and Na2CO3 Grade #1.

Table 5.12

COMPOSITION AND CONSTITUTION OF $MgO \cdot SiO_2$ BASE GLASSES

Compound	Composition of Mixture wt %			Composition after Melt wt %			Phases Present	
	SiO_2	MgO	Additive	SiO_2	MgO	Additive	Major	Minor
1	60	40	0	60	39.8	0	E	none
			CaO			CaO		
2	59.0	39.0	2.5	59.3	39.2	2.3	E	D,F
3	57.0	38.0	5.0	58.3	37.3	4.6	F	D,E
4	56.0	36.5	7.5	58.0	35.4	7.0	F	D,E
5	55.0	35.0	10.0	56.2	33.4	9.9	D	F,E
			Li_2CO_3			Li_2O		
6	59.0	39.0	2.5	60	37.7	0.8	E	F
7	57.0	38.5	5.0	61.0	37.5	1.7	F	E
8	56.0	36.5	7.5	58.4	36.4	3.5	F	E
			Na_2CO_3			Na_2O		
9	59.0	38.5	2.5	61.2	36.9	1.4	E	F
10	56.0	36.5	7.5	59.2	36.5	4.1	F	E(trace)
11	55.0	35.0	10.0	58.0	36.4	5.5	F	E(trace)
			K_2CO_3			K_2O		
12	59.0	37.5	2.5	61.5	35.8	1.5	F	E
13	57.0	38.5	5.0	60.1	36.1	3.0	F	E
14	56.0	36.5	7.5	57.3	57.3	4.7	F	E

*Phase identification; E = enstatite, D = diopside, F = forsterite.
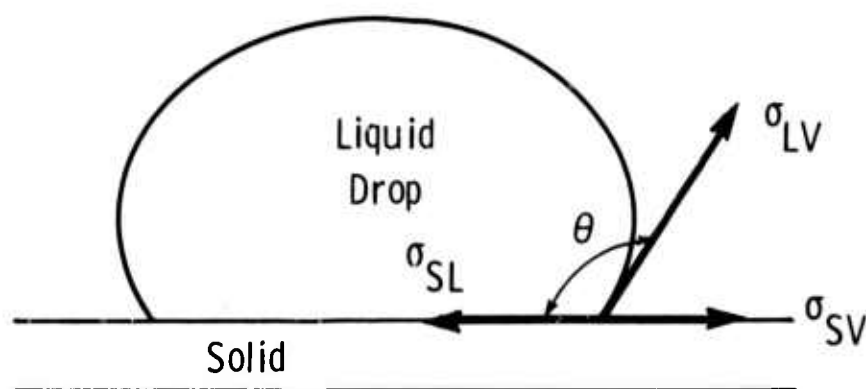
Figure 5.23   Balance of Forces Diagram of Sessile Drop on a Solid Substrate

The apparatus used to measure the contact angle is essentially an instrumented quartz tube which can be evacuated and backfilled with nitrogen as shown in Fig. 5.24. Heat is provided by induction using a boron nitride-lined graphite susceptor which radiates to the test sample. A thermocouple is used to monitor the temperature of the specimen substrate at a location just below the surface under the glass drop. The drops are photographed as silhouettes and contact angles are measured from enlarged prints of the silhouettes ($\sim$ 30X). Small tiles of Norton HS-130 Si_3N_4 containing 300 ppm combined alkaline impurity (Na, K and Ca), 0.5 w/o Fe, 0.8 w/o Al and 0.8 w/o Mg were used as substrate materials. Specimens were outgassed in vacuum and heated to 2370°F in nitrogen. The temperature was increased from 2370 to 3160°F at a controlled rate of 18°F/min.

The experiments were carried out under transient thermal conditions because:

(1) Si_3N_4 is soluble in magnesium silicate. Therefore, continuous surface reaction precludes any possibility of true equilibrium.

(2) Preliminary tests showed that θ is not reversible, i.e., there is absolutely no regression of the liquid glass drop upon cooling.

(3) The behavior of the glass-Si_3N_4 system should be examined under conditions similar to those encountered during hot-pressing where at least partial sintering is observed during controlled heat up.

Chemical analyses indicate that very little change in composition occurred during initial glass preparation (Table 5.12). Therefore, the
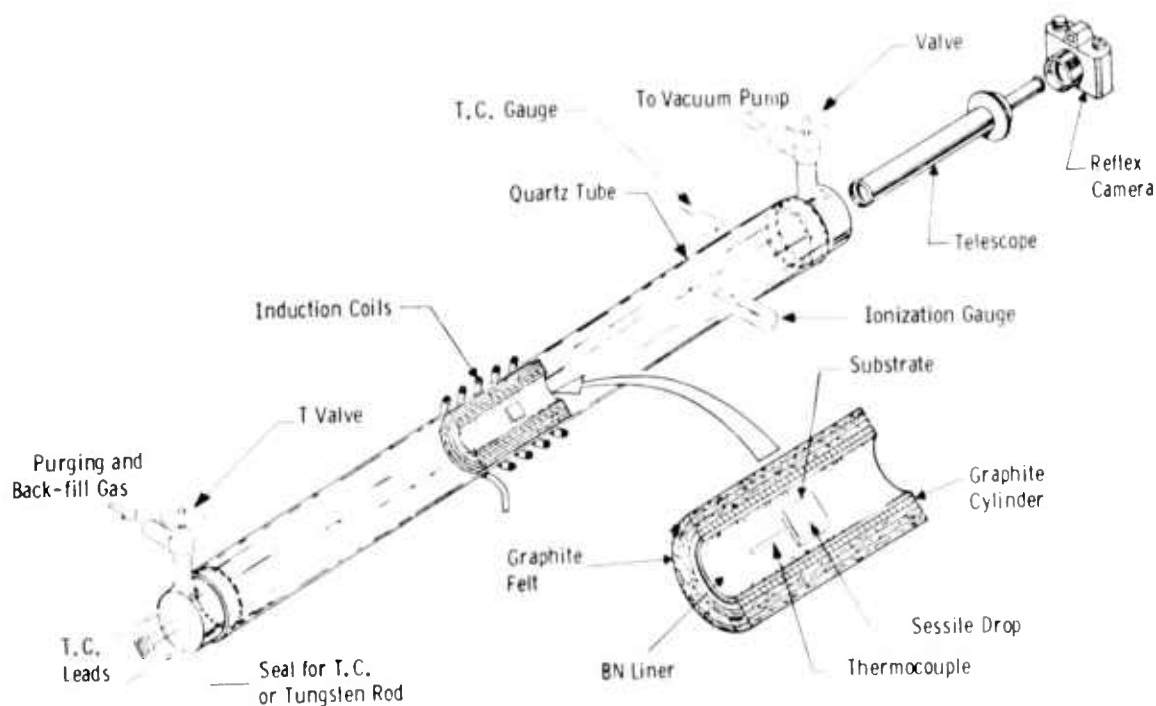
Figure 5.24   Apparatus for the Measurement of Contact Angle

composition of the glass drop was assumed to remain constant during the wetting tests. The X-ray diffraction data are in good agreement with published phase diagrams[6] and show that minute additions of alkaline oxides to pure $MgSiO_3$ result in multiple phase mixtures where enstatite rapidly forms the minor phase.

Typical examples of the sessile drop silhouettes are shown in Fig. 5.25. Wetting improves (lower contact angle) as the amount of CaO in $MgSiO_3$ is increased. The contact angle vs temperature data for all of the compounds studied appear in Fig. 5.26. These demonstrate the strong effect of alkaline oxide impurities on the wetting of Si_3N_4 by magnesium silicate although complete wetting ($\theta = 0$) is never achieved even at the highest temperature. The effect of Li_2O is more pronounced than CaO, although there appears to be a slight decrease in the degree of wetting as the lithium concentration is increased. These alkaline oxide impurities act to reduce the melting point viscosity of silicates.[7]

After reaching the maximum temperature, the furnace was turned down to cool the system at a rate of $140°F/min$. In no case was there a change in the contact angle from the minimum attained at the maximum temperature.

The liquid-solid interfaces were examined by light and scanning electron microscopy. Micrographs of the interfaces are shown in Fig. 5.27a. There is evidence of dissolution at the interface in all three systems. The interfaces are rugged, and, in many areas (arrows), particles of Si_3N_4 appear as inclusions in the glass.

2939°F	2921°F	2822°F
3020°F	2948°F	2975°F
3110°F	3038°F	3092°F
A	B	C
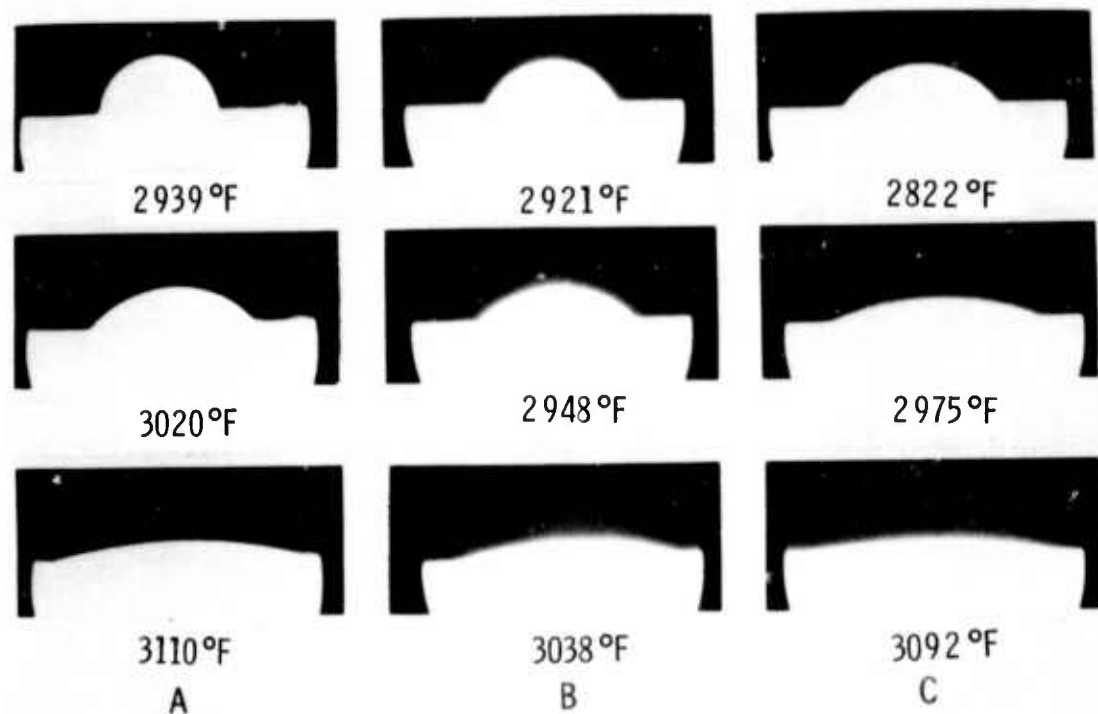
Figure 5.25   The Effect of Temperature and Composition on the Wetting of Si_3N_4 by:

(a) Pure Mg SiO_3
(b) Mg SiO_3 + 2.5% CaO
(c) Mg SiO_3 + 7.5% CaO
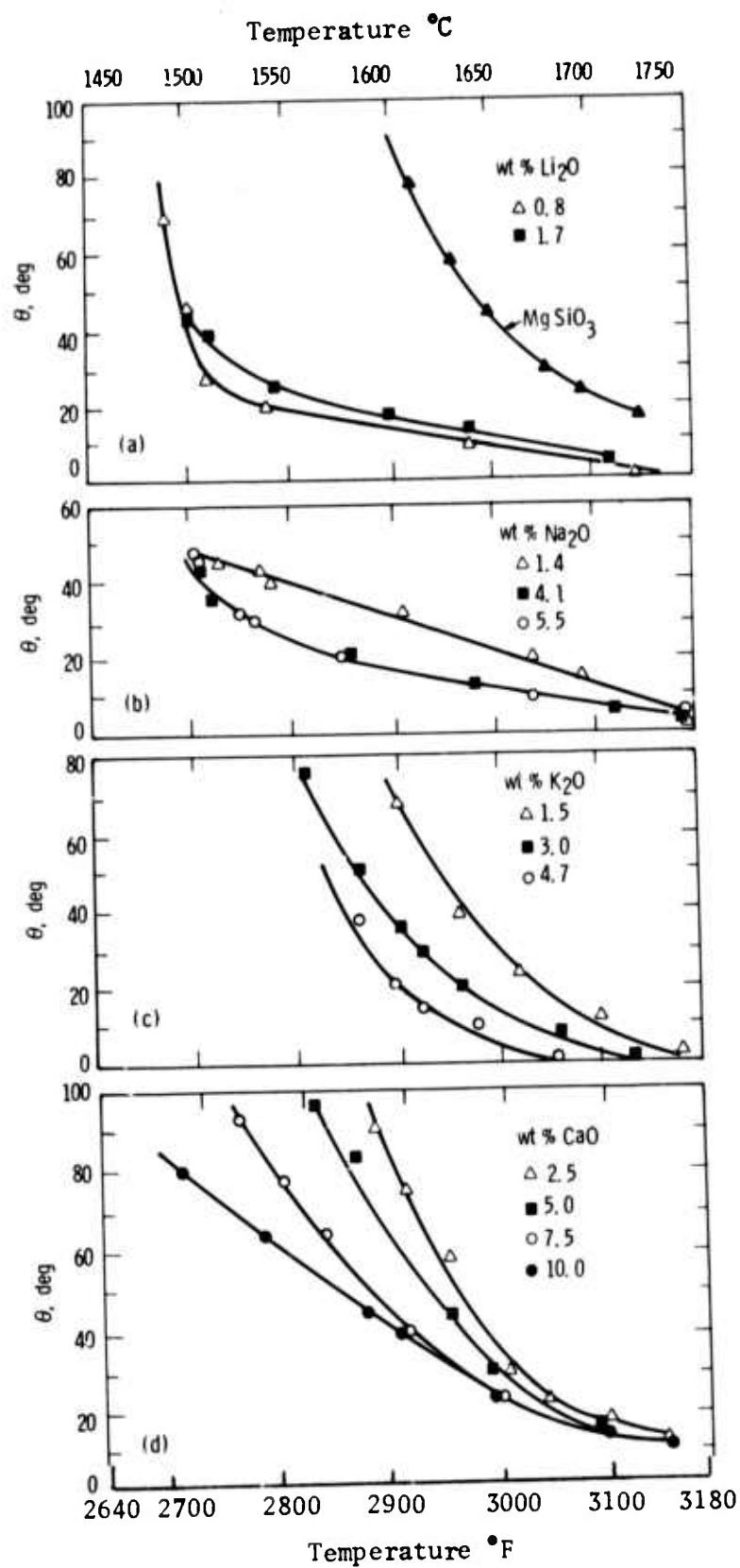
Figure 5.26   The Wetting of Si_3N_4 by $MgO \cdot SiO_2$ as a Function of Temperature and Oxide Impurity
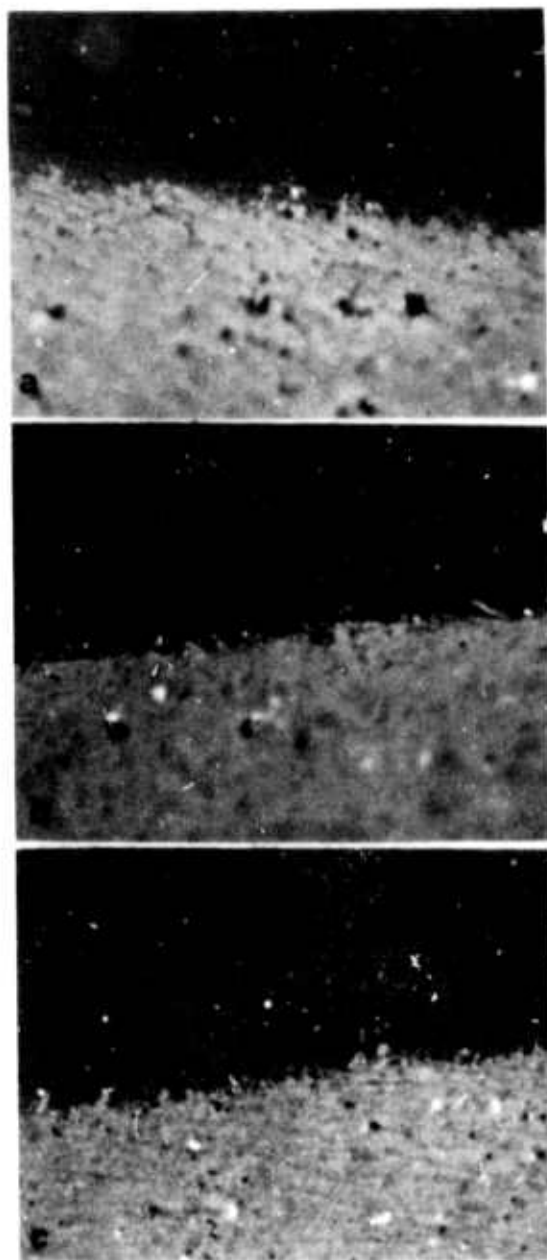
Figure 5.27   Light Micrographs of Transverse Sections Through the Glass-
Si₃N₄ Interface (1000 X)
(a) 38 MgO·57 SiO₂·5 CaO (w/o)
(b) 36.5 MgO·59 SiO₂·7.5 Na₂CO₃ (w/o)
(c) 38.5 MgO·59 SiO₂·5.0 K₂CO₃ (w/o)

The nature of the interfaces are shown in more detail in the scanning
electron micrographs of Fig. 5.28. A reaction zone of about 15 μm is
seen in Fig. 5.28a. The original Si₃N₄ surface is marked by the large
arrows in both micrographs. It is clear that well bonded interfaces
are formed between the silicate glass and the Si₃N₄ substrate.

Energy dispersive X-ray analysis was used to determine the
distribution of elements across the interface. Readings were made at
various points along the marked line in Fig. 5.28a. The results are
summarized in Fig. 5.29. Magnesium and, to some extent, calcium have
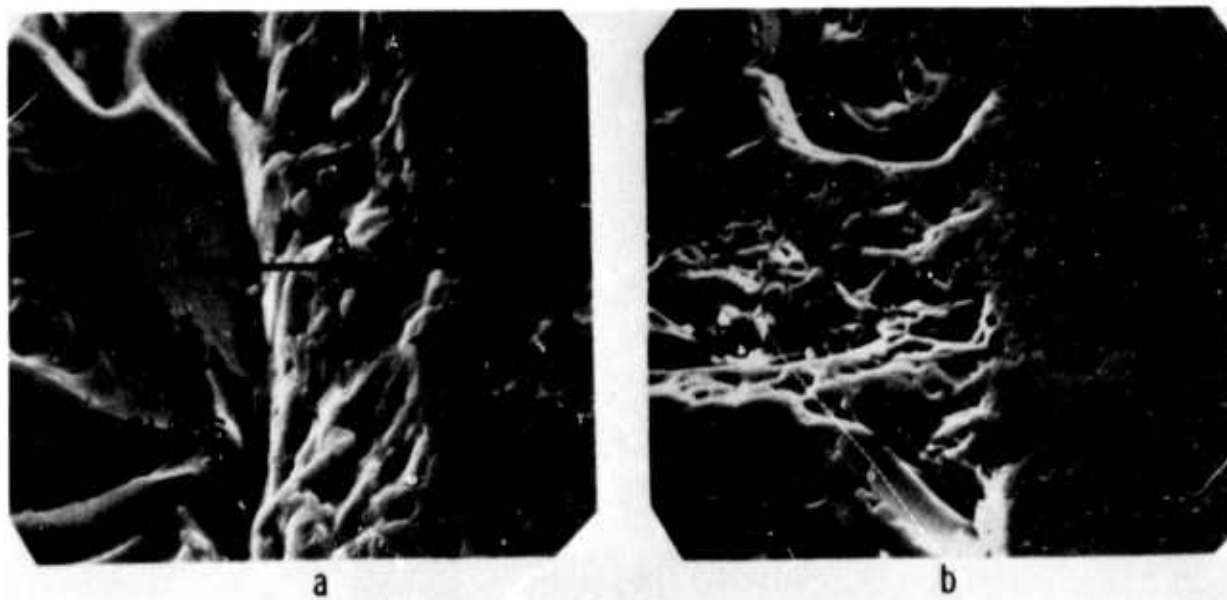
Figure 5.28   Scanning Electron Micrographs Showing the Glass-Si_3N_4
Interface for:
(a) 35 $MgO \cdot 55$ $SiO_2 \cdot 10$ CaO (w/o)
(b) 38.5 $MgO \cdot 57$ $SiO_2 \cdot 5$ K_2CO_3 (w/o)
(Original Si_3N_4 Surface Marked by Arrows, 10 μm Scale)
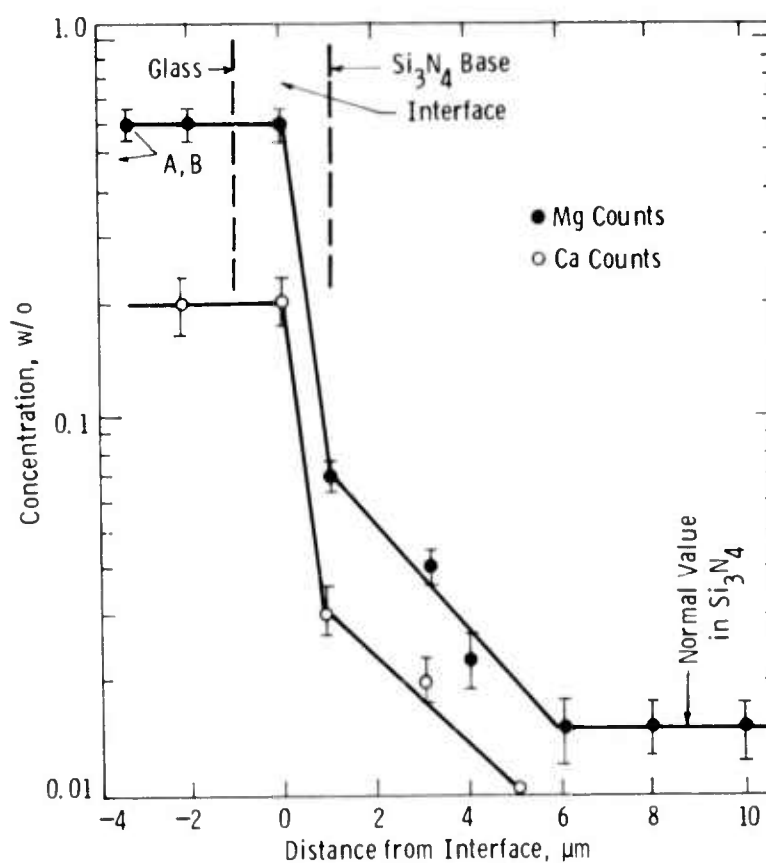
Figure 5.29   Mg and Ca Concentrations in 35 Mg·55 $SiO_2 \cdot 10$ CaO Along the
Trace in Figure 5.28

diffused into the Si_3N_4 substrate. This phenomenon is demonstrated again in Table 5.13 where count readings at the various points marked in Fig. 5.28a are summarized. The readings support the identification of the original Si_3N_4 surface as marked and show that diffusion of Mg into the Si_3N_4 does occur, apparently, for all silicate systems.

Systems richer in SiO_2 were examined also, specifically; 80 SiO2 - 20 MgO, 95 SiO2 - 5 MgO and 95 SiO2 - 5 CaO glass mixtures. Poor wetting was observed with all three systems at temperatures up to 3270°F. However, interfacial reactions similar to those whicn characterize the $MgSiO_3$-base systems (Fig. 5.28) must have occurred with the high SiO_2 systems. These are illustrated in the three SEM micrographs of Fig. 5.30. Well bonded interfaces are seen in Figs. 5.30a and b, although poor wetting is clearly visible at the left edge of Fig. 5.30a. The original Si_3N_4 surface (marked by the dotted lines) was determined by energy-dispersive X-ray analysis. Magnesium has diffused across the interface.

A somewhat rougher interface is seen in the $SiO_2 \cdot 5$ CaO system (Fig. 5.30). The general appearance is that of a well bonded interface. It seems, therefore, that the glass-substrate interfacial reactions are mainly the result of dissolution of Si_3N_4 in SiO_2 base glasses.

Time is significant in the development of the wetting angle, specifically, where strong surface reactions are involved. It was essential, therefore, to determine the development of wetting as a

Table 5.13

ENERGY DISPERSIVE X-RAY COUNT RATIOS FOR
Mg/Si AND K/Si, SYSTEM #13, FIG. 6b (CORRECTED FOR BACKGROUND)

Point #	Mg/Si	K/Si
1	0.61	0.008
2	0.55	0.007
3	0.62	ND
4	0.01	ND
5	0.61	0.009
6	0.03	ND
7	0.02	ND
8	0.01	ND
9	0.01	ND

ND = not detected
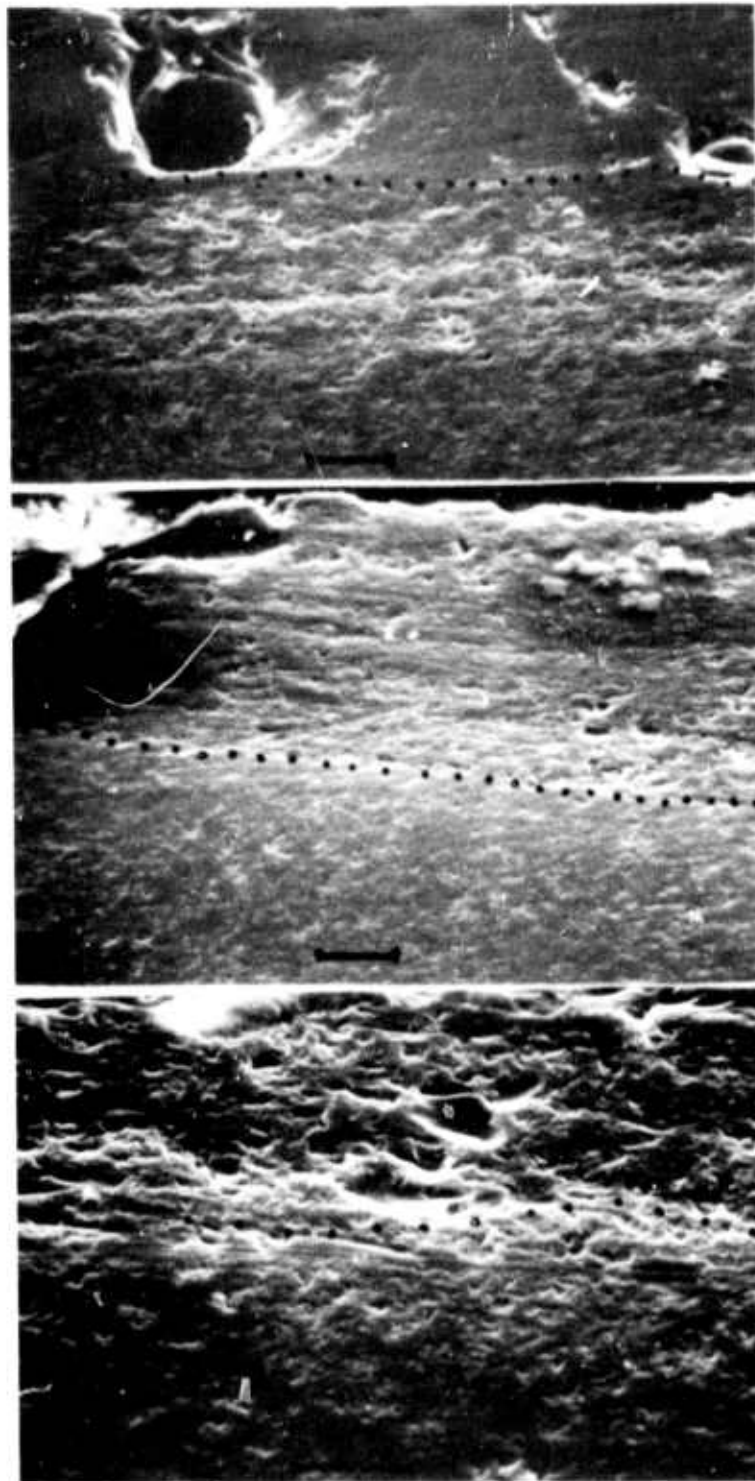
Figure 5.30   SEM Micrographs of Transverse Sections Through the Glass-
               Si_3N_4 Interface for:
                           (a) 80 SiO_2·20 MgO
                           (b) 95 SiO_2·5 MgO
                           (c) 95 SiO_2·5 CaO
               (Dotted Lines Mark Original Si_3N_4 Surface, 20 μm Scale)

134

function of time under isothermal conditions. No detectable time effect was observed for the $MgSiO_3$-Si_3N_4 system at 3130°F. A constant wetting angle was achieved quickly at 1910°F (Fig. 5.31). The $MgSiO_3 \cdot 5.2$ w/o K_2O system exhibited a large drop in the wetting angle during the first minute but an equilibrium angle was achieved in less than one minute even in this case. The interfacial reactions, apparently, occur rapidly and do not affect the wetting after the first minute or so.

Few correlations of general nature have been reported between cos θ and the energy terms in Eq. (1). Zisman[8] showed that cos θ increases linearly with the decreasing surface energy of the liquid. This relation holds for a series of homologous liquids at constant temperature. Rhee[9] found a linear relationship between cos θ and temperature. He suggested that this rate is applicable to many liquid metal-ceramic systems.
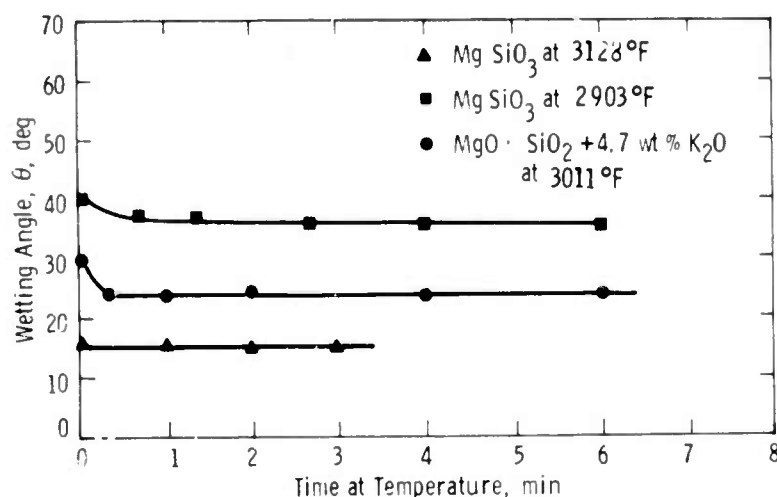
Figure 5.31   Wetting Angle as a Function of Time at Constant Temperature

Cos θ is plotted as a function of alkaline oxide addition in Fig. 5.32 where the data indicate a linear dependence of cos θ on alkaline oxide additions. The four lines in the figures extrapolate to two common points which agree well with the value of cos θ for the pure $MgSiO_3$ system. These results support the data in Fig. 5.26. Using data from Fig. 5.26:

$$\cos \theta = A + BXa \qquad (2)$$

where Xa is the fraction of alkaline oxide addition, A is the value of cos θ for pure $MgSiO_3$ and B is the slope of the line. The additions of alkaline oxide should not affect the solid-vapor energy at a constant temperature and σ_{SV} (Eq. (1)) should remain constant for the series of tests represented in Fig. 5.32. Under these conditions, Eq. (1) may be rewritten in the form;

$$\cos \theta = A' - B' \sigma_{SL} \qquad (3)$$

and combined with Eq. (2) to give;

$$\sigma_{SL} \approx \alpha - \beta Xa. \qquad (4)$$

135

which indicates that alkaline oxide additions dc affect the solid-liquid interfacial energy. The energy term controls the wetting behavior of the silicate glasses on Si_3N_4.
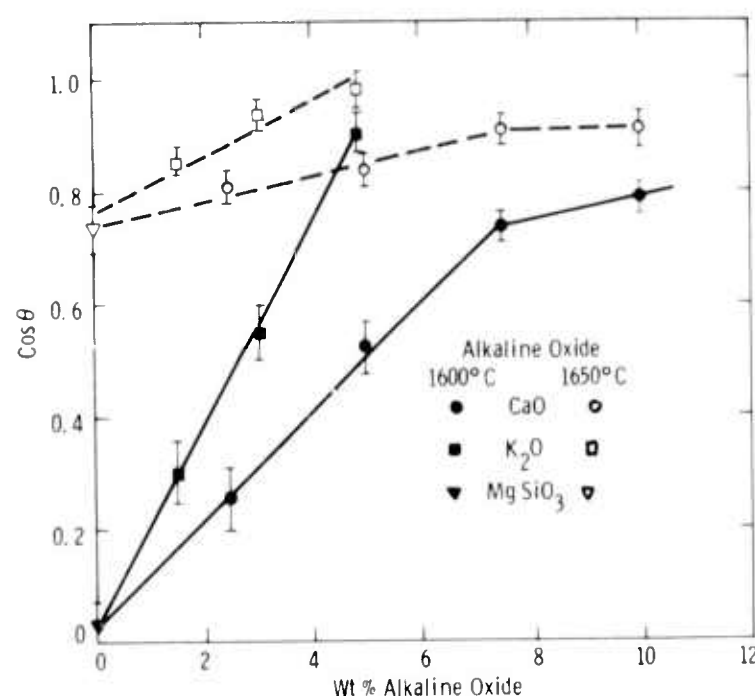
Figure 5.32   Cos θ as a Function of Oxide Content

Similar reasoning can be applied to the work of adhesion, W_A, which defines the work necessary to separate the liquid from the solid. W_A should be a measure of the strength of the liquid-solid interface where;

$$W_A = \sigma_{SV} + \sigma_{LV} - \sigma_{SL} \qquad (5)$$

If σ_{LV} and σ_{SV} are constant:

$$W_A \approx \alpha + \beta Xa \qquad (6)$$

An increase in the strength of the liquid-solid interface due to the addition of alkaline oxides to the magnesium silicate glass is indicated.

The degree of dominance of the rearrangement stage during liquid phase sintering depends on the volume fraction of the liquid. When the volume fraction of the liquid is less than 5%, the amount of shrinkage due to rearrangement is negligible.[10]   In the case of hot-pressed Si_3N_4, the volume fraction of the liquid glass does not exceed 5%. Therefore, rearrangement cannot be considered a significant factor in the densification of Si_3N_4. The process appears to be one of solution-reprecipitation where the rate of densification is controlled by the solution rate of the solid at the liquid-solid interface. Dissolution of the solid at the liquid-solid interface during hot-pressing is demonstrated in Figs. 5.27, 5.28 and 5.30.

The solution and reprecipitation process depends on a low contact angle, θ, and a low dihedral angle, φ. Alkaline oxides lower the contact

136

angle as demonstrated in Fig. 5.26. The dihedral angle given by:

$$\cos \frac{\phi}{2} = \frac{\sigma_{gb}}{2\sigma_{SL}} \, ,$$
(7)

where σ_{gb} = grain boundary energy

is a measure of the degree of intergranular penetration by the liquid phase
Even though ϕ cannot be measured reliably because of the very small grain
size in Si_3N_4, it is clear from Eq. (7) that a decrease in the liquid-
solid interfacial energy should have a significant effect on the liquid
sintering process.

Since Mg diffuses from the liquid phase into solid Si_3N_4, final
densification may result from diffusion whereby Mg ions are accommodated
within the Si_3N_4 structure.

This investigation suggests that full densification can be achieved
by Mg diffusion into the Si_3N_4 grain. A certain amount of alkaline oxide
impurity may be required to create a strong cohesive structure. An
optimum level of alkaline oxide impurity has not been determined, however.

5.2.2 GAS-SOLID REACTIONS

Introduction

The investigation of kinetic processes involved in the static oxidation and sulfidation of silicon nitride and silicon carbide is continuing. This section discusses the possible effects of sulfur in turbine fuels on the corrosion behavior of hot-pressed silicon nitride.

Composition of Combustion Gases in a Stationary Gas Turbine

The diesel fuel used in stationary gas turbines has a carbon to hydrogen ratio of approximately 1:1.78. In turbine operations at 10 atm total pressure, air to fuel ratios approximate 50:1 (by weight). If a fuel contains 0.5 wt % sulfur (a value considered characteristic of heavy residual fuels), the partial pressures of various species in the combustion gases (assuming complete combustion of the fuel) may be calculated in accordance with the following reactions:

$$CH_{1.78} + 1.445\ O_2 + N_2 \rightarrow CO_2 + 0.89\ H_2O + N_2 \tag{1}$$

$$1/2\ S_2 + O_2 \rightarrow SO_3 \tag{2}$$
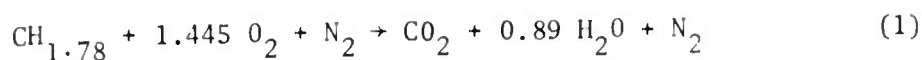
Partial pressures for the various species in the combustion gases are listed in Table 5.14. A further assumption that the oxidation of SO_2 to SO_3, according to reaction

$$SO_2 + 1/2\ O_2 \rightarrow SO_3, \tag{3}$$
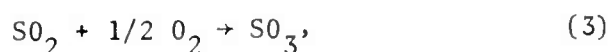
TABLE 5.14

CALCULATED PARTIAL PRESSURES OF VARIOUS SPECIES IN THE
COMBUSTION GASES IN A GAS TURBINE AT A TOTAL PRESSURE OF 10 atm

Species	Partial Pressure, atm
Nitrogen (N_2)	7.75
Oxygen (O_2)	1.47
Carbon dioxide (CO_2)	0.41
Water vapor (H_2O)	0.36
Sulfur dioxide (SO_2)	8.8×10^{-4}
Sulfur trioxide (SO_3)*	7.6×10^{-3}

*Equilibrium pressure at 1300°K.

138

is catalyzed by various metallic structural parts of the gas turbine leads to the calculation of the equilibrium SO_3 pressure corresponding to SO_2 and O_2 partial pressures in the combustion gases. This equilibrium SO_3 pressure at 1300°K also appears in Table 5.14. It is clear from Table 5.14, that the combustion gases are highly oxidizing and the SO_2 and SO_3 pressures in the turbine can be appreciable when high sulfur fuels are used.

Thermochemistry of the Si-0-S System

The only solid compound reported between silicon and sulfur is silicon disulfide (SiS_2) which melts at 1363°K. The free energies of formation ($\Delta G°$) of the various solid phases in the Si-0-S system are listed in Table 5.15. These thermodynamic data were used to construct the thermochemical phase diagram for the Si-0-S system shown in Fig. 5.33 where the partial pressure of sulfur (S_2) is plotted against the partial pressure of oxygen (O_2) on a logarithmic scale. The SO_2/SO_3 pressure ratios corresponding to various oxygen partial pressures are also shown. The various lines in the diagram separate the regions of existence for $Si(s)$, $SiS_2(s)$, and $SiO_2(s)$.

The SO_2, SO_3, and O_2 partial pressures in a gas turbine correspond to a log ρS_2 value of about -25.6 at 1300°K. It is evident from the thermochemical phase diagram, that, at these log ρS_2 and log ρO_2 values, the stable equilibrium species over silicon is silicon dioxide (SiO_2). The case for silicon nitride should be similar. Therefore, since it is thermodynamically impossible for $SiS_2(s)$ to form over Si_3N_4 in the highly oxidizing turbine environment, the scale must be $SiO_2(s)$.

TABLE 5.15

THERMOCHEMICAL DATA FOR THE Si-0-S SYSTEM

Species and Compounds	Standard Free Energy of Formation at 1300°K, (ΔG_f), cal/mol	Reference
$Si_3N_4(s)$	-75,161	11
$SiC(s)$	-15,085	12
$SiO_2(s)$	-162,207	12
$SiS_2(s)$	-33,244	13
$SiS(g)$	-12,194	13
$SO_2(g)$	-63,840	12
$SO_3(g)$	-58,426	12
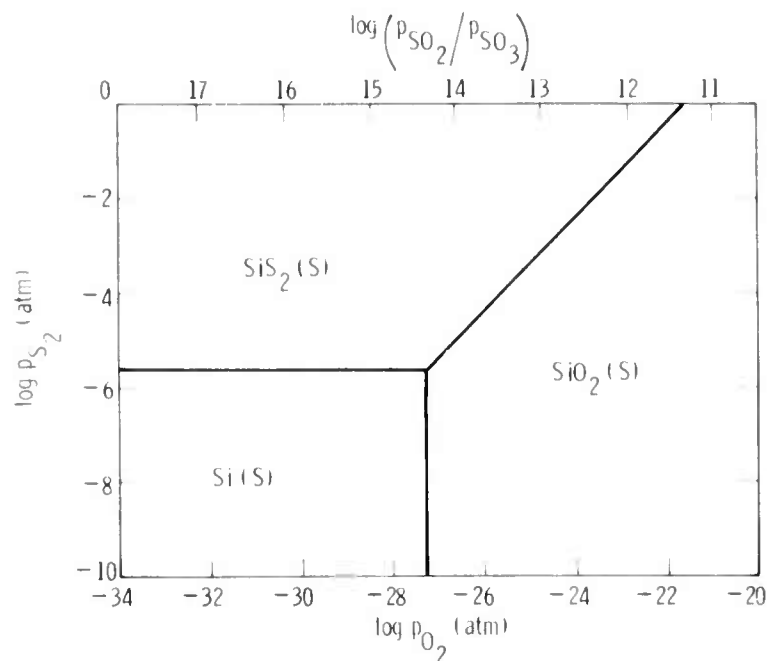
Figure 5.33   Thermochemistry of the Si-O-S System at 1300°K

It may be possible to form $SiS_2(s)$ over Si_3N_4 by the reaction:

$$Si_3N_4 + 6\ SO_2 \rightarrow 3\ SiS_2 + 2\ N_2 + 6\ O_2 \qquad (4)$$

However, the free energy (ΔG) for this reaction is highly positive at all temperatures of interest. For example, at 1300°K and at the partial pressures listed in Table 5.14, a free energy of +486 kcal is calculated. Therefore, $SiS_2(s)$ will not form.

Formation of SiS(g)

Silicon monosulfide (SiS) gas can form according to the reaction:

$$Si_3N_4 + 3\ SO_2 \rightarrow 3\ SiS(g) + 2\ N_2 + 3\ O_2 \qquad (5)$$
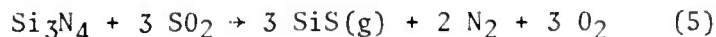
However, the partial pressure of SiS(g) formed by this reaction is only 5×10^{-16} atm at 1300°K when calculated from the appropriate SO_2, N_2, and O_2 partial pressures (Table 5.14). These extremely low SiS(g) pressures should not affect the oxidation kinetics of Si_3N_4 to SiO_2. Moreover, the formation of a $SiO_2(s)$ layer on the surface of Si_3N_4 during the initial stages of oxidation will further suppress the formation of SiS(g) according to reaction (5). Therefore, the formation of SiS(g) is of no consequence in the corrosion behavior of hot-pressed Si_3N_4 in industrial gas turbines.

Static Oxidation-Sulfidation of Si₃N₄

The simultaneous oxidation-sulfidation kinetics for Norton's HS-130 hot-pressed Si_3N_4 were studied by continuous thermogravimetry using an automatic Cahn electrobalance and procedures described previously.[2] Si_3N_4 specimens, 1/2" x 1/2" x 0.070" were suspended from the Cahn electrobalance with a sapphire fiber and held at temperature in a

140

flowing atmosphere of N_2, O_2, and SO_2. All experiments were carried out at 1 atmosphere total pressure using the following gas mixture:

N_2 89.91%

O_2 10.00%

SO_2 0.09%

A platinum wire mesh was placed in the hot zone of the reaction tube to catalyze the formation of SO_3 from SO_2. This gas mixture corresponds to a SO_2/SO_3 pressure ratio of about 25.7 at 1300°K, which is several times higher than that expected in a gas turbine even with very high, sulfur-containing, heavy residual fuels. For example, the SO_2/SO_3 ratio calculated for the gas turbine using 0.5 wt % S fuel is only about 0.116 as shown in Table 5.14.

The oxidation sulfidation experiments were performed at temperatures in the range 1800 to 2500°F. The weight gain vs time curves at all temperatures followed a parabolic behavior. The oxidation curves were identical to those obtained in pure dry oxygen.[4] The magnitude of oxidation in the oxidizing-sulfidizing gas mixture was found to be the same as that in pure oxygen within the limits of experimental uncertainty. X-ray diffraction analysis of the oxidized surfaces indicated the presence of α-cristobalite (SiO_2) with traces of silicon oxynitride (Si_2ON_2). Silicon disulfide (SiS_2) was detected confirming the results of the thermodynamic calculations. Therefore, the oxidation behavior of hot-pressed Si_3N_4 in very high sulfur fuels is expected to be similar to that observed in pure oxygen.

5.2.3 DEVELOPMENT OF INJECTION MOLDED SILICON NITRIDE

In the last report [4], experiments aimed at increasing the strength of injection molded Si_3N_4 were described. In this section, further experiments with the same objective are described. The effect of hydrogen additions to the nitriding atmosphere will be discussed in relation to the strength and creep properties of Si_3N_4. The effect of varying the particle size distributions of starting silicon metal powder, and the effect of an Fe_2O_3 nitriding additive on the strength of Si_3N_4 will also be covered.

Effect of Nitriding Atmosphere

It has been shown [4] that hydrogen additions to the nitriding atmosphere are beneficial to the strength of Si_3N_4. Figure 5.34A shows that as the
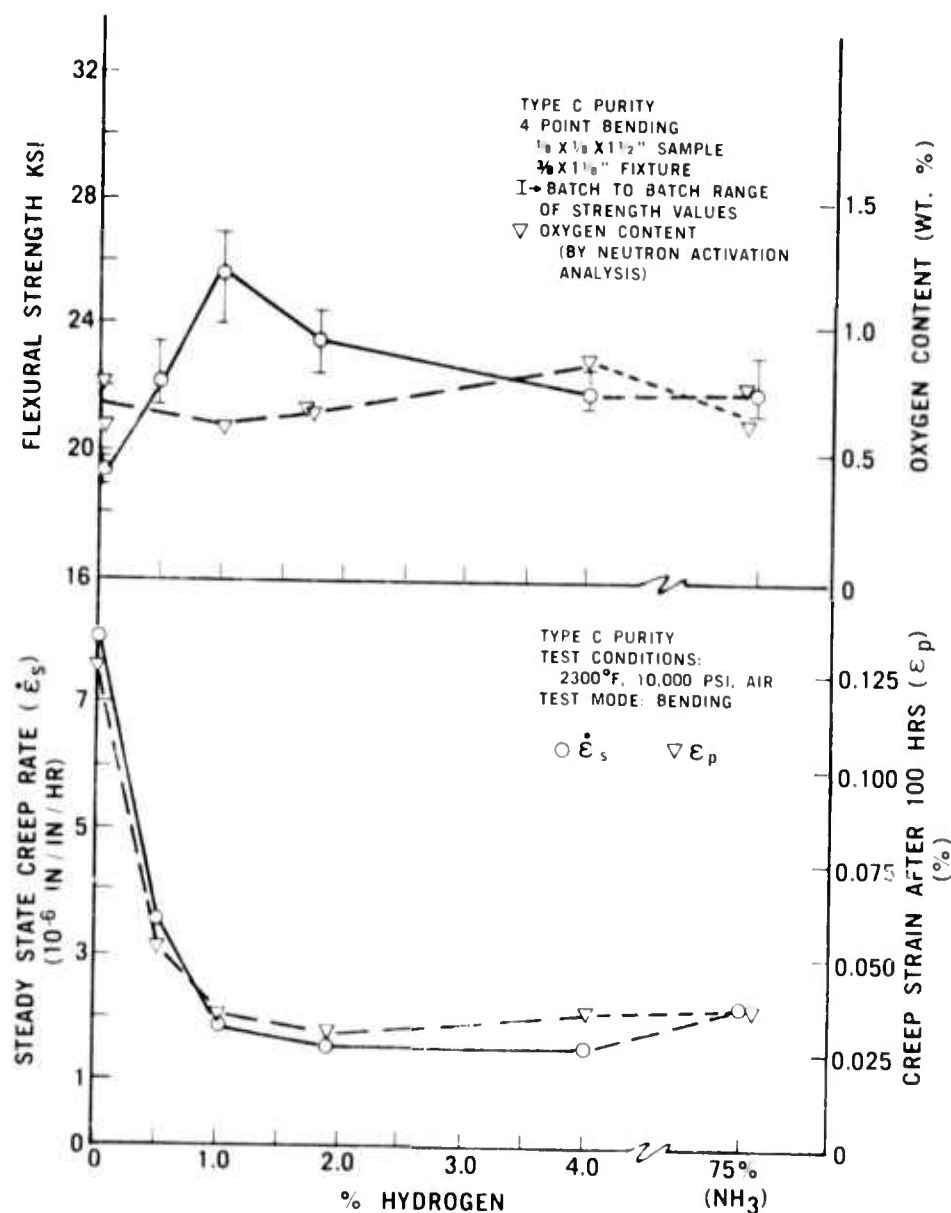
Figure 5.34   Flexural Strength, Oxygen Content, and Creep Properties of Injection Molded Silicon Nitride as the Amount of Hydrogen Added to the Nitriding Atmosphere

hydrogen concentration of the nitriding atmosphere is increased to 1%, the strength increases and reaches a maxium. The strength at this level show a batch-to-batch variation between 24,000 psi and 27,000 psi with an average value of 25,500 psi. This amounts to a 30 percent increase over the strength of material reaction sintered in nitrogen only. This data was obtained using silicon metal powder having Type C purity [4].

The oxygen content of these samples was measured by neutron activation analysis at AMMRC. Figure 5.34A also shows that the oxygen level was essentially unaffected by changes in hydrogen concentration. This fact tends to discount the hypothesis that hydrogen reduces oxide films formed on the silicon. It has been observed for the 1.8% H_2 level that a finer grain structure is developed as a result of the hydrogen treatment (described in Section 5.1.2 of this report). Thus, this increase in strength can probably be attributed to the reduction in grain size of the silicon nitride.

The creep properties as a function of hydrogen concentration in the nitriding atmosphere are shown in Figure 5.34B. As shown, the steady state creep rate and percent creep strain decrease with increasing hydrogen content and reach a minimum between 1-2% hydrogen. More detailed properties of the 1.8% H_2 level are given in Section 5.1.2 of this report, along with a proposed explanation of the mechanism involved.

In summary, the maximum strength and maximum creep resistance can be obtained simultaneously by using a nitriding atmosphere containing 1-2% hydrogen.

Effect of Silicon Metal Particle Size

Messier [14] noted that reducing the maximum particle size of the starting silicon metal powder resulted in a substantial strength increase of the resulting silicon nitride. Experiments were performed to verify this work with regard to injection molded Si_3N_4.

Silicon metal powder was air classified into various size ranges by removing the coarse fraction. Figure 5.35 shows the particle size distribution as determined by x-ray sedimentation of the starting feed material and the various classified batches. Each of these materials was then processed into a standard injection molding batch. No molding problems were encountered with either the standard or the 40μ material. The 30μ batch had to be blended with an increased amount of organic molding compound in order to mold properly. This resulted in a lower solids content and consequently lower green and fired densities. The 20μ material could not be molded under any reasonable conditions.

The three moldable batches were nitrided using a 1% H_2/N_2 atmosphere. The results in Table 5.16 show the 40μ material yielded a 10 percent higher strength. The test sample size was 1/8 in. x 1/8 in. x 1-1/2 in. long and four point bending was used with fixture knife edge spacings of 3/8 in. x 1-1/8 in; this same procedure was used for other strength measurements reported in this section.

The addition of Iron Oxide (Fe_2O_3) has been found to improve the properties of slip cast grade Si_3N_4 (Section 5.2.4 of this report). Test samples were fabricated using additions of 1% and 3% Fe_2O_3 with injection molding grade silicon metal. These samples were processed using a 1% H_2/N_2 atmosphere. Strength results are shown in Table 5.17. A 14 percent increase in strength

143

was obtained with the 3% Fe_2O_3 composition. Visual observation attributed this increase to an improved surface condition. The material appeared dense, and lacked the large surface porosity normally associated with typical injection molded Si_3N_4.

Samples were next made using a combination of all the improved processing techniques; -40µ silicon metal, 3% Fe_2O_3 additive and a 1% H_2/N_2 nitriding atmosphere. The physical properties of the resulting material are characterized in Table 5.18. As shown, a 50% strength improvement was realized over the baseline Si_3N_4 material, (100% N_2 atmosphere, shown in Figure 5.38A) and a 70% strength increased was obtained relative to standard injection molded material [3].
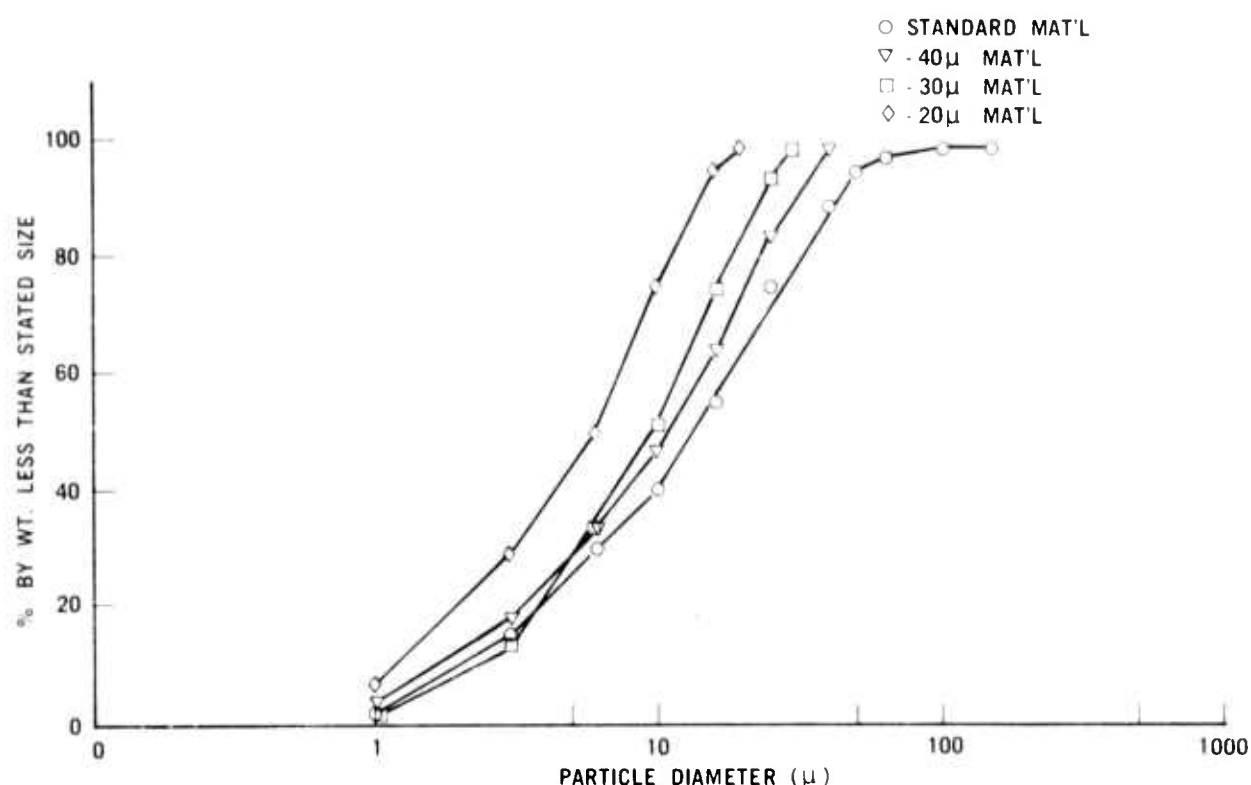
Figure 5.35   Particle Size Distribution of Silicon Metal Powders

TABLE 5.16

Effect of Particle Size Distribution on Strength
of Injection Molded Silicon Nitride

Material	Volume % Solid	Strength*	% Strength Change
Standard	62	24,150 psi	-
-40µ	62	26,600 psi	+10%
-30µ	60	22,250 psi	- 8%
-20µ		could not injection mold.	

* 1/8 x 1/8 x 1-1/2" test bars; four point loading; 3/8 x 1-1/8" fixture.

144

TABLE 5.17

Effect of Iron Oxide Additions on Strength of Injection Molded Si_3N_4

Material	Density	Strength*	% Strength Increase
No additive	2.34 gm/cc	22,300 psi	-
1% Fe_2O_3	-	22,950 psi	3%
3% Fe_2O_3	2.37 gm/cc	25,500 psi	14%

*Same bending test conditions as in Table 5.16

TABLE 5.18

Properties of Improved Injection Molded Silicon Nitride

Strength	29,700 ± 2,200 psi
Weibul Modulus	22
Density	2.33 gm/cm^3
Elastic Modulus	16 x 10^6 psi
Phase Analysis	75% α , 25% β Si_3N_4

5.2.4 DEVELOPMENT OF SLIP CAST SILICON NITRIDE

Introduction

The increased demand for reaction sintered silicon nitride as a high temperature material has focused attention on the development of silicon metal powder forming processes. These processes must be capable of producing complex shapes with properties that meet engineering design specifications. One forming technique that has received little attention in the past is slip casting. This process is used extensively in the ceramic industry to consolidate ceramic powders to high green densities.

Recently, investigators have demonstrated that metal powders such as copper, molybdenum, tungsten, and stainless steel can also be slip-cast [15]. In view of the extensive use of slip casting in the ceramic industry and recent developments in powder metal technology, slip casting is being developed as a viable forming process for silicon nitride.

The slip cast process consists of pouring a stable suspension of powder, called the slip, into an absorbant mold which represents the negative of the object being formed. The mold, through capillary action, absorbs the liquid fraction of the slip, leaving a coherent casting that has sufficient handling strength. The casting is subsequently dryed and sintered to give the component its final properties. Figure 5.36 schematically describes the basic slip casting process.

There are two major slip casting techniques, casting of solid parts and parts and drain casting of hollow parts. Solid castings are made by continuously replacing the absorbed liquid fraction with additional slip until a solid article is formed. Hollow castings are made in a similar
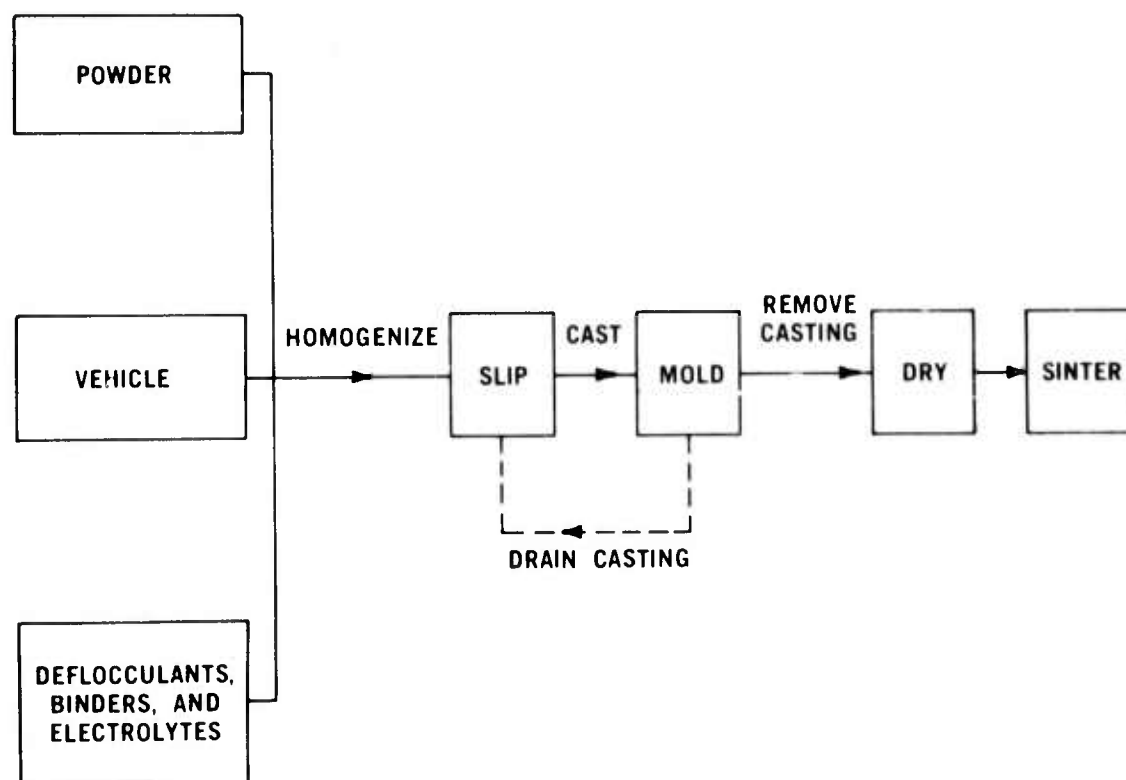
Figure 5.36   The Slip Casting Process

fashion; however, excess slip is poured out of the mold after the article as reached the desired wall thickness.

Metal Powder Slip Casting

There are many factors that affect the casting characteristics of a metal slip system; some of the more significant ones will be discussed. The critical areas that must be controlled are the properties of the metal powder, the properties of the liquid media, and the rheological additives. Many of the variables are closely related and difficult to treat independently. The important parameters of the metal powder are: 1) particle size, 2) particle reactivity, 3) particle size distribution and 4) particle shape.

The particle size and particle reactivity determine the mechanism by which a stable suspension is achieved. Suspension mechanisms are catagorized as either physical or chemical. Large (>10 microns) or high specific gravity powders require special gelling additives which physically hold the particles in suspension. High viscosity slips and low density castings are generally associated with physical suspensions. Chemical suspensions are those whose rheological properties are largely controlled by ionic interactions between the liquid and solid phase. To produce a chemical suspension the powder particles must fall within a size range where surface forces such as London-van der Waals, rather than gravity, govern their behavior. For most metals, a chemical suspension can be obtained if the bulk of the particles fall in the size range of 1-10 microns [15]. In addition to size, the surface of the particles must be such that electrical double layers, as described by Helmholtz and later by Gouy and Stern, [16] can be established. Oxide layers that form on most metals provide the means for establishing the electrical double layers, thereby creating the repulsive forces between particles necessary to establish a suspension. The oxide skin is generally a "loose" structure of the metal oxide. Under certain conditions this skin can partially or totally dissolve, can increase in volume, or can even change in type [17]. These modifications in the oxide skin can exert considerable influence on the forces that govern the suspension and thereby cause sudden undesirable rheological changes.

The particle size distribution is also an important parameter. High density castings require that voids between larger particles be filled with smaller particles; therefore, the particle size distribution must be controlled to obtain the desired particle packing efficiency. The particle size distribution also has a profound effect on casting behavior. For example, a casting composed of too many fines may crack on drying, whereas a casting with a high coarse fraction may not have sufficient drying shrinkage to facilitate extraction from the mold. The selection of an appropriate particle size distribution is essentially an emperical process, and certain compromises between casting behavior and casting properties may be necessary.

Particle packing efficiency and particle surface area are the prime factors when considering particle shape as a determining factor on the properties of a slip and the resulting casting.

The main requirements for a vehicle (liquid media) are: 1) ability to wet the metal powder, 2) chemical stability, and 3) viscosity.

To formulate a castable slip the powder particles must be perfectly wetted by the liquid fraction of the slip. Wetting agents can be used to achieve this condition. For efficient particle packing (high density) the

vehicle must provide effectual particle mobility and lubrication. The liquid must be as inactive with the metal powder as possible in order to avoid adverse reactions with the oxide skin. While water is the most commonly used vehicle, certain alchohols and other organic fluids have been used.

Special rheological additives are used to neutralize those factors which case inhomogeneity in a slip. Deflocculating agents are added to create repulsive forces necessary to establish a suspension around each particle in the vehicle. Elecrolytes such as nitric acid, sulfuric acid, and sodium and ammonium hydroxide are used to alter the ion concentration of the slips. A desisive relationship has been demonstrated [15] between the ion concentration and the viscosity of the slip. The physical properties of the cast article are also dependent upon this relationship.

Silicon Metal Slip Casting

The density of silicon nitride is directly proportional to the density of the initial silicon metal compact. High green densities are generally required because engineering properties such as strength increase with increasing Si_3N_4 density. Although the green density of a casting can be controlled by both physical and chemical suspensions, the latter when properly formulated has the inherent ability for producing higher green densities.

A chemical suspension was produced using: 1) finely divided silicon metal 2) 0.01-.06 w/o of an alkaline deflocculant 3) distilled water as the vehicle and 4) electrolytes such as nitric acid and ammonium hydroxide.

Silicon Raw Material Preparation

The as-received silicon metal was a nominal 325 mesh powder which was too coarse for establishing a chemical suspension. The powder was comminuted by dry milling in a porcelain mill with high density alumina balls. Table 5.19 summarize the chemistry of the milled silicon powder and Figure 5.37 illustrates its particle size distribution as determined by x-ray sedimentation. Practicality precluded considering particle shape as a parameter because of the expense and difficulty associated with the manufacture of silicon powders of varying shapes. Powder comminuted under the conditions described produced typical particle shapes shown in the photomicrograph of a heat treated silicon metal casting that is discussed later in this section (see Figure 5.45). The characterized silicon metal powder will be referred to as 5.5 micron powder (mean particle size by weight on the distribution curve shown in Figure 5.37).

Plaster Molds

The pottery plaster molds used in casting were made with a 1.33 plaster-water ratio. Conventional techniques were used in the fabrication of these molds.

Early in the investigation, silicon metal slips were found to wet the sides of the plaster molds improperly. This resulted in two distinct problems: sharp corners of the casting would not completely fill, and casting surfaces exhibited a rippled texture. The addition of wetting agents to the slip, and the alteration of plaster formulations resulted in little success. These problems were eliminated by coating the mold surfaces with an alginate skin. To acquire the skin, a 0.5 w/o solution of ammonium alginate was poured into the mold and drained after sixty seconds. The coating was allowed to dry before

148

TABLE 5.19

Chemical Analysis of
Ball Milled Silicon Metal

ELEMENT	WEIGHT PERCENTAGE
Fe	0.75
Al	0.33
Ca	0.03
Zn	0.02
Mg	0.02
Ni	0.04
Ti	0.04
Cu	0.01
Cr	0.07
Mn	0.07
Co	< 0.01
Si	Balance
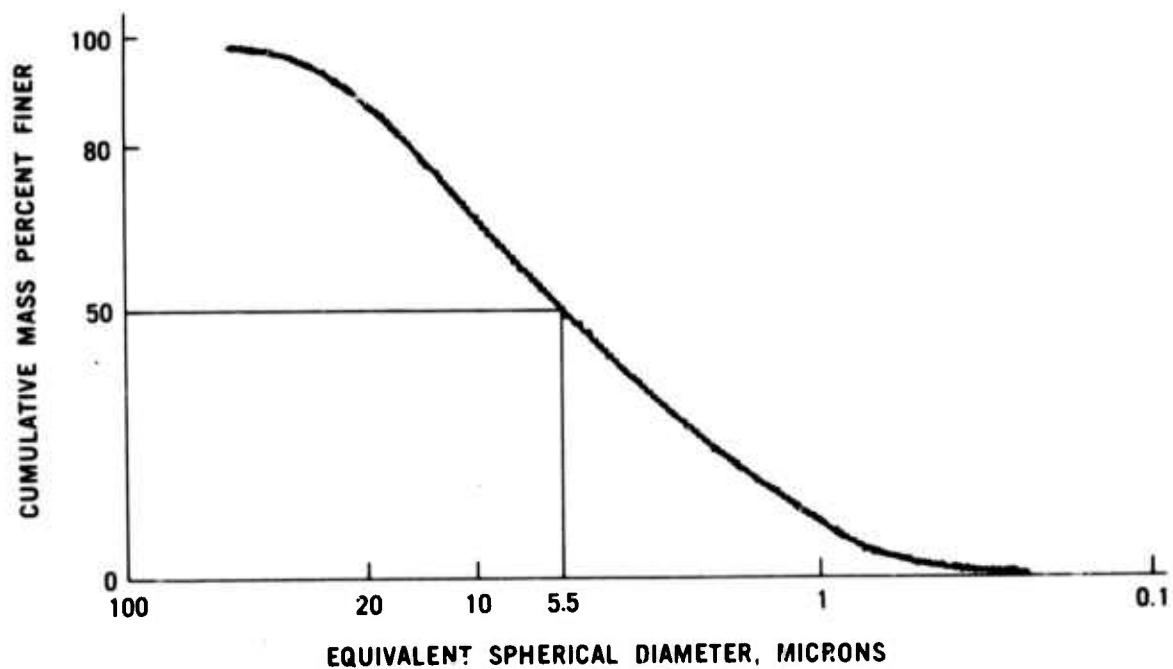
Figure 5.37   Particle Size Distribution of Ball Milled Silicon
               Metal Powder

the mold was used. After extracting the casting from the mold, the adhering skin was stripped from the casting or burned off during firing. The coating also left the mold surfaces clean by prohibiting fine particle penetration into the pores of the mold. In addition, the casting rate could also be controlled by varying the thickness of the alginate coating.

Slip Stability

As discussed previously, metal powders with chemically active surfaces can, with time, change their ionic properties and thus the rheological properties of the metal slip. It was found that silicon metal surfaces are very reactive with the vehicle-deflocculant, and certain processing procedures are required to produce a chemically stable slip.

Substantial gassing in the slip was observed when mixing the silicon metal powder with the vehicle-deflocculant. The reaction was exothermic and the expelled gas was hydrogen, indicating that adjustments in the metal oxide layer were being made through a hydrolysis reaction. The chemical stability or instability is best described in terms of pH and time as shown in Figure 5.38. Three regions of activity are defined in this figure. Gassing occurs in the first region (I) and is accompanied by a dramatic drop in the pH of the solution. Gassing is not evident in the second region (II); however, adjustments in the ionic concentration continue to occur. The third region (III) shows that the ionic concentration has reached a state of equilibrium and the slip is chemically stable. These results show that all silicon metal slips must be properly aged before they are used for casting.

Experiments have shown that chemical instability is also dependent on the particle size of the powder. For example, nominal 325 mesh silicon powder was comminuted by ball milling to an average particle size of 2.5
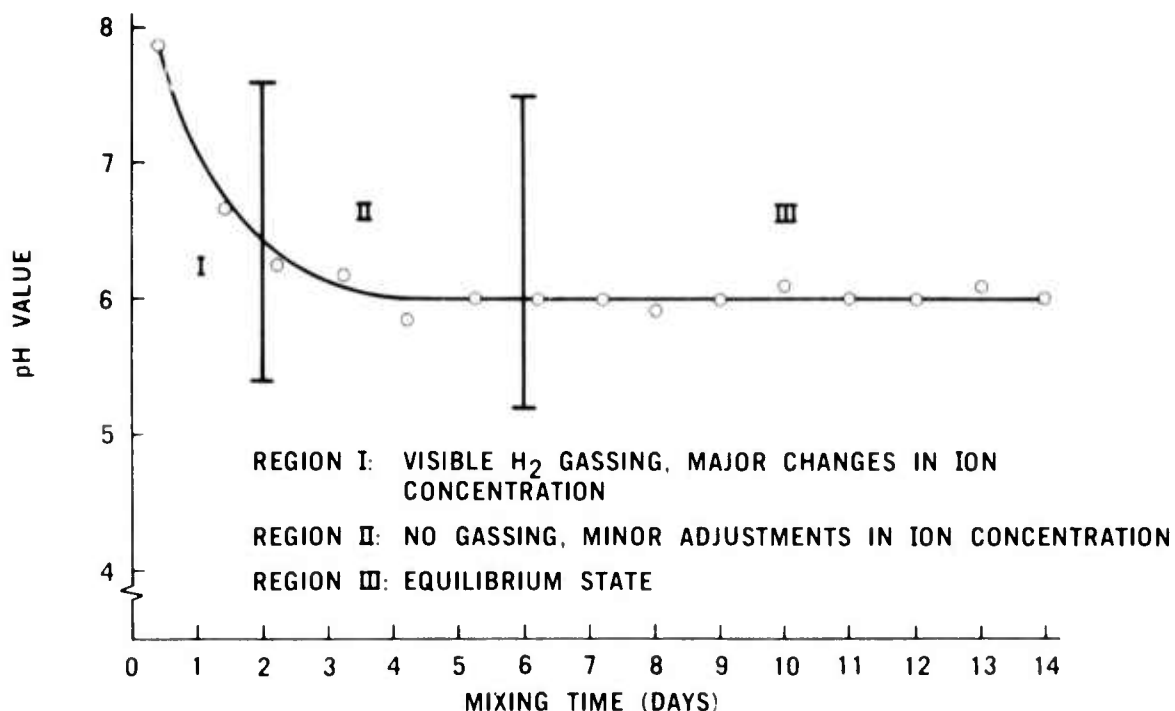
Figure 5.38   Chemical Stability of Silicon Metal Slip and Water-Deflocculant System at Constant pH

microns. Mixing the powder with the water and deflocculant resulted in a reaction that generated large quantities of hydrogen and heat and caused the fine metal powders to agglomerate and form hard pellets. This demonstrates the necessity for controlling the powder particle size to minimize the hydrolysis reaction and its effect upon the ultra fine silicon particles.

Property Measurements

All viscosity measurements were made with a RVF-100 Brookfield Viscometer using a Number 2 spindle at 50 rpm.

A Seargent-Welch Model LS pH Meter with a glass combination electrode was used to measure the ion concentration (pH) in all slips. The internal element for the glass electrode is a non-polarizable cartridge of thallium amalgam. The reference electrode utilizes a similar internal element and incorporates a porous platinum plug liquid junction. Mention should be made that very little is known about the true meaning and mechanisms of pH in non-aqueous solutions; however, ionic concentration measurements in a metal slip made with standard pH equipment are reproducible and are essential as a process control.

Green density measurements were determined on specimens that were first heat treated in an inert atmosphere. The heat treatment imparts strength to the green specimen without associated volume or weight changes; therefore, true green density determinations by the standard ASTM immersion density procedure were possible.

pH - Viscosity Relationship

St. Pierre [17] has shown that the viscosity values of metal slips are very sensitive to the ionic concentration surrounding the powder particles. To study this relationship a slip was prepared using the following; 75.00 w/o of 5.5. micron silicon powder, 24.98 w/o of distilled water and 0.02 w/o of an alkaline deflocculant. After the slip reached chemical equilibrium, the pH was adjusted to various levels and the viscosity at each of these levels was measured. The pH and viscosity values before adjusting the slip were 6.0 and 125 centipoises, respectively. The pH was lowered by using small additions of concentrated HNO_3 and raised by using small additions of concentrated NH_4OH solution. This test was terminated at a pH value of 10 because higher pH values resulted in chemical instability (gassing).

Figure 5.39 summarizes the resultant pH - viscosity relationship. The minimum viscosity was established for pH values between 6.6 and 8.5; the viscosity increased as the pH was varies from this range.

Green and Nitrided Densities

Physical properties of the green casting are controlled by the pH - viscosity relationship just discussed. Figure 5.40 gives the green density of specimens cast from various positions of specimens cast from various positions on the pH - viscosity curve. This figure shows that the highest casting density was produced from slips of minimum viscosity and that the density decreased as the viscosity of the slip increased. In addition, specimens having equal density were produced from equal viscosity slips of different pH values. Therefore, under these conditions the viscosity is the critical parameter for controlling the green density.

151
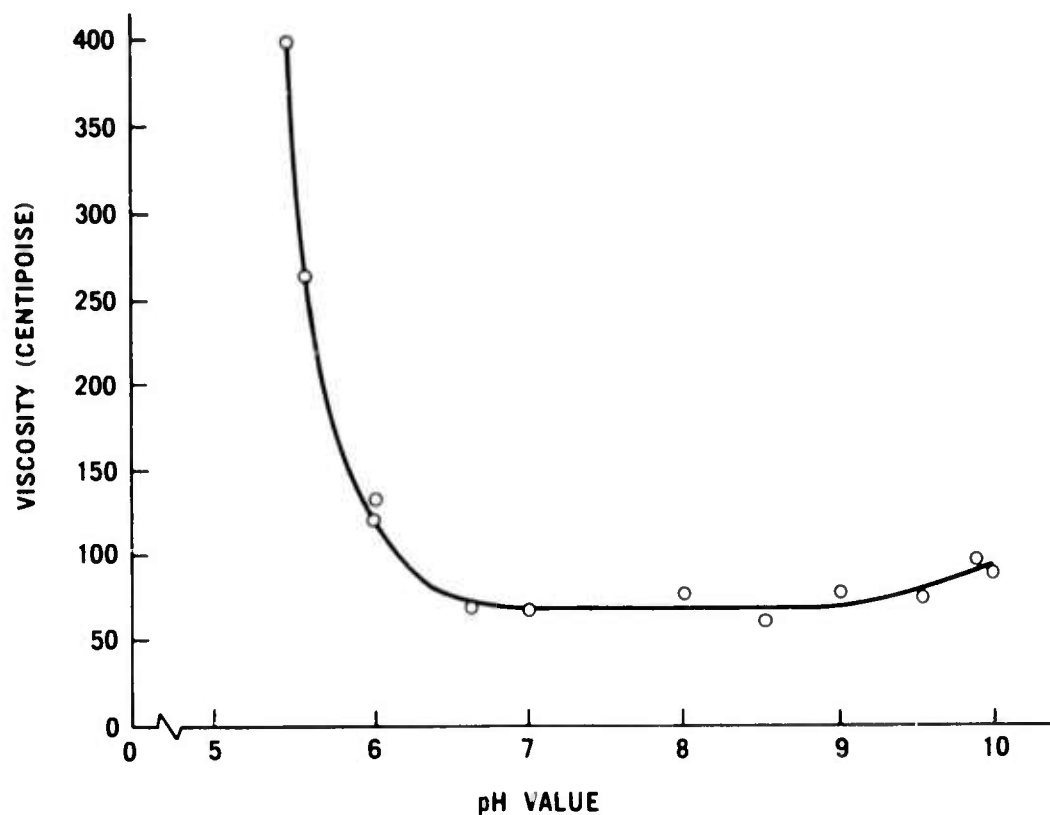
Figure 5.39   pH – Viscosity Relationship of Silicon Metal Slip
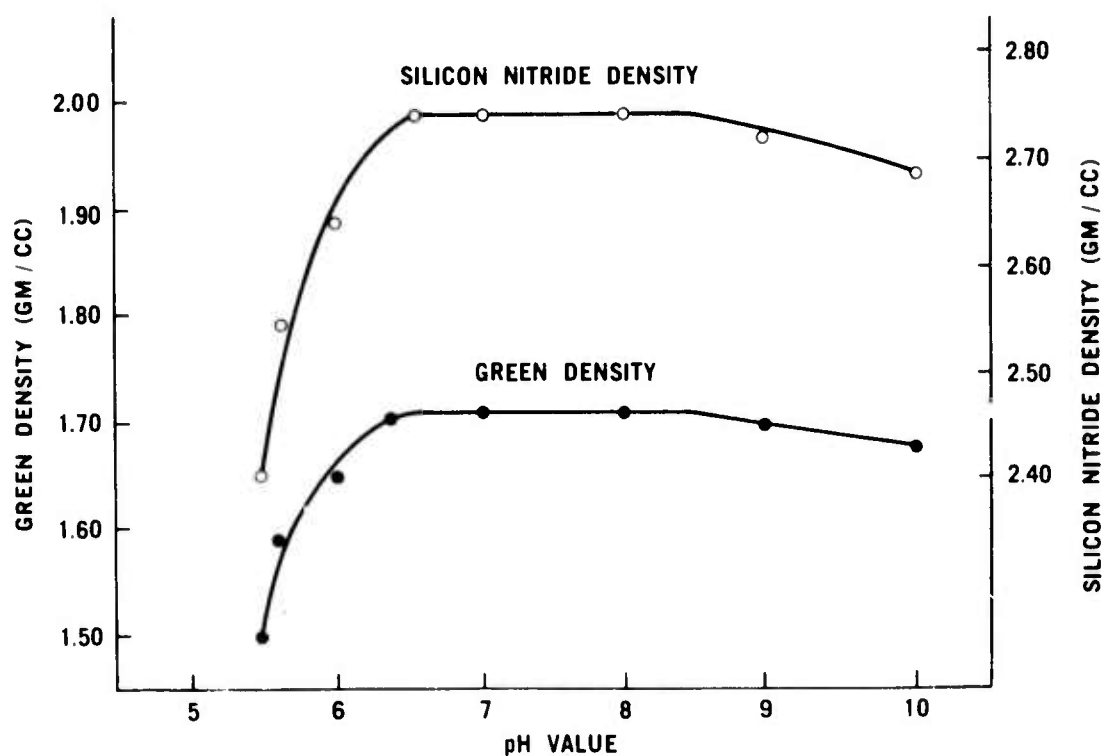
Figure 5.40   Green Density and Corresponding Sintered Silicon
Nitride Density of a Silicon Metal Slip Cast at Various
pH Ratios

Also shown on Figure 5.40 are the corresponding densities for silicon nitride. These values were calculated assuming a 60%[*] weight gain for converting silicon metal to silicon nitride. These results demonstrate the flexibility inherent in a given silicon metal slip cast system. That is, a given slip cast system can be chemically controlled to produce finished ware of various densities. From a design viewpoint, this flexibility is extremely important. For example, hardware with a large cross sectional area require castings of relatively low density so that complete nitridation is assured. The lower density can be obtained by increasing the viscosity of the silicon metal slip through controlled additions of a suitable electrolyte.

The results shown in Figures 5.39 and 5.40 are representative of only the 5.5 micron silicon metal powder characterized earlier in this section. By varying one or more of the controlling parameters in a given slip cast system, different results can be obtained. Through adjustments of the silicon particle size and particle size distribution, slips can be formulated to yield castings of much higher green densities than those indicated in Figure 5.40. Specimens with green densities of 1.82 gms/cc (calculated nitrided density of 2.91 gms/cc) were produced using a minimum viscosity (60 centipoise) silicon slip having a specific gravity of 1.78. The mean particle size by weight of the silicon powder was 5.0 microns and the distribution about this mean was similar to that shown in Figure 5.37. Figure 5.41 shows the microstructure of a heat treated specimen with a green density of 1.82 gms/cc. The relative distribution of fine coarse grains demonstrates the packing efficiency of the 5.0 micron slip cast system.

Effects of Slip Dilution

Investigators [15] have noted that the properties of metal slips and their resultant castings are dependent upon the ratio between the liquid phase and solid phase (water-metal ratio).

A dilution technique was used to determine this relationship for a silicon metal slip. A 5.5 micron slip containing 0.02 w/o of an alkaline diflocculant and having a specific gravity of 1.78 (water-metal ratio of 0.267) was prepared. Two additional specific gravity levels of 1.73 and 1.68 were prepared by diluting the original slip with distilled water. Minimum viscosities were established by adjusting the pH of each slip to 7.3; consequently, the resultant castings represented the maximum green density for each specific condition. The viscosity and the green density were determined for the three slips and these results are summarized in Figure 5.42. This figure shows that slip dilution significantly reduces the viscosity of the slip; however, slip dilution has little effect on the final density of the casting.

When casting small intricately shaped parts, such as turbine rotor blades, slips of high fluidity or low viscosity and slow casting rates are necessary to completely fill all sections of the mold cavity. By using slip dilution techniques, these requirements can be met without sacrificing the green density of the cast part. However, care must be exercised in that over-dilution may produce slips that are unable to completely suspend all of the metal particles.

---

*The theoretical weight gain for converting Si metal to Si_3N_4 is 66.67%; however, the entire gain is not realized because of silicon metal volatilization during the nitriding process.

153
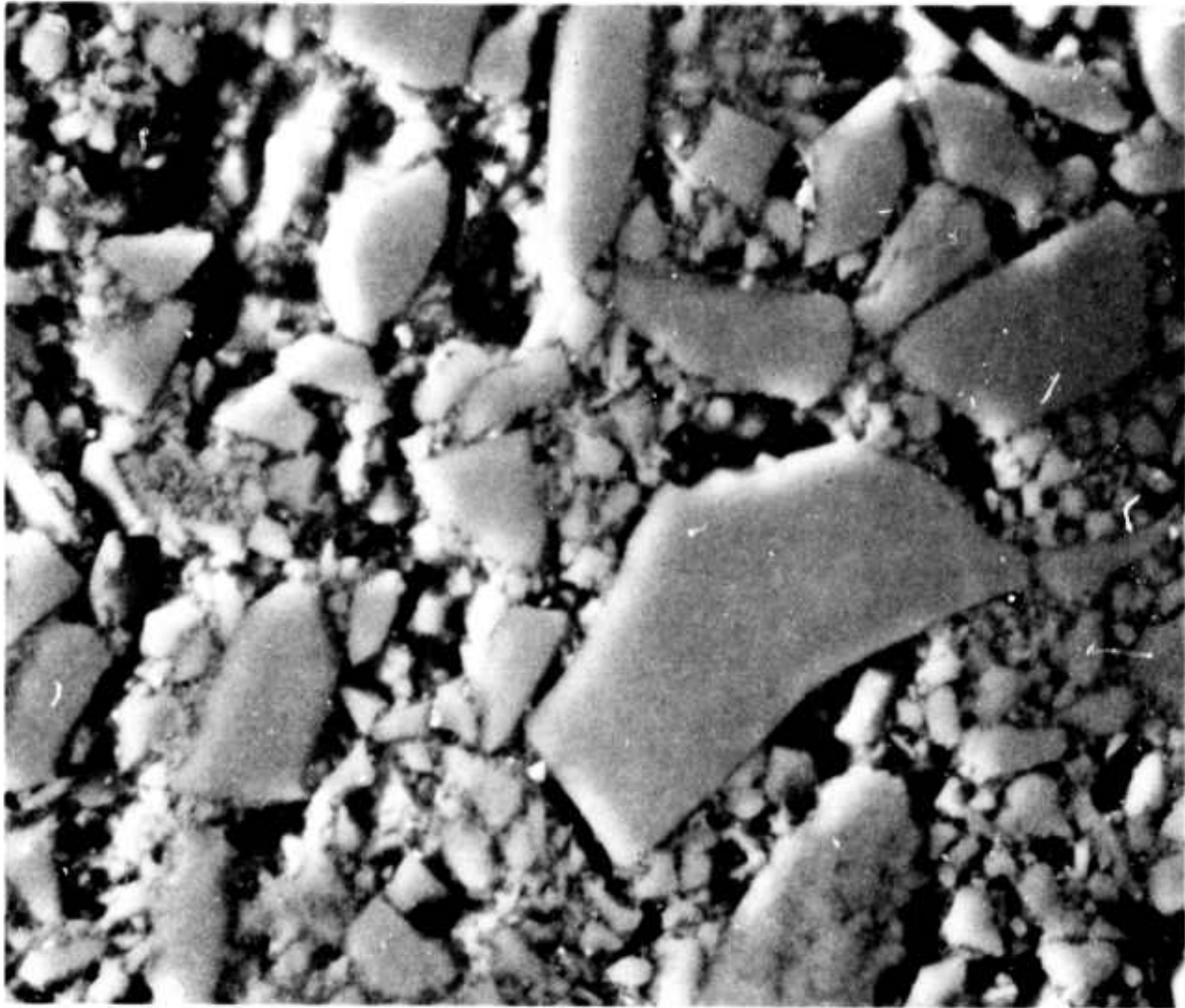
Figure 5.41   Microstructure of a Heat Treated Silicon Metal Slip Cast Specimen Which Has a Density of 1.82 gm/cm^3 (800 x)
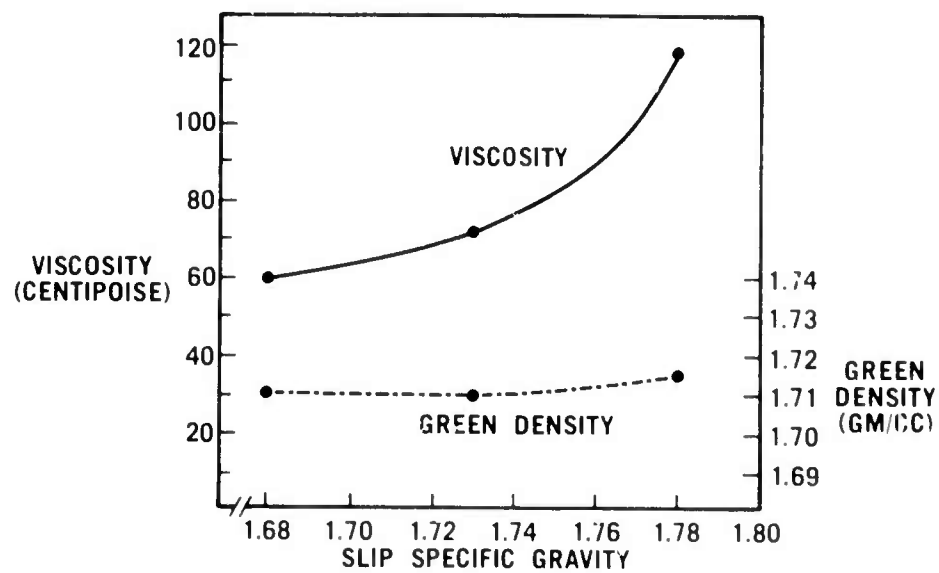
Figure 5.42   Effect of Slip Dilution on Slip Viscosity and Green Density of Silicon Nitride

154

Slip Cast Silicon Nitride Hardware

Figure 5.43 shows typical slip cast components manufactured using solid casting procedures. In particular, the turbine rotor blade segment was produced using the dilution technique described earlier. Figure 5.44 depicts typical drain cast articles. These figures show that a wide variety of different shaped components can be fabricated by the respective slip casting techniques. This demonstrated versatility is extremely important in developmental programs where a wide range of prototype components are required.

The majority of the components shown do not represent as-cast hardware; machining or grinding to final dimension was necessary.
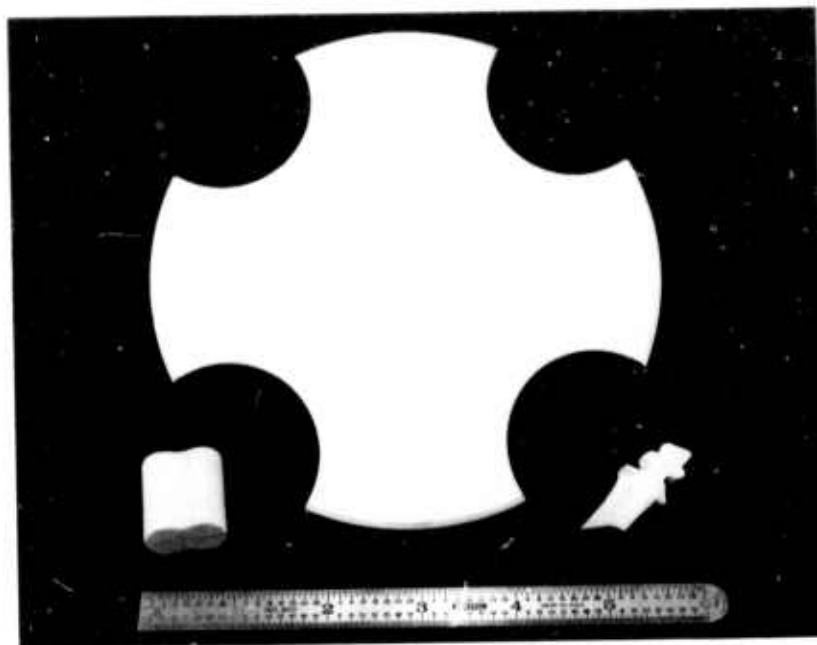
Figure 5.43   Typical Silicon Nitride Articles Formed by Solid Casting

Figure 5.44   Typical Silicon Nitride Articles Formed by Drain Casting

5.2.5 FRACTURE STUDIES

Introduction

Studies of the fracture resistance of SiC and Si₃N₄ ceramics emphasized the recognition of certain processing flaws as sites for crack initiation and the use of surface flaws of controlled size and geometry to evaluate properties fundamental to an understanding of the fracture process. The design of test specimens used for this work was as previously reported [3].

Fracture of Silicon Nitride and Silicon Carbide

Data presented in the last report [4] on the flexural strength of hot pressed Norton SiC and Refel reaction sintered SiC, with equivalent surface preparation, shows competitive strengths over the range from room temperature to 2500°F. The scatter bands of this data are portrayed as a single shaped band in Figure 5.45. Also plotted is the range of strengths obtained in preliminary studies at room temperature of Sialon type material currently under development.
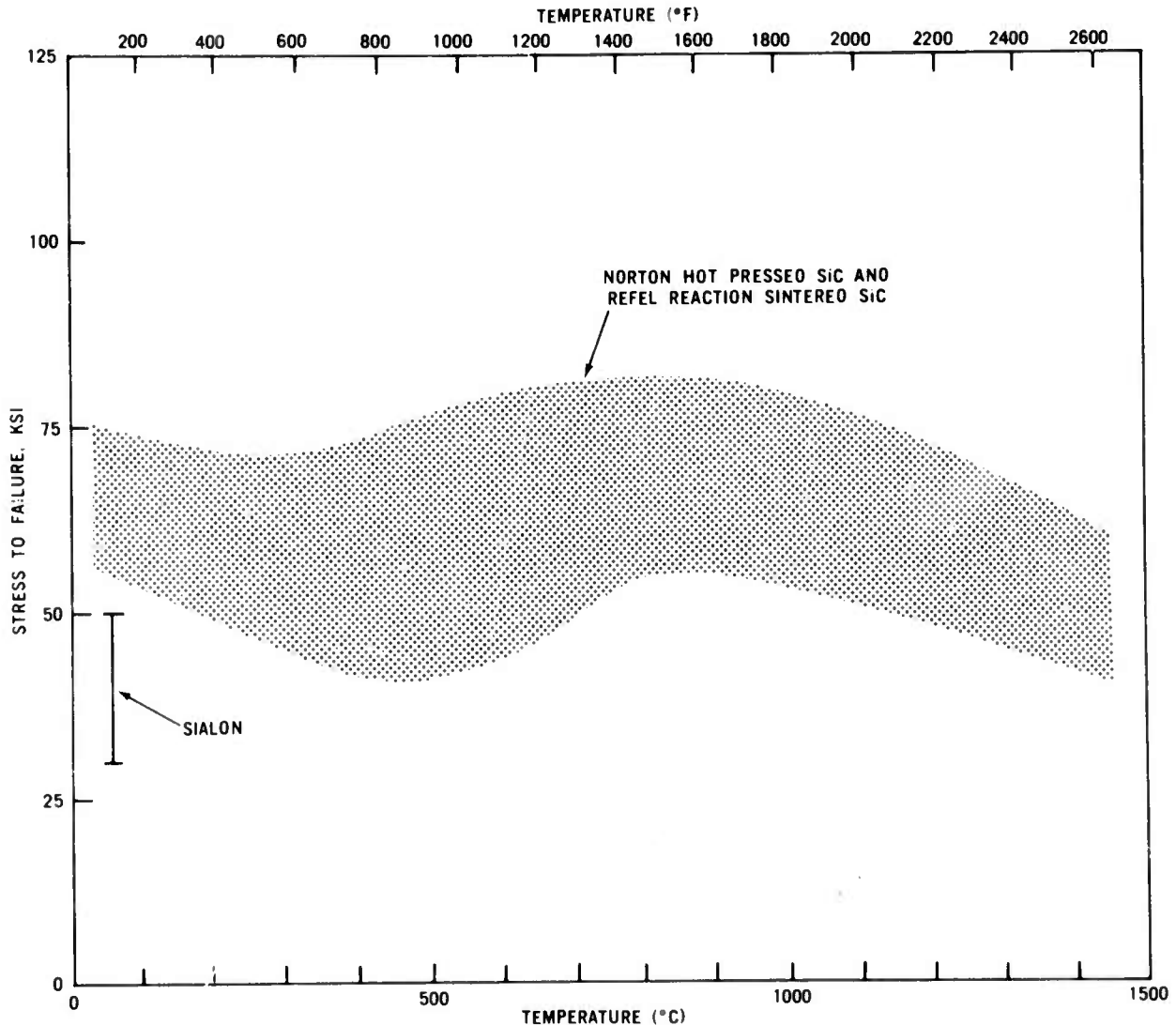
Figure 5.45   Flexural Strength Ranges of Silicon Carbide
Materials and Sialon

Preliminary fractographic investigation of Refel SiC indicates that fracture initiation in these materials could be traced to localized large pores, of the order of several grains in diameter, at the tension surface of the bend specimens. This was particularly true in specimens which supported inordinately low stresses at failure. Pores of the same type were observed on the fracture surfaces. The nature of the porosity is as shown in Figure 5.46. Neither the extensive pore shown as (a) on the fracture face nor (b) on a polished surface are characteristic of removal of unbonded material by sample preparation or "pluck-out". A surface flaw which could have been revealed by "pluck-out" and which contributed to fracture inititation is shown in Figure 5.47 as a top view (a) of the tensile surface of the
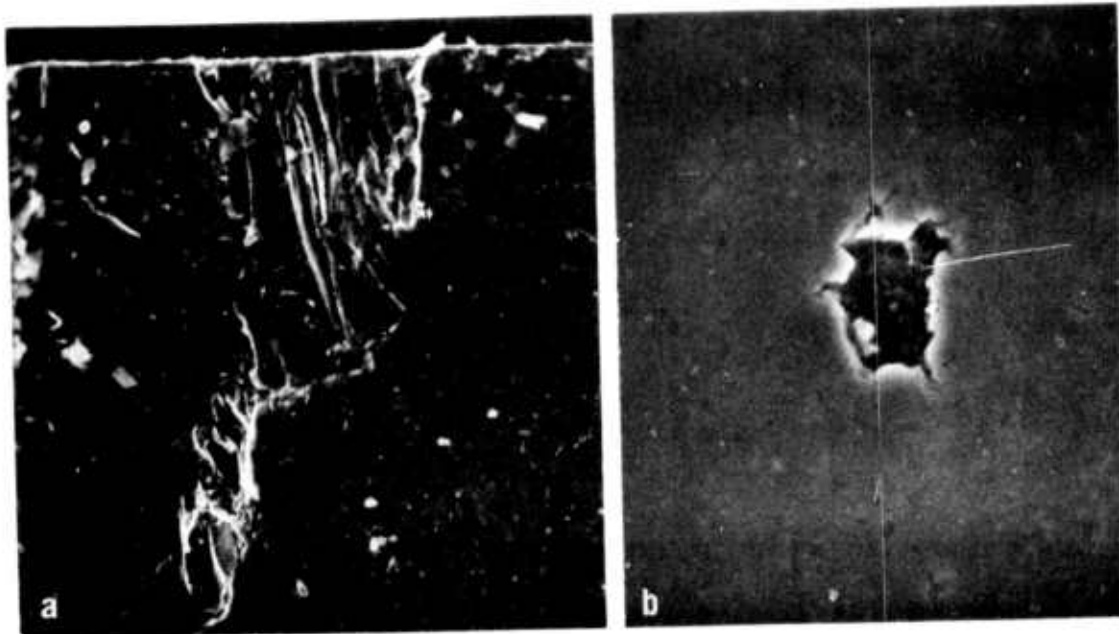
Figure 5.46   Typical Flaws at (a) The Fracture Face and at (b) on the Polished Tensile Surface Reaction Sintered Silicon Carbide
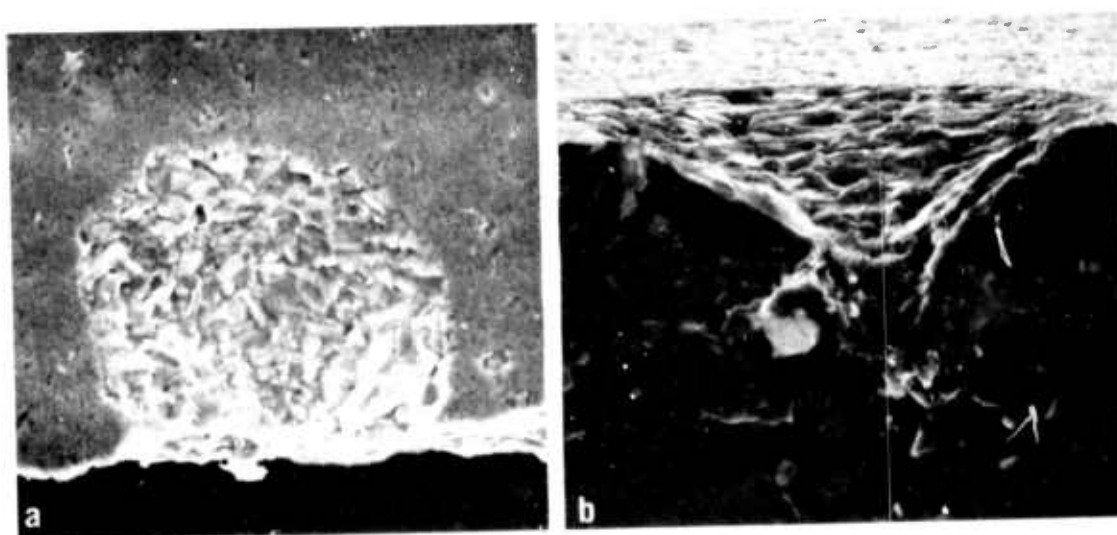
Figure 5.47   Flaw in Reaction Sintered Silicon Carbide From "Pluck-Out" of Unsintered Material by Polishing; (a) is Perpendicular to the Polished Surface, (b) is the Appearance on the Fracture Face

157

bend specimen and (b) as it appears on the fracture surface. These materials fractured by transgranular cleavage, indicting that the bond integrity between the silicon carbide grain and the silicided material is adequate. Figure 5.48 is a fracture surface in which another crack has formed in a typically transgranular manner.

A study of the fracture process resulting from the deliberate introduction of sharp cracks of a measurable size by both indentation and laser damage techniques has been initiated in hot pressed Si_3N_4. Results for room temperature fracture yield a value of approximately 15,000 ergs/cm^2 for the effective fracture surface energy of the Norton HS-130 material.

Figure 5.48   Transgranular Crack on the Fracture Surface of Reaction Sintered Silicon Carbide

5.3 NON-DESTRUCTIVE EVALUATION OF MATERIALS

SUMMARY

A very important aspect of the development of ceramic gas turbine engines is the need to meaningfully inspect and test ceramic components before installation in the engine. The objectives of the NDE work are to identify and classify defects and to gain as much information as possible on the properties of the material from which the component is manufactured. Both property and defect information are being related to performance of the component, leading eventually to routine inspection and acceptance/rejection based upon established actual performance. All available non-destructive means must be used to accomplish this goal and new methods must constantly be evaluated to determine their usefulness. Procedures utilizing ultrasonics, x-ray radiography, and acoustic emission (AE) are currently being applied to ceramic systems for evaluation purposes.

Ultrasonic inspection was evaluated for internal defect and inclusion identification in hot pressed silicon nitride. It was found that variations between transducers play a critical role in success or failure of defect location, indicating the need for careful selection and characterization of the transducers. Sensitivity capability for different transducers was established experimentally using artificially produced defects.

Acoustic emission (AE) techniques have been used to detect and record cracking of duo-density stator assemblies during elevated temperature testing. Initial results established that the cracking was time-dependent. This use of AE measurement provides useful information regarding relative stator quality, and may provide an insight into the cause of the cracking.

Work was continued comparing conventional x-ray radiography and xeroradiography. Using assembled rotor blade rings containing known flaws, no clear advantage was apparent for either process. Conventional radiography was found to be useful for detecting high density inclusions in hot pressed silicon nitride, and resolution limits were established for several defects.

In defining the status of non-destructive evaluation at this point of the program, it can be concluded that the basic tools, dye penetrants, x-ray radiography, ultrasonic scanning, and acoustic emission have been identified and are being applied. Work to define the resolution limits of x-ray radiography and ultrasonic scanning as applied to turbine ceramic materials has made considerable progress, and the major thrust of future effort will be to utilize these basic tools for the inspection of ceramic turbine components.

5.3.1 ULTRASONIC NDE

Introduction

As indicated in previous reports, efforts are continually being
made to correlate NDE results with other data acquired either through
actual engine usage or by destructive analysis. The strength and
probability of failure analysis, discussed in Section 3.1.1 of this
report, provided the opportunity to evaluate dense silicon nitride
spin disks with the of establishing a relationship between
subsurface flaws and disk burst speed.

Subsurface Flaws in Hot Pressed Silicon Nitride

Silicon nitride spin disks were evaluated for subsurface flaws by
ultrasonic and radiographic means. Material integrity was initially
verified by obtaining the sonic velocity of the disks in a perpendicular
direction at various locations from the inner to the outer diameter. An
average sonic velocity of 10.9×10^5 cm/sec was determined. The con-
sistency of the data from disk to disk implied a homogeneous material
with no apparent structure gradient. All the velocity measurements were
made with an Aerotech 5 MHz alpha transducer. The time of flight of the
ultrasonic signal within the material was measured from the maximum point
on the first RF reflection to the corresponding point on the next RF
reflection signal. Some phase distortion was apparent, but in no case
was phase reversal noted. Sonic velocity was also measured at 10 MHz
and 2.25 MHz with identical results to the 5 MHz data.

Contact scanning for subsurface flaws with the same 5 MHz trans-
ducer did not reveal any discontinuities. This same transducer had the
best resolution of any available including three 10 MHz units, but was
unable to detect subsurface defects subsequently found by x-ray radiography.
Figure 5.49 reveals the high density inclusions found in these disks
by x-ray radiography. Utilizing the radiographic step-block standard
previously described [3] resulted in obtaining optimum radiographs and
proved to be the impetus for further evaluation by ultrasonic methods.
An example of an inclusion type flaw, found after spin testing, is
shown in Figure 5.50. Its effect on crack initiation and propagation
are illustrated by the surface topography around the flaw. A zone of
fast crack propagation which encompasses the flaw is apparent with
much crack branching surrounding this region. The relative size of the
flaw further supported the need for additional, more sensitive, ultra-
sonic evaluation.

A new transducer was procured and the remaining spin disks were
again scanned for subsurface defects. The radiographs now served to
locate the defects and ultrasonic correlations were obtained. Additional
subsurface defects were noted during this ultrasonic evaluation which
were not apparent on the radiographs. These indications are evidently
too small to be resolved on film, or are lower in density than the
parent material and therefore difficult to detect by radiographic film
imaging techniques.

This new transducer was rated a 10 MHz, but subsequent analysis of
its frequency spectrum revealed its maximum power occurred at 8MHz. This
unit also had greater sound beam spread due to a smaller element diameter.
This may have been the reason for the apparently enhanced flaw detection

160
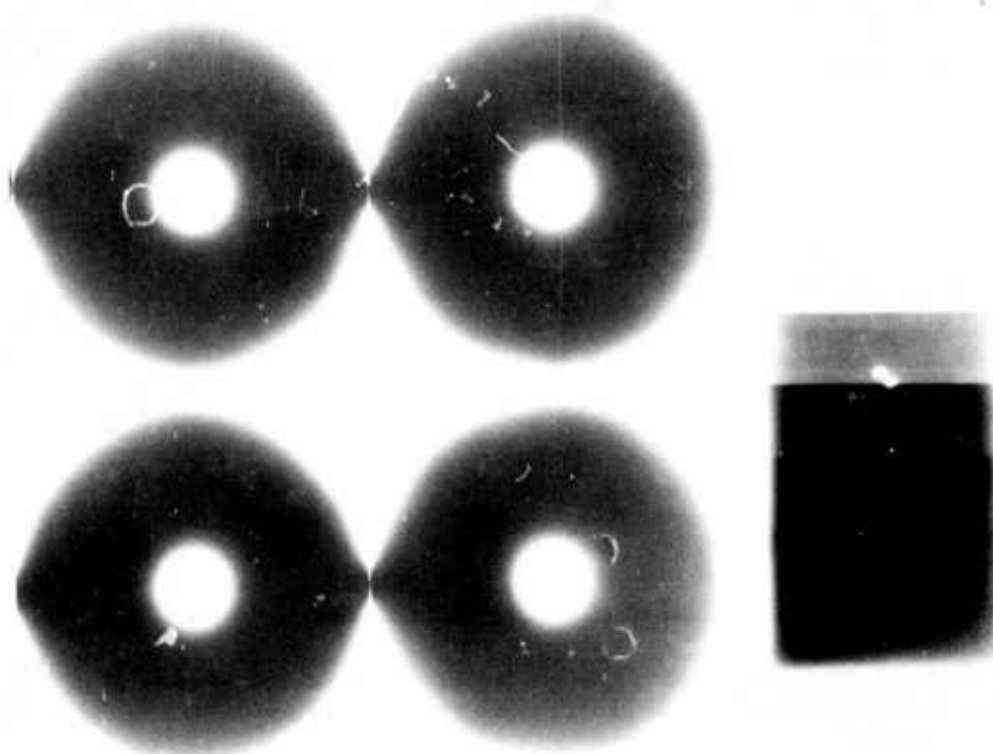
Figure 5.49   Radiograph of High Density Inclusions in Hot Pressed Silicon Nitride
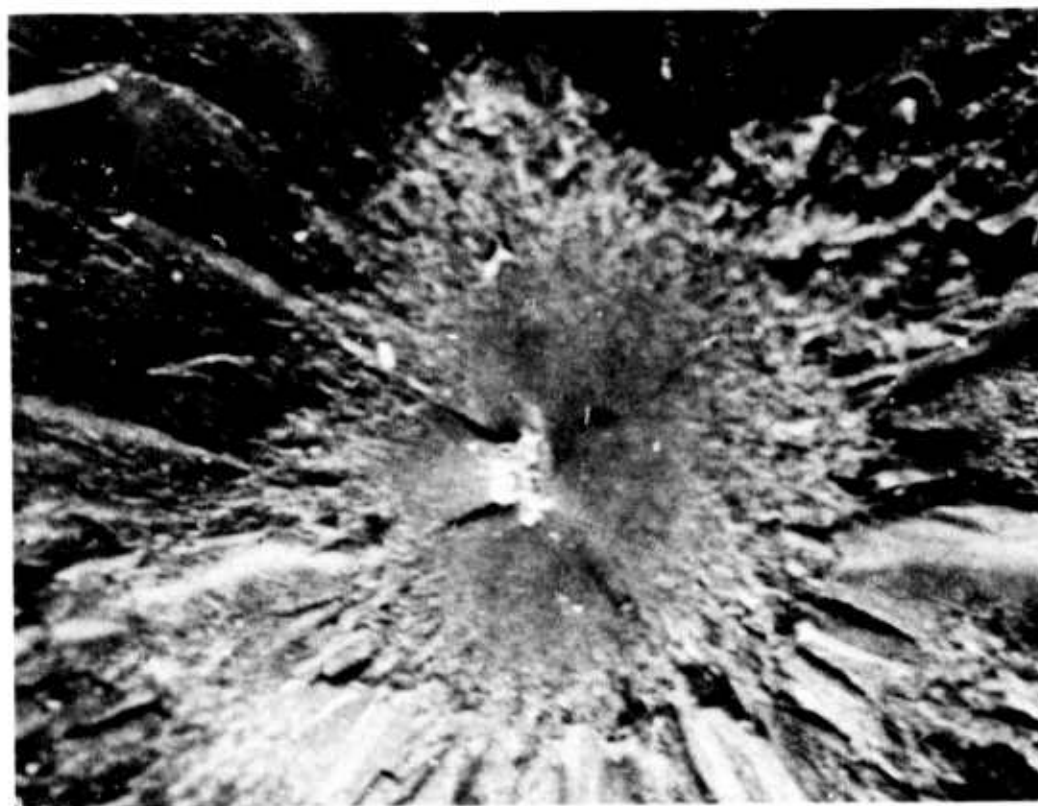
Figure 5.50   Inclusion Type Flaw Observed in Dense Silicon Nitride Spin Disk After Testing

161

since the flaw orientation and morphology is somewhat compensated for by
the greater divergence of the ultrasonic beam. In any event, the importance
of transducer characterization was pointed out. Knowledge of operating
parameters such as frequency and sound beam orthogonality with the trans-
ducer face must be established and will dictate the limits of practical
flaw detection in these materials.

The theoretical limitations governing the smallest discontinuity
detected in this material, using conventional ultrasonic equipment at
frequencies up to 15 MHz, necessitate increasing the signal-to-noise ratio
in order to approach sensitivity levels necessary for material/component
evaluation. Typical ultrasonic signals from subsurface flaws are shown
in Figure 5.51, where the need for increased signal-to-noise ratio is
visually apparent. The program presently being conducted at the University
of Michigan [4] exhibits this potential. Additional instrumentation has been
received for this program which will expand present capabilities and allow
for direct demonstration of signal enhancement in ceramic materials.

On the stationary turbine project, two methods of ultrasonic inspection
have been investigated, manual immersion A-scan and automated C-scans.

The C-scan equipment consists of an Automation Industries Style 57A2790
10 MHz focused tranducer, a Budd 725 Immerscope, and a Budd SR-154 Ultrasonic
Recording System.
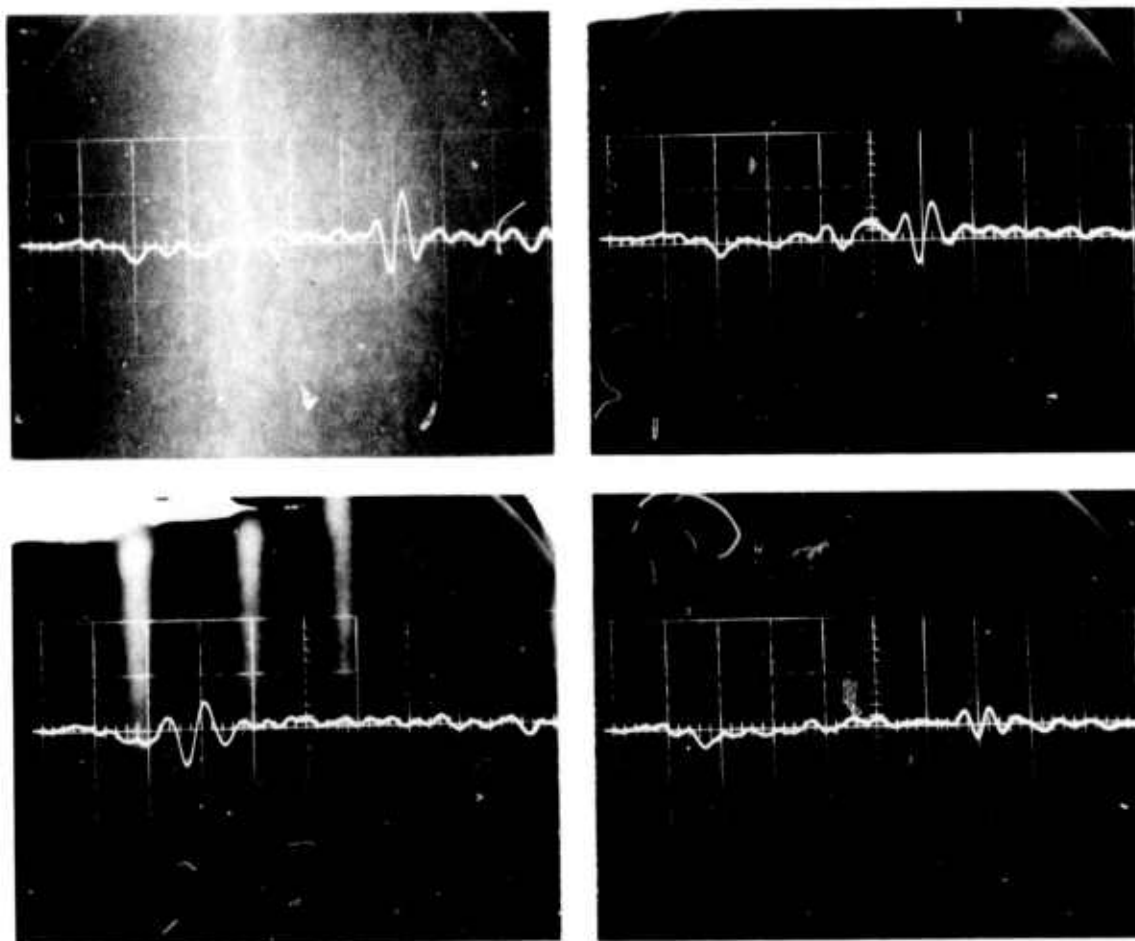
Figure 5.51   Ultrasonic Indications of Several Subsurface Flaws in
Silicon Nitride Spin Disks

162

A hot pressed Si_3N_4 block with cavitated holes and 2 laser drilled holes (Figure 5.64) was used to evaluate the resolution quality and detection limits of the ultrasonic system used with automated C-scanning. This block was immersed in water and the water path was determined by obtaining the maximum signal from the front surface. After determining and setting the optimal sensitivity of the system, water path and signal strength (DB) were varied. The results are summarized in Figure 5.52 with the beam parallel co the axes of the holes and, in Figure 5.53, with the beam perpendicular to the axes. Water path was varied from 0.25 to 2.0 inches with an amplitude range of 4 to 8 DB. The images are not sharp and only in Figure 5.52 is there any indication of good resolution of the two deepest holes. There is no indication of the laser holes in any of the scanning records shown in Figures 5.52 and 5.53. However, C-scanning does provide a fast, automated, permanent display of sound intensity variation over the area scanned. The input data arrive as intensity-real time information. Thus, the C-scan is basically a display of individual A-scans where resolution is lost during the translation process.

A-scan results on the standard block (Figure 5.64) are shown in Figures 5.54 and 5.55. Figure 5.54 shows the block and two typical scans. The major objective was to define the resolution of the small laser holes (1 and 2, Figure 5.54). The large ring holes, A to D, are used for illustrative purpose only. The sound beam was directed at the side wall of the block so that the beam was perpendicular to the axes of the holes. The tracings of the scanning results, shown in Figure 5.54, illustrate how a defect is detected and also show that the location of the defect can be found accurately by simple
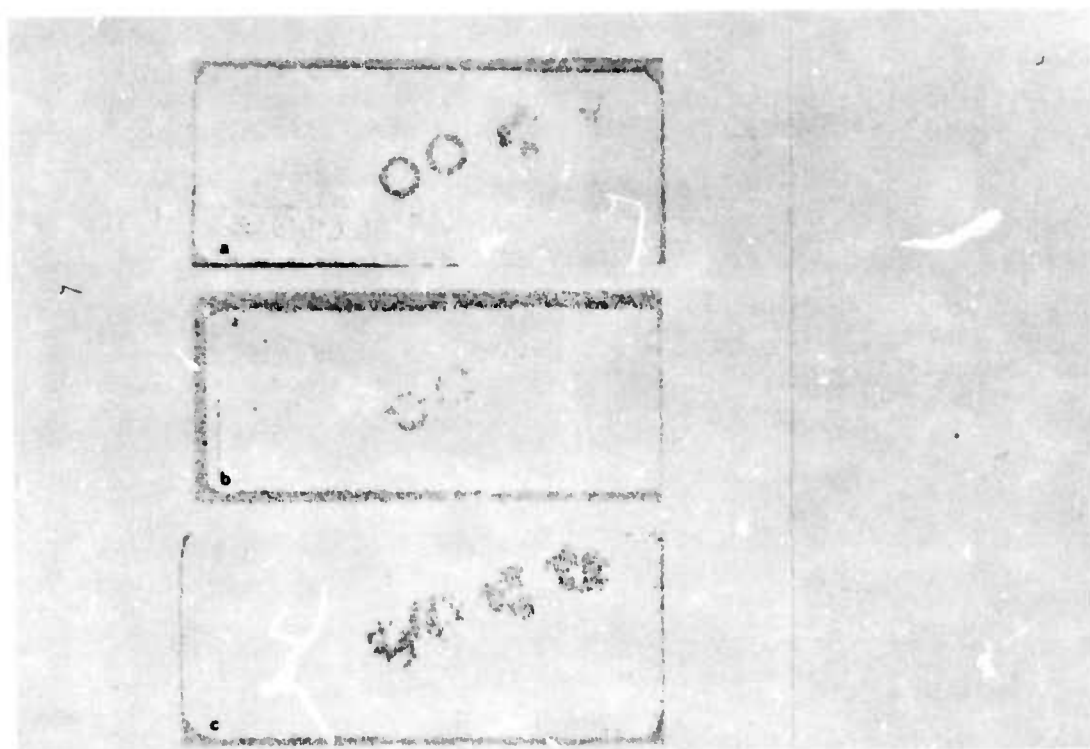
Figure 5.52   C-Scan of Standard Block, Parallel to the Axis of the Holes
(a) 4 DB 2.00 in - W.P.
(b) 4 DB 0.25 in - W.P.
(c) 8 DB 2.00 in - W.P.

163

calibration. F and B indicate the reflections from the front and back surfaces, respectively. The thickness of the block provides the necessary calibration. The reflections marked 1, 2, and D are from the respective holes. All other non-marked reflections are spurious signals.
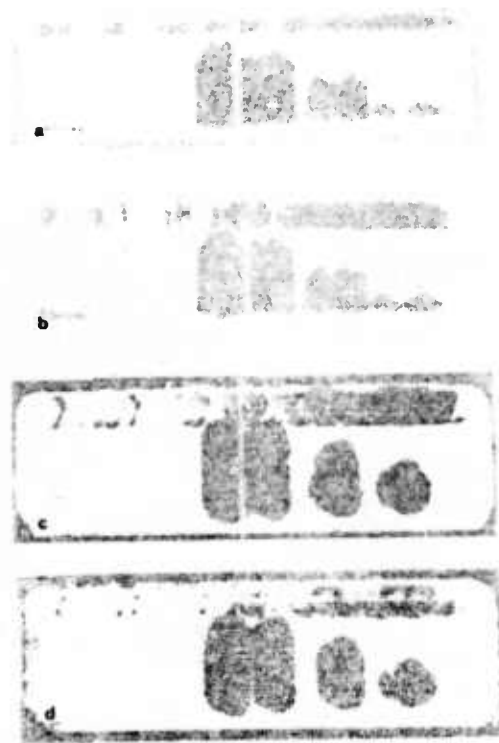
Figure 5.53   C-Scan of Standard Block Perpendicular to the Axes of
                the Holes
                    (a) 4 DB 2.00 in - W.P.
                    (b) 4 DB 0.25 in - W.P.
                    (c) 8 DB 0.25 in - W.P.
                    (d) 8 DB 1.38 in - W.P.
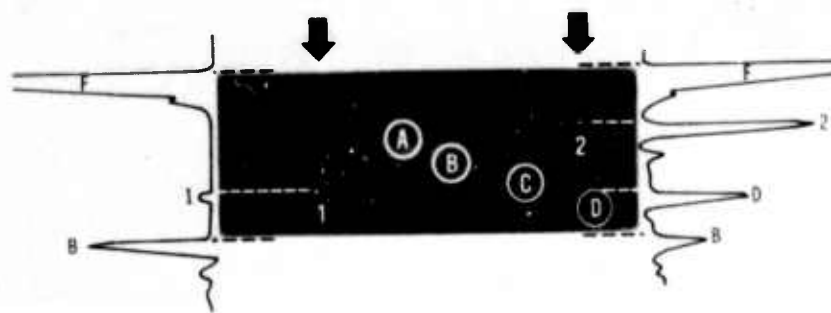
Figure 5.54   Standard Block with Four Ring Holes and Two Laser Holes
                (Arrows Indicate the Direction of the Sound Beam -
                F = Front Surface, B = Back Surface)
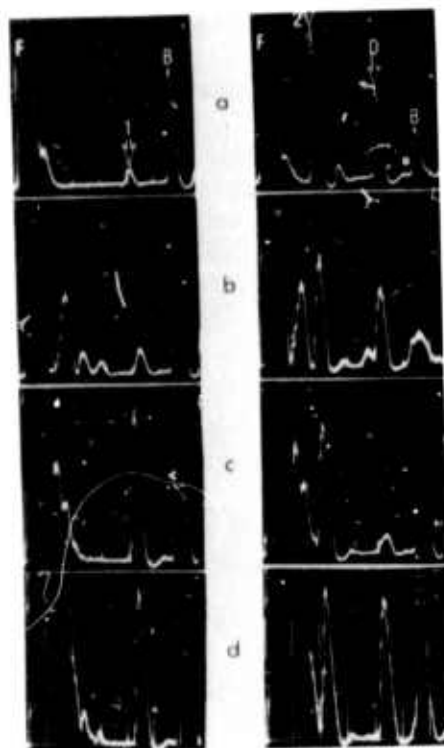
Figure 5.55   A-Scan Images from Standard Block (Fig. 5.54) (Left-Laser Hole-1, Right Laser Hole-2)
         (a) Automation Industries Transducer -
                 10 MHz - 0.5 in
         (b) Automation Industries Transducer -
                 10 MHz - 3.35 in
         (c) Branson Transducer - 10 MHz - 0.5 in
         (d) Branson Transducer - 10 MHz - 3.35 in

The effects of water path and type of transducer on the resolution limits are shown in Figure 5.55. The left side illustrates reflections from laser hole 1, while the right side shows reflections from laser hole 2 and ring hole D (Figure 5.54). The Branson focused transducer has a higher resolution capability compared to the Automation Industries transducer. Comparing the peak amplitude of laser hole 1 to laser hole 2, which are located, respectively, at 1.3 inches and 0.60 inches below the surface, gives an estimate of the resolution limit of the two transducers operating at 10 MHz. This is summarized in Table 5.20. However, the low operating frequency increases the lower limit of the thickness of Si_3N_4 material that can be examined. This is indicated by the width of the reflection from the front surface (Figure 5.55). Thus, for a sound beam directed normal to the surface, minimum material thickness is about 5 μm with the Automation Industries transducer. For the Branson transducer the limit is higher. This limitation can be overcome by increasing the driving frequency or by directing the sound beam at an angle, thereby increasing the effective lengths of the sound path through the material.

A BN inclusion in a 150 μm long cavity was detected in a 0.85 x 1.75 x 3.9 inch piece of hot pressed Si_3N_4 by directing the sound beam from the two short directions, as shown in Figure 5.56 using the Automation Industries transducer and a 0.47 inch water path. Table 5.20 indicates that, at a depth of 0.80 inch, the cavity dimensions approach the resolution limit

165

of 140 μm. Note also the decrease in signal amplitude as the depth of the defect changes from 0.62 to 0.80 inches. This is consistent with the results shown in Figure 5.55 for the same transducer and water path setting.

Finally, it is significant to note that high density inclusions were never detected by ultrasonic techniques. Apparently, reactions between Fe, W, and the Si_3N_4 matrix provide a low acoustic impedance particle-matrix interface so that the defect does not constitute a discontinuity for the sound waves.

TABLE 5.20

Detection Limits, Cavity-Type Defects, A-Scan, 10 MHz Frequency
(for material thickness up to 30 mm)

Transducer	Focal Length mm	Water Path mm	Min. Mat. Thickness, mm	Resolution Limit
Automation Ind.	60	12	5	∿ 0.007
Type 57A2790	60	85	10	∿ 0.005
Branson, Focused	200	12	15	< 0.005
Type Z1031	200	85	18	<< 0.005
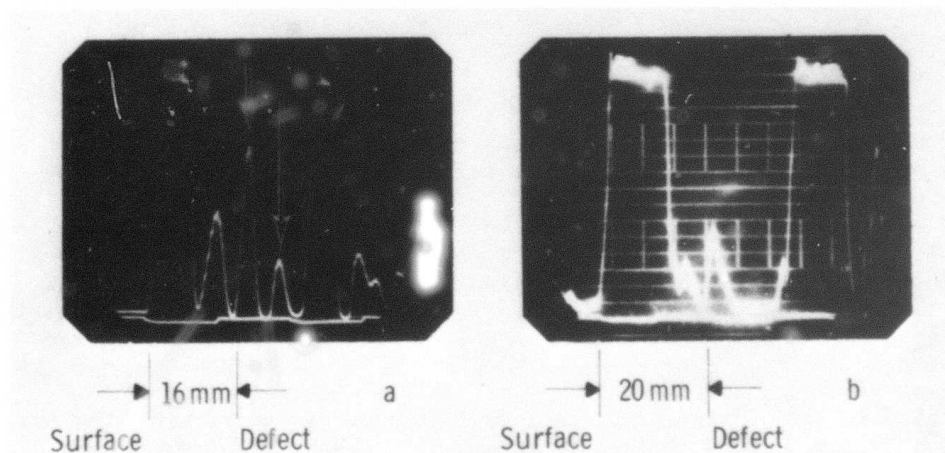
Figure 5.56   A-Scan Images from Mutually Perpendicular Surfaces -
BN Inclusion in a Si_3N_4 Block

166

5.3.2 ACOUSTIC EMISSION

Introduction

A program was initiated to monitor the acoustic emission (AE) response of stator assemblies during extended exposure to elevated temperatures. This testing was intended to augment the qualification tests conducted in engine test rigs and to establish an additional simple means of evaluating component quality. Previous test rig data indicated a major improvement in life was achieved using Design C (inverted channel) second stage stators [4], but the complexity of the test rig configuration precluded AE monitoring during qualification testing. A test sequence was established consisting of heating unrestrained stator assemblies in a furnace while monitoring the acoustic emission response during heat-up, soaking at $1900^{\circ}F$, and cool-down.

Stator Testing

A schematic diagram of the stator testing system is shown in Figure 5.57. Stator assemblies are placed in an electric air-atmosphere furnace at room temperature, with subsequent heating and cooling at normal furnace rates. A bar of slip cast silicon nitride, mounted in a positioning fixture, contacts the stator assembly on its outer shroud. This bar serves as a waveguide to transmit elastic stress waves (AE) emitted by the stator assembly to a sensor bonded to the opposite end of the bar which extends from the furnace. Slight spring pressure on the waveguide is maintained to insure a firm joint at the waveguide/stator interface. To further reduce extraneous noise, the stator is placed on a billet of hot-pressed silicon nitride, therefore eliminating relative movement due to thermal expansion differences as the furnace heats and cools. External cooling air is provided for the AE sensor to prevent damage from overheating.
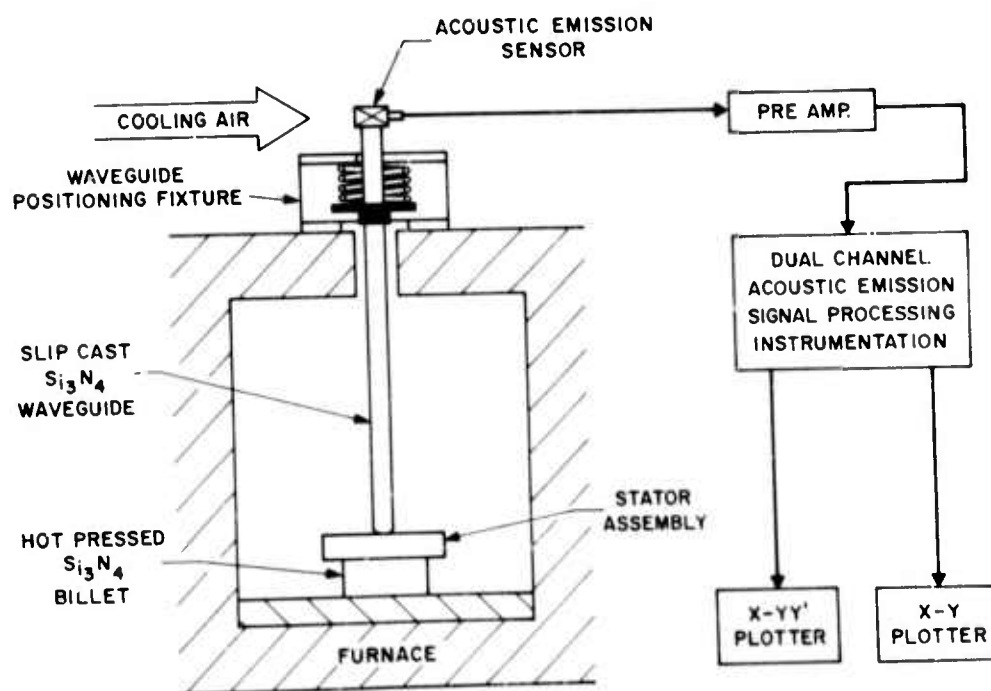
Figure 5.57   Acoustic Emission Stator Testing System

Acoustic emission activity was detected with a differential transducer having a fundamental frequency of 140 kHz. An amplifier bandwidth of 100-300 kHz provided the necessary filtering for the transducer with 90 db amplification of the AE events. Figure 5.58 indicates the AE response of a second stage stator vs time at 1900°F. This curve is the summation of all detected AE events. The magnitude of these events exceeded the scale settings of the instrument several times, resulting in this sawtooth data presentation. Figure 5.59 is the same AE information processed in a different manner. A Dunegan Model 905 Digital Envelope Processor (DEP) intercepts the AE signals and converts the AE detected within a selected time interval into single pulse, then sends the information to a separate totalizer for accumulation. This results in an AE curve which displays a pronounced sensitivity to the rate of detected events.

This rate dependence is further indicated in Figure 5.60. The data in this figure, while very generalized, does indicate several areas of interest. The multiple reset region, occurring between 60 and 80 hours, coincides with the increase noted on the DEP curve in Figure 5.59. This AE was of lower magnitude than that detected during the entire time at temperature and would indicate either crack branching or microcracking with low associated energy.

It is interesting to note, however, that after this abundance of detected AE the magnitude of emission increases significantly while the time interval between bursts diminishes (Figure 5.60). The increase in AE magnitude implies an increase in energy as would be th case for an increase in total crack area. The diminishing time between AE burst also supports the contention of a decrease in structural integrity as the stress necessary for crack extension is obtained more rapidly. While the low level AE could be the coalescence of microcracks resulting in major crack formation and/or extension, much more testing is needed to establish the validity of such a hypothesis.
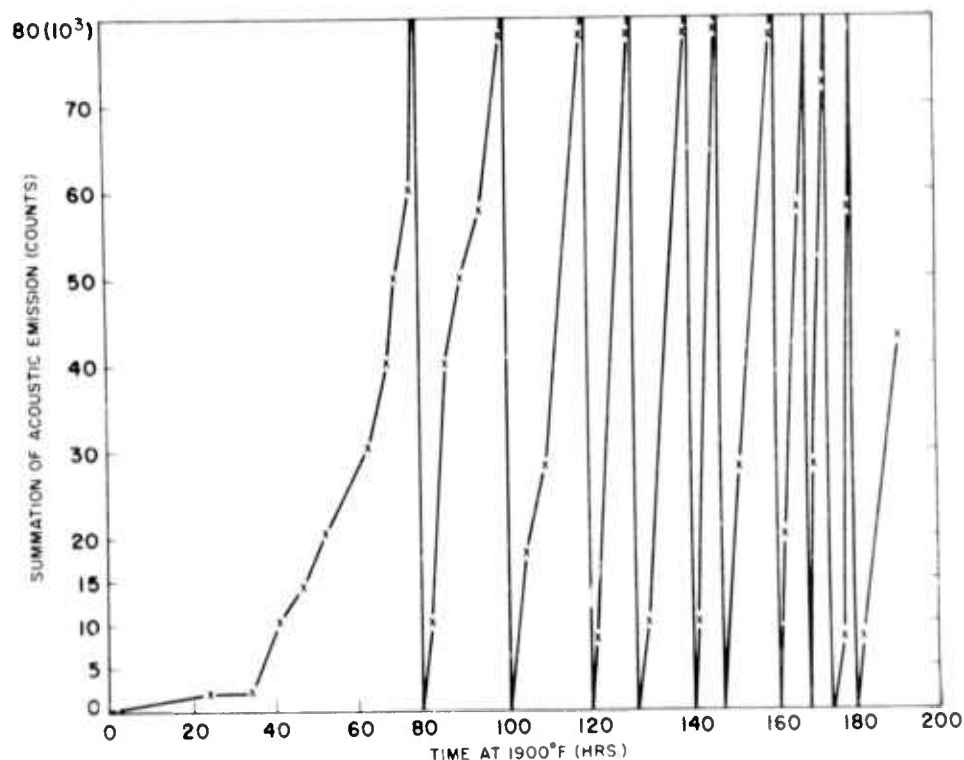
Figure 5.58   Stator Acoustic Emission Response vs Time at 1900°F, Summation Data

168
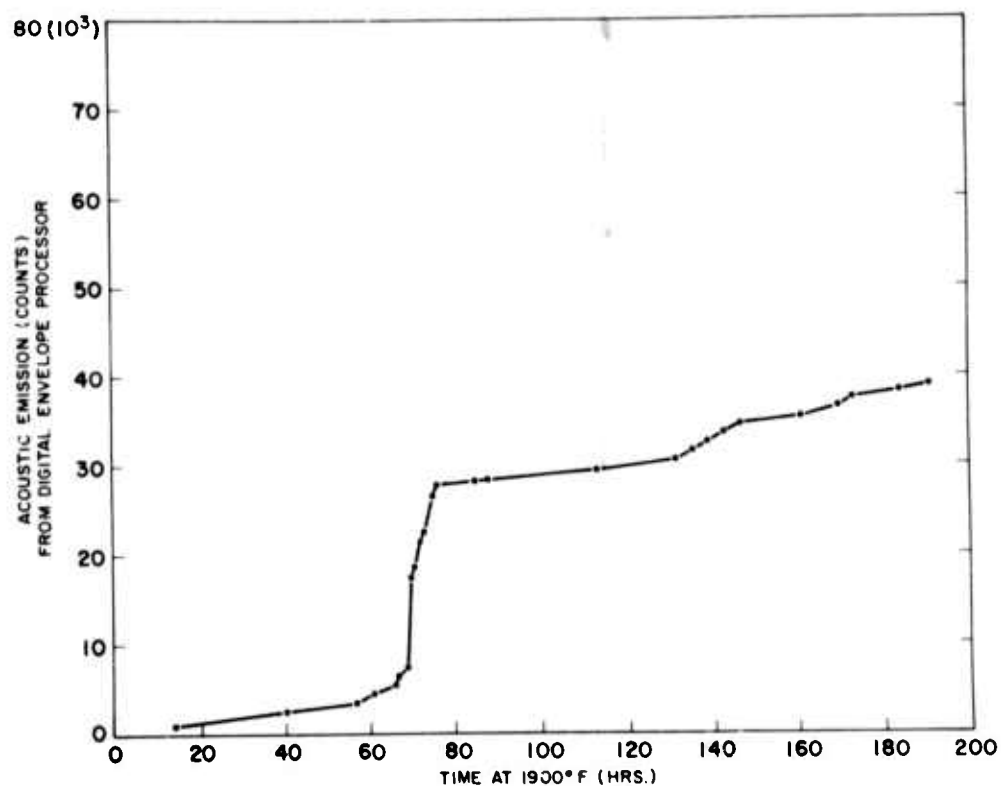
Figure 5.59   Stator Acoustic Emission Response vs Time
at 1900°F, "Burst" Data
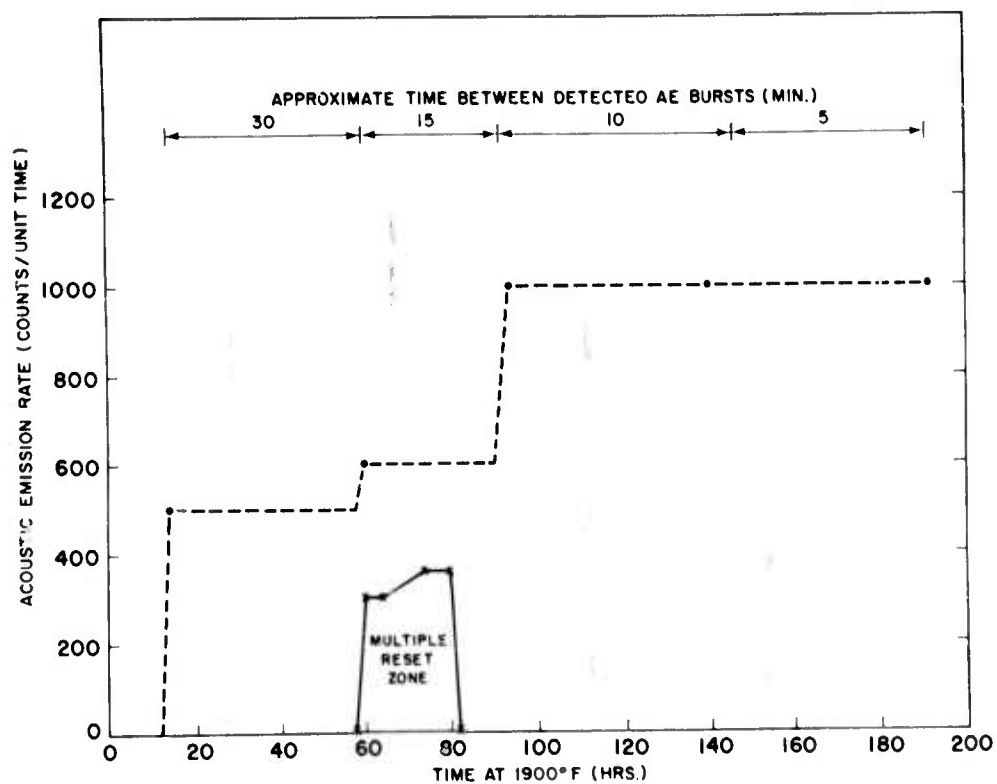
Figure 5.60   Stator Acoustic Emission Response vs Time
at Time at 1900°F, Rate Data

Upon completion of the test, the stator assembly was inspected for damage. Cracks in the outer shroud were visually apparent, however, not catastrophic. The use of 30x magnification also revealed other small cracks in the assembly.

This method of evaluating stator assemblies appears to provide useful information about stator quality. More stator assemblies will be so tested in this manner so that a more definitive quality correlation can be established.

5.3.3 X-RAY RADIOGRAPHY

Introduction

The duo-density blades and platform are made as one piece by injection molding [4] and at times subsurface flaws have been exposed during machining of the platform for assembly purposes. In order to eliminate these flawed components, work was performed in evaluating the ability of radiographic techniques for detecting these defects.

X-ray radiography has been used successfully to identify high density inclusions in hot pressed material billets and component hardware. However, this work was done with no quantitative knowledge of the resolution limits involved. Attempts have been made to define the resolution limits for both high and low density inclusions as well as voids.

Rotor Evaluation

Conventional x-ray radiography and the xeroradiographic processes [4] were compared for their usefulness at detecting subsurface flaws in as-molded rotor blade rings. The types of flaws encountered were found by excessive shrinkage during cooling subsequent to molding, laps and folds, impurities, and silicon metal/organic segregation.

Figures 5.61 and 5.62 indicate the potential of the respective processes. The flaws caused by shrinkage and laps or folds were readily detected by both techniques; however, the impurity and silicon metal/organic segregation type flaws were not. Figure 5.63 indicates an example of a shrink flaw found in an injection molded blade ring. The orientation of the void was an important factor since the indications detected by both methods were not continuous, although sectioning revealed a continuous, circumferential, shrink type of flaw. This implies that an optimum radiographic evaluation will necessitate establishing parameters in terms of several variables. Specifically, the process will be extremely dependent on the component material, the thickness of the section to be evaluated, and the geometry of the part with respect to
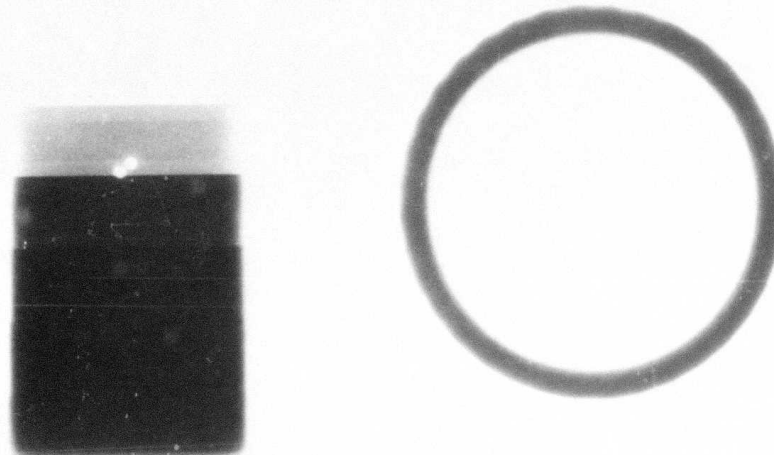
Figure 5.61   X-Ray Radiographic Reversal Print of Injection Molded Blade Ring and Platform

incident radiation. Perhaps the most important variable is the orientation of the flaw. Either the most probable flaw orientation must be established or the limiting conditions for its detection by a given technique must be determined in order to effectively evaluate a component for suspected flaws.
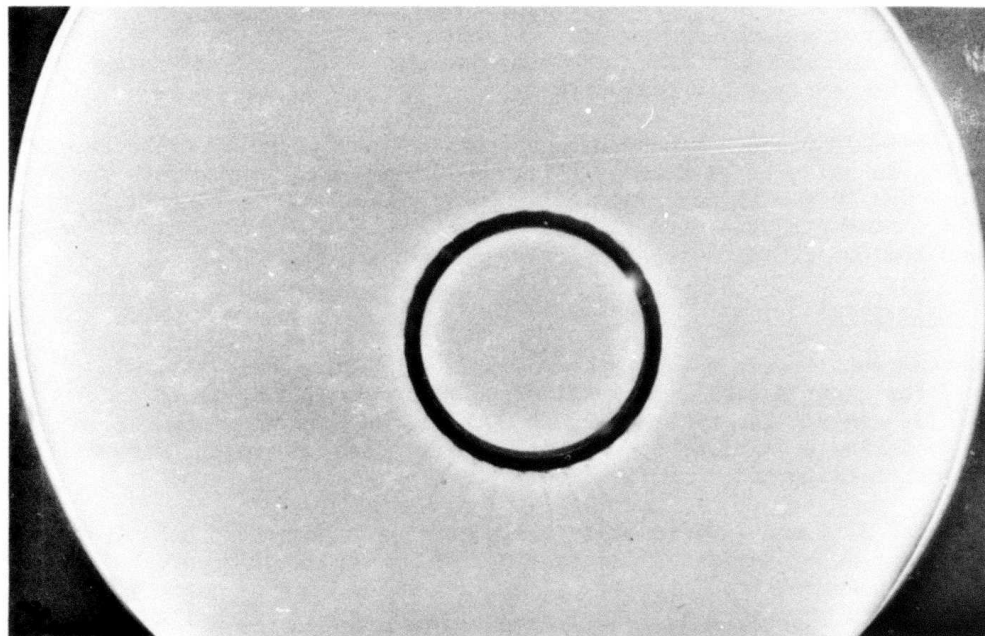
Figure 5.62   Xeroradiograph of Injection Molded Blade Ring and Platform
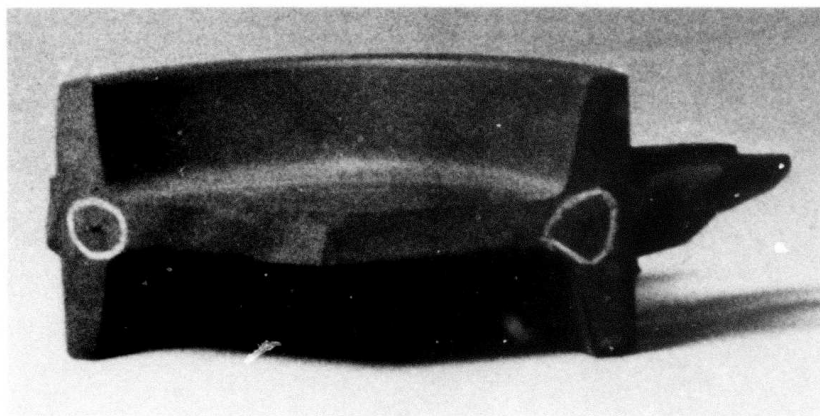
Figure 5.63   Typical Shrink Type Flaws Associated with Injection Molding a Blade Ring and Platform

High Density Inclusions

On the stationary turbine program to identify high density inclusions in hot pressed Si_3N_4, a large number of radiographs were taken with many different thicknesses of material. Initially, Kodak paper x-ray exposure

172

holders and Kodak Type M films were used. Since the objective was the detection of high density particles approaching 100 µm in size, it was essential to eliminate white artifacts caused by dust, etc. Therefore, a change was made to Kodak Type M-8 lead-pack film. Before exposure, a needle was inserted through the paper cover and the inside was evacuated. This resulted in a closer and more uniform specimen-to-film relationship. Table 5.21 summarizes the optimal exposure conditions for various thicknesses of silicon nitride.

TABLE 5.21

X-Ray Exposure Parameters For Hot-Pressed Si_3N_4

Material Thickness mm	Exposure Time Minutes	Current mA	Voltage KV	Source To Film Distance	Film	Remarks
3	3.0	10	40	60	M	
6	6.0	10	40	60	M	
12	5.0	10	60	60	M	
14	6.0	10	60	60	M	
16	7.0	10	60	60	M	
27	2.5	10	100	60	M	
30	3.5	10	100	60	M	
1.5-3	3.0	10	40	60	ML*	Vacuum
3-10	5.0	10	60	60	ML	Vacuum
12-23	4.0	10	70	60	ML	Vacuum
12-26	4.0	10	84	60	ML	Vacuum
16-27	5.0	10	70	60	ML	Vacuum
16-24	5.0	10	84	60	ML	Vacuum

*Kodak type M-8 lead-pack film.

A few controlled exposures were made to determine the sensitivity and limit of resolution of the x-ray inspection. Figure 5.64 shows prints of the x-ray radiographs of a Si_3N_4 billet containing 6 machined holes. The ring holes marked A-D were ultrasonically cavitated with a thin-wall steel tube. The rings are visible in all orientations. The holes marked 1 and 2 were drilled with a focused laser gun. Hole 1 is about 200 µm diameter and 4 mm deep, hole 2 is about 150 µm diameter and 5 mm deep. Both holes (large arrows) are detectable* in orientation a, but not in orientation b. The ratios of defect "size" to material thickness are 17% in orientation a and

---

*Note additional white artifacts. This is a drawback of printed radiographs.
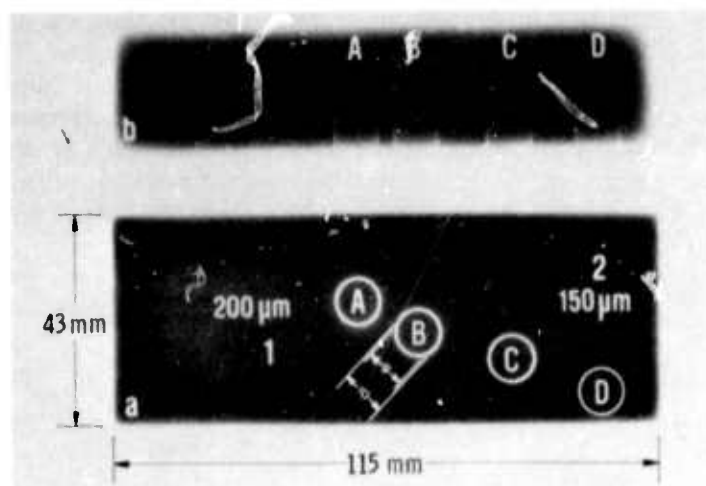
Figure 5.64   Radiograph of a Standard Si_3N_4 Block
(a-d) Ring Holes - Ultrasonically Cavitated
(1-2) Laser Holes

0.5% in orientation b. Other experiments with varying size holes show that
the resolution limit of a hole in Si_3N_4 is about 3%; that is, a cavity type
defect smaller than 3% of material thickness is not detectable. It is self-
evident that the resolution limit for a cavity containing low density Si_3N_4
will be higher than 3%.

A boron nitride inclusion, identified by ultrasonic scanning, could
not be confirmed by x-ray radiograph of the origin billets. The material
around the inclusion was cut to successively thinner sections, and radio-
graphed after each reduction. The 150 µm defect was identified at a section
thickness of 0.157 inches. Thus, the resolution limit for a BN inclusion
is of the order of 4%.

The resolution limit is related to the ratio of half value layers of
Si_3N_4 and the particular defect. A half value layer [18] is defined as
the thickness of the defect through which the attenuated radiation will
produce the same density on film as that produced by the unattenuated
beam with half the exposure. Half value is given by the expression:

$$ t_{1/2} = \frac{\ln 2}{\mu^1} $$

where μ^1 is the absorption coefficient and t is the thickness. Half value
layers for different defects found in Si_3N_4 are listed in Table 5.22 for
two conditions of radiation. The half-value layer was calculated using
appropriate absorption coefficients for the elements, and computed values
for the compounds. The resolution limits for the various defects in Si_3N_4
are also tabulated.

The resolution limit for high density particles were established by
crushing WC and sprinkling the powder on a ground surface of a piece of
Si_3N_4, 0.120 inches thick. The surface was mapped and the size of each
particle noted. The piece was then radiographed (Figure 5.65). Thickness
was built up by adding flat-ground pieces of Si_3N_4 similar to the one with the
WC particles on top. All particles remained visible at a total thickness of
1.10 inches. However, at 1.30 inches, a particle ∿125 µm became obscure.

174

Somewhat larger particles disappeared at 1.50 inches. All other particles were visible to 2.05 inches which was the maximum thickness radiographed. These data established the resolution limit for WC at about 0.5%. Similar tests were used to define resolution limit for steel particles at about 0.7%.

TABLE 5.22

Half-Value Layer in mm For Various Defects In Si_3N_4

Defect	0.04 MeV	0.08 MeV	Resolution Limit $t\ defect/t\ Si_3N_4$
Si_3N_4	7.5	22	------
BN Filled Cavity	35	46	0.04
Cavity, Hole, Crack	10^3	10^4	0.05
Steel Particle	0.24	2.1	0.007
WC Particle	0.045	0.049	0.005
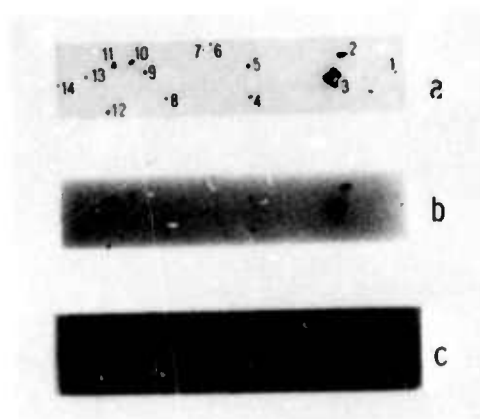
Figure 5.65   Radiography of Standard for WC Particles
(a) 0.125 in thick, 40 KV, 10 mA, 3 min
(b) 1.100 in thick, 74 KV, 10 mA, 5 min
(c) 1.300 in thick, 100 KV, 10 mA, 6 min

6. REFERENCES

1. McLean, A. F., Fisher, E. A., Harrison, D. E., "Brittle Materials Design, High Temperature Gas Turbine". AMMRC-CTR-72-3, Interim Report, March, 1972.

2. McLean, A. F., Fisher, E. A., Bratton, R. J., 'Brittle Materials Design, High Temperature Gas Turbine". AMMRC-CTR-72-19, Interim Report, September, 1972.

3. McLean, A. F., Fisher, E. A., Bratton, R. J., "Brittle Materials Design, High Temperature Gas Turbine". AMMRC-CTR-73-9, Interim Report, March, 1973.

4. McLean, A. F., Fisher, E. A., Bratton, R. J., "Brittle Materials Design, High Temperature Gas Turbine". AMMRC-CTR-73-32, Interim Report, September, 1973.

5. Prochazka, Svante, "Investigation of Ceramics for High Temperature Turbine Vanes", Contract No. N00019-17-C-0290, Final Report, March, 1972.

6. E. M. Levine, C. R. Robbins, and H. F. McMurdie, "Phase Diagrams for Ceramists", American Ceramic Soc. (1964), pp. 165, 209, and 515.

7. R. Rosen, J. Berson, and G. Urbain, "Rev. Hautes Temper et Refract". 1, (1964) pp. 159.

8. W. A. Zrsman, "Contact Angle, Wettability and Adhesion", A. F. Gould, ed., Am. Chem. Soc. (1964), p. 3.

9. S. K. Rhee, "Wetting of Ceramics by Liquid Metals", J. American Cer. Soc., Vol. 7, 1971, p. 332.

10. T. J. Whalen and M. Humenik, Jr., "Sintering and Related Phenomena", G. C. Kuszynski, N. A. Hooton and C. F. Gibbon, edts. Gordon and Breach, New York (1967), p. 715.

11. Wild, S. Grieveson, P., and Jack, K. H., "Role of Silicon Monoxide in the Production and Stability of Silicon Nitrides and Oxynitrides", Presented at 74th Annual Meeting of the American Ceramic Soc., Washington, D. C., May, 1972.

12. D. R. Stull and H. Prophet, et al., "JANAF Thermochemical Tables", NSRDS-NBS 37, (1971).

13. J. J. Byerley and W. K. Teo, "Equilibrium Formation and Thermodynamic Properties of Gaseous Silicon Monosulfide", Met. Trans., Vol. 4, 1973, pp. 419-422.

14. Messier, D. R. and Wong, P. "Dependence of Mechanical and Dielectric Properties of Si_3N_4 on Fabrication Conditions", Presented at 75th Annual Meeting of the American Ceramic Society, Cincinnati, Ohio, April, 1973.

15. Hausner, H. H., and A. R. Poster, "Slip Casting of Metal Powders and Metal - Ceramic Combinations", in Powder Metallurgy, ed. by W. Leszynski, New York: Interscience Publishers (1961), 461-506.

16. Overbeek, J. T. G., "Colloid Science", Vol. 1, ed. by H. R. Kruyt. New York: Elsevier Pub. Co. (1952).

17. St. Pierre, P. D. S., "Slip Casting Metals", Gen. Elec. Res. Rept. 59-RL-2281 M (October, 1959).

18. McMaster, Robert C., "Non-Destructive Testing Handbook", The Ronald Press, New York, 1959, p. 13-30.

ARMY MATERIALS AND MECHANICS RESEARCH CENTER
WATERTOWN, MASSACHUSETTS 02172

TECHNICAL REPORT DISTRIBUTION

No. of Copies	To
1	Office of the Director, Defense Research and Engineering, The Pentagon, Washington, D.C. 20301
12	Commander, Defense Documentation Center, Cameron Station, Building 5, 5010 Duke Street, Alexandria, Virginia 22314
1	Metals & Ceramics Information Center, Battelle Memorial Institute, 505 King Avenue, Columbus, Ohio 43201
2	Chief of Research and Development, Department of the Army, Washington, D.C. 20310 ATTN: Physical and Engineering Sciences Division (CRD PES - Dr. Sullivan)
1	Commanding Officer, Army Research Office (Durham), Bx CM, Duke Station Durham, North Carolina 27706 ATTN: Dr. H. M. Davis
1	Commanding General, U.S. Army Material Command, Washington D.C. 20315 ATTN: AMCRD-TC (Dr. El-Bisi)
1	ATTN: ANCDL (Dr. Dillaway)
1	Commanding General, U S. Army Missile Command, Redstone Arsenal, Alabama 35809 ATTN: Technical Library
1	Commanding General, U.S. Army Munitions Command, Dover, New Jersey 07801 ATTN: Technical Library
3	Commanding General, U.S. Army Tank-Automotive Command, Warren, Michigan 48090, ATTN: AMSTA-BSL, Research Library Br, ATTN: AMSTA-RKM (Mr. C. Green), ATTN: AMSTA-RGR (Mr. Engel)
1	Commanding General, U.S. Army Weapons Command, Research and Development Directorate, Rock Island, Illinois 61201 ATTN: AMSWE-RDR
1	Commanding Officer, Aberdeen Proving Ground, Maryland 21005 ATTN: Technical Library, Building 313
1	Commanding Officer, U.S. Army Aviation Material Laboratories, Fort Eustis, Virginia 23604
1	Librarian, U.S. Army Aviation School Library, Fort Rucker, Alabama 36360 ATTN: Bldg. 5907
1	Commanding Officer, USACDC Ordance Agency, Aberdeen Proving Ground, Maryland 21005 ATTN: Library, Building 350

ARMY MATERIALS AND MECHANICS RESEARCH CENTER
WATERTOWN, MASSACHUSETTS 02172

TECHNICAL REPORT DISTRIBUTION

No. of Copies	To
1	U.S. Army Air Mobility Research and Development Laboratory ATTN: J. White, Assistant Technical Director, Eustis Directorate, Ft. Eustis, Virginia 23604
1	U.S. Army Air Mobility Research and Development Laboratory ATTN: R. Berrisford, Chief, Structures Division, Eustis Directorate, Ft. Eustis, Virginia 23604
1	U.S. Army Air Mobility Research and Development Laboratory ATTN: T. Coleman, Director, Langley Directorate, Langley Research Center, Langley Field, VA 23365
2	U.S. Army Air Mobility Research and Development Laboratory ATTN: J. Accurio, Director, Lewis Directorate, NASA, Lewis Research Center, 21000 Brookpark Road, Cleveland, Ohio 44135
1	Commanding General, U.S. Army Aviation Systems Command, ATTN: R. Long, Deputy Director RD&E, P.O. Box 209, St. Louis, MO 63166
1	Office Chief Research & Development, Department of Army, ATTN: Col. J. Barnett, Physical & Engineering Sciences Division, Washington, D.C. 20315
1	Office, Chief Research & Development, Department of Army, ATTN: Lt. Col. H. B. Snyder, The Pentagon, Washington, D.C. 20310
1	Commanding General, Army Missile Command, ATTN: AMCDL, Webb Taylor, 5001 Eisenhower Avenue, Alexandria, VA 22304
1	Commanding General, Army Missile Command, ATTN: AMCRD-F, J. Beebe, Washington, D.C. 20315
1	Office, Chief Research & Development, Department of the Army, ATTN: R. Ballard, Physical & Engineering Sciences Division, Washington, D.C. 20315
1	Commander, USA Foreign Science & Technology Center, ATTN: AMXST-SD3, Mr. C. Petschke, 220 7th Street NE, Charlottesville, VA 22901
1	Mr. Irving Machlin, High Temperature Materials Div., Materials and Processes Branch, (NAIR-52031D), Naval Air Systems Command, Department of the Navy, Washington, D.C. 20360

ARMY MATERIALS AND MECHANICS RESEARCH CENTER
WATERTOWN, MASSACHUSETTS 02172

TECHNICAL REPORT DISTRIBUTION

No. of Copies	To
1	Commanding Officer, U.S. Army Engineer Waterways Experiment Station, Vicksburg, Mississippi 39180 ATTN: Research Center Library
	Commanding Officer, U.S. Army MERDEC, Fort Belvoir, Virginia 22060
2	ATTN: STSFB-EP (Mr. James Horton)
1	ATTN: STSFB-EP (Mr. W. McGovern)
1	ATTN: AMCPM-FM (Mr. Allen Elkins)
	Director, Army Materials and Mechanics Research Center, Watertown, Massachusetts 02172
2	ATTN: AMXMR-PL
1	AMXMR-PR
1	AMXMR-CT
1	AMXMR-AP
1	AMXMR-X (Dr. Gorum)
1	AMXMR-EO (Dr. Katz)
2	AMXMR-TM (Dr. Lenoe)
2	AMXMR-D (Dr. Priest)
1	AMXMR-EO (Dr. Messier)
2	AMXMR-P (Dr. Burke)
1	AMXMR-MS (Mr. MacDonald)
	Advanced Research Projects Agency, 1400 Wilson Blvd., Arlington, Virginia 22209
2	ATTN: Director
1	Dep Director
1	Director of Materials Sciences - Dr. Stickley
1	Dep. Director Materials Sciences - Dr. van Reuth
1	Tech. Information Office - Mr. F. A. Koether
1	Mr. R. M. Standahar, Office of the Director of Defense, Research and Engineering, Room 3D1085, Pentagon, Washington, D.C. 20301
1	Mr. Charles F. Bersch, Department of the Navy, Naval Air Systems Command, Washington, D.C. 20360
1	Dr. A. M. Diness, Metallurgy Branch, Code 471, Office of Naval Research, 800 N. Quincy Street, Arlington, Virginia 22217
2	U.S. Army Air Mobility Research and Development Laboratory, Advanced Systems Research Office, Ames Research Center, Moffett Field, California 94035 ATTN: F. Immen, J. Wheatly

ARMY MATERIALS AND MECHANICS RESEARCH CENTER
WATERTOWN, MASSACHUSETTS 02172

TECHNICAL REPORT DISTRIBUTION

No. of Copies	To
1	Mr. Keith Ellingsworth, Office of Naval Research, Power Program, Arlington, VA 22217
1	Mr. John Fairbanks, Naval Ships Engineering, Prince George Center, Hyattsville, Maryland 20782
1	Capt. D. Zabierek, Air Force Aeropropulsion Lab, Wright-Patterson Air Force Base, Ohio 45433
1	Capt. Smyth, Air Force Materials Laboratory, Wright-Patterson Air Force Base, Ohio 45433
1	Mr. S. Lyons, Wright-Patterson Air Force Base, Ohio 45433
3	Aerospace Research Laboratory, ATTN: ARL-LL, Wright-Patterson Air Force Base, Ohio 45433 ATTN: Dr. Henry Graham ATTN: Dr. James Wimmer ATTN: Maj. L. Jacobson
4	NASA Lewis Research Center, 21000 Brookpark Road, Cleveland, Ohio 44135 ATTN: Mr. W. Sanders Dr. Hubert Probst Dr. Robert C. Bill Mr. Donald Guentert
1	Dr. G. C. Deutsch, Ass't Director of Research (Materials), Code RR-1 NASA, Washington, D.C. 20546
1	Mr. George Staber, Office of Coal Research, U.S. Department of the Interior, Washington, D.C. 20240
1	Dr. S. Wiederhorn, Physical Properties Section, Institute for Materials Research, National Bureau of Standards, Washington, D.C. 20234
1	Mr. R. Reynik, Director, Div. of Materials Research, National Science Foundation, 1800 G. Street, N.W., Washington, D.C. 20550
1	Dr. Robb Thomson, Senior Research Scientist, Rm B109, Bld. 225, National Bureau of Standards, Washington, D.C. 20234
1	Mr. H. Morrow, Eustis Directorate, AMRDL, Fort Eustis, VA 23604
1	Dr. R. Warren, Contact Officer, Defense Research & Development Staff, British Embassy, 3100 Massachusetts Avenue N.W., Washington, D.C. 20008

ARMY MATERIALS AND MECHANICS RESEARCH CENTER
WATERTOWN, MASSACHUSETTS 02172

TECHNICAL REPORT DISTRIBUTION

No. of Copies	To
3	Environmental Protection Agency, Division of Advanced Automotive Systems, 2565 Plymouth Road, Ann Arbor, Mi 48105 ATTN: Mr. George Thur Mr. Robert Schultz Mr. Thomas Sebestyen
1	Dean Daniel C. Drucker, Engineering College, University of Illinois, Urbana, Illinois 61801
1	Professor Merton Flemings, Massachusetts Institute of Technology, Cambridge, Massachusetts 02139
1	Professor Edward E. Hucke, Materials and Metallurgical Engineering, The University of Michigan, Ann Arbor, MI 48104
1	Professor Frank A. McClintock, Department of Mechanical Engineering, Massachusetts Institute of Technology, Cambridge, Massachusetts 02139
1	Dr. R. M. Spriggs, Assistant to the President, Lehigh University, Bethlehem, Pennsylvania 18015
1	Mr. J. D. Walton, Jr., EES, Georgia Tech., Atlanta, Georgia 30332
1	Mr. Y. Baskin, Manager Inorganic Chemical Research, Technical Center, Ferro Corporation, 7500 East Pleasant Valley Road, Independence, Ohio 44131
3	Mr. Robert Beck, Dept. Head, Development Materials, Teledyne CAE, 1330 Laskey Road, Toledo, Ohio 43601 Dr. Eli Benstien, Director of Engineering Mrs. Marlene S. Dowdell, Librarian
1	Dr. J. E. Burke, General Electric Company, Corporate Research & Development, P.O. Box 8, Schenectady, New York 12301
1	Dr. C. A. Bruch, Manager, Advanced Studies, General Electric Company, Aircraft Engine Group, Cincinnati, Ohio 45215
1	Mr. A. R. Canady, Caterpillar Tractor Company, Technical Center Building F, Peoria, Illinois 61602
1	Mr. William B. Crandall, IIT Research Institute, 10 West 35th Street, Chicago, Illinois 43601

TECHNICAL REPORT DISTRIBUTION

No. of Copies	To
1	Mr. L. M. Donley, Owens Illinois Glass, 1900 North Westwood Avenue, Toledo, Ohio 43601
1	Mr. E. J. Dulis, President, Colt Industries, Materials Research Center, Box 88, Pittsburgh, PA 15230
1	Mr. O. Prachar, Passenger Car Turbine Department, Engineering Staff, General Motors Technical Center, Warren, MI 48090
1	Mr. Winston Duckworth and Mr. Lewis E. Hulbert, Battelle Columbus Laboratories, 505 King Avenue, Columbus, Ohio 43201
1	Mr. R. Engdahl, Energy Research Corporation, Bethel, Connecticut 06801
1	Mr. Peter L. Fleischner, National Beryllia Corp., Haskell, New Jersey 07420
1	Mr. O. I. Ford, Technical Manager, Combustor Systems, Aerojet Liquid Rocket Company, P.O. Box 18222, Sacramento, Calf. 95813
1	Mr. Chester T. Sims, Manager, Advanced Materials General, Electric Company, Gas Turbine Products Div., Schenectady, N.Y. 12301
1	Mr. E. W. Hauck, Market Manager Engine, Components, Norton Company, 1 New Bond Street, Worcester, Massachusetts 01606
1	Mr. M. Herman, Detroit Diesel Allison Division, General Motors Corporation, Indianapolis Operations, P.O. Box 894, Indianapolis, Indiana 46206
1	Mr. J. B. Mann, Director of Research, Chrysler Corporation, P.O. Box 1118, Detroit, MI 48231
1	Mr. James F. Holloway, Materials Project Engineer, Pratt & Whitney Corporation, 400 Main Street, E. Hartford, Connecticut 06108
1	Dr. Paul Jorgensen, Associate Director, Materials Laboratory, Stanford Research Institute, Menlo Park, California 94025
1	Dr. A. V. Illyn, Technical Director, Refractories Division, Babcock & Wilcox, Old Savannah Road, Augusta, Georgia 30903
1	Mr. Paul F. Jahn, Vice President, Fiber Materials, Inc., Broadway and Main Streets, Graniteville, Massachusetts 01829

TECHNICAL REPORT DISTRIBUTION

No. of Copies	To
1	Dr. Robert F. Kirby, Materials Engineering Dept. 93-393M, AiResearch Manufacturing Company, Div. of the Garrett Corporation, Sky Harbor Airport, 402 South 36th Street, Phoenix, Arizona 85034
1	Mr. John G. Lanning, Corning Glass Works, Corning, NY 14830
1	Mr. William D. Long, Manager, Product Development, K-Ramics, Kaman Sciences Corporation, Garden of the Gods Road, Colorado Springs, Colorado 80907
1	Mr. James Lynch, Metals & Ceramics Information Center, Battelle Columbus Laboratories, 505 King Avenue, Columbus Ohio 43201
1	Mr. C. H. McMurtry, Project Manager, Research and Development Div., The Carborundum Company, Niagara Falls, New York 14302
1	Dr. Deo Mattoon, Sing Sing Road, Horseheads, New York 14845
1	Mr. G. Kookootsedes, Market Development, Resins and Chemicals, Dow Corning, Midland, Michigan 48640
1	Professor Burton Paul, Dept. of Mechanical Engineering, University of Pennsylvania, Philadelphia, Pennsylvania 19104
1	Mr. Y. K. Pei, Owens Illinois Glass, 1020 North Westwood Avenue, Toledo, Ohio 43607
1	Dr. Jerry D. Plunkett, President, Materials Consultants, Inc., 2150 South Josephine Street, Denver, Colorado 80210
1	Mr. J. A. Rubin, President, Ceradyne Incorporated, 8948 Fullbright Avenue, Chatsworth, California 91311
1	Mr. P. Hansen, Director of Corporate Dev., Kawecki-Berylco Industries, Inc., P.O. Box 1462, Reading, Pennsylvania 19603
1	Mr. Jack W. Sawyer, Gas Turbine International, 4519 Eighteen Street North, Arlington, VA 22207
1	Mr. D. W. McLaughlin, Research & Development Div., Mechanical Technology, Inc., 968 Albany-Shaker Road, Latham, New York 12110

TECHNICAL REPORT DISTRIBUTION

No. of Copies	To
1	Mr. A. R. Stetson, Chief, Process Research Laboratories, Mail Zone R-1, Solar Div. of Int. Harvester Company, 2200 Pacific Highway, San Diego, California 92112
1	Dr. M. L. Torti, Norton Company, 1 New Bond Street, Worcester Massachusetts 01606
1	Dr. T. Vasilos, Applied Technology Division, Avco Corp., Lowell Industrial Park, Lowell, Massachusetss 01851
1	Mr. Francis L. VerSnyder, Manager, Materials Engineering and Research Lab, Pratt & Whitney Corporation, 400 Main Street, E. Hartford, Connecticut 06108
1	Mr. McCoy, Materials Engineering, Garrett-AiResearch Dept. 93-393M, 412 South 36th Street, Phoenix, Arizona 85034
1	Mr. Donald E. Weyer, Dow Corning Corporation, Midland, MI 48640
1	Dr. Michael Guinan, B. Div./L-24, P.O. Box 808, Lawrence Livermore Laboratory, Livermore, California 94550
1	Dr. Mark Wilkins, B Div./L-24, P.O. Box 808, Lawrence Livermore Laboratory, Livermore, California 94550
1	Dr. Charles J. McMahon, Jr., Assoc. Prof. Materials Science, School of Metallurgy & Materials Science, University of Pennsylvania, 3231 Walnut Street, Philadelphia, Pennsylvania
1	Mr. Gaylord D. Smith, The International Nickel Co., Inc., 1 New York Plaza, New York, New York 10004
1	Mr. H. R. Schelp, Garrett Corporation, 9851 Sepulveda Blvd., Los Angeles, California 90009
1	Dr. Robert Widmer, President, Industrial Materials Technology 19 Wheeling Avenue, Woburn, Massachusetts
1	Dr. William Wells, Lawrence Livermore Lab, Livermore, California 94550
1	Prof. R. P. Kroon, University of Pennsylvania, Philadelphia, Pennsylvania
1	Dr. Paul G. Shewmon, D212, Argonne National Laboratory, 9700 South Cass Avenue, Argonne, Illinois 60439

ARMY MATERIALS AND MECHANICS RESEARCH CENTER
WATERTOWN, MASSACHUSETTS   02172

TECHNICAL REPORT DISTRIBUTION

No. of Copies	To
1	Dr. Thomas D. McGee, Professor of Ceramic Engineering, Iowa State University, Ames, Iowa 50010
1	Mr. Joe Glotz, Department of the Navy, Naval Air Propulsion Test Center, Trenton, New Jersey 08628
1	Mr. John Miguel, Naval Underwater System Center, Newport, Rhode Island
1	Mr. Robert Benham, AEP-22, U.S. Naval Air Propulsion Test Center (AE), Philadelphia, PA 19112
1	Mr. R. Barry Strachan, Williams Research Corp., Walled Lake, Michigan 48088
1	Mr. S. Walosin, Curtis-Wright Corp. One Passaic Street, Woodridge, N.J. 07075
1	Prof. Marc Richman, Engineering Division, Brown University, Providence, Rhode Island 02912
1	Mr. R. Rice, Naval Research Laboratory, Washington, D.C. 20390
1	Mr. George A. Wacker, Head Metal Physics Br., Naval Ships Research & Development Center, Annapolis, Md. 21402, ATTN: Code 2812
1	Dr. R. Charles, Manager Ceramics Branch, General Electric Co., Corporate R & D Center, P.O. Box 8, Schenectady, New York 12301
1	Mr. C. F. Cline, Manager, Strength Physics Department, Allied Chemical Corporation, P.O. Box 1021R, Morristown, New Jersey 07960
1	Dr. J. T. Bailey, American Lava Corp., Chattanoga, Tennessee 37405
1	Mr. S. T. Wlodek, Cabot Corp. Stellite Div., 1020 West Park Avenue, Kokomo, Indiana 46901
2	Cummins Engine Company, Inc., Columbus, Indiana 47201 Mr. R. Kano, Mr. K. J. Mather
1	Mr. J. D. Mote, EF Industries, Inc., 1301 Courtesy Rd. Louisville, Colorado 80027
1	Mr. William E. Gurwell, Eaton Corporation, Research Center 26201 Northwestern Highway, Southfield, MI 48076

TECHNICAL REPORT DISTRIBUTION

No. of Copies	To
1	Mr. Robert W. Gibson, Jr., Head, Library Dept. General Motors Corporation GM Technical Center, Warren, MI 48090
1	Mr. R. L. Lormand, Lawrence Radiation Lab, P.O. Box 808, Livermore, California 94550
2	Ms. Bolick, National Aeronautics and Space Adminstration Goddard Space Flight Center, Greenbelt, Maryland 20771
1	Mr. Neil T. Saunders, Ch. Mat'ls Appl'n Branch, National Aeronautics and Space Administration, Lewis Research Center, Cleveland, Ohio 44135
1	Ms. Rayna Lee Caplan, Librarian, Northern Research and Engineering Corp., 219 Vassar Street, Cambridge, Mass. 02139
1	Mrs. Jame Bookmyer, Info. Services Div., PPG Industries, Inc., P.O. Box 11472, Pittsburgh, Pennsylvania 15238
1	Mr. P. W. Parsons, Manager, Commercial Research Dept., Stackpole Carbon Company, St. Marys, Pennsylvania 15857
1	Ms. Lucille Steelman, Order Librarian, Stanford Research Institute ATTN: G-037 Library, Menlo Park, Calif. 94025
1	Technical Library, TRW Equipment, TRW Inc., 23555 Euclid Avenue, Cleveland, Ohio 44117
1	Dr. E. P. Flint, U.S. Department of Interior, Bureau of Mines, Room 4513, Interior Bldg., Washington, D.C. 20240
1	Mr. W. Wheatfall, Naval Ship R & D Lab, Code 2812, Annapolis, Maryland 21402
1	Dr. Joseph E. Motherway, University of Bridgeport, Bridgeport, Connecticut 06602
1	Dr. Soloman Musikant, Manager, Metallurgy & Ceramics Lab General Electric Valley Forge, Valley Forge, PA
1	Dr. Bruce A. Ewing, Chief Mat'ls Development, Mat'ls & Process Technology Lab., Avco Corporation, 550 S. Main Street Stratford, Connecticut 06497
1	Mr. Donald Lapades, The Aerospace Corporation, P.O. Box 92957, Los Angeles, California 90009

ARMY MATERIALS AND MECHANCIS RESEARCH CENTER
WATERTOWN, MASSACHUSETTS 02172

TECHNICAL REPORT DISTRIBUTION

No. of Copies	To
1	Mr. Thomas J. Ahrens, Assoc. Prof. of Geophysics, California Institute of Technology, Seismological Laboratory, 295 San Rafael Avenue, P.O. Bin 2, Arroyo Annex, Pasadena, California 91109
1	Mr. Victor de Biasi, Editor, Gas Turbine World, P.O. Box 494, Southport, Connecticut 06490
1	SKF Industries, Inc., Engineering & Research Center, 1100 1st Avenue, King of Prussia, PA 19406, ATTN: Warren E. Jameson & Harish Dalal
1	Dr. Edward Reynolds, General Motors Technical Center, Passenger Car Turbine Division, Warren, MI 48090
1	Dr. Wm. R. Freeman, Jr., V.P. and Technical Director, Howmet Corporation, Superalloy Group, One Misco Drive, Whitehall, Michigan 47461
1	Mr. D. William Lee, Arthur D. Little, Inc. Acorn Park, Cambridge, Massachusetts 02140
1	Dr. L. Kaufman, Project Director, Manlabs, Inc., 21 Erie Street, Cambridge, Massachusetts 02139
1	Prof. Morris E. Fine, Northwestern University, The Technological Institute, Dept. of Materials Science, Evanston, Illinois
1	Coors Porcelain Company, 600 Ninth Street, Golden, Colorado 80401, ATTN: Mr. M. R. Nadler
1	Prototype Developments Associates, Esplanade I, Suite 204 3001 Red Hill Avenue, Costa Mesa, California 92626, ATTN: Mr. John I. Slaughter, President
1	Raytheon Company, Research Division Library, Foundry Avenue, Waltham, Massachusetts 02154, ATTN: Ms. Madaleine Bennett, Librarian
1	Prof. T. L. Chu, Southern Methodist University, Institute of Technology, Electronic Sciences Center, Dallas, Texas 75222
1	Mr. H. Stuart Starrett, Head, Mechanics Section, Southern Research Institute, 2000 Ninth Avenue South, Birmingham, Alabama 35205

ARMY MATERIALS AND MECHANICS RESEARCH CENTER
WATERTOWN, MASSACHUSETTS 02172

TECHNICAL REPORT DISTRIBUTION

No. of Copies	To
1	Dr. O. Conrad Trulson, Union Carbide Corporation, Carbide Products Division, 270 Park Avenue, New York, New York 10017
1	Prof. Earl R. Parker, University of California, Department of Materials Science and Engineering, 286 Hearst Mining Building, Berkeley, California 94720
1	Mr. Willard H. Sutton Manager, Ceramics Projects, Special Metals Corporation, New Hartford, New York 13413
1	Dr. Maurice J. Sinnott, Department of Chemical & Metallurgical Engineering, The University of Michigan, Ann Arbor, MI 48104
1	Mrs. R. J. Benacquista, R.I.A.S., 9190 Red Branch Road, Columbia, Maryland 21043
1	Prof. M. C. Shaw, Head, Department of Mechanical Engineering, Cornegie-Mellon University, Pittsburgh, Pennsylvania 15213
1	Mr. Gail Eichelman, Manufacturing Processes Div., Air Force Mateials Laboratory, Wright-Patterson AFB, Ohio 45433
1	Dr. J. C. Lewis, Metals & Minerals Economics Div. Battelle Memorial Institute, 505 King Avenue, Columbus, Ohio 43201
1	Massachusetts Institute of Technology, Cambridge, Massachusetts, 02139, ATTN: Prof. D. W. Kingery, Rm. 13-4090
1	Prof. Michael F. Ashby, Gordon McKay Professor of Metallurgy, Pierce Hall, Harvard University, Cambridge, Massachusetts 02138
1	Dr. Richard G. McKaig, Owens-Illinois Development Center, P.O. Box 1035, Toledo, Ohio 43666
1	Prof. I. B. Cutler, University of Utah, College of Engineering Division of Materials Science and Engineering, Salt Lake City, Utah 84112
1	Mr. J. A. Alexander, Manager, Materials Research Department, TRW 23555 Euclid Avenue, Cleveland, Ohio 44117
1	Airesearch Manufacturing Company, Sky Harbor Airport, 402 South 36th Street, Phoenix, Arizona 85034, Attn: Supervisor, Propulsion Engine Advanced Technology Dept., 93-12M
1	Mr. M. Blake, Norton Company, One New Bond Street, Worcester, Mass. 01606

ARMY MATERIALS AND MECHANICS RESEARCH CENTER
WATERTOWN, MASSACHUSETTS 02172

TECHNICAL REPORT DISTRIBUTION

No. of Copies	To
1	Dr. H. P. Kirchner, Ceramic Finishing Company, P.O. Box 498, State College, Pennsylvania 16801
1	Dr. Morris Berg, General Motors Corporation, AC Spark Plug Division Flint, Michigan 48556
1	Dr. Michael J. Noone, General Electric Company, Space Sciences Laboratory, Box 8555, Philadelphia, Pennsylvania 19101
1	Mr. Richard Kliener, GTE Sylvania, Tonawarda, Pennsylvania 18848
1	Mr. F. E. Krainess, Rockwell International Corporation, D/391-204 AB70 12214 Lakewood Boulevard, Downey, California 90241
1	Mr. David Cormier, Nuclear Planning Division, Stone and Webster Engineering Corporation, 99-13 High Street, Boston, Massachusetts 02107
1	Mr. John F. Burst, Technical Director, General Refractories Company, 1520 Locust Street, Philadelphia, Pennsylvania 19102
1	Mr. V. A. Chase, Chief of Development Laboratory, Whittaker Corporation, Research and Development Division, 3540 Aero Court, San Diego, Cal. 92123
1	Dr. Stanley Waugh, Research Division, Raytheon Corporation, Research Division, 28 Seyon Street, Waltham, Massachusetts 02154
1	Coors Porcelain Company, Research Department, 17750 West 32nd Avenue, Golden, Colorado 80401
1	Professor Robert F. Davis, North Carolina State University, Department of Materials Science, Box 5427, Raleigh, North Carolina 27607
1	Dr. H. von E. Doering, Manager, Fuels/Corrosion Unit, General Electric Company, Gas Turbine Products Division, Building 53-311, Schenectedy, New York 12345
1	Dr. R. Ruh, AFML/LLS, Air Force Materials Laboratory, Wright-Patterson AFB, Ohio 45433
1	Mr. Michael E. Naylor, General Motors Technical Division, Passenger Car Turbine Division, Warren, Michigan 48090
1	Mr. John V. Milewski, ESSO Research and Engineering Company, Government Research Laboratory, P.O. Box 8, Linden, New Jersey 07036
1	Mr. M. J. Klein, Research Staff Specialist, Mail Zone R-1, Solar, 2200 Pacific Highway, P.O. Box 80966, San Diego, California 92138

TECHNICAL REPORT DISTRIBUTION

No. of Copies	To
1	Dr. Frank Galasso, United Aircraft Research Laboratories, East Hartford Conn. 06108
8	Lt. Col. E. E. Chick, Chief, Materials Branch, European Research Office U. S. Army R&D Group, (EUR), Box 15, FPO New York 09510
1	Dr. Joseph Griffo, U. S. Atomic Energy Commission Space Nuclear Systems Division, Century XXI Building, Mail Station F-309, Washington, D.C. 20545
1	Mr. Joseph Simpson, Rohr Industries, Inc., Technical Library P.O. Box 1516, Chula Vista, California 92012
1	Mr. Philip J. Willson, Chemical Research, Chrysler Corporation, Box 1118, CIMS 418-19-18, Detroit, Michigan 48231
1	Mr. William Combs, Battelle Memorial Institute, 2030 M Street N.W. Washington, D.C. 20036
1	Mr. M. A. Schwartz, U.S. Department of the Interior, Bureau of Mines Tuscaloosa Metallurgy Research Laboratory, P.O. Box 1, University, Alabama 35486
1	Turbo Power and Marine Systems, Inc., ATTN: Mr. Carl Merz, Farmington, Connecticut 06032
1	Mr. R. N. Singh, Argonne National Laboratory, Materials Science Division 9700 South Cass Avenue, Argonne, Illinois 60439
1	Mr. Richard E. Engdahl, Deposits & Composites, Inc., 1821 Michael Faraday Drive, Reston, Virginia 22090
1	Mr. Leonard Topper, Office of Energy Policy, National Science Foundation 1800 G Street N. W., Washington, D.C. 20550
1	Mr. Ron Lowrey, U.S. Bureau of Mines, P.O. Box 70, Albany, Oregon 97321
1	Materials Science Corporation, Technical Library, Blue Bell Office Campus, 1777 Walton Road, Blue Bell, Pennsylvania 19422
1	Ms. Sharon Wright, Creare Inc., Technical Library, Hanover, New Hampshire 03755

ARMY MATERIALS AND MECHANICS RESEARCH CENTER
WATERTOWN, MASSACHUSETTS 02172

TECHNICAL REPORT DISTRIBUTION

No. of Copies	To
1	Mr. John Polyansky, Gas Turbine Design Engineering, Turbodyne Corporation, 626 Lincoln Avenue S E, St. Cloud, Minnesota 56301
1	Mr. Donald J. Legacy, Turbodyne Corporation, Wellsville, New York 14895
1	Mr. P. R. Miller, NASA Headquarters, Code RPD, 600 Independence Avenue S. W., Washington, D.C. 20546
1	Dr. J. J. Stiglich, Jr., Boride Products Inc., 2879 Aero Park Drive, Traverse City, Michigan 49684
1	Dr. Charles Berg, Chief Engineer, Federal Power Commission, Room 2100 825 North Capital Street, N.E., Washington, D.C. 20426
1	Mr. Michael Lauriënte, Department of Transportation, 400 Seventh Street, S. W., Washington, D.C. 20590
1	Dr. Donald Vieth, National Bureau of Standards, Administration Bldg., Room A1002, Washington, D.C. 20234
1	Dr. Leonard Topper, National Science Foundation, Office of Energy R & D Policy, Room 537, 1800 G Street NW, Washington, D.C. 20550
2	Electric Power Research Institute, P.O. Box 10412, Palo Alto, California 94304 ATTN: Dr. Richard E. Balzhiser, Dr. Arthur Cohn
1	W. C. Christensen, Assistant for Resources, Directorate for Energy, OASD (I&L), Room 2B341 Pentagon, Washington, D.C. 20301
1	Mr. Tyler Port, Special Assistant, OASA (I&L), Room 3E620 Pentagon, Washington, D.C. 20301
1	Major Jose Baca, Hdqtrs., Air Force Systems Comman/DLFP, Propulsion and Power Branch, Andrews Air Force Base, Washington, D.C. 20034
1	Mrs. Patricia Mooney, Office of Management and Budget, Energy R&D Coordination Branch, Room 8001, New Executive Office Bldg., Washington, D.C. 20503
1	James Johnson, Environmental Protection Agency, Air Technology Branch, RD-681, Room 621 W, 401 M Street, N.W., Washington, D.C. 20490
1	Mr. Thomas Gross, Staff Member, Office of Energy Conservation, Federal Energy Office, Room 4234, Columbia Plaza Bldg., Washington, D.C. 20461

ARMY MATERIALS AND MECHANICS RESEARCH CENTER
WATERTOWN, MASSACHUSETTS 02172

TECHNICAL REPORT DISTRIBUTION

No. of Copies	To
1	Dr. John S. Foster, Jr., Vice President for Energy Research and Development, TRW Incorporated, One Space Park, Redondo Beach, California 90278
1	Dr. Raymond Bisplinghoff, Deputy Administrator, National Science Foundation, 1800 G. Street, N.W., Washington, D.C. 20550
1	Dr. Alan Womack, Assistant Director, Gas Cooled Reactors, Atomic Energy Commission, Washington, D.C. 20545
1	Dr. Donald Weidhuner, Chief, Power Division, Research Development & Engineering Directorate, Army Materials Command Headquarters, 5001 Eisenhower Avenue, Alexandria, Virginia 22304
1	Dr. A. Lovelace, Deputy Assistant Secretary (R&D), Office of Assistant Secretary of the Air Force (Research & Development), Room 4E973, Pentagon, Washington, D.C. 20330
1	Dr. Neal Richardson, TRW Incorporated, One Space Park, Redondo Beach, California 90278
1	Mr. Roy Peterson, Chief, Pollution Abatement & Gas Turbine Research Ship Research & Technology Division, Naval Ship Systems Command Hqtrs., 2531 Jefferson Davis Highway, Arlington, Virginia 20362
1	Dr. Eugene C. Gritton, The Rand Corporation, Physical Sciences Department, 1700 Main Street, Santa Monica, California 90406
1	Mr. C. A. Vassilakis, Turbo Power & Marine Systems, New Britain Ave., Farmington, Conn. 06032
3	Authors
278	Total copies distributed

D16

Army Materials and Mechanic Research Center,   AD
Watertown, Massachusetts 02172

BRITTLE MATERIALS DESIGN
HIGH TEMPERATURE GAS TURBINE

Arthur F. McLean, Eugene A. Fisher, Ford
Motor Company, Dearborn, Michigan 48121
Raymond J. Bratton, Westinghouse Electric
Corporation, Pittsburgh, Pennsylvania 15235

Technical Report AMMRC CTR 74-26, April, 1974
178 pps, 135 illus, 27 tables, Contract
DAAG 46-71-C-0162, ARPA Order Number 1849,
Fifth Interim Report, July 1, 1973 to
December 31, 1973

Key Words

Gas turbine engine
Brittle design
Ceramics
High temperature materials
Silicon nitride
Silicon carbide
Non-destructive tests
Mechanical properties

The "Brittle Materials Design, High Temperature Gas Turbine" program is to demonstrate successful use of brittle materials in demanding high temperature structural applications. A small vehicular gas turbine and a large stationary gas turbine, each utilizing uncooled ceramic components, will be used in this iterative design and materials development program. Both the contractor, Ford Motor Company, and the subcontractor, Westinghouse Electric Corporation, have had in-house research programs in this area prior to this contract.

In the vehicular turbine project, Weibull theory was utilized to predict failure probabilities of monolithic hot pressed silicon nitride turbine rotors, including the effects of varying disk contours. Good agreement with theory resulted from strength testing of silicon nitride bars and disks. Processing parameters were established for the fabrication of multi-density rotors, and a number of prototype rotors were spin tested. Thermal response of stator vanes during engine operation was determined directly using a quartz window in a stator test rig. Improvements in properties were made for both injection molded and slip cast reaction sintered silicon nitride.

In the stationary turbine project, a major objective was achieved when the first static rig test of hot pressed silicon nitride stator vanes was completed at temperatures up to 2200°F. Although some vanes failed due to out-of-tolerance final machining of critical interfaces, it was encouraging that two vanes which were subjected to the highest temperatures and most severe transient effects were not damaged. Additional information was also generated on the properties and corrosion resistance of hot pressed silicon nitride.

Key Words

Gas turbine engine
Brittle design
Ceramics
High temperature materials
Silicon nitride
Silicon carbide
Non-destructive tests
Mechanical properties

The "Brittle Materials Design, High Temperature Gas Turbine" program is to demonstrate successful use of brittle materials in demanding high temperature structural applications. A small vehicular gas turbine and a large stationary gas turbine, each utilizing uncooled ceramic components, will be used in this iterative design and materials development program. Both the contractor, Ford Motor Company, and the subcontractor, Westinghouse Electric Corporation, have had in-house research programs in this area prior to this contract.

In the vehicular turbine project, Weibull theory was utilized to predict failure probabilities of monolithic hot pressed silicon nitride turbine rotors, including the effects of varying disk contours. Good agreement with theory resulted from strength testing of silicon nitride bars and disks. Processing parameters were established for the fabrication of multi-density rotors, and a number of prototype rotors were spin tested. Thermal response of stator vanes during engine operation was determined directly using a quartz window in a stator test rig. Improvements in properties were made for both injection molded and slip cast reaction sintered silicon nitride.

In the stationary turbine project, a major objective was achieved when the first static rig test of hot pressed silicon nitride stator vanes was completed at temperatures up to 2200°F. Although some vanes failed due to out-of-tolerance final machining of critical interfaces, it was encouraging that two vanes which were subjected to the highest temperatures and most severe transient effects were not damaged. Additional information was also generated on the properties and corrosion resistance of hot pressed silicon nitride.

DOCUMENT CONTROL DATA - R & D

(Security classification of title, body of abstract and indexing annotation must be entered when the overall report is classified)

1. ORIGINATING ACTIVITY *(Corporate author)*	2a. REPORT SECURITY CLASSIFICATION
Ford Motor Company	Unclassified
Dearborn, Michigan 48121	2b. GROUP

3. REPORT TITLE

Brittle Materials Design, High Temperature Gas Turbine

4. DESCRIPTIVE NOTES *(Type of report and inclusive dates)*

Interim Report Number 5, July 1, 1973 to December 31, 1973

5. AUTHOR(S) *(First name, middle initial, last name)*

Arthur F. McLean
Eugene A. Fisher
Raymond J. Bratton

6. REPORT DATE	7a. TOTAL NO. OF PAGES	7b. NO. OF REFS
April, 1974	178	18

8a. CONTRACT OR GRANT NO.	9a. ORIGINATOR'S REPORT NUMBER(S)
DAAG 46-71-C-0162	
b. PROJECT NO.	AMMRC-CTR 74-26
ARPA Order No. 1849	
c.	9b. OTHER REPORT NO(S) *(Any other numbers that may be assigned this report)*
Project Code No. 1D10	
d. Agency Accession No. DA OD 4733	

10. DISTRIBUTION STATEMENT Distribution limited to U.S. Government agencies only; Test and Evaluation data; April, 1974. Other requests for this document must be referred to the Director, Army Materials & Mechanics Research Center, ATTN: AMXMR-PL, Watertown, Massachusetts 02172

11. SUPPLEMENTARY NOTES	12. SPONSORING MILITARY ACTIVITY
	Army Materials and Mechanics Research Center, Watertown, Massachusetts 02172

13. ABSTRACT

ABSTRACT

The "Brittle Materials Design, High Temperature Gas Turbine" program is to demonstrate successful use of brittle materials in demanding high temperature structural applications. A small vehicular gas turbine and a large stationary gas turbine, each utilizing uncooled ceramic components, will be used in this iterative design and materials development program. Both the contractor, Ford Motor Company, and the subcontractor, Westinghouse Electric Corporation, have had in-house research programs in this area prior to this contract.

In the vehicular turbine project, Weibull theory was utilized to predict failure probabilities of monolithic hot pressed silicon nitride turbine rotors, including the effects of varying disk contours. Good agreement with theory resulted from strength testing of silicon nitride bars and disks. Processing parameters were established for the fabrication of multi-density rotors, and a number of prototype rotors were spin tested. Thermal response of stator vanes during engine operation was determined directly using a quartz window in a stator test rig. Improvements in properties were made for both injection molded and slip cast reaction sintered silicon nitride.

In the stationary turbine project, a major objective was achieved when the first static rig test of hot pressed silicon nitride stator vanes was completed at temperatures up to 2200°F. Although some vanes failed due to out-of-tolerance final machining of critical interfaces, it was encouraging that two vanes which were subjected to the highest temperatures and most severe transient effects were not damaged. Additional information was also generated on the properties and corrosion resistance of hot pressed silicon nitride.

DD FORM **1473** REPLACES DD FORM 1473, 1 JAN 64, WHICH IS OBSOLETE FOR ARMY USE.

14 KEY WORDS	LINK A		LINK B		LINK C	
	ROLE	WT	ROLE	WT	ROLE	WT
Gas turbine engine						
Brittle design						
Ceramics						
High-temperature materials						
Silicon nitride						
Silicon carbide						
Non-destructive tests						
Mechanical properties						